COMBUSTION, THERMAL AND EMISSION CHARACTERISTICS OF LAMINAR PREMIXED BIOGAS-HYDROGEN BUNSEN FLAME

WEI ZHILONG

Ph.D

The Hong Kong Polytechnic University

2018

The Hong Kong Polytechnic University

Department of Mechanical Engineering

COMBUSTION, THERMAL AND EMISSION CHARACTERISTICS OF LAMINAR PREMIXED BIOGAS-HYDROGEN BUNSEN FLAME

WEI Zhilong

A thesis submitted in partial fulfillment of the requirements for the Degree of Doctor of Philosophy

June 2017

CERTIFICATE OF ORIGINALITY

I hereby declare that this thesis is my own work and that, to the best of my knowledge and belief, it reproduces no material previously published or written, nor material that has been accepted for the award of any other degree or diploma, except where due acknowledgement has been made in the text.

_____ (signed)

WEI ZHILONG (name of student)

Abstract

The objective of this study is to improve the understanding on the fuel characteristics of biogas-hydrogen mixture and then promote the real applications of biogas fuel. Both experimental measurements and numerical simulations were carried out so as to investigate the combustion, thermal and emission characteristics of biogas-hydrogen flames. In the study, biogas is composed of CH_4 and CO_2 and represented by BGXX, with XX representing the volumetric ratio of CH_4 in the biogas, while hydrogen is adopted as the addition to improve fuel features of biogas. Heat fluxes, flame temperature and pollutant emissions of laminar premixed biogas-hydrogen impinging flames were measured experimentally. In addition, a one-dimensional computational model was developed using the Chemkin software to calculate the heat release rate and obtain the relative significances of exothermic reactions of biogas-hydrogen flames while a two-dimensional computational model was developed using the STAR-CD software to calculate the pollutant emissions of biogas-hydrogen impinging flames. In this study, effects of H_2, CO_2, nozzle-to-plate distance (H), equivalence ratio (ϕ) and Reynolds number (Re) on the heat release, heat transfer and pollutant emission features of laminar premixed biogas-hydrogen flames were investigated quantitatively.

For the heat release features of biogas-hydrogen flames, the complete combustion results in the maximum global heat release rate (HRR) at ϕ=1.0, while the exothermic recombination of intermediates gives rise to the enhanced HRR in the post flame region at ϕ=1.2. The primary exothermic reactions of biogas-hydrogen mixture are dominated by ϕ, and $O+CH_3=H+CH_2O$, $H+CH_3(+M)=CH_4(+M)$, $OH+H_2=H+H_2O$, $OH+CO=H+CO_2$ and $O+CH_3=>H+H_2+CO$ can play critical roles in HRR consistently with the varied ϕ. With the H_2 enrichment, $H+HO_2=2OH$ and $H+O_2=OH+H$ are accelerated effectively, leading to the enhanced HRR of the biogas-hydrogen flame, and the contributions of $OH+H_2=H+H_2O$ and $OH+H+M=H_2O+M$ on HRR are enhanced most evidently. As the CO_2 proportion in the biogas is increased, the global HRR of the biogas-hydrogen flame is reduced by the dilution/thermal effect and further aggravated by the chemical effect, and the contributions of $H+CH_3(+M)=CH_4(+M)$ and $OH+H_2=H+H_2O$ on HRR are enhanced. Furthermore, the $O+CH_3$ reactions are found to have the stable contributions on HRR of the biogas-

hydrogen flame, and the $O \times CH_3$ product is demonstrated to be a reliable indicator to reflect HRR variations in the premixed flame with the unclear equivalence ratio.

With respect to heat transfer characteristics of biogas-hydrogen flames, the total heat transfer rate of biogas-hydrogen impinging flame can be enhanced with the increased H_2. This improvement can be attributed to the enhanced flame temperature leading to the larger temperature difference and the stronger fuel diffusivity resulting in the larger heating area with high temperatures. With the increased CO_2 proportion in the biogas, its dilution and chemical effects lead to the worst heating performance of BG50-H_2 flames. Whereas, a suitable proportion of CO_2 in the fuel can reduce the decline of flame temperature in the wall jet region thanks to the larger specific heat capacity and the increased flame height, which leads to the better heating performance of the BG75-H_2 flame than that of the CH_4-H_2 flame. Thus the BG75-H_2 fuel could be a substitute of CH_4-H_2 fuel for the flame impingement heating. In addition, an empirical correlation, as a function of Pr, u/S_L and ϕ, is obtained to determine the optimal heating distance of laminar premixed Bunsen flame quantitatively.

For the pollutant emissions of biogas-hydrogen flames, the EICO is increased initially and then dropped as H is increased. The contributions of N_2O and thermal routes on the EINOx are enhanced with H, while that of prompt NO is decreased, and the contribution of NNH routes keeps relatively stable with H. The $EINO_2$ and the NO_2/NOx ratio achieve their peak values as the H is slightly less than the flame height. With the increased ϕ, EICO is enhanced evidently due to the incomplete fuel oxidization while contributions of different routes on the EINOx are changed, and the improved prompt NO leads to the higher EINOx, as well as its different profile with H, at the fuel-rich condition. The $EINO_2$ is increased with ϕ while the NO_2/NOx ratio is codetermined by concentrations of H and O_2 in the air mixing region and contribution variations of different routes on NO formation. With the increased Re, the EICO is dropped at small H but enhanced at large H while the EINOx is increased due to the improved prompt NO production. In addition, with the increased Re, the $EINO_2$ and the NO_2/NOx ratio are both decreased at small H but increased at large H.

With the hydrogen addition, the EICO is enhanced steadily due to the H_2 oxidation competing for the OH radical. In addition, with the increased H_2, the EINOx is enhanced due to the enhanced flame temperature and the increased active radicals, and

the contribution of prompt NO is decreased while that of other routes are increased steadily. With the increased H_2, $EINO_2$ is enhanced steadily thanks to the improved HO_2 production in the air mixing region, while the NO_2/NOx ratio is increased at small *H* but decreased at large *H*. As the CO_2 content is decreased in the biogas, the enhanced EICO at small *H* is caused by the better premixed combustion, while the declined EICO at large *H* is resulted from the larger post-flame region, intensive air entrainment and longer residence time. With the decreased CO_2 content, the EINOx is enhanced owing to increased active radicals and higher flame temperature, and the contributions of thermal NO and N_2O route are increased, while that of prompt NO and NNH route are dropped gradually. With the decreased CO_2 content, the $EINO_2$ is increased steadily while the NO_2/NOx ratio is decreased gradually.

List of Publications

1. **Z.L. Wei**, C.W. Leung, C.S. Cheung, Z.H. Huang. Effects of H2 and CO2 addition on the heat transfer characteristics of laminar premixed biogas–hydrogen Bunsen flame. *International Journal of Heat and Mass Transfer*, 2016, 98: 359-366.

2. **Z.L. Wei**, C.W. Leung, C.S. Cheung, Z.H. Huang. Effects of equivalence ratio, H2 and CO2 addition on the heat release characteristics of premixed laminar biogas-hydrogen flame. *International Journal of Hydrogen Energy*, 2016, 41(15): 6567-6580.

3. **Z.L. Wei**, H.S. Zhen, C.W. Leung, C.S. Cheung, Z.H. Huang. Heat transfer characteristics and the optimized heating distance of laminar premixed biogas-hydrogen Bunsen flame impinging on a flat surface. *International Journal of Hydrogen Energy*, 2015, 40(45): 15723-15731.

4. **Z.L. Wei**, H. S. Zhen, C.W. Leung, C.S. Cheung, Z.H. Huang. Experimental and numerical study on the emission characteristics of laminar premixed biogas-hydrogen impinging flame. *Fuel*, 2017, 195: 1-11.

5. **Z.L. Wei**, C.W. Leung, C.S. Cheung, Z.H. Huang. Single-valued prediction of markers on heat release rate for laminar premixed biogas-hydrogen and methane-hydrogen flames. *Energy*, 2017, 133: 35–45.

Acknowledgements

I would like to express my sincerest appreciation to my supervisors, Prof. C.W. Leung (The Hong Kong PolyU), Prof. C.S. Cheung (The Hong Kong PolyU) and Prof. Z.H. Huang (Xi'an JiaoTong University) for their guidance and assistance in the past three years. Their expertise and patience are admirable, and their dedication to research work always inspires me to work hard and overcome difficulties in the research study. They provide many professional and valuable suggestions to help me solving my confusion and difficulty of my study. Without their help, my graduate experience cannot be so productive and my dissertation would not be completed successfully.

I would also acknowledge the stipend and research fund supported by The Hong Kong Polytechnic University and the software (Chemkin & Star-CD) supported by Xi'an Jiao Tong University. Additionally, I need to give my sincere thanks to the lab technicians Dr. Tse and Mr. Tsang who gave helpful advices and considerable assistance regarding experiments. Also I would like to appreciate the lab members, Dr. Zhen Haisheng, Dr. Miao Jing, Mr. Man Xingjia, Dr. Fu jin, Mr. Wei Long, Mr. Guan Chun, Mr. Yang Ke and Ms. Zhou Quan who give kindly assistance and support in my experiments and research. I am also grateful to my dear friends, Mr. Liu Menglong, Mr. Wang Kai, Mr. Hu Qi, Mrs. Wang Meng, Mr. Li Yehai, Ms. Zhang Hao and Mr. Liao Yaozong for sharing the inspired discussions and accompanying me to have an impressive campus life.

Most importantly, I would like to express my special thanks to my family members, especially my wife. Their encouragement, unconditional love and understanding are the significant driving force of my study.

Table of Content

List of Figures

List of Tables

Nomenclature

A	Heating area, m^2
A_c	Sectional area of steam flowing to the flame, m^2
B	The constant in the Arrhenius equation
c_{CO2}	Measured volumetric concentration of CO_2, ppm
c_N	Measured volumetric concentration of pollutant N, ppm
c_p	Specific heat capacity of the mixture, kJ/(kg·K)
c_{pk}	Specific heat capacity of the kth species, kJ/(kg·K)
D	Nozzle diameter, mm
D_k	Thermal diffusion coefficient of kth species, m^2/s
E_a	Activation energy of reaction, kJ/mol
EI	Emission index, g/kg
$F_{h,j}$	Diffusional energy flow component in the x_j direction, kJ/(m^2·s)
$F_{k,j}$	Diffusional flux component of kth species in the x_j direction, kg/(m^2·s)
$f(z)$	Standard normal probability distribution function
f_c	Contribution of a reaction, %
H	Nozzle-to-plate distance, mm
$H_{flame.}$	Flame height, mm
H_m	Optimal heating distance, mm
h_k	Specific enthalpy of the kth species, kJ/mol
h	Static enthalpy of fluid, kJ/mol
k_f	Reaction rate constant of the forward reaction
M_{fuel}	Molecular weight of fuel, g/mol
M_N	Molecular weight of pollutant N, g/mol

$\dot{M}$	Mass flow rate, kg/s
m_{biogas}	Mass fraction of biogas in the biogas-hydrogen mixture
n_c	Moles of carbon contained in a mole of fuel, mol
Pr	Prandtle number
p	Pressure, Pa
Q	Total heat release of all reactions in the reaction zone, kJ/(m^2·s)
q_{local}	Measured local heat flux, kW/m^2
q_{r}	Total heat release of a reaction in the reaction zone, kJ/(m^2·s)
q_{total}	Calculated total heat transfer rate, kW
R	The universal gas constant, J/(mol·K)
Re	Reynolds number of unburned gases
r	Radius of heating area, mm
s_h	Energy source, kJ/(m^3·s)
s_i	Momentum source, N/m^3
s_k	Mass production rate of kth species, kg/(m^3·s)
s_m	Mass source, kg/(m^3·s)
T	Temperature, K
T_{max}	Maximum flame temperature, K
t	Time, s
u	Fluid velocity, m/s
u_i	Absolute velocity component in the x_i direction, m/s
$\dot{V}_{CH4}$	Volumetric flow rate of methane, L/min
$\dot{V}_{CO2}$	Volumetric flow rate of carbon dioxide, L/min
$\dot{V}_{H2}$	Volumetric flow rate of hydrogen, L/min
$\dot{V}_{air}$	Volumetric flow rate of air, L/min

$\dot{V}_{fuel}$	Volumetric flow rate of fuel, L/min
v_k	Diffusional velocity of the *k*th species, m/s
$\mathcal{V}_{\mathrm{k}}$	The ordinary diffusion velocity term, m/s
$\nu''_{r,k}$	Stoichiometric coefficient of *k*th species in reaction *r* in the products
$\nu'_{r,k}$	Stoichiometric coefficient of *k*th species in reaction *r* in the reactants
$\overline{W}$	Mean molecular weight of mixture, g/mol
W_k	Molecular weight of *k*th species, g/mol
$\mathcal{W}_{\mathrm{k}}$	The thermal diffusion velocity, m/s
w_{r}	Net reaction rate of reaction *r*, mol/(L·s)
X_{Hmax}	Maximum mole fraction of H radical
X_k	Mole fraction of the *k*th species
x	Spatial coordinate for 1-D flame, m
x_i	Cartesian coordinate system (i=1, 2, 3), m
Y_k	Mass fraction of the *k*th species
$\alpha_{\mathrm{H_2}}$	Volume fraction of hydrogen in the fuel
β	Temperature exponent in the Arrhenius equation
χ	Calculated result
$\overline{\chi}$	The mean of multiple measurements
χ_n	Measured value of *n*th measurement
$\delta\chi$	The overall uncertainty of a variable
$\delta\chi_n$	The uncertainty of χ_n
ϕ	Equivalence ratio
λ	Thermal conductivity of mixture, J/(m·K·s)

ρ	Mass density, kg/m^3
σ	Standard deviation of experimental measurements
τ_{ij}	Pressure tensor component, Pa
$\dot{\omega}_k$	Molar rate of production by reactions of the *k*th species, mole/(m^2·s)

Abbreviations

CHP	Combined heat and power
CI	Compression ignition
DME	Dimethyl ether
GHG	Greenhouse gases
HRR	Heat release rate
IDF	Inversed diffusion flame
LNG	Liquid natural gas
LPG	Liquid petroleum gas
PDF	Probability distribution function
PLIF	Planar laser-induced fluorescence
RTFO	Renewable Transport Fuel Obligation
SI	Spark ignition
TCHR	Thermochemical heat release

1 Introduction

1.1 Biogas and Hydrogen

At present, thanks to the widespread availability and convenience of gaseous and liquid fossil fuels, they are used extensively with respect to the electricity generation, transportation vehicle and heating appliances and their usage can satisfy a considerable proportion of the world energy demand [1]. However, due to the continuous and fast growth of world energy demand, the drastically increased consumption of fossil fuels leads to a large amount of pollutant emissions released into the air, which has caused several adverse environmental concerns, such as climate change and acid rain. Furthermore, it is known that the fossil fuel formation requires millions of years typically, thus its finite reserve seems to be difficult to accommodate the increase of world energy demand in the future. Consequently, in order to cope with the explosively growing demand on energy production and increasing concerns on the environmental issues, more and more efforts have been made to explore and study the sustainable and environmentally friendly fuel in recent decades.

Biogas, which can be produced by the anaerobic digestion or fermentation of biodegradable materials, is considered to be an excellent renewable and sustainable fuel in the future and has attracted increased attention in recent years. In Germany, biogas is primarily utilized for the combined heat and power (CHP) generation, and the amount of biogas-based power plants has been increased apparently over the last few decades [2]. In Sweden, the CHP plants fuelled by biogas are also promoted extensively, and the amount of biogas utilized as the vehicle fuel accounts for an enhanced part of total biogas production [3]. The Renewable Transport Fuel

Obligation (RTFO) established by the UK government is expected to promote the biofuels utilization in the country [4]. European Union expects to replace 10% of fuels used in the transportation system with the biofuels by 2020 [5]. In Brazil, the biogas is expected to supply the bus fleet so as to substitute a part of fossil fuels and then reduce the fuel costs and greenhouse gases (GHG) emission [6]. Besides, biogas has been widely utilized for heating purpose in China and its consumption is expected to be increased rapidly in the future [7].

Biogas can be generated from various materials such as sewage, municipal waste and crops, thus its composition can be changed significantly at different areas. Typically, the main compositions in the biogas are methane (CH_4, 40-80%) and carbon dioxide (CO_2, 20-60%), while water (H_2O), nitrogen (N_2), hydrogen (H_2) and hydrogen sulphide (H_2S) can also accounts for a small part of biogas [8-11]. In addition, compared to the traditional gaseous fossil fuels, such as liquid petroleum gas (LPG), biogas does not contribute to the increase in GHGs thanks to its short carbon cycle [12]. Although biogas has several advantages in the aspect of GHGs reduction and resource-efficiency, the existence of carbon dioxide in the biogas and its variable compositions make it to suffer some drawbacks which can restrain its practical applications in the combustion devices. Compared to the natural gas, it is apparent that the heating value of biogas can be much lower due to the reduced combustible component in the fuel. As a result, although most of biogas in the world can be used to generate heat and electricity directly via the CHP system, the development of biogas utilized in CHP production is still inhibited considerably due to its lower heating value [13]. Furthermore, the chemical and thermal effects of carbon dioxide can drastically influence the combustion characteristics, such as laminar burning velocity, flame temperature, flammability and combustion efficiency [14-17], which causes several

difficulties of biogas utilization in combustion engines. In addition, it may be complicate to design a combustion facility fueled by biogas because its variable compositions can lead to the variable fuel characteristics and combustion processes. In conclusion, considering its sustainable and renewable feature, biogas is expected to be utilized more extensively in a variety of combustion facilities to replace a larger part of fossil fuels. In order to achieve this purpose, some targeted technologies and techniques need to be developed and adopted to improve the fuel features of raw biogas and/or promote its practical applications and development.

In recent years, several related technologies and techniques have been proposed and developed so as to promote the biogas utilization in the combustion facilities, which can compensate or minimize primary disadvantages of biogas while maintaining its environmentally friendly feature. Among these available methods, they can be roughly divided into two aspects: developing the new combustion technology and promoting fuel characteristics.

For the method of developing new combustion technology, it can utilize the biogas directly by eliminating its drawbacks with the specific combustion control or the particularly designed combustor, however it might be restricted to the limited combustors or conditions due to the particular requirements and designs. An attractive technology in this aspect is the mild combustion mode. The mild combustion or flameless combustion, as a comparatively new proposed combustion mode, has been regarded as a promising combustion technology which has attracted increasing attentions in recent years [18-20]. For the mild combustion mode, the fuel is injected into the combustion chamber with the high temperature oxidizer which provides the energy required for the sustained chemical reactions. During the combustion process,

chemical reactions can proceed comparatively slowly and then lead to the relatively moderate heat release. Consequently, compared to the traditional high temperature combustion, the mild combustion is featured by the relatively lower combustion temperature and homogeneous temperature distribution in the combustion device [21]. Considering characters of the mild combustion mode, it is thus known that it can neglect the fuel drawback of low calorific value and could be quite suitable for the biogas combustion. For example, with the mild combustion technology, the biogas combustion can reduce the emission generation and obtain the high efficiency in the CHP system [13]. Whereas, due to its unique combustion control, the mild combustion of biogas is not likely to be utilized extensively in the real combustion equipment [22].

Compared with developing the new combustion technology, the improvement on the fuel characteristics is considered to be a more effective method to improve the biogas utilization, because it has the possibility to make the improved biogas fuel to be an eligible substitute of the conventional gaseous fossil fuels and then directly adopted in a variety of existed combustion equipment. With respect to improving the fuel characteristics of biogas, some critical factors need to be considered by the combustion researchers and engineers in advance. Compared to the conventional fossil fuels, the improved biogas fuel needs to not only have the improved fuel economy and the reduced pollutant emission, but also have the ability to maintain the similar level of outstanding performance, durability and reliability. For the sake of satisfying these requirements, the biogas upgrading and dual fuel mode are proposed as two possible solutions to improve the fuel characteristics. The biogas upgrading can enhance the heating value of biogas by removing non-combustible gases from raw biogas. Several upgrading techniques including cryogenic, chemical absorption and

membrane have been proposed and developed [9, 23-25]. The product obtained by utilizing these techniques would be composed of almost pure methane content, which means that the product could have the similar features to that of the natural gas. Thus the upgraded biogas can be not only transported and stored conveniently using the existed facilities of the natural gas, but also directly adopted in various combustion devices fuelled by methane or natural gas. Nevertheless, the biogas upgrading process is relatively complicated and expensive, which is regarded as a major barrier for its practical development [25]. For the dual-fuel mode, it is a conventional and efficient technique to improve the fuel characteristics and obtain a desirable combustion process. Thanks to the different features of fuels, the fuel characteristics of the hybrid mixture can be modified properly through varying the proportions of two fuels in the mixture. In the practical applications, it is general that one fuel is regarded as the addition that is introduced into another fuel to improve its combustion characteristics, and the availability and reliability of this method have been discussed and evaluated by plenty of works [26-30]. Compared to the new combustion technology and the biogas upgrading, the dual-fuel mode has several obvious advantages in the aspect of lower cost and the better applicability in the combustors. Specifically, the dual-fuel mode has the possibility to improve the fuel characteristics of biogas effectively with a relatively lower cost while promote the applicability of biogas combustion in the various combustion devices simultaneously.

For the biogas, its low calorific value, as a primary barrier of its applications, can be promoted effectively by blending it with another high-calorific-value hydrocarbon fuel such as LPG and propane. Several researches have been carried out to explore the applicability of this method. Lee et al. [31] compared the flame stabilities of biogas, biogas-CH_4 and biogas-C_3H_8 fuels experimentally using the domestic appliances and

swirl combustors. The improvements on the burning velocity and flame stability of biogas blended fuels are reported in their study. Lee et al. [32] performed another experiment to explore the interchangeabilities of biogas-LPG fuel in the aspect of applications in domestic combustors, and found that the biogas-LPG fuel with a suitable proportion of LPG can be eligible to be used in the existing appliances directly. Cardona et al. [33] measured the laminar burning velocity of biogas-propane-hydrogen mixture and proposed that this mixture can be regarded as a substitute of the natural gas due to the similarity of their Wobbe Indexes and flame speeds. These researches demonstrate that biogas-mixed fuel can be a feasible and effective method to improve the biogas combustion or even make it to be an eligible substitute of LPG or liquid natural gas (LNG).

Hydrogen (H_2), as a carbon-free gaseous fuel, has been widely accepted as an almost perfect clean energy and has a promising prospect in combustion engineering. Hydrogen has the excellent mass-basis calorific value which makes it to be adaptable to various combustion devices in domestic, industrial and transportation fields. In addition, since no carbon atom is contained in the hydrogen, the product of hydrogen combustion is almost pure water vapour and does not contribute to the GHGs emissions. Although the high temperature of hydrogen combustion may give rise to the NOx generation, the amount of pollutant emissions produced during the hydrogen combustion process can be much lower than that of the hydrocarbon fuel. Besides, due to the high reactivity and diffusivity of hydrogen, it has the low minimum ignition energy, extensive flammability and the quite high flame propagation speed [34, 35]. These above mentioned characteristics make the hydrogen to be a potential excellent addition to improve fuel and combustion characteristics of hydrocarbon fuels. In recent decades, numerous works have been conducted to investigate influences of the

hydrogen enrichment on the fuel characteristics of methane, propane and butane, and suggest the distinct improvement of hydrogen addition on the fuel and combustion characteristics, such as the enhanced flame propagation speed, the improved flame stability and the extended flammability limits [36-39]. For the biogas, its low calorific value, narrow flammability and lower laminar burning velocity are the major defects to hamper its real applications which are likely to be improved by using the hydrogen enrichment in consideration of the excellent features of hydrogen. Consequently, the biogas-hydrogen fuel would have a promising prospect in promoting practical applications of the biogas in various combustion devices.

Compared to the biogas-hydrocarbon fuels, the biogas-hydrogen mixture has some apparent superiority with respect to GHGs emissions and resource efficiency. Firstly, there is no further GHGs emission contribution. The reason is obvious that biogas does not contribute to the GHGs emission due to its short carbon cycle while the hydrogen combustion releases no GHGs emission since its product is water. Secondly, as an important energy carrier, hydrogen can be produced by various resources via different production technology [40, 41]. Specifically, the fossil fuels such as methane, coal and oil can be used to produce the hydrogen via the reforming or gasification process. In addition, with the electrolysis technique, hydrogen can be obtained by splitting the water molecules into hydrogen and oxygen molecules in the electrolyser facility. Another method to produce hydrogen is to use the sustainable energy, such as wind energy and nuclear energy, to convert water into hydrogen and oxygen via the electrolysis or thermal decomposition processes. Apart from the above methods, a more environmental friendly technique for the hydrogen production is using biological techniques such as nitrogenase and hydrogenase to produce the hydrogen from the biomass materials, which requires lower energy input and less initial investment cost

compared to the fossil gasification and the electrolysis of water. Overall, it is known that both hydrogen and biogas can be obtained from a variety of materials. Hence, the biogas-hydrogen mixture can still maintain the sustainable and renewable features, which can provide a brighter prospect of its utilization in the future than that of the biogas-hydrocarbon mixture. Besides, compared to other hydrocarbon fuels, hydrogen seems to be more suitable as an addition for biogas fuel. Some critical fuel characteristics of hydrogen, methane, propane and butane are summarized and compared in Table 1.1 [42-48]. It can be seen that, compared to properties of other hydrocarbon fuels, the hydrogen has the much higher heating value, quite extensive flammability limit, dramatically lower minimum ignition energy and extremely high flame speed, which means that blending hydrogen could be more effective to promote fuel characteristics of biogas than that of blending other gaseous hydrocarbon fuels. In conclusion, the biogas-hydrogen mixture is expected to have the superior performance than that of biogas mixed with hydrocarbon fuels.

Table 1.1 The physical and chemical properties of hydrogen, methane, propane and butane [42-48].

Property	**Hydrogen**	**Methane**	**Propane**	**Butane**
Molecular weight (g/mol)	2.016	16.04	44.10	58.12
Higher heating value (MJ/kg)	142.0	55.5	50.2	49.5
Lower heating value (MJ/kg)	120.0	50.0	46.3	45.3
Flammability limits (vol. %)	4.0-75.0	5.3-15.0	2.1-10.4	1.8-8.4
Diffusion coefficient in NTP air (cm^2/s)	0.78	0.16	0.10	0.10
Minimum ignition energy at stoichiometric condition (mJ)	0.02	0.3	0.25	0.25
Peak flame speed in NTP air (cm/s)	265-325	37-45	35-42	34-42

Whereas, it should be noted that there still exist several problems when using the biogas-hydrogen mixture as the fuel. For the hydrogen, it can be obtained by different techniques from a variety of resources, but there exists a trade-off between its production capacity and its production cost for a specific technology [40]. In addition,

thanks to its smallest molecule, low density and wide flammability limit, the hydrogen storage and delivery still have several challenges with respect to the storage capacity, delivery cost and the safety [41]. Besides, for the biogas-hydrogen mixture, the existence of carbon dioxide could affect the effectiveness of hydrogen addition as its amount is varied in the biogas. Considering the physical and chemical properties of carbon dioxide, it has the possibility to negate effects of the constant hydrogen enrichment as the proportion of carbon dioxide is comparatively high, which means that the optimum hydrogen addition may need to be adjusted properly according to the specific biogas composition. Apart from this, due to the existence of carbon dioxide in the biogas fuel, the large discrepancy between the diffusivity of biogas and hydrogen might exert some influences on the combustion process in the flame, especially for the diffusion flame whose combustion is more dependent on the diffusion of different species. Furthermore, as the hydrogen accounts for a relatively large part of fuel, its high mass diffusivity and reactivity can affect the flame front structure considerably while the water vapour, as the product of hydrogen combustion, can influence the radiation features of flame due to its triatomic molecular structure. Additionally, effects of hydrogen addition on the CO emission of biogas fuel are unclear because it is codetermined by the dilution effects and chemical effects of hydrogen enrichment, as well as the chemical effects of carbon dioxide. Hence, for the sake of the real utilization and development of biogas-hydrogen fuel, much more efforts are needed to study the complicate combustion process of biogas-hydrogen mixture and understand the interactions between these two fuels in the flame.

1.2 Laminar premixed Bunsen flame

In the various real combustion facilities, such as combustion engine, combustion turbine and furnace, one of most common and significant combustion patterns is the turbulent premixed combustion. For the turbulent premixed combustion, the turbulence and combustion are coupled intimately in the flame, and their interactions are quite complex owing to the wide ranges of time scale and length scale of the turbulence and chemical reactions in the flame, as well as the sensitive dependence of turbulence and combustion parameters on the drastically varied flame temperature. As a result, it is difficult to study the turbulent premixed combustion process directly by conducting the experiment and/or adopting the theoretical analysis. Generally, in order to deal with this dilemma, the simplified models to describe the phenomenon, as well as the simplified theory based on several reasonable hypotheses, are adopted to simplify problems related to the complex combustion process and then study the major interested features of the turbulent premixed combustion.

In order to facilitate the modeling of turbulent premixed combustion, the turbulent combustion diagram developed by Borghi [49] and Peters [50] can be used to determine the regime of turbulent premixed combustion. On the basis of velocity and length scale ratios, three regimes of turbulent premixed combustion are defined, namely the flamelet zone, the thin reaction zone and the broken reaction zone. In the practical combustion facilities, the turbulent premixed combustion is primarily located in the flamelet zone [50]. Therefore, the flamelet concept is utilized extensively for the turbulent premixed combustion analysis and modeling. The flamelet assumption is that chemical reactions proceed in a thin layer owing to its fast reaction rate while the turbulent flow can only distort this reaction layer and enlarge the flame front rather

than entering the reaction zone. In this assumption, since the chemical reactions in the thin layer are unaffected by the turbulent fluctuations, the thin layer has a similar flame structure to that of the laminar flame whose local burning rate can be influenced by stretch effects of the turbulence disturbance. Consequently, based on the flamelet concept, the turbulent premixed flame front can be considered to be composed of continuous quasi-steady laminar premixed flamelets whose local flame structure and combustion characteristics can reflect the global combustion features of the turbulent premixed flame to some extent. It is thus known that the investigation on the real turbulent combustion phenomenon can be simplified significantly by focusing on the study of local combustion characteristics. Furthermore, the local flamelet property is considered to be similar to that of the laminar premixed flame based on the flamelet assumption, several laminar premixed flames, such as the counter flame, sphere flame and Bunsen flame, can be thus adopted for the sake of studying the local combustion characteristics of turbulent premixed flame and improving the understanding on the turbulent premixed combustion [51-54].

Laminar premixed Bunsen flame is a stable and continuous burning laminar premixed flame whose flame tip structure is similar with the curvatures of turbulent premixed flames. Hence, the flame tip of the laminar premixed Bunsen flame can be regarded as a prototype of the corrugated flamelet existing in the turbulent premixed flame [55]. Based on the assumption of flamelet concept, the flame structure and combustion characteristics of flame tip in the Bunsen flame can reflect the local features of the turbulent premixed flame reasonably. Furthermore, the curved flame front and combustion process in the laminar premixed Bunsen flame is affected by fewer factors compared to that in the turbulent premixed flame. This means that the effects of curvature and stretch rate on the local flame structure and combustion characteristics

can be discussed more clearly by using the laminar premixed Bunsen flame. Overall, the laminar premixed Bunsen flame is an ideal prototype to study local characteristics of the turbulent premixed flame, which can provide several useful points to improve the understandings of the turbulent premixed flame [55-57].

Apart from the significance of laminar premixed Bunsen flame on the study of turbulent premixed flame, the laminar premixed Bunsen flame can also play critical roles in the investigation of the laminar premixed combustion. Typically, the conical flame front excluding the flame tip is affected slightly by the stretch effects, thus the combustion process in this part of flame front can be regarded to be approximate to the 1D laminar premixed combustion. This approximation can facilitate the experimental investigation on combustion characteristics of the non-stretched laminar premixed combustion. For example, the parameters of combustion process, such as active radical distributions and temperature variation, across the conical flame front can be measured experimentally, which can provide the valuable experimental data as the validation and comparison for the numerical simulation and the theoretical analysis [58-60]. In addition, it is known that the flame front becomes stable as its laminar burning velocity is equal to the velocity of unburned gases. For the laminar premixed Bunsen flame, the laminar burning velocity is equal to the unburned gases velocity component normal to the flame front. Based on this, the laminar premixed Bunsen flame can be adopted to measure the laminar burning velocity of gaseous fuel conveniently [14, 61, 62].

Overall, considering its importance on the study of turbulent premixed combustion and laminar premixed combustion, the laminar premixed Bunsen flame could be a powerful tool to investigate the fuel characteristics of gaseous fuel including

combustion, thermal and emission characteristics. Specifically, the fuel characteristics at laminar and turbulent conditions can be both discussed in the Bunsen flame while the simple flame structure can facilitate to investigate various effects on the fuel characteristics more clearly. As a result, it is expected that utilizing the laminar premixed Bunsen flame can make for the investigation on combustion, thermal and emission characteristics of the biogas-hydrogen fuels.

1.3 Objectives and scope of the present study

The biogas-hydrogen mixture is expected to be adopted as a fuel to promote the practical applications of biogas fuel in consideration of their several excellent features, but there still exist some uncertainties of utilizing this mixture as a fuel based on the discussions in the previous section. Hence, a study on the fuel characteristics of biogas-hydrogen mixture can not only improve the comprehensive understandings on these fuels in the aspect of energy utilization and combustion science, but also provide some useful information and guidelines for its practical utilization. Furthermore, by using the laminar premixed Bunsen flame, it is expected to study effects of various parameters on the fuel characteristics of biogas-hydrogen mixture more clearly. In this study, both experimental and numerical approaches will be adopted to fully explore and analyze the combustion, thermal and emission characteristics of laminar premixed biogas-hydrogen Bunsen flames. The scope of present study is shown as follows:

(1) To numerically study the combustion characteristics of the biogas-hydrogen mixture, mainly focusing on the heat release characteristics including the heat release rate and primary exothermic and endothermic reactions. To analyze the effects of equivalence ratio, hydrogen addition and carbon dioxide percentage on the heat release features of the biogas-hydrogen fuel.

(2) To experimentally investigate the heat transfer characteristics of the biogas-hydrogen flames by measuring its impinging flame temperature and flame impingement heat flux. To identify the effects of hydrogen addition and carbon dioxide percentage on the combustion and heat transfer processes of biogas-hydrogen flames while to derive a function to predict the optimal heating distance of laminar premixed biogas-hydrogen flame through analyzing effects of heating distance, Reynolds number and equivalence ratio on the heating performance.

(3) To investigate emission characteristics of the biogas-hydrogen flames experimentally and numerically by measuring the pollutant emissions (CO, NOx and NO_2) of laminar premixed biogas-hydrogen flames while developing a computational model to calculate biogas-hydrogen flames. To investigate the effects of separated distance, equivalence ratio, Reynolds number, hydrogen addition and carbon dioxide percentage on the pollutant emissions of biogas-hydrogen flames with the experimental data and numerical simulation.

1.4 Thesis organization

Chapter 1 mainly focuses on the background and the objectives of this work, and then the related previous studies are reviewed and evaluated in Chapter 2. The experimental apparatus and computational models are presented in Chapter 3. Detailed experimental and numerical results are given and discussed in Chapter 4, Chapter 5 and Chapter 6. In Chapter 7, the main conclusions of the current study, as well as the recommendations emerged from this study, are presented.

2 Literature review

The review of fundamental study and practical utilizations of biogas combustion and the hydrogen enriched combustion are presented firstly so as to provide the fundamental information to understand the individual features of these two fuels, as well as the guidelines for the investigation on the biogas-hydrogen fuel. Based on this, the recent efforts on exploring the fuel characteristics of biogas-hydrogen fuel are described. Since the laminar premixed Bunsen flame is adopted to burn the biogas-hydrogen blends, the studies concerned with the laminar premixed Bunsen flame are necessary to be reviewed to understand the basic information of this flame. Specifically, the investigations on heat release characteristics, impingement heat transfer and pollutant emissions under impingement condition of the biogas-hydrogen flame are involved in this work. Thus previous studies related to these aspects are reviewed so as to identify the blanks to be filled in this study.

2.1 Biogas combustion

The fundamental study plays a significant role in understanding the combustion features of a new fuel by providing various fundamental and critical parameters of its combustion process, such as laminar burning velocity and flammability limit. Meanwhile, utilizing a fuel in the practical burner or combustion facility can evaluate its combustion performance for the particular application directly, which can also provide valuable information to understand the fuel characteristics of a new fuel. Hence, the investigations on the biogas combustion in these two aspects are reviewed in this section respectively, which can facilitate to establish a fundamental and comprehensive understanding of the biogas fuel.

Table 2.1 Experimental conditions for laminar flame speed determination of biogas

Composition (% vol)	Pressure (atm)	Temperature (K)	ϕ	Technique	References
CH_4/CO_2(0–60)-air	1	Ambient	-	Numerical	[63]
CH_4/CO_2 (0–60)-air	0.5-10.4	293-454	0.6-1.4	Spherical bomb & Theoretical	[64]
CH_4/CO_2 (0–60)-air	1-4	300	0.5-2	Numerical	[65]
CH_4/CO_2 (0–60)-air	1	300	<1	Stagnation flow	[65]
CH_4/CO_2 (0–60)-air	1	307	0.8-1.3	Heat flux burner	[66]
CH_4/CO_2(20-40)-air	1	Ambient	0.7-1.3	Bunsen burner	[67]
CH_4/CO_2(36-76)-air	1	1	298	Spherical bomb	[68]
CH_4/CO_2(55/45)-air CH_4/CO_2 (75/25)-air	1-4	298	0.8-1.2	Counterflow	[69]
66.4CH_4/30.6CO_2/3N_2-air	1	Ambient	0.5-1.3	Spherical bomb	[12, 70]
66CH_4/34CO_2	0.828	298.3	0.6-1.3	Contoured slot burner	[33]
CH_4/CO_2 (0–40)-air	1-8	298-520	0.7-1.4	Spherical bomb	[71]
CH_4/CO_2 (0–20)-air	1-5	298	0.7-1.3	Heat flux burner	[72]
CH_4/CO_2 (75/25)-air CH_4/CO_2 (50/50)-air	0.5, 1	Ambient	0.6-1.3	Spherical bomb	[73]
CH_4/CO_2 (0-50)-air	1	298	0.8-1.3	Heat flux burner	[74]
CH_4/CO_2 (30-50)-air	1, 3, 5	300	0.8-1.2	Spherical bomb	[75]

For a combustible mixture, the laminar flame speed is one of the most important and fundamental combustion parameters. The experimental data of laminar flame speed, as the validation of the simulation results, are critical for the development of kinetic mechanism, and it also plays a significant role in the practical utilizations including combustor design and combustion controlling because it reflects the fuel burning rate in the real combustion equipment that can affect the flash-back, blow-off and combustion instability. For the biogas, its laminar flame speed has been measured experimentally or determined numerically in a few research using different methods [12, 33, 63-74]. Considering the resource-efficiency of biogas and its various applications, the biogas fuels with varied methane percentages are adopted in these studies and tested in a wide range of initial conditions. The experimental conditions of these studies are summarized in Table 2.1. These studies can provide the valuable data to facilitate the understanding on the biogas features and promote its real utilizations. Besides, compared to that of methane flames, the decreased laminar flame speed of biogas is confirmed in these studies, and this declining trend is found to be

comparatively moderate at elevated pressures due to the suppression of high pressure on the laminar burning rate. Consequently, when the real combustion facility is fuelled by biogas, several problems might be induced owing to its lower laminar flame speed. For example, the lower laminar flame speed might increase the likelihood of knocking in the internal combustion engine fuelled by the biogas fuel. In addition, the laminar flame speed has a close relationship with the adiabatic flame temperature [76]. It is thus known that the temperature of biogas flame should be lower than that of methane flame, which reflects the lower heating value of biogas.

Another critical parameter for the fuel is the flammability limit which can not only reflect the burning ability of a fuel but also provide safety guidelines for the practical applications of the fuel. The flammability limit is a range of the fuel concentration in which the fuel-air mixture can be ignited, and the minimum fuel concentration required for the ignition is defined as the lower flammability limit while the maximum fuel concentration to be ignited is regarded as the upper flammability limit [77]. Considering the variable compositions of biogas, the flammability limit could be changed considerably and is predominated by the methane proportion in the biogas. Few works were conducted to determine the flammability limits of biogas, and the narrower flammability limit of biogas than that of methane is confirmed experimentally and/or numerically.

Qin et al. [65] conducted numerical simulations to determine the turning point of biogas flames, described as the concentration limits beyond which flame propagation cannot occur, and discussed effects of CO_2 on the turning point by increasing its proportion up to 60% in the biogas. They proposed that the turning point is dominated by the thermal radiation, and the flammability range is reduced drastically at a

constant ϕ as the CO_2 concentration is increased. Another numerical study was performed by Ju and his co-workers to study the radiation influences of CO_2 on the flammability limits of methane combustion [78]. The results suggest that CO_2 component can lead to the substantial reabsorption of emitted radiation in the combustion, which gives rise to the higher burning velocity and extended flammability limits than that calculated by optically thin radiation models. Anggono et al. [70, 73] conducted experiments to investigate the flammability limits of biogas fuel using a fan-stirred combustion vessel and suggested that CO_2 can exert stronger suppression on the flammability limit of fuel-rich mixture than that of fuel-lean mixture due to its much higher concentration at fuel-rich condition. The effects of temperature on the flammability limits of biogas were investigated experimentally using a spherical explosion vessel by Dupont and Accorsi [79]. Compared to that of methane fuel, the narrow flammability limits is confirmed in their study while the upper flammability limit of biogas is found to be declined more noticeably at higher temperatures. In another research, a free-falling spherical combustion bomb was adopted to discuss the effects of CO_2 on the flammability limits of methane combustion [68]. They suggested that the reduced flammability range of CH_4/CO_2 mixture can be primarily attributed to the temperature drop and the increased radiation heat loss caused by the CO_2 existence. In a recent study, the flammability limits of biogas were measured experimentally at the atmospheric and elevated pressures, and effects of the increased pressure on the flammability range of biogas were investigated [75]. The results show that the enhanced pressure can extend the flammability limits of biogas and this improvement is more evident for the rich flammability limit.

Apart from the laminar flame speed and flammability limits, a vast quantity of studies were performed to investigate other fundamental features of biogas flame and

combustion, such as flame stability and pollutant emissions. The researches with respect to the flame stability are generally conducted using a variety of burners or combustor, because the flame stability is not only related to the fuel characteristics, but also depends on the operation conditions. Generally, the flame stability diagram can be divided into three regimes of blow-off, stable and flash-back which are typically codetermined by the laminar flame speed and the flow velocity. With the flame stability diagram, there is no doubt that the fuel with a wider flame stability region is the preferred one to generate flames. For the biogas, due to its variable fuel compositions, its flame stability region for a specific burner can be varied significantly with the CO_2 proportion at a constant operation condition [31, 80-83]. Furthermore, a study was conducted to determine the relative significances of CO_2 effects, including pure dilution, thermal and chemical influences, on the flame stability of a flame configuration and reported that the dilution effects exert most effective impacts on the flame stability [84]. In addition, several researches were conducted to investigate the pollutant emissions of biogas combustion, reporting the decreased soot formation and NO production but the enhanced CO emission [72, 85-88]. Apart from this, the biogas flame structures are also investigated experimentally or numerically by several scholars [86, 89, 90].

Based on the above review of the fundamental study, it is known that effects of CO_2 and variable fuel compositions of biogas might cause some problems for the efficient use of biogas in the real combustion facilities. Hence, the studies on real combustors fuelled by biogas can provide more practical information and guidance for its applications. Spark ignition (SI) engine and compression ignition (CI) engine have been used in the transport and industrial fields extensively to convert the chemical energy of fuels into the needed mechanical energy. This stimulates plenty of works to

be carried out in order to examine the combustion and emission characteristics of SI engine [91-96] and CI engine [10, 97-100] fuelled by biogas. Compared to the traditional fossil fuels, biogas can lead to the evident decline of NOx emission and efficiency of an SI engine as shown Fig. 2.1 while the drastically lower temperature of biogas combustion, as well as the large amount of CO_2, can result in the enhanced CO and HC emissions in the SI engine. Several methods have been proposed to improve the defects of biogas combustion in the SI engine [101]. For the CI engine, biogas fuel exerts the similar effects on its emissions (NOx, CO and HC) as that of the SI engine. Furthermore, the soot formation of the CI engine is found to be suppressed by burning the biogas fuel while the ignition delay time is prolonged [102]. Apart from this, several studies were conducted to investigate the biogas combustion in the gas turbine so as to further explore the feasibility of biogas fuel in the industrial utilization [103-105].

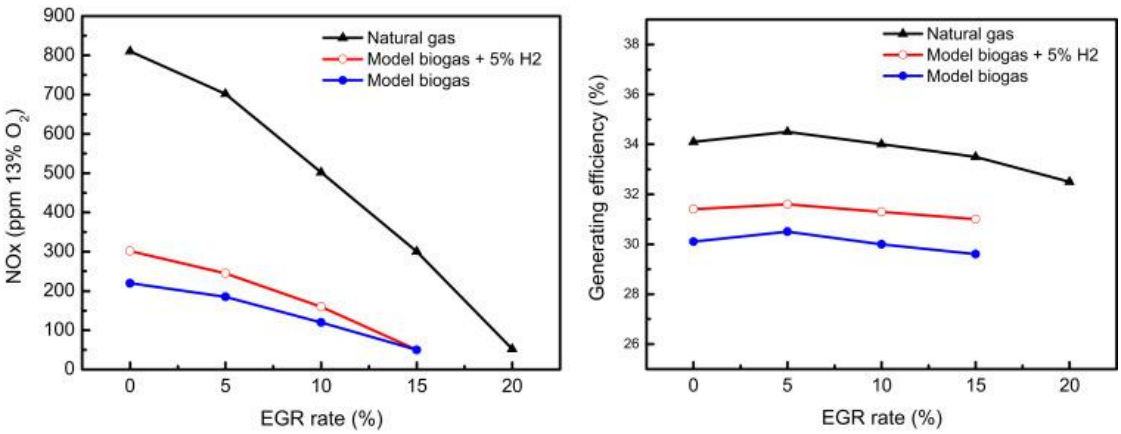

Fig. 2.1 The comparison of NOx emission and efficiency of SI engine fuelled by biogas and natural gas [91].

2.2 Hydrogen enriched combustion

Due to the high reactivity and diffusivity, the pure hydrogen combustion is restricted considerably in the practical applications for the safety consideration. Consequently,

hydrogen is generally adopted as an excellent addition to adjust the combustion features of other hydrocarbon fuels. In this section, similar to the review of biogas combustion, the research on the hydrogen enriched combustion is summarized from two aspects of its fundamental features and practical applications in order to obtain a comparatively comprehensive understanding.

Hydrogen has a much higher laminar flame speed than that of hydrocarbon fuels [106]. This means that the hydrogen addition could be a useful method to enhance the laminar flame speed of hydrocarbon fuels, which has been confirmed by plenty of works using various experimental equipment [36, 37, 39, 107-110]. Furthermore, the nonlinear improvement of hydrogen enrichment on the laminar flame speed of hydrocarbon fuels were observed in these studies whose results indicate that the improvement on laminar flame speed is moderate as hydrogen addition is less than 40% but become substantially evident when the hydrogen proportion is further increased. The reason is that the fuel dominating the combustion process is varied from hydrocarbon fuel to hydrogen as the hydrogen addition is increased [111]. In addition, it is proposed that the hydrogen addition can affect the laminar flame speed via three mechanisms, including thermal effect, transport effect and kinetic effect. Among these three mechanisms, the kinetic effect is found to exert most impacts on enhancing the burning flux due to the strong reactivity of hydrogen [112].

Considering the broad flammability limits of hydrogen, several works were carried out to investigate the effects of hydrogen addition on the flammability limits of hydrocarbon fuels, primarily focused on the methane fuel. The flammability limits of methane-hydrogen mixture were determined by some researchers as shown in Fig. 2.2 [113-117]. It can be seen that the flammability limits is extended gradually with the

increased hydrogen enrichment, and the improvement is more evident as the hydrogen addition is larger than 80%. Apart from this, the hydrogen addition can accelerate the production of H and OH radicals considerably to reduce the required ignition energy or temperature and then promote the ignition of hydrocarbon fuels in both premixed and diffusion combustion [118-121]. Furthermore, as another critical fundamental parameter to reflect the auto-ignition feature of fuels, the ignition delay time plays an important role in understanding the knocking in the internal combustion engines and is regarded as the reliable reference to validate the chemical mechanisms. Considering the broad flammability limits and excellent ignition characteristics of hydrogen, several studies have been performed to determine the ignition delay time of hydrogen-hydrocarbon mixture experimentally and discussed the impacts of hydrogen addition on the ignition delay time quantitatively. However, it should be noted that the effects of hydrogen addition on the ignition delay time of hydrocarbon fuels are comparatively difficult to investigate because the ignition delay time are dependent on pressure, temperature and fuel chemical kinetics simultaneously. Several works found that the hydrogen addition can reduce the ignition delay time of methane [122-124] or carbon monoxide [125-127] in a wide range of temperature and pressure. Lee and Song [128] measured the ignition delay time of methyl butanoate/*n*-heptane/hydrogen mixture experimentally, and found that the hydrogen addition can increase the ignition delay time of methyl butanoate/*n*-heptane mixture apparently. Besides, the ignition delay time of dimethyl ether (DME)-hydrogen mixture was determined and investigated numerically [129]. Results show that, with the hydrogen addition, the ignition delay time shows the evident rising trend at low temperatures but the moderate decline at high temperatures. In other studies, the hydrogen addition is found to decrease the ignition delay time of propane under most of tested conditions, but the

longer ignition delay time is exhibited at lower pressures and high temperatures when the hydrogen proportion in the fuel exceeds 95% [130, 131].

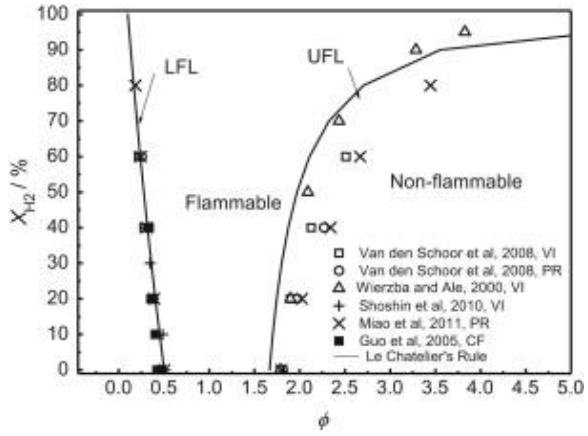

Fig. 2.2 Flammability limits of methane-hydrogen-air mixture at 1 atm and room temperature [112].

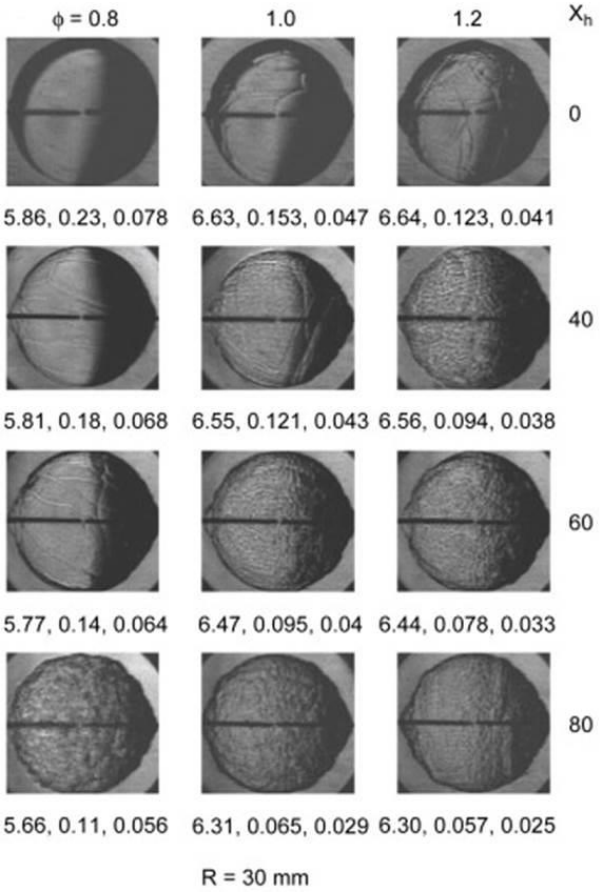

Fig. 2.3 The schlieren photos of spherical propagating propane-hydrogen flames [132].

Flame front instability can lead to the self-acceleration of flame propagation or even the detonation transition in the combustor, which might cause equipment damages and safety problems. Thus the flame instability is a significant topic in the fundamental study of combustion science. Three mechanisms responsible for the flame front instability have been identified and well established: hydrodynamic instability, diffusional-thermal instability and body-force induced instability [133]. For the hydrogen enriched combustion, the strong reactivity and diffusivity of hydrogen may increase the occurrence possibility of the flame front instability or exacerbate this phenomenon as shown in Fig. 2.3. Therefore, plenty of fundamental studies have been conducted to investigate the effects of hydrogen addition on the flame front instability [53, 134-137]. On the whole, it is concluded that the hydrogen addition can suppress the body-force instability due to the improvement on the flame speed, while improve the hydrodynamic instability owing to the reduced flame thickness. For the thermal-diffusion instability of heavy-hydrocarbon combustion, hydrogen addition exerts improvement at fuel-lean conditions but the suppression at fuel-rich conditions. For the pollutant emissions, hydrogen addition can increase the NOx emission due to the increased temperature [28, 138], but its effects on the CO emission of hydrocarbon fuels depend on the specific conditions. Some previous studies report the decreased CO emission of hydrocarbon-hydrogen mixture [139, 140], while others proposed the enhanced CO emission [141, 142].

The broad flammability limits of hydrogen make it to be an ideal fuel to improve the lean limit of natural gas which has been adopted in the internal combustion engines. By using the natural gas-hydrogen blends, the extended lean limit allows the leaner combustion to be sustained in the engine, which has the possibility to achieve the equivalent zero emissions [143]. In general, the hydrogen addition can lead to the

better combustion in a wide range of conditions for the engines fuelled by natural gas while it can also give rise to the lower emissions and the higher efficiency of engines [144-146]. Additionally, for the engines utilizing the liquid fuels such as diesel and gasoline, the major motivation of introducing hydrogen is to reduce pollutant emissions. By using the exhaust gas recirculation and hydrogen addition, the reduced HC, CO, CO_2 and NOx emissions can be achieved in the SI and DI engines [147-152]. Furthermore, the improvement of hydrogen addition on the peak in-cylinder pressure, brake thermal efficiency and NO_2 emission were also reported in these works.

2.3 Biogas-hydrogen combustion

Although a vast quantity of fundamental works has been carried out to study the fuel characteristics of biogas combustion, as well as the hydrogen enriched combustion, there are few research conducted to investigate the fundamental fuel features of biogas-hydrogen blends.

Leung and Wierzba [153] conducted an experiment to investigate the stability limits of diffusion biogas-hydrogen flames with the air co-flow around it, and effects of the methane proportion (50% and 60%), the hydrogen addition (0-30%) and the nozzle diameter were discussed in the study. The results show that the increased CO_2 amount can narrow the stability limits of the diffusion biogas flame, while the poor stability performance of diffusion biogas flame can be improved effectively by introducing a small amount of hydrogen (less than 10%). In addition, it was observed that the flame stability of biogas-hydrogen flame becomes insensitive to the further increased H_2 addition (10-30%).

Chen and Zheng [154] performed the numerical simulations to study the mild combustion characteristics of biogas-hydrogen mixture, and the influences of preheated temperature, oxygen concentration and hydrogen addition on the flame structure were investigated quantitatively. They suggested that the mild combustion of oxy-biogas fuel can be sustained more easily while the lower preheated temperature is preferred for obtaining the stable mild combustion of biogas-hydrogen mixture.

Another experiment was carried out to discuss the effects of hydrogen addition on the stability, emissions and impingement heat transfer of the biogas diffusion flame [155]. Results shows that the flame stability and flame temperature of biogas flame are enhanced with the hydrogen enrichment, while the impingement heat transfer performance of biogas flame become poorer owing to the lower energy input. Besides, Zhen et al. [156] conducted another experiment to investigate the flame characters of premixed biogas-hydrogen flame. The variable biogas compositions (40-60% CH_4) with the hydrogen addition (0-50%) were adopted to generate the premixed flames and the laminar flame speeds of biogas-hydrogen-air mixture were measured using the Bunsen method. The results indicate that blending hydrogen can improve the flame stability and laminar flame speed, and reduce the CO emission effectively.

In order to further investigate fuel characteristics of biogas-hydrogen mixture, more fundamental studies were performed experimentally using premixed and diffusion flames by Zhen and his co-workers [157-159]. The heat transfer performance of premixed and diffusion flames burning biogas-hydrogen blends were compared quantitatively. The premixed flame is found to have a better heating performance than that of the diffusion flame thanks to its higher flame temperature. In addition, it is interesting that the hydrogen addition exerts the contrary influences on the total heat

transfer rate of premixed and diffusion biogas flames. The impingement heating performance of the premixed flame is enhanced by the hydrogen addition, while that of the diffusion flame is declined. In addition, since the hydrogen addition can lead to the increased flame temperature and reduced biogas proportion, the NOx emission is enhanced by the improved thermal NO production, while the CO emission is reduced due to the lower carbon content and the accelerated CO oxidization.

In order to investigate the flame structure and emissions of the biogas-hydrogen counter-flow diffusion flame, Mameri and Tabet performed the numerical simulations with the detailed chemical reaction mechanism in a wide range of conditions [160]. Results show that blending hydrogen can reduce the emitted radiation of biogas-hydrogen combustion compared to that of raw biogas combustion, but it can hardly affect the chemical effects of CO_2. The reactivity of CO_2 can reduce the peak mole fraction of OH radical, but lead to the higher concentrations of CO and NO in the flame. Besides, although hydrogen addition promotes the NO formation of biogas flame, this improvement can be suppressed by enhance the scalar dissipation rates. On the contrary, although the maximum CO mole fraction of biogas-hydrogen flame can also be enhanced with the increased hydrogen enrichment, this enhancement can be further improved rather than suppressed by the larger scalar dissipation rate.

Compared to the limited efforts made on the fundamental study of biogas-hydrogen blends, more works have been conducted to evaluate the performance of this new blend in the real combustion equipment. Due to the relatively large amount of CO_2 in the biogas, burning raw biogas can reduce the indicated mean effective pressure and thermal efficiency due to the decreased combustion temperature and the larger specific heat capacity. Furthermore, the CO_2 component can also cause the fluctuation

of engine cycle which can be improved by adding hydrogen into the biogas fuel [101, 161]. Porpatham and his co-worker [162] examined the performance of a SI engine fuelled by biogas blended with a small amount of hydrogen (5%-15% on the energy basis). The improvements of hydrogen addition on the combustion features of the SI engine including combustion rate, lean flammability limit, brake thermal efficiency and brake power were verified in the study. By adjusting the ignition timing to avoid the knocking, the hydrogen addition leads to the reduction of peak pressure and heat release rate while maintains a relatively stable level of NOx emission. In another research, by using a quasi-dimensional multi-zone model, the biogas-hydrogen combustion in a single cylinder engine was investigated by Rakopoulos and his co-workers, and the shorter flame development period was observed for the biogas-hydrogen combustion [163]. Jeong and colleagues [164] measured the generating efficiency and emissions of a SI engine generator fuelled by biogas-hydrogen blends. They found that the generating efficiency, peak in-cylinder pressure and NOx emission can be enhanced by increasing the hydrogen addition. Furthermore, a similar research was carried out to examine the generating efficiency and NOx emission of an engine generator by further introducing the EGR system [91]. Results indicate that burning biogas-hydrogen blends leads to the higher generating efficiency and NOx emission than that of raw biogas, while the EGR rate can reduce the generating efficiency and NOx emission owing to the incomplete combustion and lower temperature. Besides, the effects of EGR rate and hydrogen addition on the engine performance of an 8L engine fuelled by biogas-hydrogen mixture were examined by Park and his co-workers [165, 166]. It is found that the thermal efficiency of the engine is enhanced initially and then declined with the hydrogen addition, and the

EGR technique is suggested to be adopted when the engine is fuelled by the biogas with high hydrogen addition, which can give rise to an improved thermal efficiency.

2.4 Laminar premixed Bunsen flame

As a stationary flame, the laminar premixed Bunsen flame can be used to measure the laminar flame speed of gaseous fuels, such as hydrogen [167], syngas [14, 168] and methane [169, 170]. However, it should be noted that the laminar flame speed at higher initial temperatures and elevated pressures or the laminar flame speed of liquid fuel can be hardly measured by utilizing the Bunsen type flame due to the restrictions of its intrinsic features. Apart from this, several studies have been carried out to study the flame structure and combustion characteristics of laminar premixed Bunsen flame. Kalta and Roquemore [171] calculated the laminar premixed hydrogen-air Bunsen flame using the detailed chemical mechanism and analyzed the effects of Lewis number and buoyancy on the flame structure, combustion process and the emission formation. The results show that combustion process along the flame front can be influenced by the variation of Lewis number, and the buoyancy can cause the vortices in the flame and lead to the flame flickering. In another research, the species distributions and temperature fields of laminar premixed methane Bunsen flames were measured experimentally using the techniques of Raman-Rayleigh scattering and planar laser-induced fluorescence (PLIF), and the measured data were expected to provide the reliable reference to validate the numerical simulation of the laminar premixed Bunsen flame [58]. Ramie et al. [172] measured the width and velocity of burned gases of the laminar premixed Bunsen flame experimentally and obtained a theoretical expression to predict these two critical parameters with a satisfactory accuracy. Fu et al. [173] examined the OH distributions of the laminar premixed

syngas Bunsen flame with the OH-PLIF technique, and found that the hydrogen proportion can change the combustion pattern considerably thanks to the strong mass diffusivity of hydrogen. The flame stability of the laminar premixed Bunsen flame was also examined by some researchers [61, 156], and the cool burner rim is proposed to cause the heat loss and radical loss that plays a significant role in the flame quenching. Higuera [174] performed a numerical study to investigate the effects of flow field on the shape of a slender Bunsen flame. The results elucidate that the burned gases can exert the pressure on the flame, which is composed of a constant part and a variable part. The constant part of the exerted pressure does not affect the fresh gas velocity. However, the variable part is increased from flame tip to the bottom, which can induce the fresh gas acceleration and then lead to the variation of the flame shape.

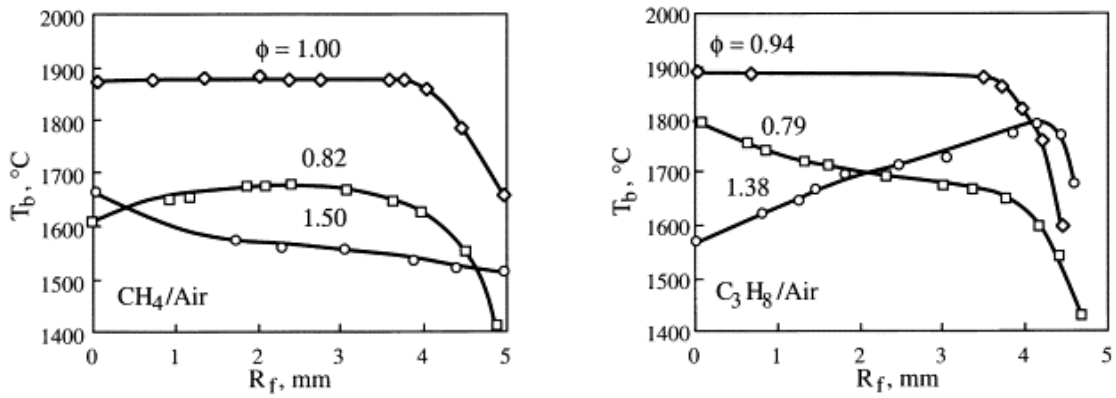

Fig. 2.4 Flame temperature variations along the flame front of methane and propane Bunsen flames [175].

The laminar premixed Bunsen flame has the strong negative stretch and the corrugated flame front which make it to be an ideal flame to study effects of the flame stretch and the curvature on the flame properties. The effects of preferential diffusion and flame stretch on combustion intensity of Bunsen flame tip were investigated by Sivashinsky [176], Law et al. [177, 178] and Mizomoto et al. [179, 180] utilizing numerical or

experimental method. Their results illustrate that the local combustion intensity can be varied by the simultaneous effects of the flame stretch and the preferential diffusion, which can be reflected by the variation of flame front temperature as shown Fig. 2.4. The reasons for the variation of local combustion intensity can be explained by effects of heat and mass transfer or the interaction between preferential diffusion and flame stretch. In addition, the effects of flame stretch and preferential diffusion on the combustion process at the Bunsen flame tip were further investigated by adopting new diagnostic techniques in recent studies. The local stretch rates caused by flame curvature and flow strain were isolated and determined, and the negative stretch rate at the flame tip is found to be dominated by the flame curvature effects [54]. Besides, the local Karlovitz number is suggested to have a close and constant relationship with the tip opening phenomenon [57]. Apart from this, some works found that the local fuel burning rate can be affected by the local flame stretch, and the negative flame stretch at the flame tip of Bunsen flame can enhance the local flame speed there [55, 181, 182]. Yamamoto and his co-workers [183] measured the OH concentration and local burning velocity of the laminar premixed Bunsen flame and examined the correlation of peak OH concentration and local flame speed. The results indicate that the peak concentration of OH radical has the linear relationship with the local burning speed, and it suffers similar influences of the flame stretch as that on the local flame speed, confirming that the peak OH concentration is a good indicator of the flame speed. Higuera [184] analyzed the relationship between the flame tip curvature and the unburned gas velocity, and suggested that the curvature of laminar premixed Bunsen flame tip is proportional to the ratio of fresh gas velocity and the planar flame speed.

2.5 Heat release of combustion

For a new fuel, the study on its heat release characteristics can help to identify its major exothermic and endothermic reactions and obtain the heat release rate variation at various conditions, which can facilitate the comprehensive understanding on this fuel and then provide some useful information to guide its practical utilization. In addition, the study on the heat release characteristics of the fuel and its practical combustion process and flames has the practical significance for the combustion monitoring and control in the combustion facilities. Specifically, the energy intensive area in a combustion equipment plays the critical role in several physical processes such as noise generation, pulsed combustion and thermoacoustic instability [185-187] which have the possibility to induce the severe damage to the combustion facilities. In order to avoid these damages, the energy intensive areas need to be identified, which can be accomplished by the measurement of heat release distribution, so as to control the combustion process in the combustor. Whereas, the direct measurement of HRR distribution is still a challenging work at this time due to the complexity of chemical reactions and the real combustion process. Consequently, plenty of works have been conducted to explore and develop a reliable method for the HRR measurement. The general method is that the HHR is expected to be determined by using a correlation between the HRR and another quantity which can be determined experimentally with a satisfactory accuracy. In the internal combustion engine, instead of the direct measurement, the HRR is generally calculated based on the measured pressure data in the cylinder [188]. However, this method is restrained to be utilized in the engine experiments due to its unique combustion condition and cannot be applied in other combustors. By contrast, establishing the relation between the HRR and species can improve the applicability of HRR measurement in various facilities, thus a vast

quantity of research have been carried out in the past decades and have proposed several correlations between the HRR and the mole fraction of certain species [186, 189-197].

Najm and his co-workers [189-191] conducted the experimental and numerical studies to compare the marker performance on the HRR estimation in methane flames and suggested the formyl radical, HCO, as a qualified indicator to predict the local HRR in methane flames. In their studies, the HCO concentration is demonstrated to have a stable correlation with the HRR in both temporal and spatial distributions, and its correlation with the local HRR is hardly affected by the flame stretch. Furthermore, they elucidated that the comparatively reliable correlation of the HCO and HRR can be resulted from three aspects: (1) the more rapid consumption rate of HCO makes its concentration to be proportional to its production rate directly; (2) HCO is an important intermediate to produce CO, thus it can reflect carbon flow in the oxidation process of CH_4 and (3) the CH_2O predominates the production of HCO and is primarily generated via the reaction $O+CH_3=CH_2O+H$ which is found to account for a large part of the HRR. Although HCO has been demonstrated to be an excellent marker to estimate the HRR, the low concentration in the flames inhibits its practical utilization in HRR imaging considerably owing to the poor signal-to-noise ratio in the optical diagnostic. In order to cope with this, the $OH\times CH_2O$ product is expected to be a possible marker for the HRR estimation. $OH+CH_2O=HCO+H_2O$ is a major contributor on the HCO production, which means the HCO concentration can be reflected reasonably by the product of OH and CH_2O concentrations. Furthermore, OH and CH_2O radicals have the much higher concentrations than that of HCO in the flame, which can improve the signal-to-noise ratio of the measured data. In order to examine the ability of the $OH\times CH_2O$ product to predict the HRR, the correlations of

the $OH \times CH_2O$ product and the local HRR have been established and investigated in the laminar and turbulent flames at various conditions [186, 192-197]. By adopting the OH and CH_2O PLIF, the transient and spatial signals of OH and CH_2O radicals were measured simultaneously and the accuracy of $OH \times CH_2O$ product to discern the HRR location was confirmed. In a recent research, the flame structures of turbulent premixed methane flames were investigated by utilizing several high resolution imaging measurements simultaneously [198]. The results show that CH_2O signal represent the preheat zone in the flame while OH signal denotes the oxidization zone, and the overlap region of these two signals can agree well with that of HCO. However, it is found that the increased turbulence intensity can affect the accuracy of these markers on determining the reaction zones due to the rapid turbulent transport of radicals. Additionally, a numerical study was performed to discuss the validity of $OH \times CH_2O$ product as a robust HRR marker in the premixed methane and multi-component fuel flames [199]. In their results, some alternative markers, including $H \times HO_2$, $H \times CH_2O$, $O \times CH_4$ and $O \times HO_2$, were proposed to have a better performance for the HRR visualization at specific conditions. Based on this study, Mulla et al. [60] conducted another experiment to examine the accuracy of the $H \times CH_2O$ product on the estimation of spatial local HRR and the total HRR variation with equivalence ratio. The results show that, compared to that of the $OH \times CH_2O$ product, the $H \times CH_2O$ product shows the similar performance for estimating the spatial HRR but presents a poorer performance to reflect the total HRR variation with equivalence ratio. Apart from this, several experimental and/or numerical studies suggested that the reaction rate of $O+CH_3$ reactions can correlate well with HRR in non-premixed methane-air flames [200, 201]. The feasibility of CH radical was also investigated by some researchers, and found that the HRR correlates with CH concentration poorly

compared to that with the $OH \times CH_2O$ product because the CH concentration can be more sensitive to the high flame stretch and the varied fuel composition [202, 203].

2.6 Flame impingement

Flame impingement exists in the combustion equipment extensively, which can affect the combustion process and the flame structure significantly. Furthermore, for the practical application aspect, the impinging jet flames are widely employed for heating purpose in the industrial fields such as metal melting and glass shaping. Thus plenty of works have been conducted to investigate the flame structure, combustion and heat transfer mechanisms of the impinging jet flames, which facilitates to obtain a comprehensive understanding on the features of the flame impingement. In this section, the studies on the impinging jet flames are reviewed according to three aspects: the characterization of impinging jet flames, the flame impingement heating and the pollutant emissions of impinging flames.

2.6.1 Flame structures of impinging jet flames

Compared to the isothermal jet, the flow field of the impinging flame is suggested to have the similar structures composed of three characteristic regions including the free jet region, the stagnation region and the wall jet region [204]. Furthermore, several studies compared the flow fields of the isothermal jet and the single flame jet, and found that the flame jet has the similar aerodynamics [205], pressure and the axial velocity fields [206, 207] to that of the isothermal jet. However, due to the existence of combustion process in the flame jet, the flow fields of the flame can be more complicate as the reaction zone occurs in the different characteristic regions.

For the impinging jet flames, the flame shape can be changed by the nozzle exit velocity, the nozzle-to-plate distance and the locations to ignite the flame, and the flame can be stabilized by the nozzle rim and the impingement plate [208]. Thus there exist four characteristic flame shapes at different operation conditions which are the ring flame, the conical flame, the disc flame and the envelope flame as shown in Fig. 2.5. The conical flame and envelope flame are both stabilized on the burner rim, but they are formed as the nozzle-to-plate distance is comparatively larger and smaller than the flame height, respectively. With the high velocity of unburned gases, the flame can be pushed away from the burner rim, and then the disc flame can be established near the plate. For the ring flame, it can be formed by initialize the flame at the impinging jet edge when the radial flow speed is higher than the flame propagation speed. Furthermore, the plate temperature can also exert influences on the flame shape such as the ring size.

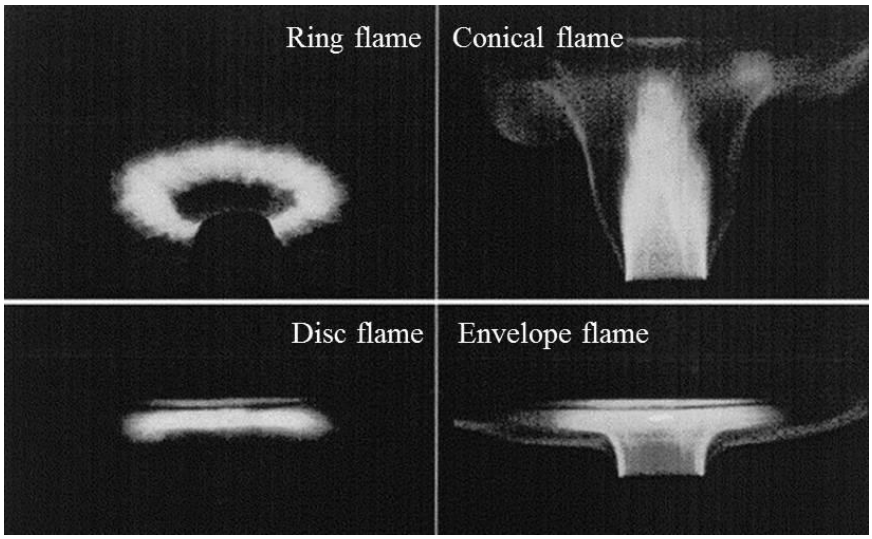

Fig. 2.5 Typical patterns of impinging jet flames [208].

For the laminar premixed impinging flame, the flame structure variation is primarily dominated by the nozzle-to-plate distance as shown in Fig. 2.6. The laminar premixed flame is composed of a premixed combustion zone and a diffusion combustion zone.

As the nozzle-to-plate distance is large enough, the premixed and diffusion combustion zones of the flame are both not influenced by the plate, which is regarded as the Type-A flame as shown in Fig. 2.6. As the nozzle-to-plate distance is decreased, the diffusion combustion zone can be initially affected by the plate while the premixed combustion zone can still maintain its complete shape, which is thus defined as the Type-B flame. When the nozzle-to-plate distance is further decreased, both the premixed combustion zone and diffusion combustion zone can be affected by the plate. The Type-C flame can be thus formed as shown in Fig. 2.6, which allows the unburned gases to impinge the plate directly and establish a cool core in the stagnation region.

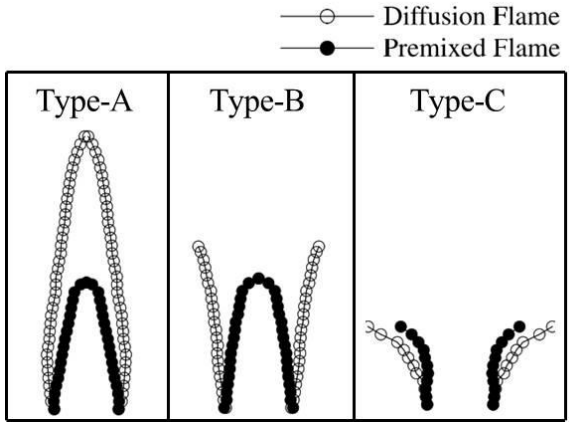

Fig. 2.6 Typical structures of the laminar premixed impinging flame [209].

2.6.2 Flame impingement heat transfer

Flame impingement is generally utilized for the heating purpose. Compared to the isothermal jet, the impinging jet flame has a better forced convection process and the much higher temperature. However, the impinging jet flame has a non-uniform distribution of heat flux due to the existence of reaction zone in the flame. This makes its impingement heat transfer process to be more complicate than that of the isothermal jet. It has been widely accepted that there are six heat transfer mechanisms

responsible for the impingement heat transfer of impinging jet flames, which are convection, conduction, radiation, thermochemical heat release (TCHR), condensation and boiling [204]. Generally, the relative significances of these six mechanisms can be changed considerably at various conditions. For example, the radiation mechanism plays a dominated role in heat transfer process inside a furnace, but it accounts for a negligible part of total heat transfer when the flame impingement occurs in the ambient temperature. In addition, the convection and conduction mechanisms can be regarded as the significant contributors on the heat transfer in most of heating facilities. For the flame impingement heat transfer, it is known that both the combustion process and the heat transfer process can affect its heating performance significantly, thus the impingement heat transfer can be influenced by a variety of factors including the burner configuration, the fuel composition, Reynolds number and the equivalence ratio. As a result, various studies have been performed so as to establish a comprehensive understanding on the flame impingement heat transfer.

Due to the extensive utilization of flame impingement, various burners have been designed to obtain an improved heat transfer. Thus several studies have been carried out to evaluate the heating performance of different burners. Dong et al. [210] conducted an experiment to study the heat transfer of a premixed butane flame jet which is stabilized on a Bunsen burner. Nondimensional correlations to predict the Nusselt number were obtained based on the experimental data as a function of separated distance, Reynolds number and equivalence ratio. Wu et al. [211] conducted an experiment to investigate the heating performance of the radial jet reattachment flame, and found that radial jet reattachment combustion nozzle can promote the fuel/air mixing, which can then enhance the impingement heat transfer rate. Dong et al. [212] investigated the heat transfer characteristics of a slot flame jet in another study,

and found that more uniform heat flux and larger total heat transfer rate can be obtained by a slot burner compared to that of a circular burner. Hindasageri et al. [213] performed an experiment to study the heat transfer distribution of a swirling flame jet. The results show that the swirl can improve the heat transfer process at low Reynolds number but suppress the heating performance at higher Reynolds number. Ng et al. [214] adopted an inversed diffusion flame (IDF) to measure its heat flux experimentally and discussed the effects of equivalence ratio and Reynolds number on the heating performance. They suggested that the IDF burner can provide a comparable or even better heat transfer performance than that of the premixed flame. Zhen et al. [215] experimentally compared the heating performance of a turbulent IDF burner and a normal IDF burner. Results elucidate that although swirling effects can result in a more complete combustion, it can also bring more air entrainment to cool down the temperature, which can thus lead to a worse heating performance of the swirling IDF than that of the normal IDF. Apart from the study on the single burner, several researches were performed to investigate the heat transfer process of flame arrays, which suggested that the flame arrays can obtain an enhanced heat transfer rate and a more uniform distribution of heat fluxes [216-219].

Considering that the impingement plate can influence the heat transfer and the flame structure, many works have been carried out to examine the effects of plate on the heating performance. Baukal and Gebhart [220] experimentally examined effects of the plate surface condition on the heat transfer process and found that the blackened plate results in the best heating performance, while the polished one leads to the lowest heat fluxes. Furthermore, they suggested that nonluminous flame radiation, as well as the TCHR from surface catalytic, can play a comparatively unimportant role in the heat transfer process. Zhao et al. [221] carried out an experiment to examine the

effects of brass and stainless steel plates on the heat transfer process of a premixed flame, and found that the stainless steel plate can lead to a much lower heat flux in the stagnation region due to its larger resistance, but it exert quite slight influences on heat fluxes in the wall jet region. Agrawal et al. [222] developed a computational model to investigate the heat transfer process of a premixed flame impinging on an inclined plate. The results show that the heat flux in uphill part is higher due to the more extensive distribution of high temperature, and the heat flux near the plate center can be more sensitive to the inclination angle than the heat flux in the outer region. Li et al. [223] experimentally investigated effects of the plate temperature on the heating performance of impinging flames, and suggested that the heat flux is reduced with the increased plate temperature due to the reduced temperature difference across the plate. Apart from the extensive research focusing on the heat transfer mechanism of flames impinging on a plate, some other studies were carried out to study the heat transfer mechanisms of flames impinging on the different configurations including the cylinder [224, 225] and round surface [226, 227].

The nozzle-to-plate distance is a critical parameter affecting the heating performance of impinging flames. Thus its effects on the heat transfer process of impinging flames have been discussed in a number of studies. Kataoka [228] studied the optimal separated distance experimentally in order to obtain the best heating efficiency of a premixed methane flame. They found that the heat flux at the stagnation point becomes the maximum when the plate is located at the flame tip, and developed a model to predict the stagnation-point heat flux in a wide range of conditions. Dong et al. [210] experimentally examined effects of the heating distance on the peak Nusselt number, and suggested that the optimal heating distance can be varied significantly with the equivalence ratio. Hou and Ko [209] conducted an experiment to examine

effects of the heating distance on the flame structure and the heating efficiency of a laminar impinging flame. The results indicate that the heating efficiency is increased initially and then declined with the increased heating distance, and the optimal heating distance to achieve the peak thermal efficiency is qualitatively proposed that is slightly lower than the conical height of laminar premixed flames. Furthermore, they carried out another experimental study to discuss effects of the heating distance on the heat transfer process of an inclined impinging jet flame, and found that the heating performance is still increased firstly with the heating distance and then reduced at the larger heating distance [229]. Ramie et al. [230, 231] conducted two theoretical studies to develop an analytical expression describing the heat flux of a laminar impinging flame. They found that the heat flux is dependent on the heating distance and it can keep constant at large heating distance but enhance rapidly at smaller distance. Chander and Ray [232] investigated the off-stagnation peak heat flux of a laminar methane flame by utilizing both experimental and numerical methods, and found that the off-stagnation peak heat flux is caused by the lower velocity field above the flame tip and can be codetermined by the nozzle-to-plate distance and the tip-to-plate distance. In another research, they studied effects of the separated distance on the stagnation heat flux experimentally and numerically [233]. The results indicate that the stagnation heat flux is dropped initially with the increased heating distance and then keeps a relatively stable level at large heating distance.

At a same operation condition, the fuel composition can also affect the heating performance significantly. Typically, the fuel composition influences the heat transfer performance due to the varied energy input and the combustion temperature. For example, the hydrogen enrichment or the oxy-fuel can promote the total heat transfer rate to some extent due to the more intensive combustion which can increase the

temperature difference between the plate surfaces [156, 234, 235]. Furthermore, effects of Reynolds number and equivalence ratio on the flame impingement are also discussed elaborately in various studies, because Reynolds number can affect the forced convection process significantly while the equivalence ratio can dominate the combustion process. A number of works suggested that the higher Reynolds number can enhance heat fluxes effectively by improving the forced convection process and the larger heating area [236-238]. In addition, effects of the equivalence ratio on the heating performance are dependent on the specific conditions. It is general that the stoichiometric condition is proposed to have the best thermal efficiency due to the complete fuel combustion [220, 239]. However, the optimal equivalence ratio for the best thermal efficiency can be changed in turbulent flames because the heat transfer process can be codetermined by the equivalence ratio and the turbulence intensity in the turbulent flames [204, 213, 215, 240].

2.6.3 Pollutant emissions of impinging flames

Apart from the heat transfer characteristics, the pollutant emissions of impinging jet flames should also be paid attention due to the extensive practical utilization of flame impingement. Furthermore, the impingement can exert significant influences on the emission formation process and then lead to a more complex production process of exhausted emissions in the impinging flames than that of the free flames. Whereas, compared to the huge number of works focusing on the heat transfer mechanism of flame impingement, there are much less studies conducted to investigate the pollutant emissions of impinging flames. Mohr et al. [241] performed an experiment to measure the pollutant emissions of a radial jet reattachment combustion flame burning the natural gas, and found that this flame produce much less CO, NOx and soot than that

of co-axial-flowing flame. The low CO and NOx emissions of the radial jet reattachment combustion flame were also validated in another experimental study [211]. Dong et al. [242] experimentally determined the exhausted gases of a premixed slot butane/air flame under the impingement condition. They observed that HC and O_2 emissions can be enhanced when the cool core appears at small separated distances, and the flame at the transitional condition can lead to high emissions of CO, NO and CO_2 but low HC and O_2 emissions around the stagnation point when the separated distance is comparatively small. Mishra [243] performed an experiment to measure pollutant emissions of the premixed LPG flame impinging to a cold flat plate. Results show that pollutant emissions can be influenced by the nozzle-to-plate distance significantly, and CO concentration is elevated while NO production is suppressed as the equivalence ratio is increased. Saha et al. [244] investigated the emission characteristics of methane and ethylene impinging flames experimentally. It is found that the larger nozzle-to-plate distance can decrease the CO emission but enhance the NOx emission of rich methane and ethylene flames, and the larger Reynolds number can increase the CO concentration but decrease the NOx concentration of the ethylene flame due to the less residence time for CO oxidization and the NO production. Li et al. [223] experimentally discussed the influences of plate temperature on the CO and NOx emissions of a premixed LPG/air flame impinging normally to a plate. It is observed that the higher plate temperature can contribute to the lower CO emission but the higher NOx emission, which is caused by the improved CO oxidization and the promoted NO production. Furthermore, Li et al. [219] discussed nozzle effects on the CO emission of a premixed impinging flame in another experimental study. Results indicate that the triple-nozzle burner produces less CO emission than the single nozzle burner. Zhen et al. [235] carried out an experiment to investigate effects

of hydrogen addition on the pollutant emissions of a premixed LPG/hydrogen impinging flame. The results show that hydrogen addition enhances the flame temperature and then gives rise to the enhanced NOx emission and the declined CO emission. Furthermore, Zhen et al.[159] performed another experiment to measure the exhausted gases of impinging biogas-hydrogen flames, and observed that the premixed flame produces lower CO and NOx emissions than that of the diffusion flame and NOx emission can be promoted with the hydrogen addition, the equivalence ratio and the Reynolds number owing to its sensitivity to both flame temperature and flame volume.

2.7 Summary

From the above literature review, it is found that the biogas combustion, compared to conventional gaseous fuels, has both merits and defects in various aspects, and its fuel features can be affected considerably by its variable fuel composition. Besides, the hydrogen addition can be a feasible method to promote the biogas combustion, but the effects of hydrogen addition on the biogas combustion are relatively complex owing to the fuel characters of hydrogen. Thanks to the variable combustion features of biogas and the complex effects of hydrogen addition, fuel characteristics of the biogas-hydrogen blends have been not well understood with the limited fundamental studies, and more research on the biogas-hydrogen blends need to be carried out in order to improve the comprehensive understanding of this new fuel. In addition, based on the previous studies, it is demonstrated that the laminar premixed Bunsen flame plays significant roles in both combustion research and exploration of fuel properties. Therefore, the laminar premixed Bunsen flame can be utilized to not only explore the

fuel characteristics of biogas-hydrogen mixture but also investigate combustion features of biogas-hydrogen mixture under laminar and turbulent conditions.

The study on the heat release features of biogas-hydrogen mixture can improve the understanding on this fuel and provide useful information to control its combustion process in the real combustion equipment, it is thus necessary to conduct a study to investigate the heat release characteristics of biogas-hydrogen mixture. Furthermore, based on the literature review, it is known that the HRR markers identified by previous works are qualified to discern HRR locations in the flame, but some prediction uncertainties on HRR variation can be caused when utilizing these markers in the real flames. It is general that the turbulent stratification combustion takes place in the real combustion devices, which means that different equivalence ratios can exist simultaneously in the flame. If the correlation of a HRR marker with HRR is sensitive to the equivalence ratio, this marker could be not eligible to reflect the HRR variation accurately. Specifically, when a constant value of the marker is observed at two locations of the turbulent stratification flame, the actual values of HRR might not be the same due to different local equivalence ratios which could result in the different correspondence of this marker with HRR. In order to improve the accuracy of HRR imaging, it is thus necessary to examine the correlation of markers and HRR at various equivalence ratios and fuel compositions and evaluate the ability of a marker for the single-valued prediction on HRR.

Biogas has been extensively utilized for heating purpose, but its heat transfer features are not well understood with limited studies. Furthermore, much less studies were conducted to investigate the heat transfer characteristics of biogas-hydrogen flames. Since both CO_2 and H_2 in the fuel can influence the combustion and heat transfer

processes effectively, the variable fuel composition makes the heat transfer process of biogas-hydrogen flames to be more complex. Thus the study needs to be performed to identify the effects of CO_2 and H_2 on the heat transfer characteristics of biogas-hydrogen flames. Besides, although effects of the nozzle-to-plate on the heating performance are discussed in a large number of works, the optimal heating distance to achieve the best thermal efficiency is still proposed qualitatively rather than using a quantitative function to describe it. Hence, it is necessary to derive a function to predict the optimal heating distance with an improved accuracy, which can also facilitate to identify effects of related parameters on the optimal heating distance.

From the review on the studies about the pollutant emissions of impinging flames, it is known that few studies are conducted to investigate emission characteristics of impinging flames, thus emission formation process under the impingement condition have been not well understood. Furthermore, the pollutant emissions of biogas-hydrogen flames can be affected considerably by the variable proportions of CO_2 and H_2, thus more works need to be carried out in this aspect to improve the understanding on the emission characteristics of biogas-hydrogen fuel. Besides, it is known that NO can be produced via different routes (thermal route, prompt route, NNH intermediate based mechanism and N_2O intermediate based mechanism), but no research is performed to investigate the effects of nozzle-to-plate distance, equivalence ratio, Reynolds number and fuel composition on the NO production of the biogas-hydrogen impinging flame via these different mechanisms. Hence, it is necessary to examine the NO productions via different formation routes in the impinging jet flames in order to improve the understanding on both impinging flames and the biogas-hydrogen fuel.

3 Experimental apparatus and numerical methodology

3.1 Introduction

This chapter describes the experimental apparatus and numerical methodology adopted in this study. The impinging flame was used to investigate heat transfer and emission characteristics of laminar premixed biogas-hydrogen flame, and two experimental setups were utilized to measure the heat fluxes and pollutant emissions of biogas-hydrogen flames respectively. In addition, a one-dimensional numerical model was used to analyze heat release characteristics of the biogas-hydrogen combustion while a two-dimensional computational model was developed to calculate impinging flames to facilitate the analysis on the formation process of pollutant emissions in biogas-hydrogen impinging flames. The procedures of experimental measurements and numerical simulations are elucidated in detail while the uncertainty analysis on the experimental data and the validations of computational models are provided in this chapter.

3.2 Experimental apparatus

3.2.1 Burner and fuel supply

The schematic of laminar Bunsen burner is illustrated in Fig. 3.1. It is seen that the main parts of the laminar Bunsen burner are the burner head and the burner chamber. In this study, the burner head is made of brass while the burner chamber is made of stainless steel. To prevent the fuel leakage, a rubber seal ring is used between the burner head and the burner chamber when assembling the burner. The straight nozzle of the burner head has an inner diameter of 9 mm and a length of 40 cm. This nozzle

length can guarantee to obtain the fully developed laminar flow and a parabolic velocity distribution at the nozzle exit. Furthermore, another burner head with a different nozzle was adopted as deriving the function to predict the optimal heating distance, and the inner diameter and length of this nozzle are 12 mm and 50 cm, respectively. In addition, the burner chamber has an inner height of 7 cm and an inner diameter of 10 cm, which allows fuel and air to be fully mixed and achieve the homogeneous unburned mixture to generate the premixed flame. Several layers of wire nets are placed in the chamber in order to promote the mixing process and prevent the flash back of the premixed flame for the safety purpose.

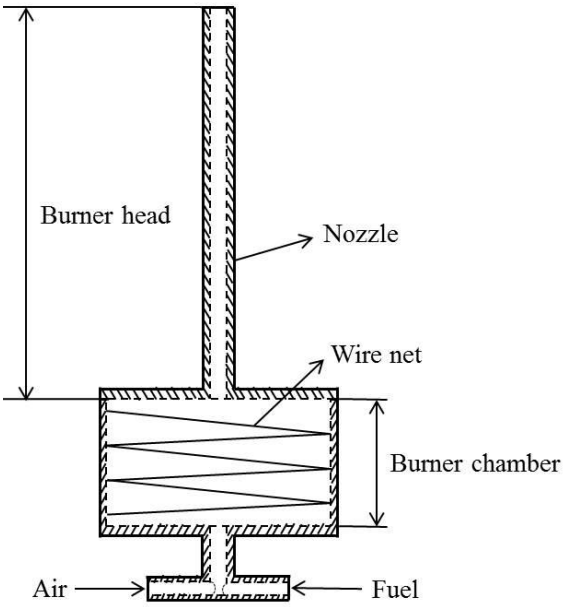

Fig. 3.1 The schematic of laminar Bunsen burner.

Biogas was achieved by blending pure commercial gases of CH_4 and CO_2 according to different volumetric ratios and named based on the methane proportion in the biogas. For example, the biogas composed of 75% CH_4 and 25% CO_2 is denoted as BG75 in the study. Furthermore, the commercial gas of H_2 was adopted as the addition for the simulated biogas. The level of hydrogen addition is defined by $\alpha H_2 = \dot{V}_{H2} / (\dot{V}_{CH4} + \dot{V}_{CO2})$ where $\dot{V}$ denotes the volumetric flow rate of a gas. The air was

supplied by an air compressor in the laboratory. The purity of CH_4, CO_2 and H_2 adopted in the experiment are over 99.99%. Additionally, in order to control and measure flow rates of these gases, several high accuracy flow meters were utilized in the experiment, which are Model FM-1050 series produced by the Matheson Corporation. These flow meters can ensure an accuracy of ±5% of the full scale flow rate. Furthermore, when using the reference scales, the accuracy can be further improved to ±1% of the full scale flow rate. For these flow meters, the flow scale on the flow meter does not equal to the real flow rate, which means that the correlation between the flow scale and the real value of flow rate needs to be established before the experimental measurement as shown in Fig. 3.2. With the correlation, the flow meter can be then used to control the flow rate at a specific condition. The experiment was conducted at the room temperature (298K) and ambient pressure (0.1 MPa), and fluid properties were calculated with the reference temperature of 298K and reference pressure of 0.1 MPa. Additionally, the average flow velocity in the nozzle was set to suitable values, and the Reynolds number of unburned flow is guaranteed to be less than 2000 so as to ensure the laminar flow in the nozzle.

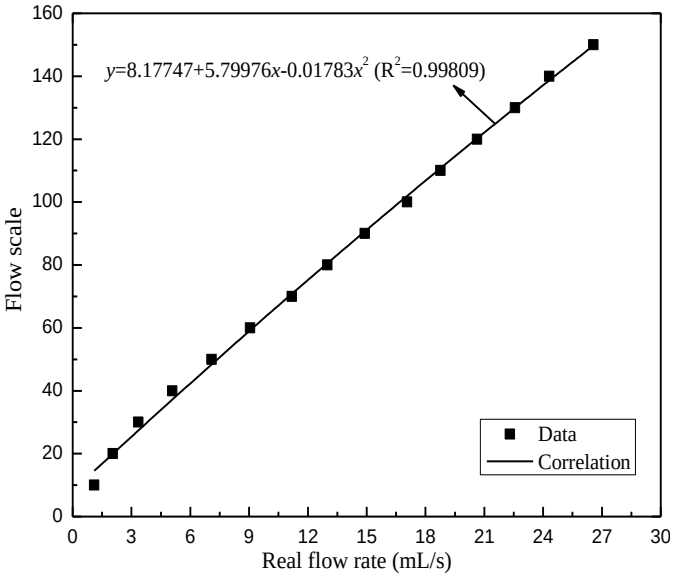

Fig. 3.2 The correlation between flow scale and real flow rates of methane.

For the fuel and air mixture, the equivalence ratio (ϕ) is a critical parameter that is defined as:

$$\phi = \frac{(\dot{V}_{air} / \dot{V}_{fuel})_{stoic}}{(\dot{V}_{air} / \dot{V}_{fuel})_{actual}} = \frac{(\dot{V}_{fuel} / \dot{V}_{air})_{actual}}{(\dot{V}_{fuel} / \dot{V}_{air})_{stoic}} \qquad \text{Equation 3-1}$$

where $\dot{V}_i$ represents the volumetric flow rate of fuel or air, and the subscript *actual* and *stoic* denote the fuel/air ratio or air/fuel ratio at real condition and stoichiometric condition, respectively. The chemical reactions of methane/air and hydrogen/air mixtures at the stoichiometric condition are given as follows:

$$CH_4+2(O_2+3.76N_2) = CO_2+2H_2O+7.52N_2$$

$$H_2+0.5(O_2+3.76N_2) = H_2O+1.88N_2$$

Thus it is known that the stoichiometric air/fuel ratios for methane and hydrogen are 9.52 and 2.38, respectively. According to Equation 3-1, the equivalence ratio of biogas-hydrogen mixture can be then defined as:

$$\phi = \frac{\frac{1}{1+\alpha H_2} \times \frac{\dot{V}_{CH_4}}{\dot{V}_{CH_4}+\dot{V}_{CO_2}} \times 9.52 + \frac{\alpha H_2}{1+\alpha H_2} \times 2.38}{\left(\frac{\dot{V}_{air}}{\dot{V}_{CH_4}+\dot{V}_{CO_2}+\dot{V}_{H_2}}\right)_{actual}} \qquad \text{Equation 3-2}$$

With this equation, the mole fractions of air, CH_4, CO_2 and H_2 can be calculated at a specific ϕ for a given fuel composition, and then the real flow rates of these gases can be obtained with the total flow rate.

3.2.2 Heat transfer measurement

The experimental apparatus to measure the heat flux and the impinging flame temperature is shown in Fig. 3.3. The setup to measure heat fluxes of impinging flames consists of a flat impingement plate and a data acquisition system. The impingement plate is a square plate with the side length of 60 cm and a thickness of 8 mm, which is made of copper in consideration of its excellent thermal conductivity. In addition, the targeted impingement surface is painted black to minimize the thermal radiation effects of plate on the heat transfer process. The impingement plate is cooled on the back side with a cooling water jacket which is covered by a plexiglass plate that can facilitate the observation of the water flow. Furthermore, the cooling water is maintained to 313 K by a thermostat (Julabo Labortechnik GmbH, Model fc 1600s), which can prevent the water vapor produced by the combustion process to be condensed on the plate and then eliminate effects of liquid water on the heat transfer process so as to improve the data accuracy. In order to support the impingement plate, a stainless steel frame was constructed and utilized. Additionally, several layers of screen mesh were placed around the flame to minimize the disturbance of ambient flow on the flame and make for the steady heat transfer process. The data acquisition system is composed of a ceramic heat flux sensor (Vatell Corporation, Model HFM-6D/H), voltage amplifier (Vatell Corporation, Model AMP-6), an analog/digital converter (IOtech Personal Daq/56^{TM}) and a computer. The heat flux sensor, which is coated by zynolyte with the emissivity of 0.94, is embedded in the center of the plate to collect the heat transfer data. This heat flux sensor has an effective size of 2 mm×2 mm×0.08 mm, implying that the heat absorbed by the sensor is negligible. As the sensor is heated by an impinging flame, the voltage signal generated by the sensor is amplified by the amplifier initially before to be converted to the digital signal in the

analog/digital converter. After this, the data are recorded in the computer and converted to heat flux values with an accuracy of ±3% by utilizing a NIST traceable calibration certificate which is provided along with the sensor. With the data collection system, 300 samples can be recorded per minute, and heat flux measurement at a location was sustained to 1 min in the experiment so as to obtain the average value. In addition, in order to facilitate the analysis on heat transfer process, the impinging flame temperature was also measured utilizing an uncoated type-B thermocouple which has a wire diameter of 0.25mm. Due to the small diameter, the heat conduction between flame and thermocouple can be neglected. Furthermore, measured temperature data were corrected for the radiation loss.

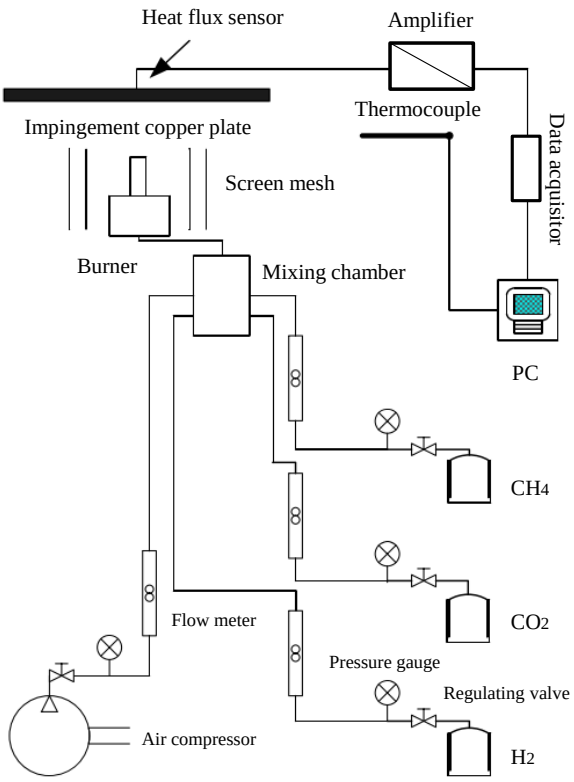

Fig. 3.3 The experimental apparatus for heat flux measurement.

Since the laminar premixed flame is an axial symmetry flame, the heat flux along the radial direction can be measured from the center point, and the total heat transfer rate can be then calculated with the measured data and the annulus area as shown in Fig.

3.4. Based on the measured local heat flux (q_{local}), the total heat transfer rate (q_{total}) can be obtained with the following equation:

$$q_{total} = \iint^{A} q_{local} dA = 2\pi \int q_{local} r dr \qquad \text{Equation 3-3}$$

where q_{local} and q_{total} represent the measured heat flux and calculated total heat transfer rate, respectively; r and A denote the radii of the round heating area and the annulus element of the heating area, respectively. When measuring heat fluxes of an impinging flame, the burner was fixed on a three-dimensional positioner which can set the flame position with an accuracy of 1 mm in one direction. At a nozzle-to-plate distance, radial heat fluxes of the flame was measured by moving the burner horizontally, and distance between each measure point was fixed to 1 mm which can enable to capture the heat flux distribution with a satisfactory accuracy. The maximum radii of 30 mm was adopted for the heat flux measurement in the study considering that heat fluxes outside this region contribute a negligible part of total heat transfer rate. Similarly, the radial distribution of impinging flame temperature was also obtained by moving the burner relative to the thermocouple. Since the nozzle-to-plate distance can affect the heat transfer rate considerably, heat fluxes of the laminar premixed Bunsen flame were measured experimentally at different nozzle-to-plate distance which is increased from 5 mm to 30 mm with an interval of 5 mm.

To investigate the heat transfer characteristics of biogas-hydrogen flames, BG50, BG75 and methane with hydrogen addition (αH_2=0, 0.1, 0.3, 0.5) were utilized to generate laminar premixed flames, and the ϕ was kept to 1.2 at which the flame is relatively stable. Effects of H_2 and CO_2 on the heat transfer process will be investigated. To derive the correlation of optimal heating distance, effects of nozzle-

to-plate distance, Reynolds number and equivalence ratio on the heating performance will be discussed. The Reynolds number considered in this part was varied from 600 to 1000 while the tested equivalence ratios were 0.8, 1.0, 1.2 and 1.4. It should be noted that measurements of the heat flux and the temperature were mainly conducted by utilizing the burner with a diameter of 9 mm. Whereas, the burner with a diameter of 12 mm was also adopted as deriving the quantitative correlation of the optimal heating distance so as to ensure the applicability of this correlation.

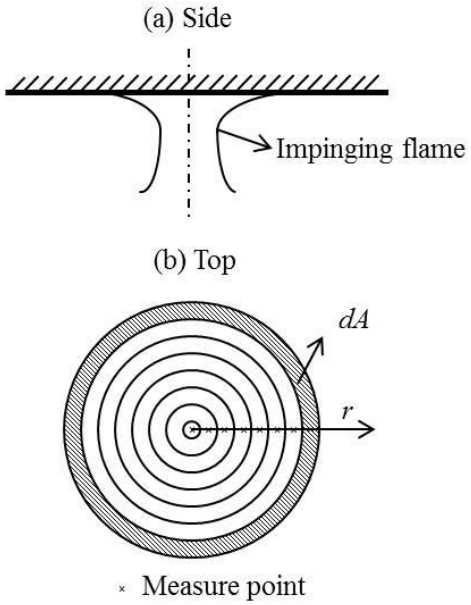

Fig. 3.4 The schematic of heat flux measurement.

3.2.3 Pollutant emission measurement

The experimental setup to measure the overall pollutant emissions of impinging flames is illustrated in Fig. 3.5. The equipment is composed of a flue gas collection system and a gas analysis system. The emission collection system has a conical hood, filters, a condenser and a pump. A smaller copper plate was adopted here to facilitate the collection of burned gases. This plate has a diameter of 200 mm and is also cooled by the water jacket which is fixed to 313 K by the thermostat. Considering the size of laminar premixed Bunsen flame, this plate is large enough to cool down the burned

gases and then frozen the reactions effectively at the edge of plate, which can ensure that all the pollutant emissions are formed under the impingement condition and will be not further affected. In order to measure the overall pollutant emissions, the hood method [245] was utilized to collect the burned gases completely. As shown in the figure, a conical stainless steel hood is placed over the copper plate, and it has a base-diameter of 300 mm and a height of 300mm. The larger diameter of the hood can ensure the complete collection of the burned gases. When the burned gases pass through the upper nozzle of the hood, the gaseous emission can be sampled and transported to the gas analyzers by the pump in the gas collection system. At each condition, in order to ensure the equilibrium condition of flue gases in the hood, the sampling was conducted after the flame was sustained to 5 min at this condition. As the flue gas is collected, it needs to pass through a double tube initially in which the cooling air can flow in the outer channel to cool down the exhausted gases. This cooling process can impede the further reactions in the burned gases effectively. Before entering the gas analyzer, the cooled sampling needs to further pass through several filters and a condenser for the dehydrated purpose. The gas analyzer system contains two gas analyzers which were utilized to measure and analyze four gaseous emissions (CO, CO_2, NO and NO_2) of impinging flames experimentally. Specifically, the CO and CO_2 were measured simultaneously using the Non-dispersed Infrared Sensor (California Instruments Corporation, Model 300, NDIR) while the NO and NO_2 were analyzed utilizing the Heated Chemiluminescence Analyzer (California Instruments Corporation, Model 600, HCLD). By using these gas analyzers, 150 data can be recorded per minute. Thus the experimental measurement was sustained to 1min at each condition so as to calculate the average value of pollutant emissions. In addition, both zero and span calibrations were performed using the standard gases

before the measurement, which can ensure the accuracy of the experimental data. Besides, the impinging flame temperature was also measured using the type-B thermocouple to facilitate the analysis, and measured temperatures were corrected by considering radiation and conduction losses.

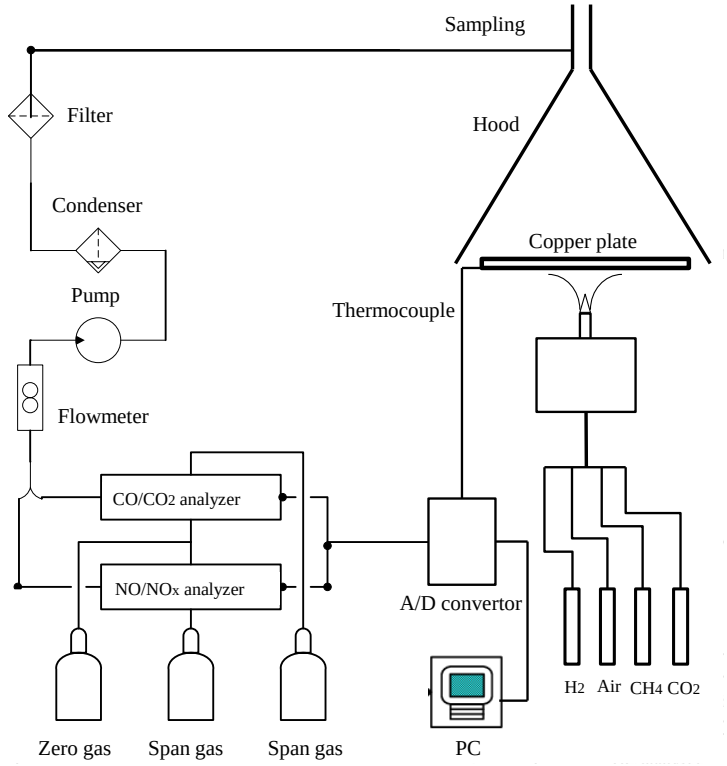

Fig. 3.5 The experimental apparatus for pollutant emission measurement.

Emission index is a dimensionless quantity which can facilitate the data comparison among different conditions and the analysis on the emission formation process. Thus the emission indexes were calculated based on the measured data as follows:

$$EI_N = \frac{1000 \cdot n_c c_N M_N}{c_{CO_2} M_{fuel}} \qquad \text{Equation 3-4}$$

where c_N and c_{CO2} denote the measured volumetric concentrations of the pollutant N and CO_2, respectively. M_N and M_{fuel} represent the molecular weights of the pollutant N and the fuel, respectively. n_c symbolizes the moles of carbon contained in a mole of

fuel. For example, n_c is equal to 1 as CH_4 is used as the fuel, but n_c would be smaller than 1 for the methane-hydrogen fuel because hydrogen is a carbon-free fuel. In addition, it should be noted that only CO_2 concentration was considered in the equation to represent the consumed fuel concentration in the flame because concentrations of other carbon-containing species such as HC and CO were found to be several orders lower than that of CO_2. In addition, considering that the biogas is the only resource to produce CO emission in the biogas-hydrogen flames, the biogas-based emission index can be more effective to discuss influences of fuel compositions on the CO formation process. The biogas-based emission index was obtained by the following equation:

$$EI = \frac{EI_N}{m_{biogas}} \qquad \text{Equation 3-5}$$

where m_{biogas} is the mass fraction of biogas in the biogas-hydrogen mixture. Consequently, EICO and EINOx were obtained based on the measured data. Besides, it is found that NO_2, as a more toxic emission than NO, contributes to a significant proportion of NOx in this study, thus the $EINO_2$ and NO_2/NOx ratio were also obtained to investigate the formation process of NO_2 in the impinging flames.

In this study, the pollutant emissions of impinging flames were measured at different nozzle-to-plate distances (5-50 mm) so as to examine its effects on the emission production. In order to discuss effects of CO_2 on the pollutant emissions, BG50, BG75 and methane with hydrogen addition (αH_2= 0.1) were utilized as the fuel to generate laminar premixed flames at Re=1000 and ϕ=1.2. To investigate influences of H_2 on the emission formation, the BG75 with hydrogen enrichment (αH_2= 0, 0.2, 0.4, 0.6) was used to generate impinging flames at Re=1200 and ϕ=1.2. In addition, only BG75

with hydrogen addition of αH_2= 0.1 was adopted as the fuel so as to investigate effects of Reynolds number (*Re*= 600, 800, 1000, 1200) and equivalence ratio (ϕ = 0.8, 1.0, 1.2, 1.4) on the production of CO, NO_2 and NOx in flames. It should be noted that only the burner with a diameter of 9 mm was utilized here to generate laminar premixed impinging flames.

3.2.4 Uncertainty analysis

For the experimental study, it is customary that both experimental data and related uncertainty analysis are presented. The uncertainty analysis is quite significant to the rational evaluation on the repeatability of experimental data, and it can help to identify the major reasons causing the data uncertainty and then improve the reliability and accuracy of the experimental data. In addition, the data user can use the uncertainty range to examine the reliability and accuracy of their data. Generally, the data uncertainty is composed of systematic and random uncertainties. The systematic uncertainty is caused by the experimental instruments and techniques while the random uncertainty is attributed to the unpredictable variation during the experimental measurements. With the careful calibrations of instruments and the repeat measurements, the systematic and random uncertainties can be improved to obtain the better precision and accuracy of experimental data. Hence, experimental instruments in this study were calibrated carefully before the measurements and the experiments were performed several times at the same condition, which is expected to promote the precision and accuracy of the measured data. Furthermore, the uncertainty analysis was performed based on the method proposed by Kline and McClintock [246].

For a variable χ_n, it consists of two parts: the mean of multiple measurements ($\overline{\chi}$) and the uncertainty ($\delta\chi_n$) as follows:

$$\chi_n = \bar{\chi} + \delta\chi_n \qquad \text{Equation 3-6}$$

For the measured data obtained in the experiment, the first order uncertainty analysis is adopted with the assumption of that the uncertainty statistics follows the Gaussian distribution. The Gaussian distribution of a variable can be then described by the following standard normal probability distribution function (PDF):

$$f(z) = \frac{1}{\sqrt{2\pi}} e^{-\frac{z^2}{2}} \qquad \text{Equation 3-7}$$

where z denotes the variable. With the 95% confidence level, 95% of experimental data need to fall within the uncertainty interval. Based on this, the following equation can be then obtained by applying a particular value of z:

$$\int_{-z_a}^{z_a} f(z)dz = 0.95 \qquad \text{Equation 3-8}$$

Subsequently, the uncertainty ($\delta\chi_n$) can be obtained as follows:

$$\delta\chi_n = 1.96\sigma \qquad \text{Equation 3-9}$$

where σ represents the standard deviation of the experimental measurements.

The calculated result based on the multiple measurements can be written as follows:

$$\chi = f(\chi_1, \chi_2, ..., \chi_n) \qquad \text{Equation 3-10}$$

where χ and χ_n represent the calculated result and the measured value of nth measurement, respectively. The total uncertainty can be then calculated according to the following equation:

$$\delta\chi^2 = \left(\frac{\partial\chi}{\partial\chi_1}\delta\chi_1\right)^2 + \left(\frac{\partial\chi}{\partial\chi_2}\delta\chi_2\right)^2 + \cdots + \left(\frac{\partial\chi}{\partial\chi_n}\delta\chi_n\right)^2 \quad \text{Equation 3-11}$$

where $\delta\chi$ and $\delta\chi_n$ denote the overall uncertainty and the uncertainty of the *n*th measurement.

Based on the above method, using the 95% confidence level, the uncertainties of the measured data in this study were calculated and summarized in Table 3.1.

Table 3.1 The Uncertainties of experimental data.

Parameters	Uncertainty (%)
Heat flux	0.9
Flame temperature	0.8
Flame height	0.5
CO	1.2
CO_2	0.4
NO	1.5
NOx	1.4

3.3 Numerical methodology

3.3.1 One-dimensional laminar premixed flame (Chemkin)

In this study, the PREMIX code [247] of the CHEMKIN-II was adopted to calculate the one-dimensional non-stretched laminar premixed flames and then investigate the heat release characteristics of biogas-hydrogen mixture. The governing equations for the steady, isobaric, 1-D propagation flame are described as follows:

Continuity: $$\dot{M} = \rho u A_c \quad \text{Equation 3-12}$$

Energy: $$\dot{M}\frac{dT}{dx} - \frac{1}{c_P}\frac{d}{dx}\left(\lambda A_c \frac{dT}{dx}\right) + \frac{A_c}{c_P}\sum_{k=1}^{K}\rho Y_k v_k c_{Pk}\frac{dT}{dx} + \frac{A_c}{c_P}\sum_{k=1}^{K}\dot{\omega}_k h_k W_k = 0 \quad \text{Equation 3-13}$$

Species: $$\dot{M}\frac{dY_k}{dx}+\frac{d}{dx}\left(\rho A_c Y_k v_k\right)-A_c\dot{\omega}_k W_k=0 \quad (k=1, 2,\ldots, K)$$ Equation 3-14

State equation: $$\rho=\frac{p\bar{W}}{RT}$$ Equation 3-15

where $\dot{M}$ and ρ are the mass flow rate and mass density, respectively; u and A_c denote the fluid velocity and the sectional area of steam flowing to the flame, respectively; x is the spatial coordinate; c_p and c_{pk} are the constant pressure heat capacities of the mixture and kth species, respectively; Y_k and v_k denote the mass fraction and the diffusional velocity of the kth species, respectively; $\dot{\omega}_k$, h_k and W_k are the molar rate of production by reactions, specific enthalpy and molecular weight of the kth species; $\bar{W}$ is the mean molecular weight of the mixture; T and λ are the temperature and the thermal conductivity of the mixture, respectively; p and R represent the pressure and the universal gas constant, respectively.

Additionally, the net production rate of kth species is resulted from all the elementary reactions involving the kth species. In order to calculate the production rate of the kth species by each reaction, the elementary reaction is assumed to proceed according the law of mass action, and the Arrhenius equation describing the forward reaction rate coefficient is give as follows:

$$k_f=BT^{\beta}e^{\frac{-E_a}{RT}}$$ Equation 3-16

where k_f and E_a are the reaction rate constant of forward reaction and the activation energy of the reaction, respectively. B and β denote a constant and the temperature exponent, respectively.

For the numerical simulations of laminar premixed flames, the initial pressure and temperature of the biogas-hydrogen mixture were set to 1 atm and 298 K which are consistent with the environment in the laboratory while the initial mass flow rate of unburned gases was set to be 0.04 g/cm^2. In addition, apart from the soret effect, the multicomponent diffusivity model was also considered in the calculations. In the multicomponent diffusivity model, the diffusion velocity is defined as:

$$v_k = \mathcal{V}_k + \mathcal{W}_k \qquad \text{Equation 3-17}$$

where $\mathcal{V}_k$ and $\mathcal{W}_k$ are ordinary diffusion velocity term and the thermal diffusion velocity, respectively. These two terms are defined as:

$$\mathcal{V}_k = \frac{1}{X_k \bar{M}} \sum_{j \neq k}^{K} W_j D_{k,j} \mathbf{dj} \qquad \text{Equation 3-18}$$

$$\mathbf{dj} = \nabla X_k + (X_k - Y_k) \frac{1}{p} \nabla p \qquad \text{Equation 3-19}$$

$$\mathcal{W}_k = -\frac{D_k^T}{\rho Y_k} \frac{1}{T} \nabla T \qquad \text{Equation 3-20}$$

where X_k and D_k denote the mole fraction and the thermal diffusion coefficient of kth species. Besides, the thermodynamic and transport properties of species, as well as the chemical reactions, are described in the files provided by the detailed chemical mechanism, which can be accessed by the software before the calculation. The computation domain was defined from 0.0 cm to 10.0 cm along the x coordinate, which is long enough to achieve the equilibrium condition in the downstream. The adaptive mesh was adopted in the computational domain to facilitate the convergence of solution, and the damped modified Newton algorithm combined with the time

integration were utilized to solve the governing equations of the flames. The gradient and curvature were defined to 0.2 and 0.4 respectively so as to control the adaptive mesh.

In particular, in order to investigate the heat release characteristics of premixed flames, the total HRR of a reaction and the combustion process can be calculated as follows:

$$q_r = \int_x w_r \sum_k h_k (v''_{r,k} - v'_{r,k}) dx \qquad \text{Equation 3-21}$$

$$Q = \sum_r q_r \qquad \text{Equation 3-22}$$

where q_r and Q are the total HRR of an elementary reaction and the combustion process, respectively; w_r is the net reaction rate of reaction r; h_k is the formation enthalpy of kth species; $v''_{r,k}$ and $v'_{r,k}$ are the stoichiometric coefficients of kth species in reaction r in the products and reactants, respectively. Furthermore, the fractional contribution of a reaction to the total HRR (f_c) can be then determined by $f_c = 100 \cdot q_r/Q$.

To discuss the heat release features of biogas-hydrogen flams, BG50, BG75 and methane with different hydrogen addition (αH_2 = 10%-50%) were used as the fuel to calculate the laminar premixed flame at various equivalence ratio (ϕ = 0.8, 1.0, 1.2). Effects of ϕ, H_2 and CO_2 on the HRR and primary exothermic reactions of biogas-hydrogen flames will be discussed quantitatively. Furthermore, it is known that CO_2 exerts influences through its dilution/thermal effects and chemical effects. In order to further clarify the influences of CO_2 on the heat release characteristics, a fictitious CO_2, denoted as FCO_2, was utilized in this study to isolate these two effects. FCO_2 is assumed to have same thermochemical property, transport property and third-body collision efficiency as that of normal CO_2, while it has no reactivity to participate in

reactions. In the study, CH_4/FCO_2 represents the fuel composed of 50% methane and 50% FCO_2. Consequently, the influences of FCO_2 on heat release characteristics can be considered to be the pure dilution/thermal effects, while the difference between heat release characteristics of BG50 and CH_4/FCO_2 can be then attributed to the chemical effects of CO_2.

Table 3.2 The fuel compositions in molar percentages.

Flame series	ϕ	αH_2	X_{CH4}	X_{CO2}	X_{H2}	X_{AIR}
1_BG50	0.8	0.0	0.0719	0.0719	0.0000	0.8561
2_BG50	0.8	0.1	0.0681	0.0681	0.0136	0.8503
3_BG75	0.8	0.0	0.0756	0.0252	0.0000	0.8992
4_BG75	0.8	0.1	0.0727	0.0242	0.0097	0.8934
5_CH_4	0.8	0.0	0.0775	0.0000	0.0000	0.9225
6_CH_4	0.8	0.1	0.0752	0.0000	0.0075	0.9173
7_BG50	1.0	0.0	0.0868	0.0868	0.0000	0.8264
8_BG50	1.0	0.1	0.0820	0.0820	0.0164	0.8196
9_BG75	1.0	0.0	0.0921	0.0307	0.0000	0.8771
10_BG75	1.0	0.1	0.0885	0.0295	0.0118	0.8703
11_CH_4	1.0	0.0	0.0951	0.0000	0.0000	0.9049
12_CH_4	1.0	0.1	0.0921	0.0000	0.0092	0.8987
13_BG50	1.2	0.0	0.1007	0.1007	0.0000	0.7987
14_BG50	1.2	0.1	0.0950	0.0950	0.0190	0.7911
15_BG75	1.2	0.0	0.1079	0.0360	0.0000	0.8561
16_BG75	1.2	0.1	0.1035	0.0345	0.0138	0.8482
17_CH_4	1.2	0.0	0.1119	0.0000	0.0000	0.8881
18_CH_4	1.2	0.1	0.1083	0.0000	0.0108	0.8808
19_BG75	1.2	0.2	0.0994	0.0331	0.0265	0.8410
20_BG75	1.2	0.3	0.0956	0.0319	0.0382	0.8343
21_BG75	1.2	0.4	0.0921	0.0307	0.0491	0.8281
22_BG75	1.2	0.5	0.0888	0.0296	0.0592	0.8223

When examining the single-valued prediction of HRR marker on HRR, the peak-to-peak and peak-to-integrated correlations of markers and HRR will be established in a wide range of conditions, and the sensitivity of HRR markers to the equivalence ratio and the fuel composition will be examined. To examine the sensitivity to the equivalence ratio, BG75 and methane without hydrogen enrichment were adopted as the fuel, and equivalence ratio was increased from 0.6 to 1.4 with an interval of 0.1. Furthermore, the sensitivity to the fuel composition will be examined by employing a

wide range of fuel compositions which are presented in Table 3.2. It can be noted that only three equivalence ratios (ϕ = 0.8, 1.0, 1.2) were considered in this part.

3.3.2 Two-dimensional laminar premixed impinging flame (STAR-CD)

In order to investigate the formation process of gases emissions, the CFD simulations of impinging flames were conducted to obtain more information on the combustion process of impinging flames. The STAR-CD software [248] was employed to calculate the laminar premixed impinging flames. The laminar premixed Bunsen flame is an axis-symmetric flame, thus two-dimensional computational domain was adopted to reduce the calculation cost. The schematic of the rectangular computational domain is illustrated in Fig. 3.6. The radial size of the domain is set to be 100mm in order to ensure the equilibrium condition of the burned gases at the outlet boundary. Furthermore, since the impinging flame needs to be calculated at different separated distances, five domains were established with different axial sizes which is increased from 10mm to 50mm with the interval of 10mm. To guarantee the calculation accuracy of combustion process and the thermal boundary layer, grids in the flame region (i.e., $0 \leq r \leq 6$mm and $0 \leq z \leq 30$ mm), as well as in the region near the impingement plate (i.e., $24 \leq z \leq 30$ mm), were refined to 0.15 × 0.15mm. Outside these regions, the grids were increased to 1 × 1mm gradually. It is noted that increasing the grids resolution did not improve the numerical solution significantly.

According to the experimental condition, the boundaries were well defined as shown in Fig. 3.6. It is seen that the impingement plate can be treated as a wall at the fixed temperature of 313K with the no-slip condition. Although the radial plate temperature can be affected by the impinging flames in the experiment, its variation is generally slight and exerts negligible effects on the simulation results. Hence, utilizing the

constant plate temperature is considered to be sufficiently accurate for our purposes. In the experiment, the ambient air has the possibility to flow in the domain from the outlet boundary, but it can induce negligible effects on the burned gases considering the large range of domain in the *r* direction. Thus the outlet can be adopted reasonably and defined with a constant outflow of 10^{-5} kg/s. The pressure boundary was defined with the atmosphere pressure and a constant temperature of 298 K, and the mass fraction of oxygen at this boundary was set to 0.233 that is consistent with the ambient air. Since the laminar flow of unburned gases is fully developed in the nozzle, the axial velocity at the exit of nozzle should have the parabolic distribution. Thus, based on the average exit velocity in the corresponding experimental condition, the parabolic profile of inlet velocity was prescribed at the inlet boundary. The inlet temperature of unburned mixture was defined to be 298K while the mass fractions of related gases at the inlet boundary were consistent with the respective experimental data. In addition, a wall with the constant temperature of 298K was adopted to represent the burner rim, and the centerline of the burner was defined by the axisymmetric boundary.

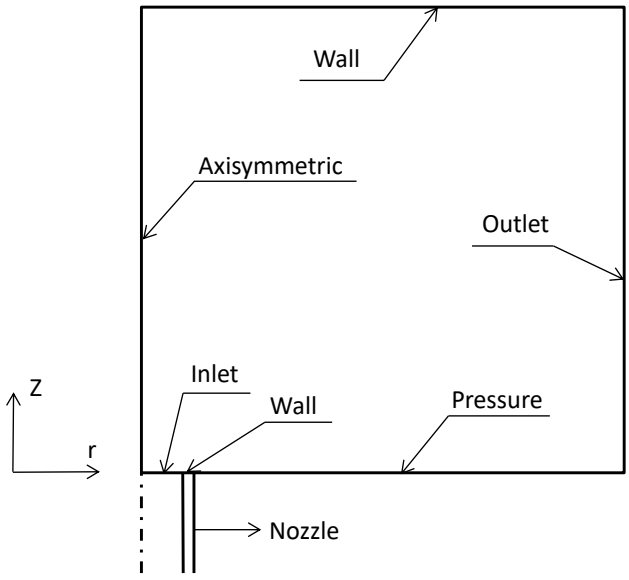

Fig. 3.6 The computational domain and the boundary conditions.

In the STAR-CD software, the governing equations of mass, momentum and enthalpy for the compressible laminar reactive flow and the conservation equation for the constituent species can be described as follows:

$$\frac{\partial \rho}{\partial t} + \frac{\partial}{\partial x_j}\left(\rho u_j\right) = s_m \qquad \text{Equation 3-23}$$

$$\frac{\partial \rho u_i}{\partial t} + \frac{\partial}{\partial x_j}\left(\rho u_j u_i - \tau_{ij}\right) = -\frac{\partial p}{\partial x_i} + s_i \qquad \text{Equation 3-24}$$

$$\frac{\partial \rho h}{\partial t} + \frac{\partial}{\partial x_j}\left(\rho h u_j - F_{h,j}\right) = \frac{\partial p}{\partial t} + u_j \frac{\partial p}{\partial x_j} + \tau_{ij}\frac{\partial u_i}{\partial x_j} + s_h \qquad \text{Equation 3-25}$$

$$\frac{\partial}{\partial t}\left(\rho Y_k\right) + \frac{\partial}{\partial x_j}\left(\rho u_j Y_k + F_{k,j}\right) = s_k \qquad \text{Equation 3-26}$$

where ρ is the mass density; t is the time; x_i denotes the Cartesian coordinate system (i=1, 2, 3); u_i is the absolute velocity component in the x_i direction; p and τ_{ij} are the pressure and the pressure tensor component, respectively; h is the static enthalpy; $F_{h,j}$ and $F_{k,j}$ represent the diffusional energy flow component and the diffusional flux component in the x_j direction, respectively; s_m, s_h, s_i and s_k denote the mass source, energy source, momentum source and the mass production rate of kth species, respectively. Y_k is the mass fraction of the kth species.

Based on the Finite Volume Method, convection terms and diffusion terms were discretized by the second-order upwind scheme and the central difference scheme, respectively, and the coupling between velocity and pressure was completed by the PISO algorithm. For the calculation of the compressible reactive flow, a CHEMKIN-compatible complex chemistry is incorporated in the STAR-CD software, which can

solve all types of reactions including Standard Arrhenius type reaction, Three-body reaction, Pressure-dependent fall-off reaction and Landau-Teller reaction. By employing the Point-coupled method, the net formation rates of species during the combustion process can be calculated. Buoyancy effect is not included in the model considering that the laminar premixed Bunsen flame is a momentum dominated flame while including buoyancy effect did not affect simulation results significantly.

Thermo-physical properties of the species were calculated as functions of temperature, mass fraction and other variables. For each species, the kinetic theory was adopted to calculate its viscosity, thermal conductivity and binary mass diffusivity while the temperature dependent polynomial function was employed to obtain its specific heat capacity. In addition, the density of fluid was calculated with the mixture molecular weight and the ideal-gas equation of state. The molecular viscosity and thermal conductivity of the mixture follow the Wilke and Mathur formulas respectively while the specific heat capacity of the mixture was calculated as the mass-weighted average of its component values.

For the hydrocarbon fuels that contain no nitrogen, the NO can be formed primarily by four mechanisms including thermal route, prompt route, NNH intermediate route and N_2O intermediate route [249]. In order to obtain a clear understanding on the NO emission, the NO formations via these routes can be calculated separately and then identify their relative significances on the NO formation in the impinging biogas-hydrogen flames. This was completed by gradually removing the initiation reactions of different routes in a series of simulations. The reactions to initialize the NO production of different mechanisms are summarized in Table 3.3. To perform the simulation at a condition, the first simulation (SIM I) was conducted with the

complete chemical mechanism, and the second simulation (SIM II) was carried out by removing the initiation reactions of prompt NO. The initiation reactions of prompt and NNH routes were both removed in the third simulation (SIM III). In the fourth simulation (SIM IV), the initiation reactions of prompt, NNH and N_2O routes were removed. Consequently, it is known that the NO amount produced via prompt route is the difference between SIM I and SIM II, while the difference in NO between SIM II and SIM III is attributed to the NNH route. The NO amount contributed by N_2O route is the difference between SIM III and SIM IV, and then the NO formed via thermal route can be determined in the SIM IV.

Table 3.3 The initiation reactions of NO formation mechanisms.

NO routes	**Reactions to initialize NO formation**
Thermal route	$N_2+O = NO+N$
	$O_2+N = NO+O$
	$N+OH = NO+H$
Prompt route	$N_2+CH = HCN+N$
	$N_2+CH_2 = HCN+NH$
NNH intermediate	$NH+N = N_2+H$
	$NH+NO = N_2+OH$
	$NNH = N_2+H$
	$NNH+M = N_2+H+M$
	$NNH+O_2 = HO_2+N_2$
	$NNH+O = OH+N_2$
	$NNH+H = H_2+N_2$
	$NNH+OH = H_2O+N_2$
	$NNH+CH_3 = CH_4+N_2$
N_2O intermediate	$N_2O+OH = N_2+HO_2$
	$N_2O(+M) = N_2+O(+M)$
	$N_2O+H = N_2+OH$
	$N_2O+O = N_2+O_2$

For each simulation, the cold flow simulation was carried out firstly till achieving the stable condition. After this, a small ignition region with a high temperature (2000K) was activated near the nozzle exit in order to initialize the chemical reactions in the computational domain. The total run time for each simulation is about 0.3s, with a

constant time step of 1×10^{-5}s. The longer run time and the smaller time step did not affect the numerical results significantly.

3.3.3 Chemical mechanisms

As investigating the heat release characteristics, the GRI mechanism [250] and San Diego mechanism [251] were adopted in the Chemkin simulations. The GRI mechanism consists of 325 elementary chemical reactions and 53 species while the San Diego mechanism consists of 268 elementary chemical reactions and 57 species. These two mechanisms have been validated for the methane combustion by a large amount of experimental data. It should be noted that the investigation on the heat release characteristics was mainly performed based on the simulation results of GRI mechanism while the San Diego mechanism was adopted as studying the HRR markers so as to eliminate result sensitivity to the mechanism. In addition, considering the balance between the calculation accuracy and calculation cost, the chemical mechanism composed of methane mechanism developed by Peters and Rogg [252] and the NO mechanism of San Diego mechanism [251] was utilized in the CFD simulations. This mechanism consists of 95 elementary chemical reactions and 32 species.

3.3.4 Validations of computational models

The GRI mechanism was adopted to conduct the majority of simulations of one-dimensional laminar premixed flames, thus only the validation of GRI mechanism for the biogas-hydrogen combustion is performed. The laminar flame speed is a critical parameter to evaluate the accuracy of a chemical mechanism, thus the measured laminar flame speeds of biogas-hydrogen fuel and numerical simulation results of GRI mechanism are compared in Fig. 3.7. It can be seen that the calculated laminar

burning velocities show satisfactory agreement with the measured data, indicating that the GRI mechanism is capable of describing the combustion process of one-dimensional laminar premixed biogas-hydrogen flames with a satisfactory accuracy.

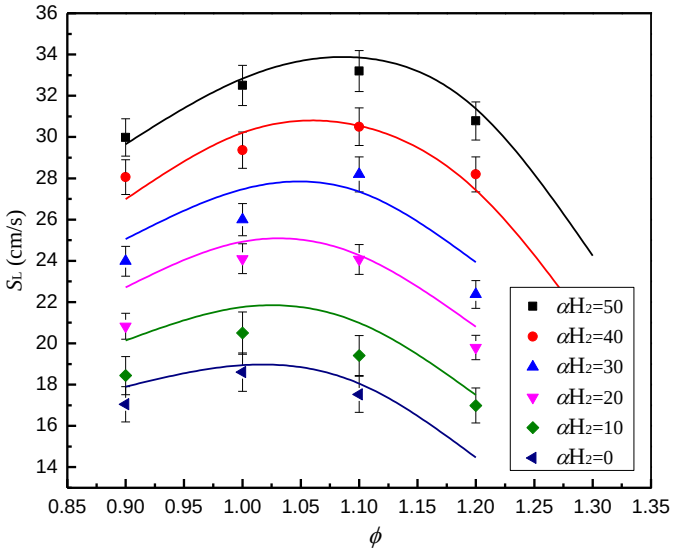

(a) BG50

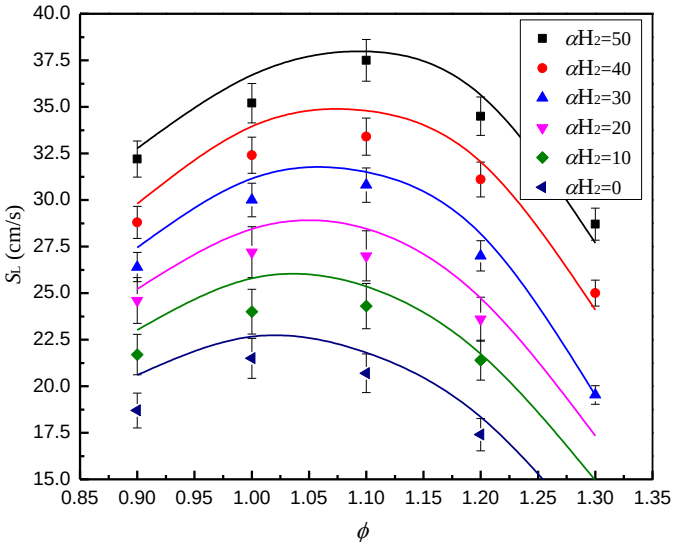

(b) BG60

Fig. 3.7 The comparison of experimental and calculated laminar flame speeds of biogas-air mixtures at 1 atm and 298K.

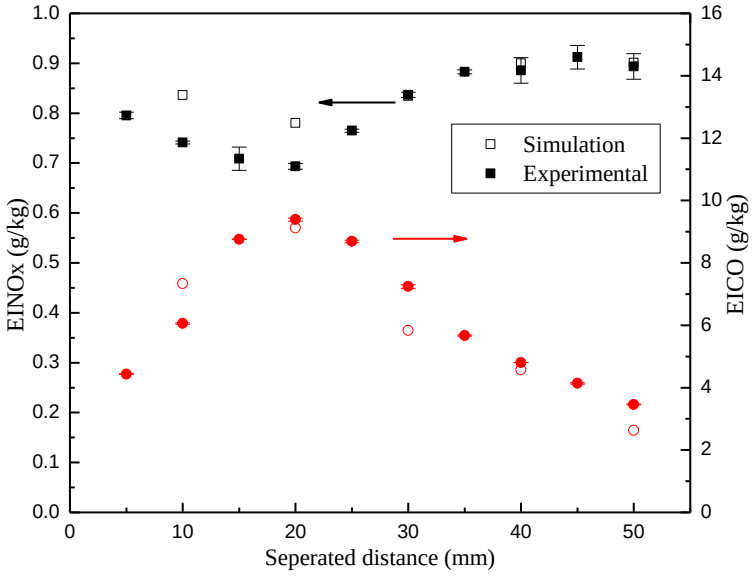

(a) EICO and EINOx

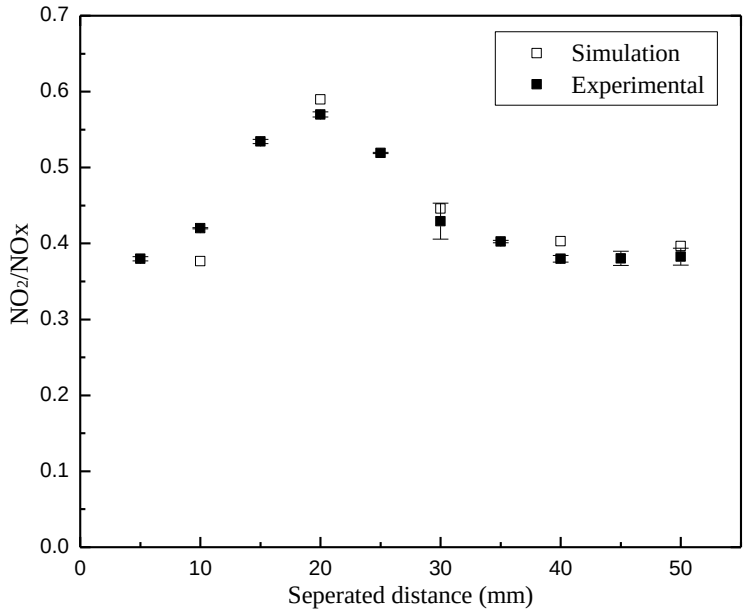

(b) NO_2/NOx ratio

Fig. 3.8 The comparison of experimental and simulation data (EICO, EINOx and NO_2/NOx ratio) of laminar premixed BG75 impinging flame at ϕ=1.2, αH_2=0.1 and *Re*=1000.

For the two-dimensional simulations, the numerical results and experimental data of laminar premixed BG75 impinging flames at ϕ =1.2, αH_2=0.1 and *Re*=1000 are compared in Fig. 3.8. It is seen that the simulation results of emission indexes and NO_2/NOx ratio agree well with the experimental data, and the variation trends of experimental data with the nozzle-to-plate distance can be reflected accurately by the

simulation results. However, it is noted that there still exist slight differences between the experimental data and the simulation results, which can be caused by the exclusion of radiation model in the simulation and the uncertainties of experimental data. Hence, it is concluded that this two-dimensional computational model has the capability to predict pollutant emissions of laminar premixed biogas-hydrogen impinging flames with a satisfactory accuracy and then can be used to achieve our objectives.

4 Heat release characteristics of laminar premixed biogas-hydrogen flame

4.1 Introduction

This chapter presents the numerical data of heat release characteristics of laminar premixed biogas-hydrogen flames [253, 254]. In the first part, using the PREMIX code of CHEMKIN II and the GRI 3.0 mechanism, the global heat release rate, mole fractions of major and minor species, and HRR contributions of primary elementary reactions were obtained for the laminar premixed biogas-hydrogen flames at various conditions. Effects of equivalence ratio, hydrogen addition and carbon dioxide proportion on above parameters will be discussed quantitatively while major exothermic and endothermic elementary reactions of biogas-hydrogen fuel will be identified. Additionally, $O+CH_3$ reactions were found to have a stable contribution on total HRR in our study, which means that $O\times CH_3$ product is likely to be an eligible HRR marker for the determination of HRR location and its value in the practical premixed flames. Hence, the investigation on HRR markers (HCO, $OH\times CH_2O$, $O\times CH_3$, $H\times CH_2O$ and $H\times HO_2$) of laminar premixed biogas-hydrogen flames will be conducted quantitatively using the PREMIX code of CHEMKIN II in the second part. In order to guarantee the accuracy of numerical results, both GRI 3.0 and San Diego mechanism were adopted in this part to evaluate the performance of HRR makers in the biogas and methane flames with hydrogen enrichment. The peak-to-peak and peak-to-integrated correlations of markers and HRR will be established, and the best marker which has the most stable relation with HRR at various conditions will be identified.

4.2 Numerical investigation on heat release characteristics

4.2.1 Effects of equivalence ratio

The global heat release rate variations with the flame temperature for the premixed BG75 flames at different ϕ are illustrated in Fig. 4.1. It can be seen that the peak heat release rate at ϕ=1.0 is maximum while that at ϕ=0.8 is minimum, and the heat release rate at ϕ=1.0 is improved evidently in the low temperature zone compared to that at either lean or rich condition. Though the global heat release rates at ϕ=0.8 and ϕ=1.2 show the similar increasing trends in the low temperature zone, the flame at ϕ=1.2 can release more heat at high temperatures with the higher HRR. The higher global heat release rate at ϕ=1.0 is resulted from its complete combustion, while the higher HRR in the high temperature zone at the rich condition is attributed to the exothermic recombination of active radicals which can be produced by the excess fuel.

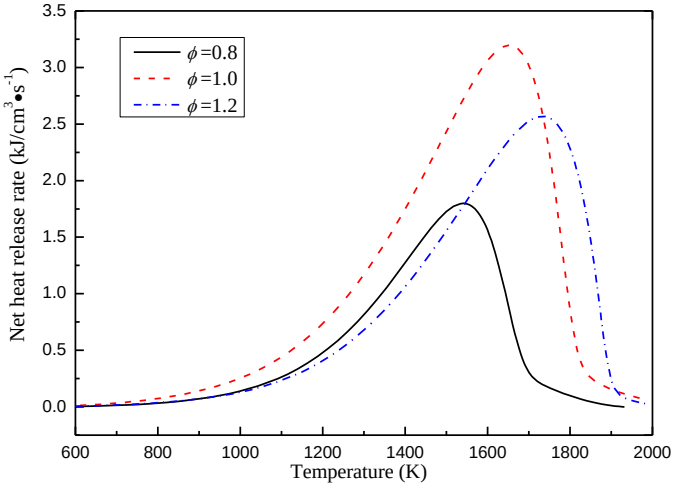

Fig. 4.1 Global HRR of laminar premixed BG75 flame at different ϕ.

Fig. 4.2 shows the main exothermic and endothermic chemical reactions of the laminar premixed BG75 flames at different equivalence ratios. Only the top 13 heat release reactions and the top 2 heat consuming reactions are given in Fig. 4.2, and the

negative and positive values denote heat release and heat consuming, respectively. As the equivalence ratio varies, the primary endothermic reaction is R38: $H+O_2=OH+O$, which always consumes approximately 12% of heat released by the combustion. Meanwhile, the secondly significant endothermic chemical reaction is changed at different conditions with the much less contributions than that of R38. In addition, the major exothermic chemical reactions are almost unchanged, but their contributions are considerably varied. It can be seen that R10: $O+CH_3=H+CH_2O$, R52: $H+CH_3(+M)=CH_4(+M)$, R84: $OH+H_2=H+H_2O$, R99: $OH+CO=H+CO_2$ and R284: $O+CH_3=>H+H_2+CO$ can always rank in the top seven heat-release reactions as ϕ increases. Apart from this, R35: $H+O_2+H_2O=HO_2+H_2O$ and R287: $OH+HO_2=O_2+H_2O$ are also quite significant for the flames at ϕ=0.8 and ϕ=1.0 while R43: $H+OH+M=H_2O+M$ can contribute a considerable part of total HRR at ϕ=1.0 and ϕ=1.2. Besides, R158: $2CH_3(+M)=C_2H_6(+M)$, which is not important for the flames at ϕ=0.8 and ϕ=1.0, can play a relatively important role in the total HRR at the rich condition. Though the contributions of the above exothermic reactions change significantly with the equivalence ratio, they can always account for about 60% of integrated heat release rate.

As shown in Fig. 4.2, it can be noted that the contribution of R52 is increased obviously from about 6% at ϕ=0.8 to around 14% at ϕ=1.2, and it becomes the most important exothermic reaction at rich condition. This increasing trend can be attributed to the increased mole fractions of H and CH_3 as shown in Fig. 4.3(b). The mole fractions of H and CH_3 are increased significantly as ϕ increases, which can be attributed to the increased mole fraction of CH_4 and H_2 as shown in Fig. 4.3(a). The production of the radical CH_3 can be promoted effectively by the increased CH_4

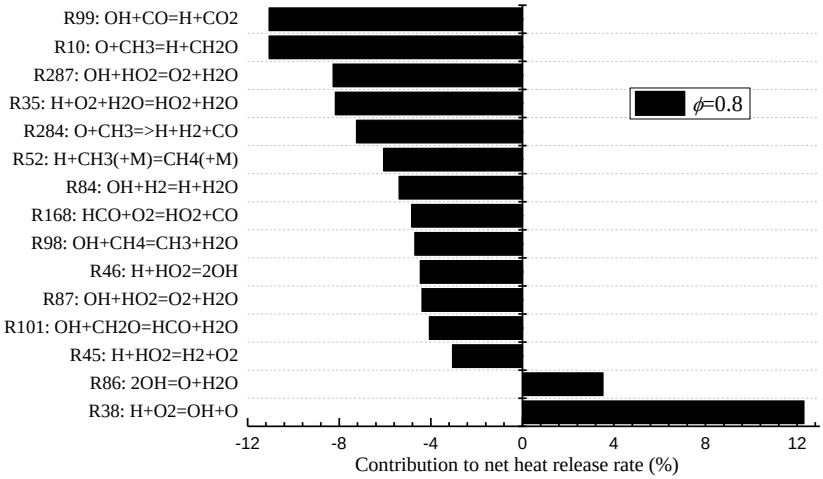

(a) ϕ=0.8

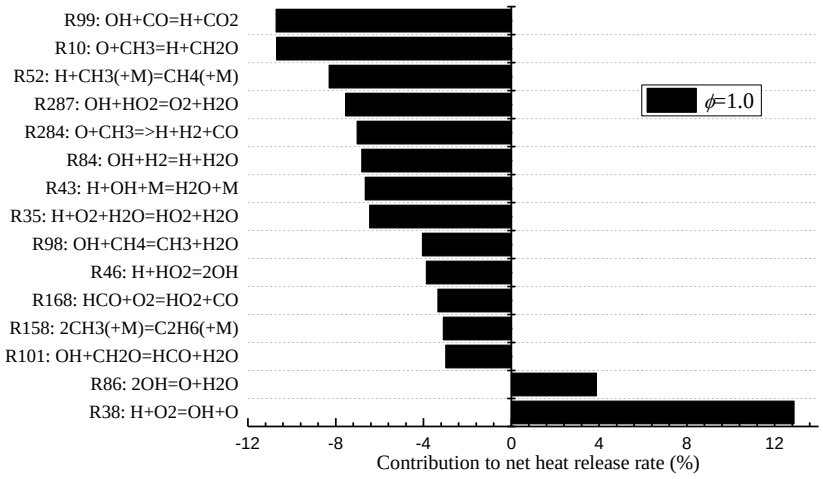

(b) ϕ=1.0

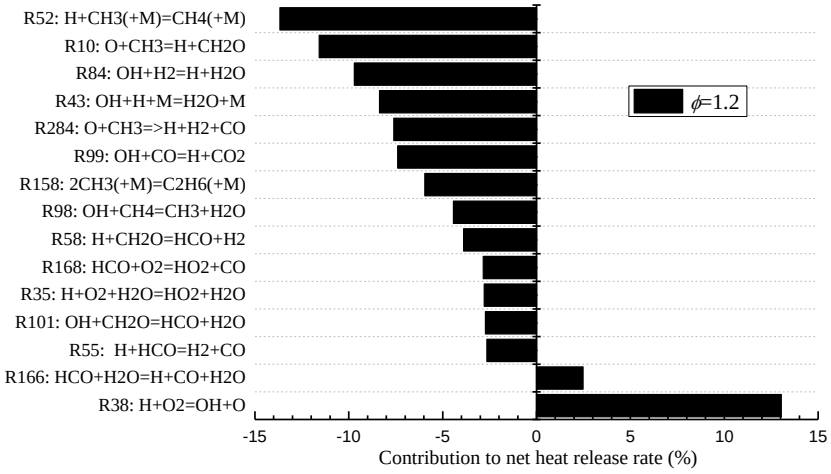

(c) ϕ=1.2

Fig. 4.2 The contributions of the main chemical reactions to the heat release of laminar premixed BG75 flames at different ϕ.

concentration through the dehydrogenation reaction of methane. Meanwhile, CH_3 and H_2 are the main sources to generate the H radical, indicating the improvement of the increased concentrations of CH_3 and H_2 on the production of H. Eventually, the reaction rate of R52 can be enhanced effectively with the increased mole fractions of CH_3 and H, bringing about its increased contribution on the total HRR. Additionally, the contribution of R84 increases slightly as ϕ increases from 0.8 to 1.0, but it shows a more apparent rising trend as ϕ increases to 1.2. Contrarily, the contribution of R99 shows a decreasing trend, and the decreasing rate becomes much larger as ϕ increases from 1.0 to 1.2. The reasons for the variations of these two reactions can be explained as follows. The oxidizer O_2 at both lean and unity conditions can be available to generate enough OH, which is primarily generated through R38, to react with H_2 and CO. What is more, the mole fractions of H_2 and CO are also enhanced with the increased ϕ as shown in Fig. 4.3(a). This contributes to increasing trends of the reaction rates of R84 and R99. However, it is noted that H_2 is more active and would compete with CO to react with OH while the CO_2 in the unburned mixture can further directly suppress the forward reaction of R99. Consequently, though the reaction rates of R84 and R99 are both promoted at unity condition as shown in Fig. 4.4, the increasing rate of R84 is much larger than that of R99. Furthermore, owing to the evident increased global heat release rate, the contributions of R84 and R99 are slightly increased and decreased, respectively. Besides, when ϕ increases from 1.0 to 1.2, the mole fraction of OH is reduced evidently due to the insufficient oxidizer O_2 as shown in Fig. 4.3(b), however the mole fractions of H_2 and CO are still enhanced effectively. Thanks to the higher reactivity of H_2 and the increased concentration of CO_2 in the unburned mixture, the reactions rate of R84 is further promoted slightly but that of R99 is decreased apparently as shown in Fig. 4.4. The suppression on R99 can

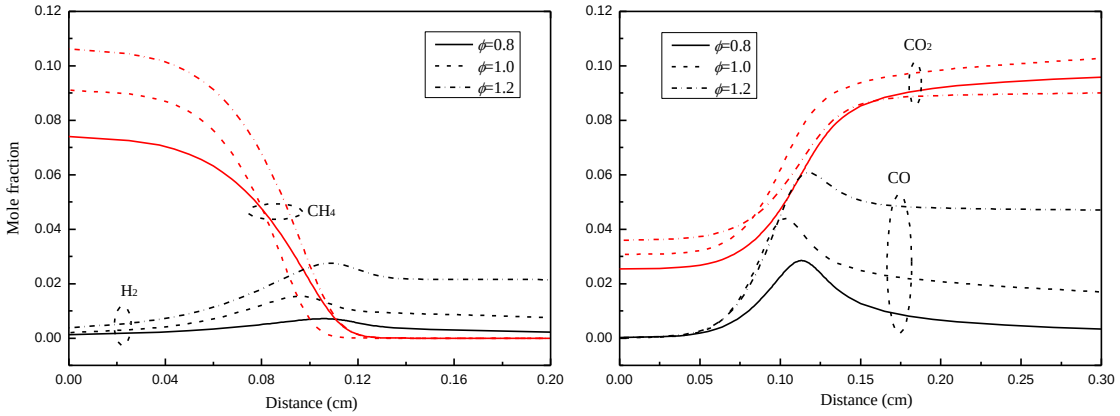

(a) Mole fractions of major species

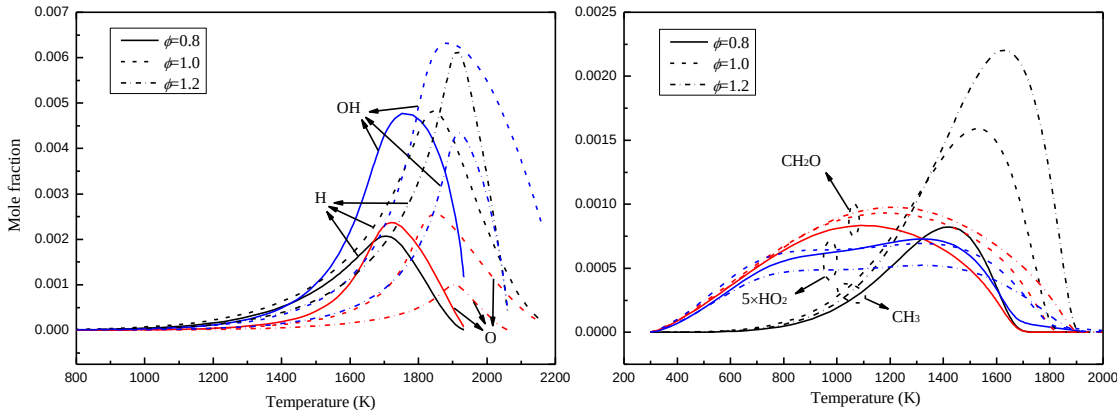

(b) Mole fractions of minor species

Fig. 4.3 The mole fractions of laminar premixed BG75 flames.

also be reflected by the reduced CO_2 concentration in the burned mixture as shown in Fig. 4.3(a). It is noted that, as shown Fig. 4.1, the global heat release rate is just slightly decreased at rich condition. Hence the contributions of R84 and R99 are remarkably enhanced and declined, respectively. In addition, the contributions of R10 and R284 are relatively stable at different conditions, with the values of around 10% and 7%, respectively. It can be known that the reaction rates of R10 and R284 are concerned with the mole fractions of O and CH_3. As ϕ increases, the mole fraction of O is increased initially but decreased at rich condition while that of CH_3 is enhanced steadily as shown in Fig. 4.3(b). Meanwhile, the variation of the O×CH_3 product with the global heat release rate is given in Fig. 4.5. The O×CH_3 product is obtained

through multiplying the mole fraction of O by the mole fraction of CH_3. It can be seen that, due to the variations of the mole fractions of O and CH_3, the peak O×CH_3 product has a positive relationship with the peak global heat release rate as ϕ varies. Furthermore, considering the correlation of the reaction rate and heat release rate, this means that the heat release rates of R10 and R284 are changed proportionally with the global heat release rates as ϕ changes. Consequently, this gives rise to their relatively stable contributions on the total HRR.

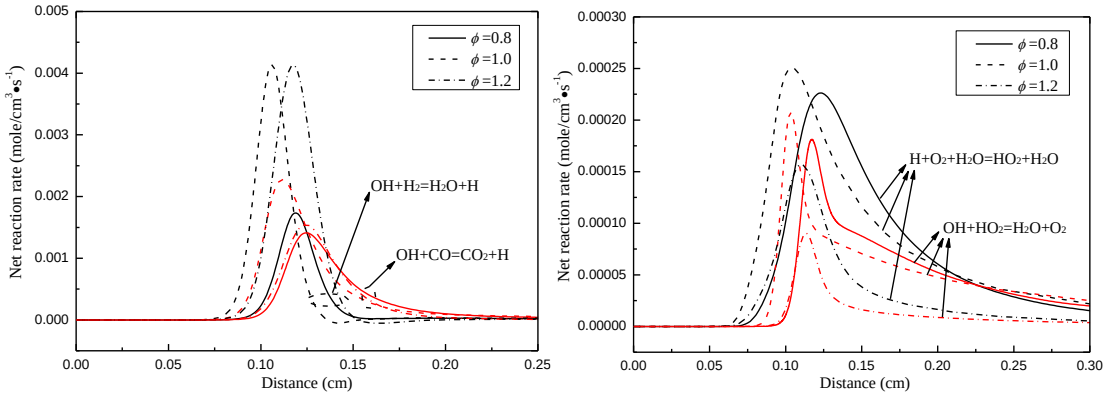

Fig. 4.4 Net reactions rates of R84, R99, R35 and R287 of laminar premixed BG75 flames.

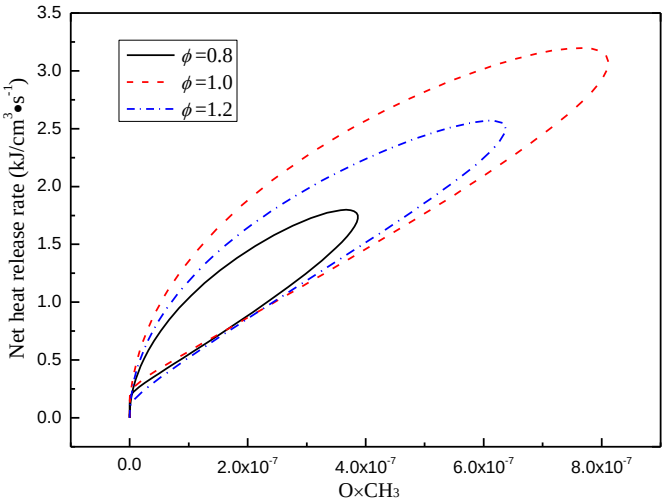

Fig. 4.5 The laminar premixed BG75 flame: O×CH_3 product vs. global heat release rate.

Besides, the heat released by R35 and R287 can account for a considerable proportion of the total HRR at lean and unity condition but not at rich condition. The reaction rates of R35 and R287 are illustrated in Fig. 4.4. It can be seen that the reaction rates

of these two reactions are quite low at rich condition and their heat release zones become narrow compared to that at other conditions. Since R35 is a third-body reaction, the concentration of H_2O can exerts critical influences on its reaction rate. As ϕ increases from 0.8 to 1.0, due to the slight reduced mole fraction of O_2 and the evidently increased mole fraction of H and H_2O, the reaction rate of R35 is slightly increased as shown in Fig. 4.4. Nevertheless, considering that the global heat release rate is drastically elevated as ϕ increases to 1.0, the slight improvement on the reaction rate of R35 can only give rise to its declined contribution on the total HRR though it is still a quite important exothermic reaction with about 6% contribution. Furthermore, due to the insufficient O_2 at rich condition, the probability of the occurrence of this third-body reaction is further declined, resulting in the significant reduction of its reaction rate as shown in Fig. 4.4. This leads to the quite low contribution of R35 at rich condition. Similarly, R287 is slightly improved with the increased mole fractions of OH and HO_2 at unity condition as shown in Fig. 4.3(b) and Fig. 4.4. It is noted that most of O_2 would be consumed through R38 and R168: $HCO+O_2=HO_2+CO$ which are the main reactions to generate OH and HO_2. Therefore, the production of OH and HO_2 can be hindered owing to the relatively low concentration of O_2 at rich condition, leading to the decreased mole fractions of OH and HO_2 as shown in Fig. 4.3(b). Combining with the increased mole fraction of H_2O, this finally brings about the drastic decline of the reaction rate of R287, as well as its negligible role in the total HRR, at rich condition. What is more, R43 become increasingly significant at unity and rich conditions owing to the obviously increased mole fraction of OH and H. Meanwhile, thanks to the increased CH_4 concentration at the rich condition, the production of CH_3 is improved effectively as shown in Fig. 4.3(b), which brings about the improvement on the reaction rate of R158 and indicates that the contribution of

R158 can no longer be neglected. Overall, R10, R52, R84, R99 and R284 can always play significant roles in the total HRR as ϕ varies. Besides, thanks to the stable contribution of R10 and R284, the total HRR can be reasonably predicted with the $O \times CH_3$ product across the reaction zone.

4.2.2 Effects of H_2 addition

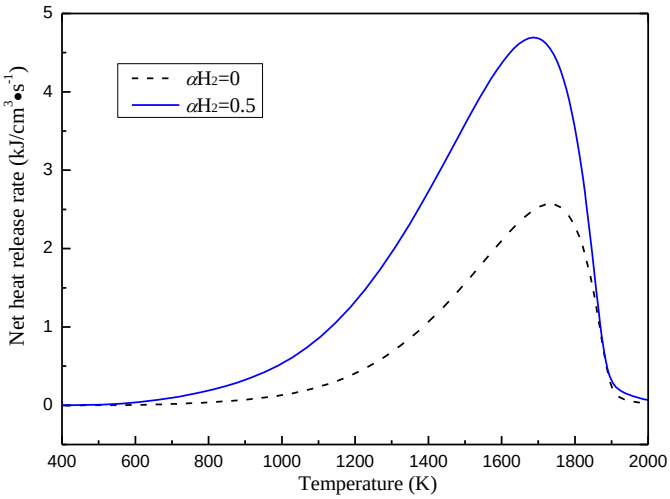

Fig. 4.6 Global HRR of raw BG75 flame and BG75 flame with hydrogen enrichment at ϕ=1.2.

The global heat release rates of raw biogas and biogas with hydrogen enrichment are illustrated in Fig. 4.6. At low temperatures, the hydrogen enrichment can accelerate the reaction rate of R46: $H+HO_2=2OH$ [255], which gives rise to a boosted OH concentration in the low temperature zone (below approximately 1200K). Due to the higher reactivity of H_2, it can be oxidized by the OH radical to release heat and promote the production of H at the lower temperatures. This leads to the early rise of heat release rate than that without hydrogen enrichment as shown in Fig. 4.6. In addition, the radicals and intermediate species produced by hydrogen oxidization can then react with methane and promote the reaction rate of R38. At high temperatures, R38 is the primary chain branching reaction to release O and OH which are quite significant to the total HRR [256]. Consequently, the improvement of H_2 enrichment

on R38 contributes to the increase in the maximum heat release rate in the high temperature zone. As shown in Fig. 4.6, the maximum global heat release rate is significantly increased by about two times.

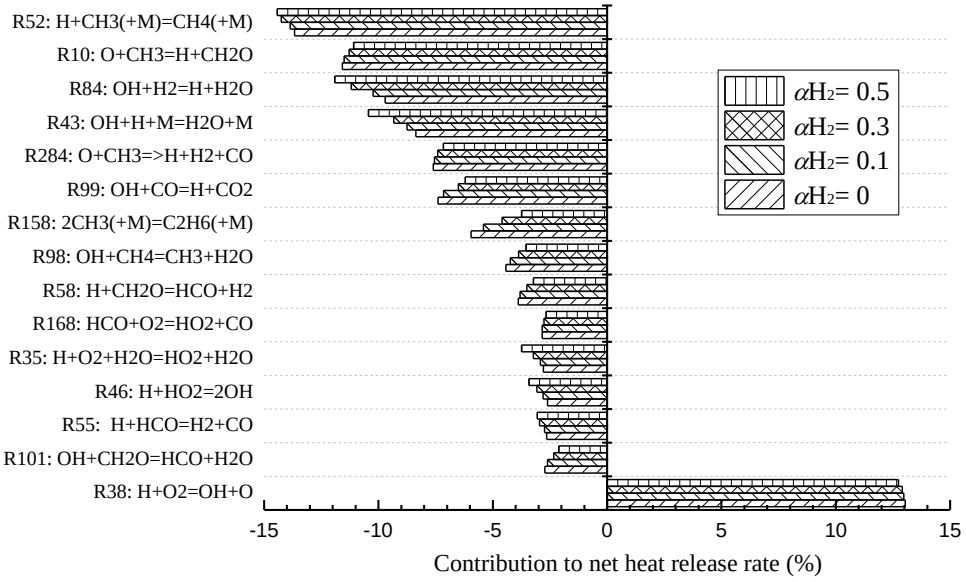

Fig. 4.7 The contributions of the main chemical reactions to the heat release of laminar premixed BG75 flames with hydrogen addition at ϕ=1.2.

Fig. 4.7 gives the main exothermic and endothermic chemical reactions of biogas-hydrogen flames. As shown in Fig. 4.7, for all conditions, the chain branching reaction R38 is the major heat consuming reaction, whose contribution slightly decreases as αH_2 increases due to the reduction in O_2 mole fraction. For the raw biogas, the major exothermal reactions are R52 followed by R10 and R84. For αH_2=0.5, though R52 is still the most important heat release reaction, the contribution of R84 surpasses that of R10 due to the hydrogen enrichment. Apart from the top three exothermal reactions, R43, R284, R99 and R158 also contribute considerable amount of total HRR. The heat released by the top seven exothermal reactions can account for more than 60% as αH_2 varies. It can be seen that contributions of these reactions are influenced by the hydrogen addition, which can directly reflect the significance variation of an

exothermal reaction on the total HRR. What is noteworthy is that, among the top seven exothermal reactions, only R52, R84 and R43 show the rising trends as hydrogen proportion increases. This means these three reactions would play an increasingly pivotal role in the total HRR when hydrogen is added to the raw biogas.

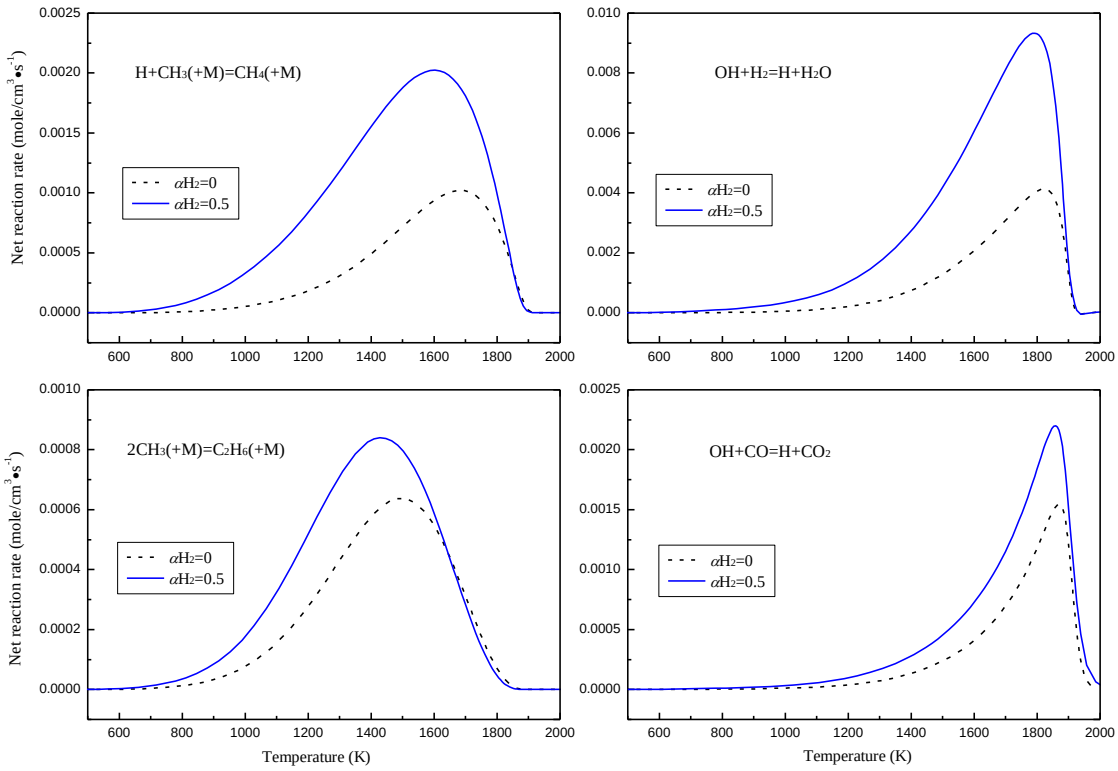

Fig. 4.8 Net reaction rates of R52, R84, R158 and R99 of laminar premixed BG75 flames at ϕ=1.2.

The reactions rates of R52, R84, R158 and R99 with/without hydrogen enrichment are illustrated in Fig. 4.8 while the mole fractions of significant minor species are shown in Fig. 4.9. It is manifest that all the reactions are improved with the hydrogen enrichment, but the improvements are not quite the same. For R52, as the previous statement, the hydrogen enrichment, which gives rise to the increased mole fraction of H_2 as shown in Fig. 4.9(a), can lead to the higher concentration of OH at low temperatures as shown in Fig. 4.9(b). Subsequently, OH can react with H_2 and CH_4 to generate H and CH_3, respectively, contributing to the considerably early rise of

reaction rate as shown in Fig. 4.8. This brings about its apparent increase in heat release rate at low temperatures. At high temperatures, though the maximum CH_3 concentration is almost unchanged as shown in Fig. 4.9(b), the maximum reaction rate of R52 is still promoted quite significantly owing to the increased H concentration as shown in Fig. 4.9(b). As a result, its contribution on total HRR is increased slightly. Meanwhile, R84, as a pivotal reaction of hydrogen oxidization, is also improved obviously at low and high temperatures. It is noted that, due to the both higher concentrations of OH and H_2, the peak reaction rate of R84 is elevated more than twice as that without the H_2 enrichment. This brings about its greatly enhanced contribution on total HRR as shown in Fig. 4.7. Besides, due to the improved methane oxidization, the CH_3 concentration is slightly increased so as to facilitate the reaction R158 at low temperatures. However, because the maximum CH_3 concentration is not significantly increased, the hydrogen enrichment only exerts limited improvement on the peak reaction rate of R158. Due to the remarkable enhancement of global heat release rate, the slight improvement on the heat release of R158 leads to its evidently declined importance on the total HRR. Additionally, since CO is an intermediate species during the methane combustion, its concentration is relatively lower at low temperatures. Meanwhile, CO needs to compete with other more active species, such as H_2 and CH_4, so as to react with OH radical. Hence, though the OH concentration is remarkably increased due to the hydrogen enrichment, the R99 reaction rate can only be improved slightly at either low or high temperatures, leading to the drop of its contribution on the total HRR. Meanwhile, due to the obviously increased mole fraction of H and OH as shown in Fig. 4.9(b), the reaction rate of R43 is promoted effectively, giving rise to its increasingly significant role in total HRR. Apart from this, R10 and R284 mainly occur at higher temperatures, meaning the improvement of H_2

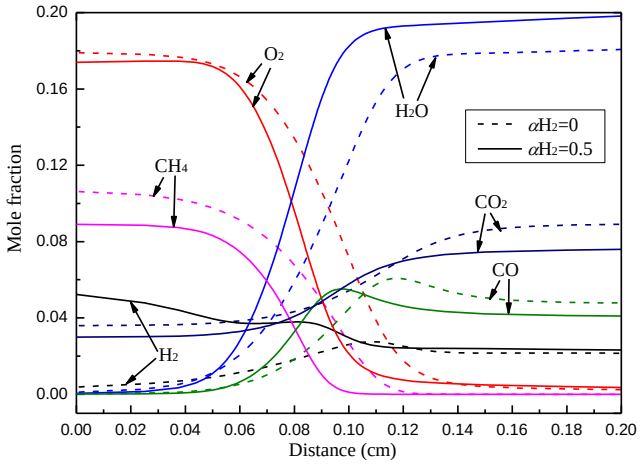

(a) Mole fractions of major species

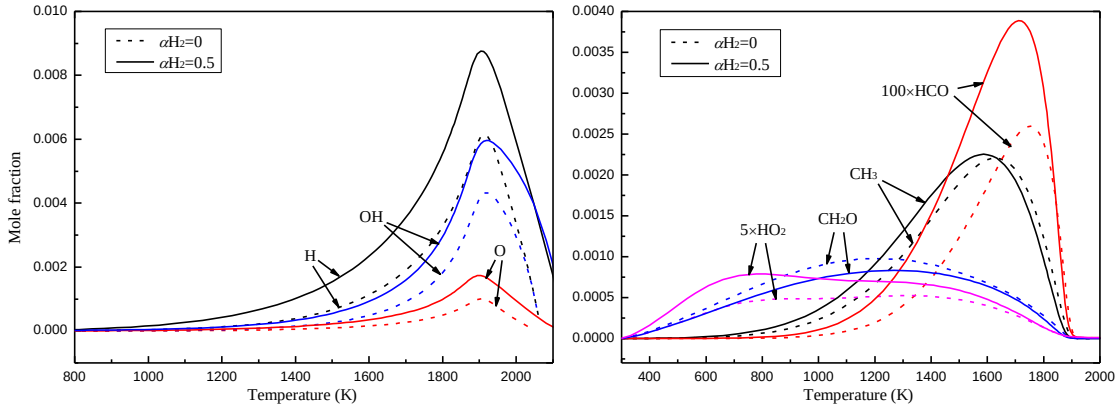

(b) Mole fractions of minor species

Fig. 4.9 The mole fractions of raw BG75 flame and BG75 flame with hydrogen enrichment at ϕ=1.2.

enrichment at low temperatures can be neglected for these two reactions. Furthermore, due to the almost unchanged CH_3 concentration, the increased concentration of O can exert limited improvements on R10 and R284, eventually leading to the decreases in their contributions. What is more, as the hydrogen proportion increases, the variations of other reactions' contributions can be explained by the decreases in the mole fractions of CH_2O, CH_4 and CO, the stable mole fraction of CH_3 and the increased mole fractions of H_2, H_2O, H, HO_2 and HCO. In conclusion, the hydrogen enrichment can improve the heat release at both low and high temperature zones, and exert

evident improvement on the reaction rates of R52, R84 and R43, leading to their increasingly significant roles in total HRR, especially for R84 and R43.

4.2.3 Effects of CO_2 percentage

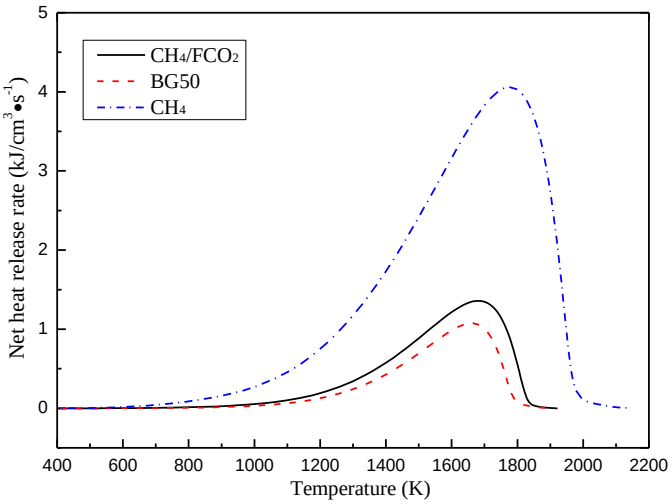

Fig. 4.10 Global HRR of laminar premixed biogas and methane flames at ϕ=1.2.

The global heat release rates of biogas and methane flames at ϕ=1.2 are shown in Fig. 4.10. It can be seen that the global heat release rate is apparently decreased as the FCO_2 is introduced, and the decreasing trend is further aggravated as the FCO_2 is replaced by CO_2. This variation can be attributed to the reduction of combustible fuel and the chemical effects of CO_2. The main elementary reactions of biogas flames with different CO_2 proportions contributing to the total HRR are illustrated in Fig. 4.11. It can be seen that the main heat consuming reaction is still R38 while the top seven main exothermal reactions are R52, R10, R84, R43, R284, R99 and R158. Though the contributions of these reactions are changed with the CO_2 proportion, their sequences are not varied drastically. The contribution of R10 is exceeded by that of R84 for the BG50 flame. In addition, top seven major exothermal reactions can always constitute more than 60% of integrated heat release rate as the percentage of CO_2 varies.

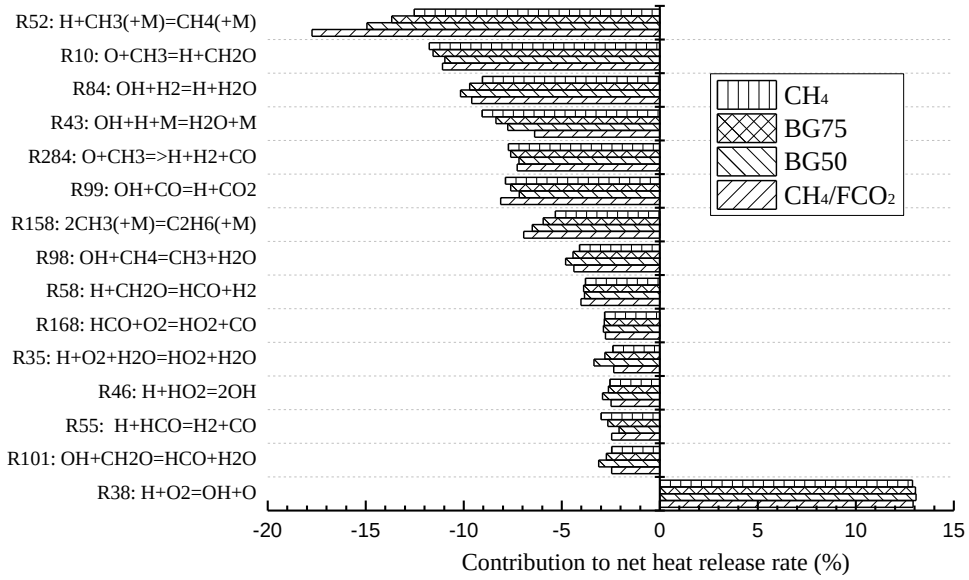

Fig. 4.11 The contributions of the chemical reactions to the heat release of laminar premixed biogas flames at ϕ=1.2.

As shown in Fig. 4.11, the dilution/thermal effects on heat release contributions can be investigated by comparing the data of CH_4 and CH_4/FCO_2. It can be seen that R52 becomes much more significant when fuel is diluted with the FCO_2, and the contributions of R84 and R158 are also increased slightly, however the contribution of R43 is decreased evidently. Meanwhile, contributions of other reactions are changed less obviously or even unchanged. These variations can be explained with the changes of reaction rates and mole fractions. The reaction rates of R52, R84, R158 and R43 are illustrated in Fig. 4.12 while the mole fractions of CH_4/FCO_2 and CH_4 are shown in Fig. 4.13. As shown in Fig. 4.12, the decreasing rate (up to about 50%) of reaction rate of R52 is less than the dropping rate (up to around 66%) of the global heat release rate, giving rise to the apparent increase of its contribution. Meanwhile, the declining rates of R84 and R158 are slightly less than that of the global heat release rate, leading to their moderately boosted contributions. The normalized mole fractions of minor species are given in Fig. 4.13. The normalized mole fraction is defined as X_k/X_{Hmax} where X_k and X_{Hmax} denote the mole fraction of species k and the maximum H mole

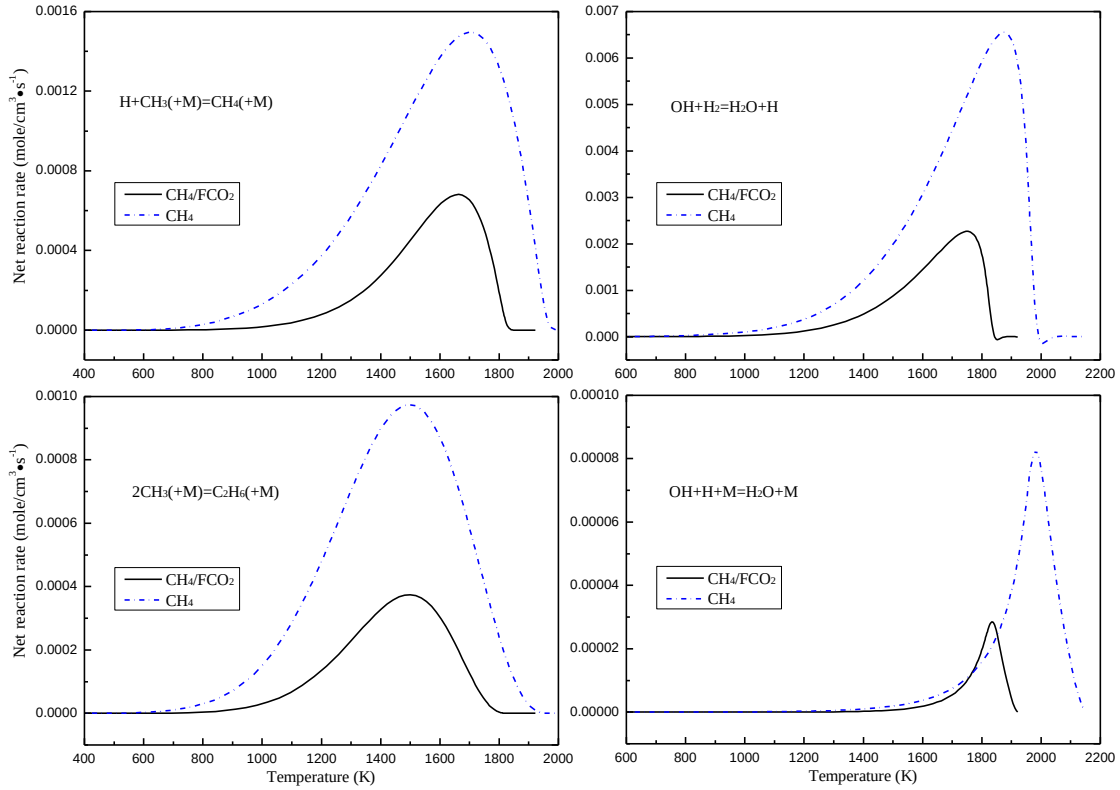

Fig. 4.12 Net reaction rates of R52, R84, R158 and R43 of laminar premixed biogas flames at ϕ=1.2.

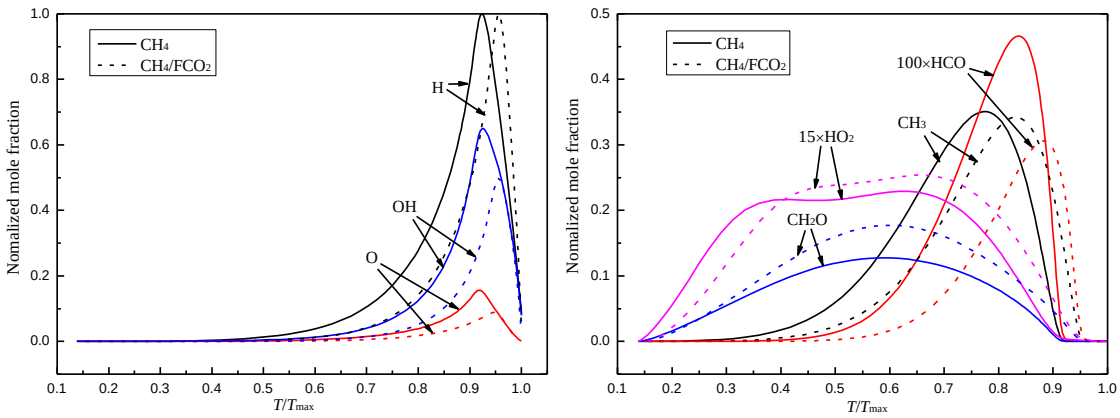

Fig. 4.13 The normalized mole fractions of laminar premixed CH_4/FCO_2 and methane flames at ϕ=1.2.

fraction for such a fuel, respectively. Furthermore, the normalized temperature T/T_{max} is adopted to facilitate the comparison in the whole region. It can be noted that, as FCO_2 is added, the normalized mole fractions of OH, O and HCO drop evidently while that of CH_3 just decreases slightly, however mole fractions of CH_2O and HO_2

are increased. This means that, comparing to the methane flame, H, HO_2 and CH_2O can account for a larger part of total radicals while CH_3 can keep a relatively stable proportion in the dilution condition. These variations can be attributed to the declined concentration of O_2 and the high reactivity of H_2. Thanks to the high reactivity of H_2, R84 can be affected more slightly than other reactions when the mole fraction of OH is decreased, which means that more OH would be consumed by H_2 through R84. Hence, the increasing proportions of H and the stable level of CH_3 in the total radicals, as well as the high reactivity of H_2, can lead to the rising trends of R52, R84 and R158 contributions. Nevertheless, due to the dilution effects of FCO_2, the amount of OH and H are significantly reduced, which means that the reaction rate of the third-body reaction R43 can be drastically decreased. As shown in Fig. 4.12, the reaction rate of R43 is dropped drastically with the maximum value reduced by about 70%, leading to its declined contribution on the total HRR. Meanwhile, the slight variations of other reactions can be explained by further considering the larger fraction of CH_2O and HO_2 but fewer proportions of OH, O and HCO in the total radicals when FCO_2 is introduced.

On the other hand, the chemical effects on heat release contribution can be determined by the data discrepancies between BG50 and CH_4/FCO_2 shown in Fig. 4.11. It can be noted that contributions of R52 and R99 are dropped apparently while others are also affected to some extent. These observations can be explained as follows. R99: $OH+CO=H+CO_2$ plays a pivotal role to exert the chemical effects of CO_2 [257]. As CO_2 percentage is enhanced, its reactivity can promote the backward reaction of R99 effectively, which can contribute to the increase in CO mole fraction and convert H to OH to reduce H/OH ratio. This can be confirmed by the mole fraction distribution shown in Fig. 4.14. Particularly, it should be noted that the CO_2

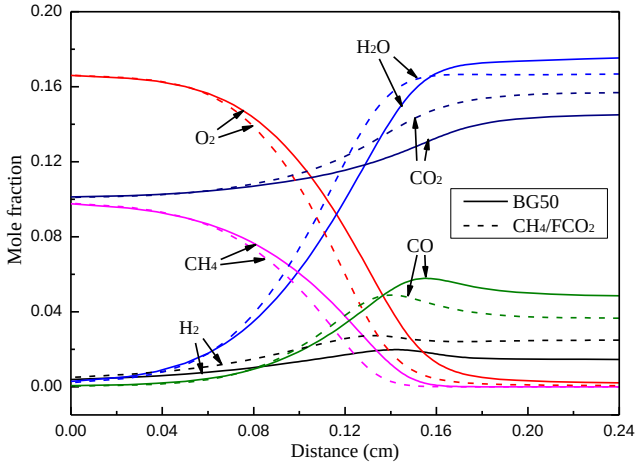

(a) Mole fractions of major species

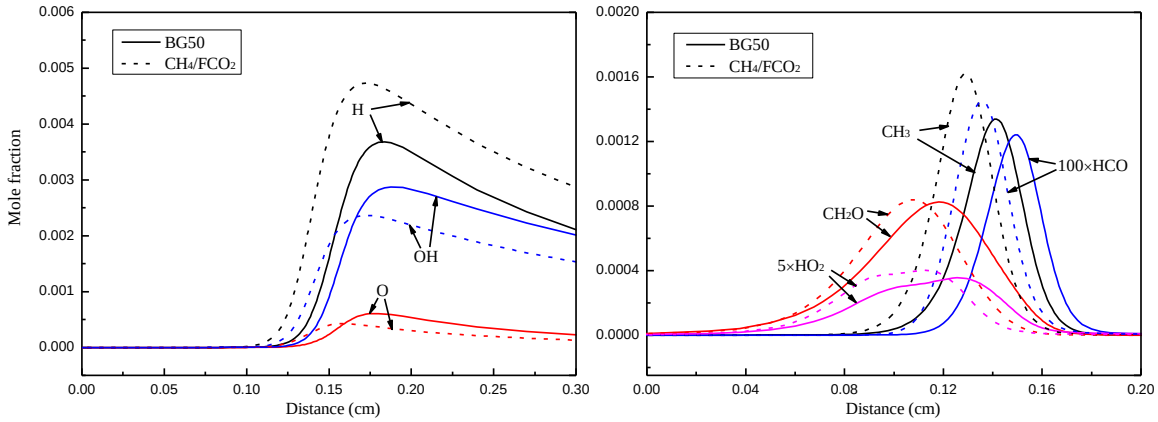

(b) Mole fractions of minor species

Fig. 4.14 The mole fractions of laminar premixed BG50 and CH_4/FCO_2 flames at ϕ=1.2.

mole fraction of CH_4/FCO_2 shown in Fig. 4.14(a) is the sum of normal CO_2 and FCO_2 for the sake of illustrating the chemical effects. The decreased CO_2 mole fraction can further confirm the consumption of CO_2 induced by its reactivity. Hence, the evident decreased H and the reactivity of CO_2 can directly induce the sharp reductions of R52 and R99 contributions, respectively. However, the decreased H/OH ratio can exert the improvements on R84 and R43 as shown in Fig. 4.11, which can also be reflected by the decreased mole fraction of H_2 and the increased mole fraction of H_2O shown in Fig. 4.14(a). Apart from this, the changes of other reactions induced by chemical

effects can be explained with the decrease in CH_3, HO_2 and HCO mole fraction, and the almost unchanged CH_2O mole fraction as shown in Fig. 4.14(b).

It can be seen that dilution/thermal effect and chemical effect of CO_2 can codetermine the variation of reaction contribution. Among the top seven exothermal reactions, the increasing significances of R52 and R158 are determined by the dilution/thermal effect, while the decreasing trends of R43 and R99 are dominated by the dilution/thermal effect and chemical effect, respectively. Meanwhile, the variations of other three reactions are affected by the simultaneous positive or negative effects of these two aspects.

4.3 Heat release marker for laminar premixed biogas-hydrogen flames

Based on the above investigation on heat release characteristics, the $O+CH_3$ reactions were found to be the stable contributors on the total HRR, which implies that the $O \times CH_3$ product is likely to be an excellent HHR marker for the practical premixed flame. In order to confirm this, the performance of the $O \times CH_3$ product need to be evaluated and compared with other available HRR markers. The $OH \times CH_2O$ product is adopted in consideration of that it has been utilized in the HRR imaging extensively. Besides, the recently proposed HRR markers ($H \times CH_2O$ and $H \times HO_2$) by Nikolaou and Swaminathan [199] are also considered because they are suggested to have the improved accuracy than the $OH \times CH_2O$ product on HRR prediction. Since HCO has been widely accepted as a robust HRR marker, its data are obtained as the comparison for other HRR markers. Consequently, these HRR markers are considered and will be investigated simultaneously in this part.

4.3.1 The linearity between local HRR markers and local HRR

The linearity of marker and local HRR is firstly examined at several equivalence ratios. In order to evaluate the linearity of markers accurately, the error estimator method used to assess the linear quality [199] is adopted here, the product of concentrations instead of the reaction rate is used in this study considering that species distribution are generally measured in experiments. The quantitative evaluation on the linearity of the considered markers (HCO, $OH \times CH_2O$, $O \times CH_3$, $H \times CH_2O$ and $H \times HO_2$) is summarized in Table 4.1. In the table, the larger value of the error estimator means that this marker has the poorer linear relationship with the local HRR across the reaction zone at the specific condition. As shown in Table 4.1, the linearity of the $OH \times CH_2O$ product is slightly poorer than that of HCO. Besides, the error estimator of the $O \times CH_3$ product is approximately twice of that of the $OH \times CH_2O$ product, indicating its relatively poorer linearity with the local HRR. Additionally, the $H \times CH_2O$ and $H \times HO_2$ products have the better linearity with the local HRR than the $OH \times CH_2O$ product at fuel-lean and stoichiometric conditions as given in Table 4.1. This result is in accordance with that proposed by Niklaou and Swaminathan [199]. Besides, it is noted that the $H \times CH_2O$ and $H \times HO_2$ products can also correlate with the local HRR better at fuel-rich condition. In particular, the linearity of the $H \times CH_2O$ product is even better than that of the HCO as shown in Table 4.1. It can be seen that, except the $O \times CH_3$ product, the other markers show good linearity at different equivalence ratios. Whereas, it should be noted that the good marker identified based on the above discussion cannot be guaranteed to reflect the discrepancy of HRR at different equivalence ratios. In this method, the values of HRR and markers are normalized at different ϕ. This means that the effects of variable correlation between HRR and marker at different ϕ on the prediction accuracy can be eliminated. For a

premixed flame with a constant ϕ, this cannot affect the prediction accuracy of the identified marker. However, for a premixed combustion process that various equivalence ratios exist simultaneously, the marker identified based on this method may not reflect the HRR change accurately due to its variable correlation with HRR. Thus the single-valued prediction of marker on HRR needs to be investigated.

Table 4.1 Error estimator of markers for laminar premixed BG75 flames.

HRR Marker	ϕ = 0.8	ϕ = 1.0	ϕ = 1.2
HCO	687.241×10^{-6}	531.679×10^{-6}	328.593×10^{-6}
OH×CH_2O	751.387×10^{-6}	782.84×10^{-6}	678.723×10^{-6}
O×CH_3	165.613×10^{-5}	149.767×10^{-5}	137.577×10^{-5}
H×CH_2O	658.861×10^{-6}	307.486×10^{-6}	160.294×10^{-6}
H×HO_2	548.114×10^{-6}	710.693×10^{-6}	352.113×10^{-6}

4.3.2 The peak-to-peak correlation

Table 4.2 Position discrepancy (z) of peak values of HRR and markers for BG75 flames.

HRR Marker	**ϕ=0.8**		**ϕ=1**		**ϕ=1.2**	
	z_G (μm)	z_S (μm)	z_G (μm)	z_S (μm)	z_G (μm)	z_S (μm)
HCO	9.37	9.63	9.38	8.06	4.69	5.37
OH×CH_2O	14.06	22.46	18.75	24.17	18.75	26.86
O×CH_3	23.44	19.25	18.75	18.80	18.75	21.49
H×CH_2O	4.69	3.21	0.00	5.37	4.69	10.74
H×HO_2	4.69	6.42	4.69	13.43	14.06	26.86

Table 4.3 The width (δ) of marker profile for BG75 flames.

HRR Marker	**ϕ=0.8**		**ϕ=1**		**ϕ=1.2**	
	δ_G (μm)	δ_S (μm)	δ_G (μm)	δ_S (μm)	δ_G (μm)	δ_S (μm)
HRR	921.93	867.92	691.71	797.58	579.64	726.20
HCO	413.65	390.86	361.52	363.63	437.99	472.31
OH×CH_2O	433.62	385.90	378.80	354.94	456.96	457.39
O×CH_3	367.40	335.96	324.44	327.07	385.87	413.56
H×CH_2O	448.05	398.69	392.12	365.62	468.67	465.72
H×HO_2	1135.61	1006.22	1333.31	1076.43	1091.60	712.93

In order to evaluate the accuracy of markers to determine the HRR location, the position discrepancy (z) between the maximum local HRR and the peak value of a marker is given in the Table 4.2 while widths (δ) of the HRR and marker profiles are

given in Table 4.3. It should be noted that subscripts G and S denote the GRI mechanism and the San Diego mechanism, respectively. As illustrated in Fig. 4.15, the position discrepancy z is determined as the distance between positions at which the values of local HRR and marker are maximum while the distribution width of HRR, as well as that of markers, is defined as the distance between the location that the profile rises 5% of its peak value and the location that it drops to 5% of its peak value. It is seen that both z and δ of a marker can be affected by the equivalence ratio due to the varied combustion process. For the position discrepancy, although values obtained by two chemical mechanisms are not exactly the same, both results indicate that the $OH \times CH_2O$ product and the $O \times CH_3$ product have a comparatively poor accuracy on determining the peak HRR location compared to that of HCO radical. Furthermore, the $H \times CH_2O$ product is found to have an improved accuracy to discern the location of maximum HRR than that of the $OH \times CH_2O$ product and the $O \times CH_3$ product, which can be confirmed by results of two mechanisms. For the $H \times HO_2$ product, it has a satisfactory accuracy at ϕ=0.8 and 1.0 but shows a poor performance at ϕ=1.2. Anyhow, considering the practical utilization of the $OH \times CH_2O$ product, the comparable or better performances of other markers on discerning the peak HRR location should be acceptable for the practical applications. For the distribution width, all the markers except for the $H \times HO_2$ product have the narrower distribution than that of the HHR distribution as shown in Table 4.3 and Fig. 4.16. This can be resulted from that a marker represents the related reaction path which can only contribute a part of total heat release in the reaction zone, thus its existence could be restricted in a limited region of the reaction zone and then lead to a narrower distribution than that of HRR. However, the $H \times HO_2$ product profile is observed to have a wider distribution,

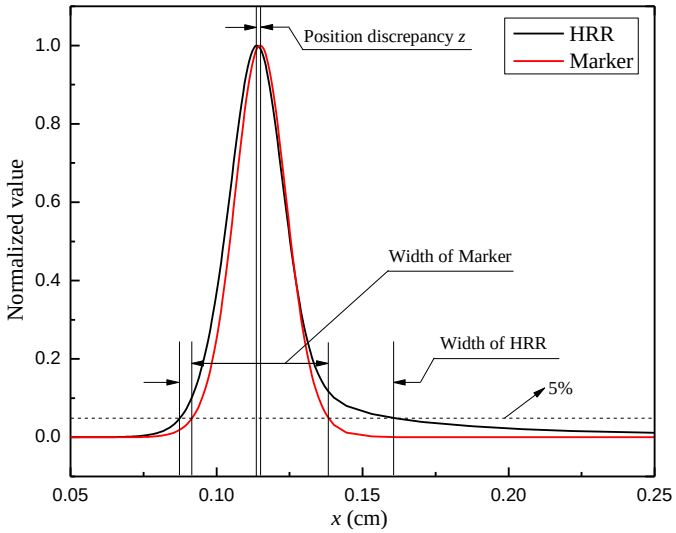

Fig. 4.15 The determination of position discrepancy (z) and profile width (δ).

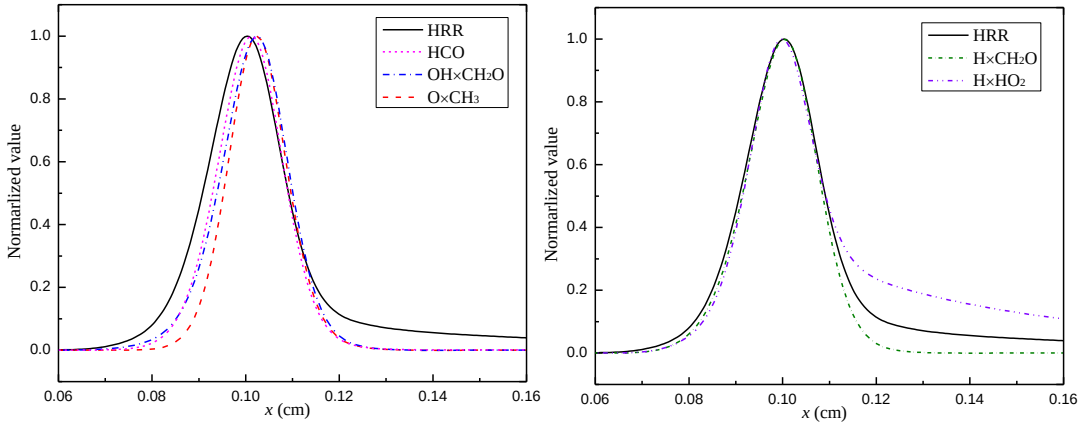

Fig. 4.16 The calculated distributions of HRR and markers in the reaction zone for the BG75 flame at ϕ=1.0 (GRI mechanism).

which might be primarily dominated by the extensive distribution of HO_2 in the reaction zone. Furthermore, as shown in Fig. 4.16, it is apparent that the $H \times CH_2O$ product, as well as the $H \times HO_2$ product, can track the local HRR variation more accurately than other markers. However, it can be concluded that the primary heat release zone can be discerned reasonably by these markers in consideration of that the accuracy of the HCO radical and the $OH \times CH_2O$ product has been accepted for discerning the HRR location in the previous studies [191, 192]. In conclusion, these HRR markers can be considered to be qualified to determine the HRR location with

the acceptable accuracy for the practical applications. Based on this, the single-valued prediction on the peak HRR by these markers are compared and discussed in the following part.

In order to identify the best HRR marker whose correlation with the HRR is insensitive to the equivalence ratio, the normalized peak-to-peak correlations of markers and HRR (peak values of marker and local HRR across the reaction zone) at ϕ = 0.6-1.4 for laminar premixed methane and BG75 flames are shown in Fig. 4.17. For a constant fuel composition, nine peak HRR can be obtained by varying ϕ from 0.6 to 1.4 while there also exist nine corresponding peak values of a marker. The obtained nine data of peak HRR can be normalized by its maximum data while nine values of peak marker can also be normalized by its maximum value. Hence, nine sets of data of HRR and a marker can be then plotted in the figure and obtain the profile shown in Fig. 4.17. As shown in Fig. 4.17(a), although the constant value of HCO mole fraction or the $O \times CH_3$ product corresponds to different values of HRR at fuel-lean and fuel-rich conditions, the discrepancies between these two HHR values are relatively small. This means that peak HRR has the almost constant relation with the peak HCO concentration or the peak $O \times CH_3$ product at different equivalence ratios. In other words, their correlations with HRR are not sensitive to the equivalence ratio. Hence, the peak HRR can be determined uniquely by the measured peak HCO or the peak $O \times CH_3$ product without considering the specific equivalence ratio in the flame. Furthermore, it can be seen that the data distribution of the $O \times CH_3$ product appears to be more compact than that of the HCO radical as illustrated in Fig. 4.17 (a). It is known that more compact data distribution means the better single-valued correspondence between the marker and the HRR, thus the $O \times CH_3$ product could have the better accuracy for the single valued prediction on peak HRR. Specifically, for a

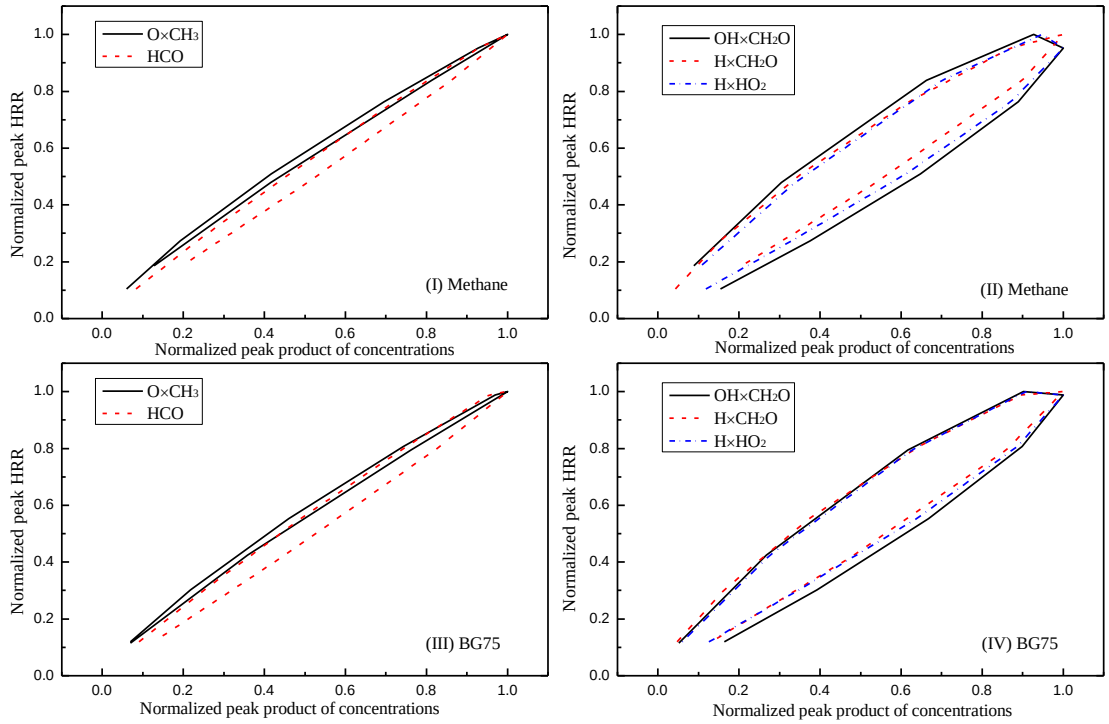

(a) GRI 3.0 mechanism

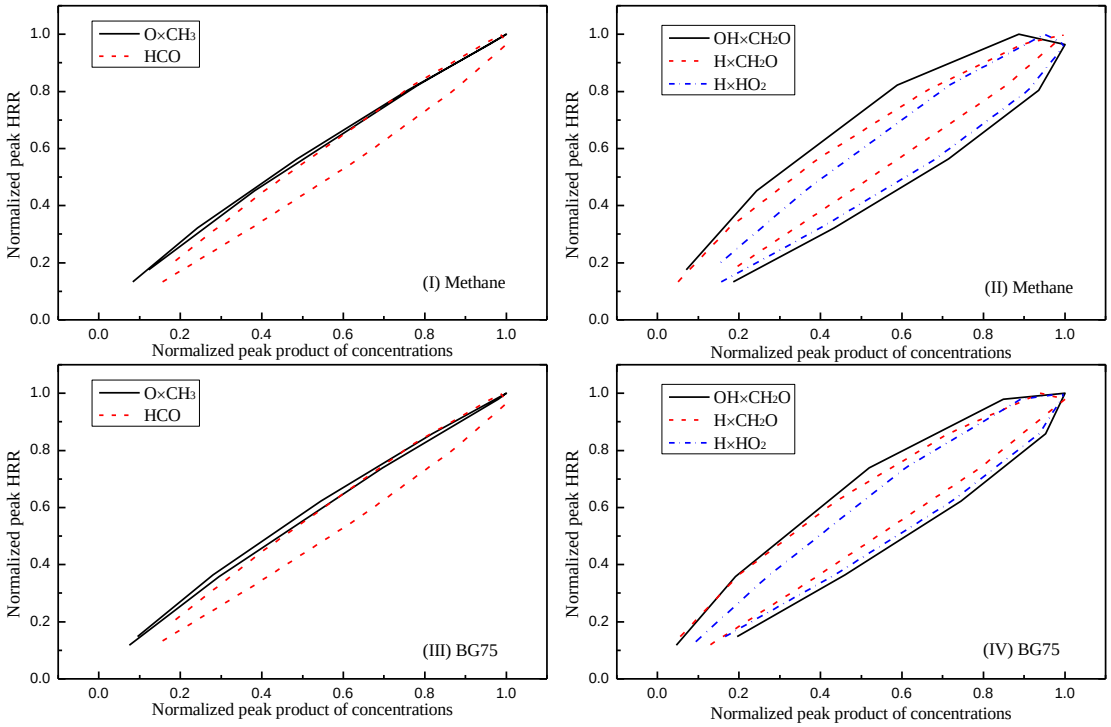

(b) San Diego mechanism

Fig. 4.17 The normalized peak-to-peak correlations of premixed methane and BG75 laminar flames at various equivalence ratios (ϕ = 0.6-1.4).

given value of a HRR marker, the maximum discrepancy on HRR estimation by the $O \times CH_3$ product is much smaller than that of the HCO radical. Therefore, it is known that the correlation of the peak $O \times CH_3$ product and peak HRR is least sensitive to the equivalence ratio, indicating that the $O \times CH_3$ product can predict the HRR more accurately in the premixed flame under the unclear condition. Additionally, the correlations of $OH \times CH_2O$, $H \times CH_2O$ and $H \times HO_2$ products for the BG75 and methane flames are also provided in the Fig. 4.17(a). It is obvious that these markers correlate with peak HRR to a poorer extent due to the more scattered data distribution. For a given value of these three markers, the prediction uncertainty on the peak HRR can be much larger than that of the HCO and the $O \times CH_3$ product. Apart from this, the data obtained by San Diego mechanism show the similar trends as shown in Fig. 4.17(b). In particular, the HCO correlates with peak HRR slightly worse than the data obtained by GRI mechanism thanks to its more scattered data distribution, while the plots of $O \times CH_3$ product performs even better. Based on this, it is confirmed that the correlation of peak $O \times CH_3$ product with peak HRR is most insensitive to the equivalence ratio, indicating its best accuracy to determine the HRR at the condition with the unknown equivalence ratio.

In order to further validate the prediction performance of the discussed HRR markers, more fuel compositions given in Table 3.2 are examined to evaluate the sensitivity of their correlations to the fuel composition and further confirm their sensitivity to the equivalence ratio. Only GRI mechanism is employed in this part considering that similar results were obtained by both chemical mechanisms in the above discussion. The peak-to-peak correlations of considered markers and HRR at various conditions are provided in Fig. 4.18 and Fig. 4.19 while values of peak HRR for tested flames are presented additionally so as to correlate data to the flame series given in Table 3.2. In

the figures, the data of $OH \times CH_2O$, $H \times CH_2O$ and $H \times HO_2$ products are fitted at different equivalence ratios with the fitting index r^2, while the fitting lines of HCO and $O \times CH_3$ product are only provided for their whole data with the fitting index R^2 considering that they have the more compact data distributions. It can be seen that the peak value of local HRR is linearly proportional to the marker's peak value at a particular equivalence ratio, and the correlation of a marker with the peak HRR shows a dependence on the equivalence ratio. Specifically, thanks to the compact data distributions in shown in Fig. 4.18 and Fig. 4.19(a), the correlations of the HCO and $O \times CH_3$ product with HRR can be considered to be unaffected by the equivalence ratio and fuel composition. As shown in Fig. 4.18, a fixed value of HCO corresponds to a slightly higher local HRR at fuel-lean condition than other conditions, but this slightly scattered distribution of HCO can still be acceptable for its single-valued prediction on the peak HRR. Additionally, the data of the $O \times CH_3$ product has a higher fitting index than the HCO data as shown in Fig. 4.19(a) due to its more compact data distribution. Thus the correlation of the $O \times CH_3$ product and the peak HRR is most insensitive to the equivalence ratio and the fuel composition, which further confirms its excellent single-valued correspondence with the peak HRR. By contrast, the data of $OH \times CH_2O$ product for the tested conditions are considerably scattered but the data at a constant equivalence ratio show a good single-valued correspondence with HRR as shown in Fig. 4.19(b). Specifically, the peak values of $OH \times CH_2O$ product and HRR for the BG75 flame at $\phi = 0.8$ are 5.69×10^{-7} and 1.8 $kJ/cm^3 \cdot s^{-1}$ respectively, while the data at $\phi = 1.2$ are 5.25×10^{-7} and 2.7 $kJ/cm^3 \cdot s^{-1}$ respectively. It can be seen that the peak HRR at $\phi = 1.2$ is around 50% higher than that at $\phi = 0.8$ even though they corresponds to a similar value of $OH \times CH_2O$ product. This elucidates that the correlation of $OH \times CH_2O$ product with peak HRR is insensitive to the fuel composition at a constant

equivalence ratio. However, when the equivalence ratio is unknown, its inadequate ability for the single-valued prediction of HRR is further confirmed. Besides, for the $H \times CH_2O$ and $H \times HO_2$ products, it is noted that although the data of $H \times CH_2O$ and $H \times HO_2$ products seem to be less scattered as shown in Fig. 4.19(c) and Fig. 4.19(d), there still exists the considerable uncertainty for the estimation on peak HRR. Specifically, the peak value of the $H \times CH_2O$ product for the BG50 flame at $\phi = 1.2$ is about twice of that at $\phi = 0.8$, but the corresponding values of HRR at these two conditions are almost the same with the value of 1 $kJ/cm^3 \cdot s^{-1}$. Therefore, the $H \times CH_2O$ and $H \times HO_2$ products are also not eligible for the single-valued determination on the peak HRR. In conclusion, the correlations of $OH \times CH_2O$, $H \times CH_2O$ and $H \times HO_2$ products with the peak HRR are sensitive to the equivalence ratio but comparatively insensitive to the fuel composition. In addition, the $O \times CH_3$ product is confirmed to be the most reliable marker for the peak HRR prediction since its correlation with peak HRR is insensitive to both equivalence ratio and fuel composition.

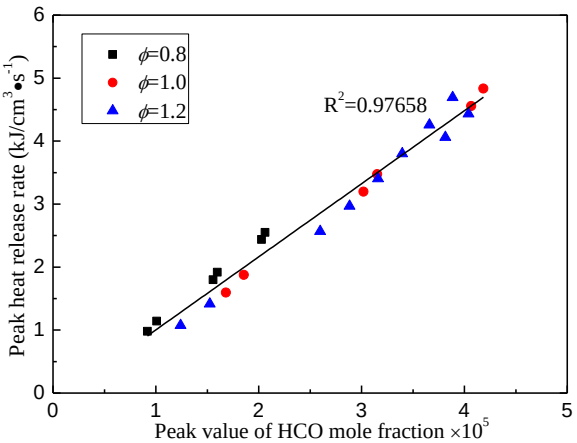

Fig. 4.18 The peak-to-peak correlation of HCO and peak HRR for the tested flames shown in Table 3.2.

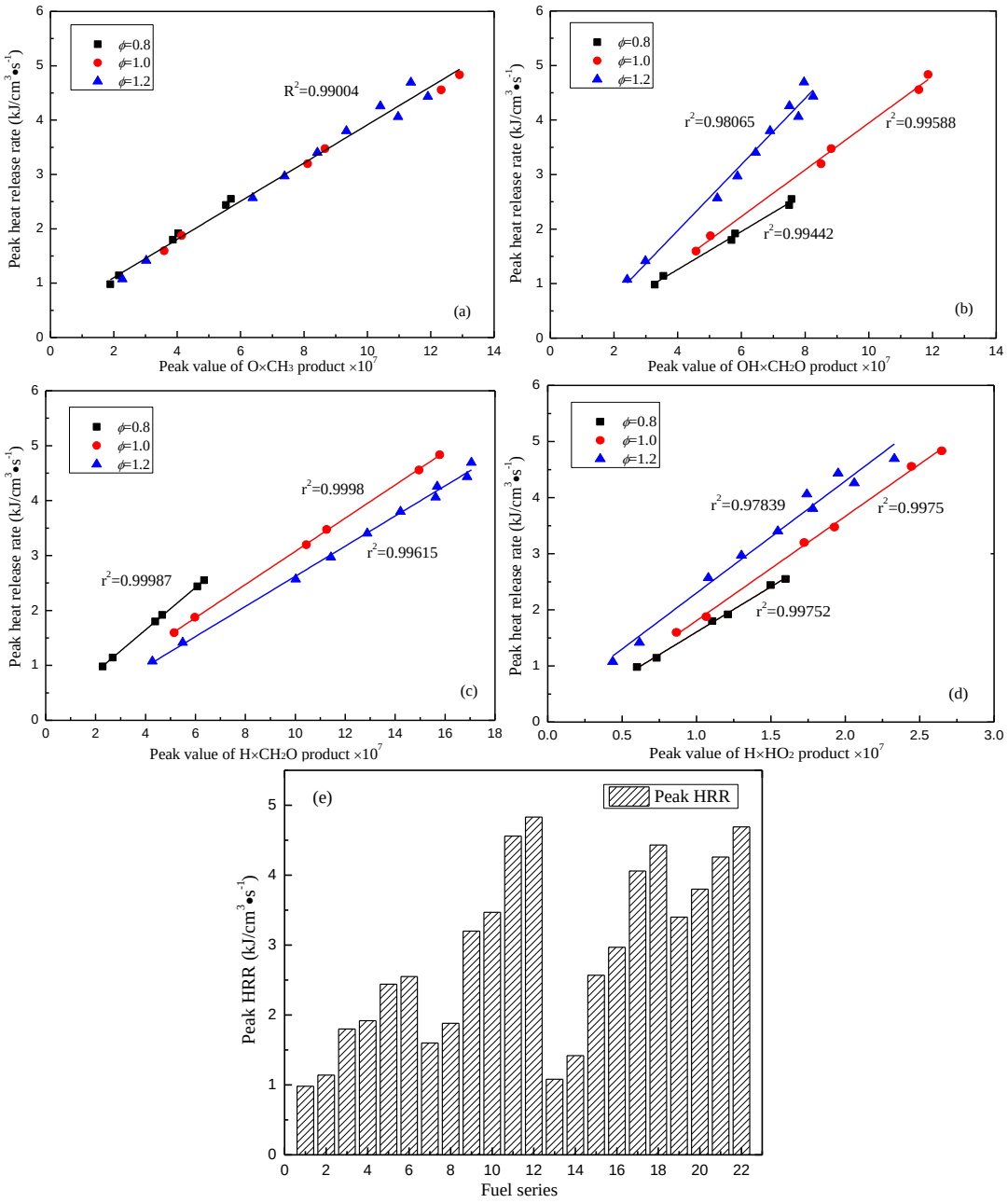

Fig. 4.19 The peak-to-peak correlations of HRR markers and peak HRR for the tested flames shown in Table 3.2.

4.3.3 The peak-to-integrated correlation

The proposed markers by the previous linearity method is qualified to reflect the change of local HRR at a fixed equivalence ratio, but it is inadequate to reflect the HRR variation in the practical premixed flames due to its possibly variable correlation with HRR at different ϕ based on the above discussion. Hence, it is known that, for the

point-to-point correlation method, the eligible marker should have a good and constant linear relation with the local HRR at different equivalence ratios, which can then guarantee its prediction accuracy on the HRR variation at any conditions. With this requirement, HCO is still the most preferred marker for HRR visualization. However, researchers are more interested in the global distribution and change of HRR in the combustion devices, which can provide much more valuable information to improve the understanding of the combustion process and facilitate the combustion control. This reduces the relative importance of the accurate prediction on the local HRR in the reaction zone. In consideration of this, the total HRR across the reaction zone can be more helpful and convenient for HRR visualization in the flame, and using the correlation of marker and total HRR can neglect the requirement of the excellent linearity between marker and local HRR in the reaction zone. This method can facilitate to find out a suitable marker to be utilized in the global HRR visualization. The above discussed markers have been demonstrated to be eligible to discern the HRR location reasonably, thus the accuracy of determining the HRR location by these markers can be guaranteed when using the peak-to-integrated correlation (the peak value of marker and total HRR across the reaction zone). Based on this, the peak-to-integrated correlation of markers and total HRR will be examined in this part, and the HRR marker having a constant correlation with the total HRR is expected to be identified.

The peak-to-integrated correlations of markers and total HRR at ϕ = 0.6-1.4 for the BG75 and methane flames are given in Fig. 4.20 to initially examine the correlation dependence on the equivalence ratio. As shown in Fig. 4.20(a), it can be seen that the data of HCO and $O \times CH_3$ product still have the relatively compact distributions, meaning that their correlations with total HRR are comparatively insensitive to the

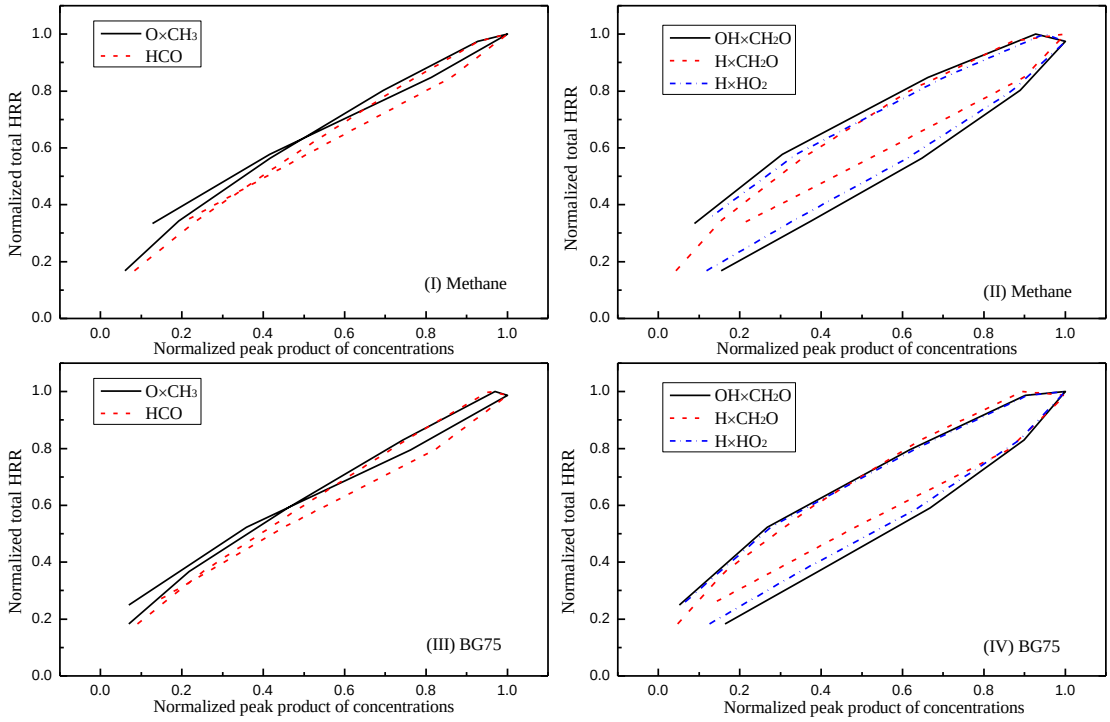

(a) GRI 3.0 mechanism

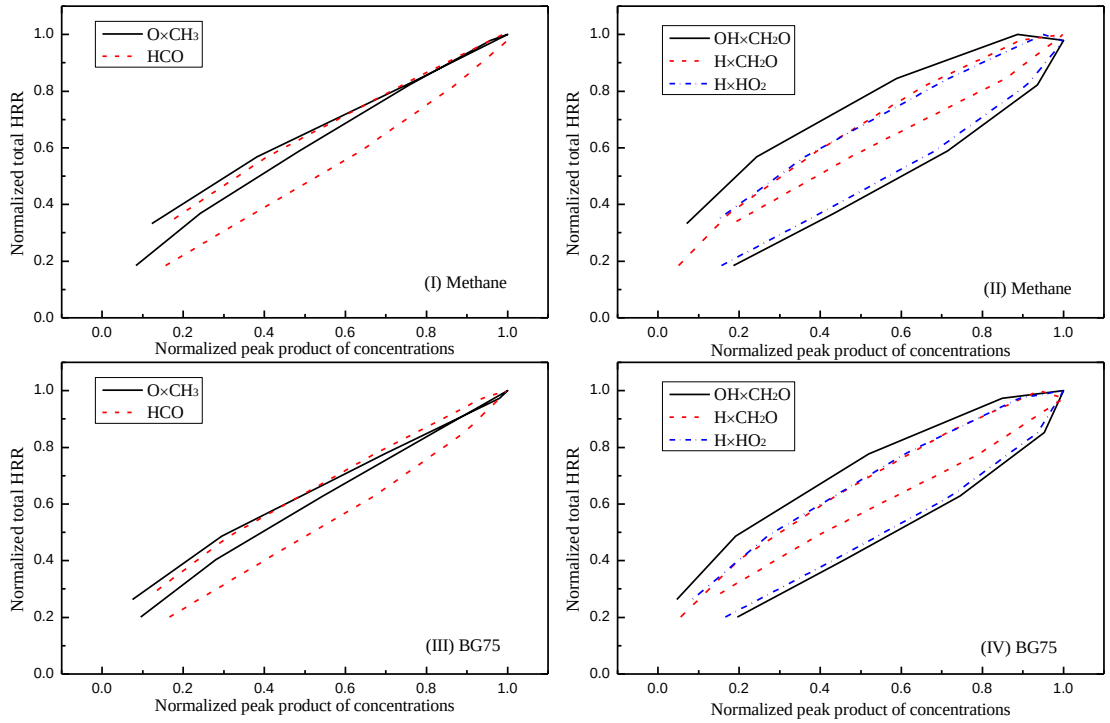

(b) San Diego mechanism

Fig. 4.20 The normalized peak-to-integrated correlations of premixed methane and BG75 laminar flames at various equivalence ratios (ϕ = 0.6-1.4).

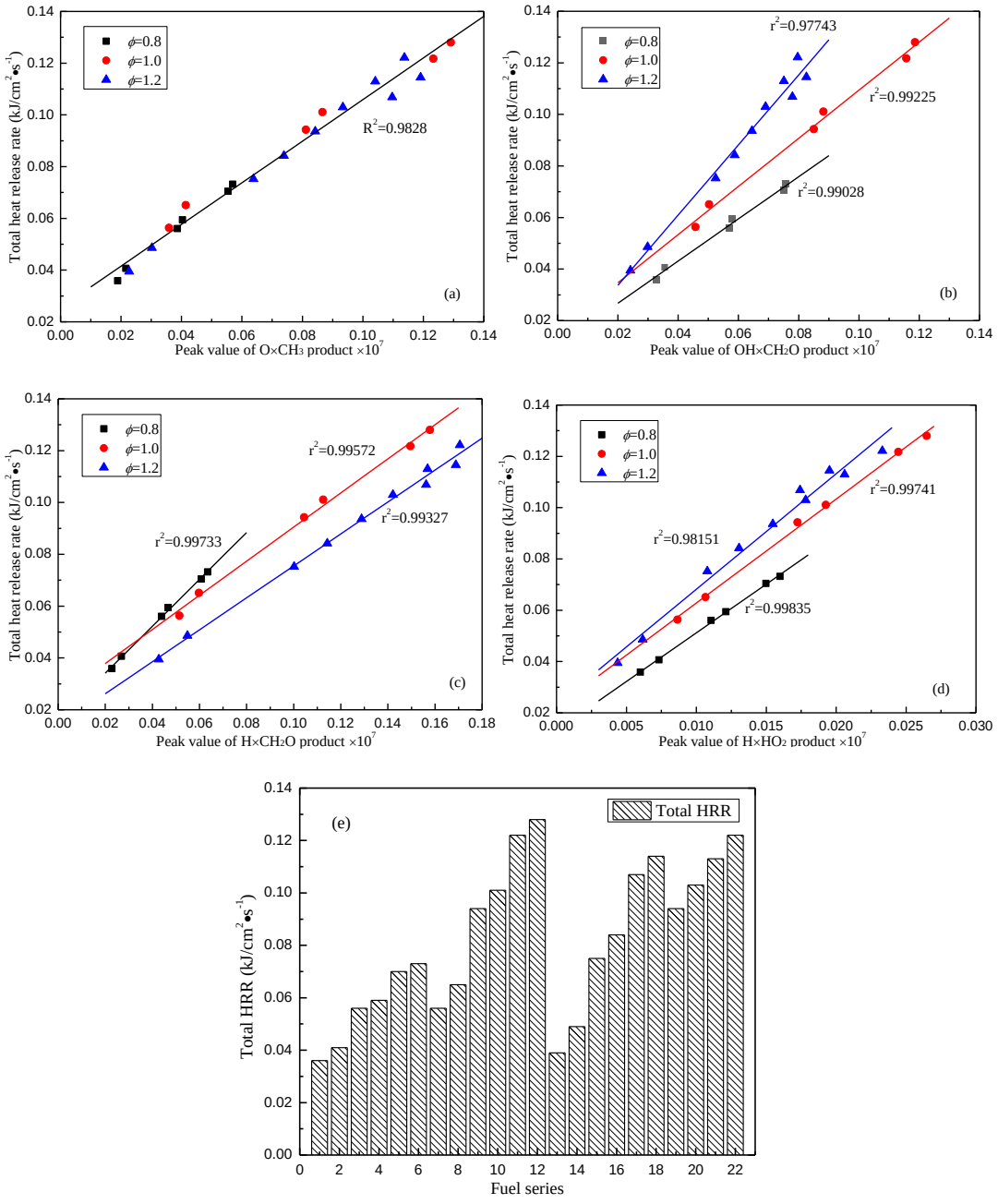

Fig. 4.21 The peak-to-integrated correlations of HRR markers and total HRR for the tested flames shown in Table 3.2.

equivalence ratio and they have a better single-valued correspondence with total HRR. In addition, the severe uncertainty in total HRR prediction by the $OH \times CH_2O$, $H \times CH_2O$ and $H \times HO_2$ products can be anticipated in the figure due to their scattered data distribution. This means that their correlations with total HRR are still sensitive to the equivalence ratio and they are not eligible to reflect the total HRR variation

accurately at the unclear conditions. By contrast, the data obtained by San Diego mechanism show several differences as illustrated in Fig. 4.20(b). The $O \times CH_3$ product still perform better than other markers with its relatively compact data distribution, however the HCO appears to perform relatively poorer than data obtained by GRI mechanism. This means that the $O \times CH_3$ product can be confirmed to be a reliable marker to predict the total HRR, while the prediction accuracy of HCO on the total HRR cannot be guaranteed due to its sensitivity to the chemical mechanism. Besides, the data of $H \times CH_2O$ product derived from San Diego mechanism show a slightly improved performance than that obtained by GRI mechanism, but its performance is still worse than the $O \times CH_3$ product and can induce a relatively severe uncertainty in total HRR estimation. Overall, since the correlation of HCO with total HRR is relatively sensitive to the chemical mechanism, the peak-to-integrated correlations of HCO and total HRR will not be further discussed for more fuel compositions. In order to examine the correlation sensitivity of these markers with total HRR to the fuel composition, as well as further confirm their sensitivity to the equivalence ratio, the peak-to-integrated correlations of the other four markers and total HRR for more fuel compositions are illustrated in Fig. 4.21 while the values of total HRR for these flames are presented additionally in order to correlate data to the flame series given in Table 3.2. Similarly, only GRI mechanism is employed in this part, since the results obtained by both chemical mechanisms show the slight discrepancy for these four markers in the above discussion. It is seen that the $O \times CH_3$ product has a significantly compact data distribution as shown in Fig. 4.21(a), indicating its good single-valued correspondence with the total HRR. This elucidates that its correlation with total HRR is still insensitive to the equivalence ratio and fuel composition. This demonstrates that the $O \times CH_3$ product has the excellent ability for the single-valued prediction on

total HRR. Besides, the data of the $OH \times CH_2O$, $H \times CH_2O$ and $H \times HO_2$ products show the poor performance in correlating with the total HRR due to the evidently scattered data distribution as shown in Fig. 4.21. Specifically, they have their respective correlations with the total HRR at a constant equivalence ratio because their correlations with total HRR are dependent on the equivalence ratio but relatively insensitive to the fuel composition. In conclusion, the $O \times CH_3$ product is the most reliable marker to predict the total HRR at the unknown conditions.

The different performances of considered HRR markers can be explained by the stability of fractional contributions of related elementary reactions on the total HRR. Since GRI and San Diego mechanisms give the similar results of the $OH \times CH_2O$, $O \times CH_3$, $H \times CH_2O$ and $H \times HO_2$ products, only the GRI mechanism is adopted here. The related reactions are illustrated as follows:

R10: $O+CH_3 = H+CH_2O$
R101: $OH+CH_2O = HCO+H_2O$
R58: $H+CH_2O = HCO+H_2$
R45: $H+HO_2 = H_2+O_2$
R46: $H+HO_2 = 2OH$

The peak-normalized fractional contributions of related elementary reactions for the considered fuel compositions in Table 3.2 are presented in Fig. 4.22. The fractional contributions f_c of a reaction is normalized by its peak value. The averaged fractional contributions, standard deviations and the relative standard deviations (RSD) of these reactions are presented in Table 4.4. It can be seen that R10: $O+CH_3 = H+CH_2O$ contributes a considerable and stable proportion of total HRR for the considered fuels as shown in Fig. 4.22 and Table 4.4. This means that the HRR of R10, as well as its net reaction rate, has a relatively constant relation with HRR at different conditions. Furthermore, considering the relation between the reaction rate and concentrations of

O and CH_3, the variations of O and CH_3 mole fractions should be the main reason for the stable fractional contribution of R10. At different equivalence ratios, the O and CH_3 mole fractions can reflect the consumptions of oxidizer and fuel which can influence the heat release during the premixed combustion process directly. Therefore, the variation rate of $O \times CH_3$ product is almost consistent with that of HRR as ϕ and fuel composition are changed. This contributes to the constant relation between the $O \times CH_3$ product and the HRR at different conditions. Besides, the fractional contributions of R101: $OH+CH_2O = HCO+H_2O$ on the total HRR drops rapidly from fuel-lean to fuel-rich condition as illustrated in Fig. 4.22. Its relative standard deviation is much higher than that of R10 as provided in Table 4.4, indicating its seriously fluctuated fractional contribution as equivalence ratio and fuel composition are varied. This means the variation rate of the $OH \times CH_2O$ product is different from that of HRR as ϕ and fuel composition are changed, which finally leads to its scattered data distribution as shown in Fig. 4.21(b). For the $H \times CH_2O$ and $H \times HO_2$ products, the elementary reactions proposed in Ref. [199] are adopted to calculate the fractional contributions as shown in Fig. 4.22 and Table 4.4. As ϕ is increased, the contribution of R58: $H+CH_2O = HCO+H_2$ is increased, while that of R45: $H+HO_2 = H_2+O_2$ and R46: $H+HO_2 = 2OH$ are both decreased. The relative standard deviation of R58, R45 and R46 contributions are quite high as given in Table 4.4, indicating their significantly fluctuated fractional contributions at different conditions. Thus the relations of these markers and HRR also show the dependence on ϕ, making them not suitable for the single-valued prediction on HRR. Based on the above discussion, it is known that a HRR marker having a close relation with consumptions of fuel and oxidizer is more likely to be eligible and reliable for the HRR prediction in a wide range of conditions. Consequently, it is concluded that the correlation between the

$O \times CH_3$ product and HRR remains almost constant as ϕ or fuel composition varies, while other considered markers have their respective correlations with HRR at different equivalence ratios and the correlations are relatively insensitive to the fuel composition. The $O \times CH_3$ product can be thus seen as the best marker to predict the peak HRR or total HRR with its corresponding correlations for the premixed flame with the unclear equivalence ratio, such as the turbulent stratification flame.

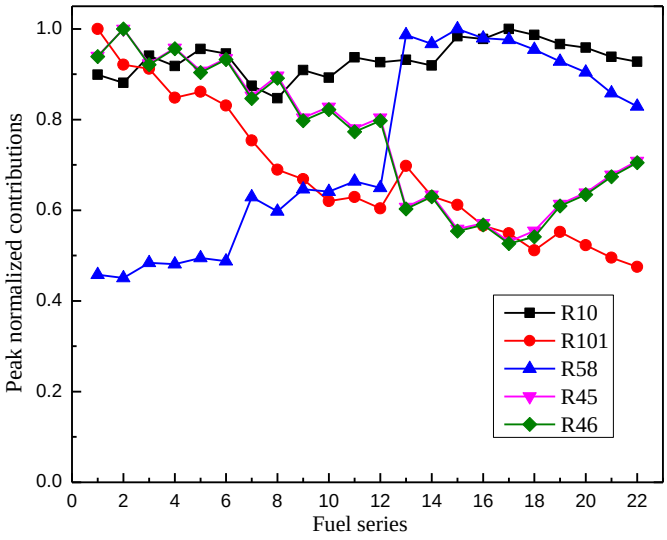

Fig. 4.22 The normalized f_c of elementary reactions given in Table 4.4 for the tested fuel compositions in Table 3.2.

Table 4.4 The fractional contributions and its standard deviation of related reactions on the total HRR for the tested flames.

Elementary Reaction	**Average f_c (%)**	**Peak f_c (%)**	**Standard Deviation**	**RSD (%)**
R10: $O+CH_3 = H+CH_2O$	10.97	11.76	0.45	4.08
R101: $OH+CH_2O = HCO+H_2O$	3.03	4.46	0.67	22.15
R58: $H+CH_2O = HCO+H_2$	2.84	3.89	0.79	27.79
R45: $H+HO_2 = H_2+O_2$	2.51	3.30	0.50	19.84
R46: $H+HO_2 = 2OH$	3.66	4.84	0.74	20.10

For the $O \times CH_3$ product, CH_3 might be difficult to be measured due to a strong predissociation of its electronically excited states [258], but some efforts have been made on its spatially resolved quantitative measurements in the premixed flame using

the lase diagnostics [259, 260], which can give rise to the practical utilization of $O\times CH_3$ product in HRR imaging. Besides, although $OH\times CH_2O$ and $H\times CH_2O$ products are found to have a poor performance on single-valued prediction of HRR, they can still be quite useful to discern the energy intensive region experimentally due to their applicability in the conventional laser diagnostics [60, 192]. For the $H\times HO_2$ product, it is suggested to have an improved accuracy to determine the HRR location [199] but it is demonstrated to be not eligible for the singe-valued prediction of HRR in this study. Furthermore, its application in the laser diagnostics may be difficult because the HO_2 radical cannot be measured directly by LIF [261]. Overall, this work is expected to provide some useful information or guidelines for the practical HRR imaging and the development of related techniques.

4.4 Summary

Numerical simulations were conducted to investigate the heat release characteristics of the laminar premixed biogas flames with hydrogen enrichment at various fuel compositions and equivalence ratios. The heat release rates, reaction rates and mole fractions of species were obtained while the contributions of major elementary reactions were calculated based on the simulation data. Effects of equivalence ratio, as well as the H_2 and CO_2 proportions, on the heat release characteristics were analyzed quantitatively. The peak-to-peak and peak-to-integrated correlations of HRR marker and HRR were established in a wide range of conditions. The validity of several HRR markers for the single-valued prediction on the HRR was discussed. The results are summarized as follows:

The maximum global HRR of the biogas-hydrogen flame at ϕ=1.0 is resulted from its complete combustion, while the exothermic recombination of radicals contributes to

the higher HRR in the post flame zone at the fuel-rich condition. With the H_2 enrichment, $H+HO_2=2OH$ and $H+O_2=OH+H$ can be accelerated effectively, which can enhance the amount of active radicals at both low and high temperatures and then lead to the higher HRR. With the increased CO_2 proportion in the biogas, the dropping trend of global HRR is dominated by the dilution/thermal effect and further aggravated by the chemical effects.

For the biogas-hydrogen combustion, the primary endothermic reaction is $H+O_2=OH+H$ while $O+CH_3=H+CH_2O$, $H+CH_3(+M)=CH_4(+M)$, $OH+H_2=H+H_2O$, $OH+CO=H+CO_2$ and $O+CH_3=>H+H_2+CO$ play significant roles in HRR consistently at different ϕ. Additionally, $H+O_2+H_2O=HO_2+H_2O$ and $OH+HO_2=O_2+H_2O$ cannot be neglected for the flames at ϕ=0.8 and ϕ=1.0, while $H+OH+M=H_2O+M$ becomes more significant at ϕ=1.0 and ϕ=1.2 compared to that at fuel-lean condition. Besides, $2CH_3(+M)=C_2H_6(+M)$ can play an increasingly important role at the fuel-rich condition.

The contributions of $OH+H_2=H+H_2O$ and $OH+H+M=H_2O+M$ on the HRR are enhanced most evidently with the hydrogen addition, indicating their increasingly significant roles in the heat release of hydrogen enriched combustion. With the increased CO_2 proportion in the biogas, the increased importance of $H+CH_3(+M)=CH_4(+M)$ and $2CH_3(+M)=C_2H_6(+M)$ are dominated by the dilution/thermal effect, while the decreased contributions of $OH+CO=H+CO_2$ and $H+OH+M=H_2O+M$ are determined by the stronger chemical effect and dilution/thermal effect, respectively. Additionally, $H+CH_3(+M)=CH_4(+M)$, $2CH_3(+M)=C_2H_6(+M)$ and $OH+H_2=H+H_2O$ become increasingly significant on HRR as CO_2 is added.

For the laminar premixed biogas-hydrogen flames, the $O \times CH_3$ product has the best performance on the single-valued prediction of HRR, thus it is the most reliable marker to reflect the HRR variation in the premixed flame with the unclear equivalence ratio. This can be attributed to that the concentrations of CH_3 and O can be considered as the indicators of the fuel and oxidizer consumptions in the flame, and the $O+CH_3$ reaction is a primary contributor on total HRR. HCO is still a reliable HHR marker whose correlation with HRR is insensitive to both equivalence ratio and fuel composition. The $H \times CH_2O$, $H \times HO_2$ and $OH \times CH_2O$ product cannot be used for the single-valued prediction of the HRR owing to their variable correlations at different ϕ.

5 Heat transfer characteristics of laminar premixed biogas-hydrogen Bunsen flame

5.1 Introduction

The experimental data of heat transfer characteristics of laminar premixed biogas-hydrogen flame are presented in this chapter [262, 263]. In the first part, the heat fluxes of BG75 flame with increased hydrogen enrichment were measured at different heating distances, and effects of hydrogen reactivity and diffusivity on the combustion and heat transfer processes will be investigated quantitatively. The optimum hydrogen addition will be suggested for the laminar premixed BG75 impinging flame. Besides, with the same hydrogen addition, the impinging flame temperature and heat fluxes of BG50, BG75, methane and LPG flames were measured experimentally. The chemical and thermal effects of CO_2 on the combustion and heat transfer processes will be investigated based on the experimental data. In the second part, in order to derive the correlation to predict the optimal heating distance of the laminar premixed biogas-hydrogen Bunsen flame, the heat flux and impingement flame temperature of laminar premixed BG75-hydrogen impinging flame were measured in the experiment, and then effects of heating distance (H), Reynolds number (Re) and equivalence ratio (ϕ) on its heat transfer process and total heat transfer rate will be investigated quantitatively. Finally, a nondimensional quantitative correlation of the optimal heating distance will be derived as a function of Pr, u/S_L and ϕ, and this correlation will be validated by our experimental data.

5.2 The effects of H_2 and CO_2 on the heat transfer characteristics

In order to better compare the heating performance of different fuels, the energy input of tested flames and corresponding adiabatic flame temperatures are provided in Table 5.1. It can be seen that the energy input and the adiabatic flame temperature of biogas fuel are decreased and increased respectively, which are caused by the lower volumetric heating value and the higher adiabatic flame temperature of hydrogen. Meanwhile, the CO_2 can reduce the energy input and adiabatic flame temperature effectively. Based on the energy input, the heating performance of various fuel compositions can be evaluated quantitatively.

Table 5.1 The energy input of tested flames and corresponding adiabatic flame temperatures.

Fuel	ϕ	*Re*	αH_2	Energy input (J/s)	Adiabatic flame temperature (K)
BG75	1.2	1000	0.0	480.4	2052
BG75	1.2	1000	0.1	480.2	2063
BG75	1.2	1000	0.2	480.0	2074
BG75	1.2	1000	0.3	479.8	2084
BG75	1.2	1000	0.4	479.6	2093
BG75	1.2	1000	0.5	479.4	2102
BG50	1.2	800	0.1	359.7	1929
BG75	1.2	800	0.1	384.1	2063
CH_4	1.2	800	0.1	398.1	2141
LPG	1.2	800	0.1	414.9	2207

5.2.1 Effects of H_2 addition

Fig. 5.1 illustrates the digital images of laminar premixed BG75 impinging flames with different hydrogen enrichment at *Re*=1000, ϕ=1.2 while Fig. 5.2 shows the corresponding flame height and laminar burning velocity of free BG75 flames with different hydrogen enrichments. It is obvious that, with the increase in αH_2, the flame surface become much brighter and the steadily decreased flame height causes the

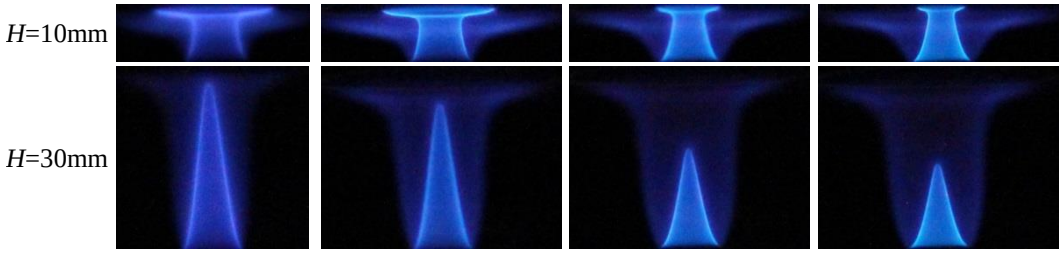

Fig. 5.1 Digital images of BG75 impinging flames with hydrogen enrichment at ϕ=1.2 and *Re*=1000.

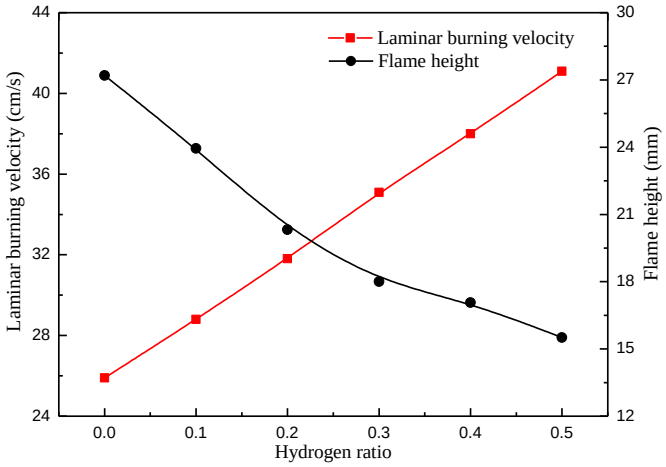

Fig. 5.2 Flame height and laminar burning velocity of premixed BG75 Bunsen flames with different hydrogen addition at ϕ=1.2 and *Re*=1000.

varied impinging flame structure as shown in Fig. 5.1 and Fig. 5.2. The flame heights were measured using the digital images with the software while the laminar burning velocity was calculated using the PREMIX code of CHEMKIN II with the mechanism GRI 3.0. The ideal flame height H_{flame} can be obtained using the equation as follows [61]:

$$H_{\text{flame}} = \frac{D}{2} \bullet \frac{\sqrt{u^2 - S_{\text{L}}^2}}{S_{\text{L}}} \qquad \text{Equation 5-1}$$

where D, u and S_{L} denote the nozzle inner diameter, the average flow velocity at nozzle exit and the laminar burning velocity, respectively. Apparently, according to the Equation 5-1, though S_{L} increases linearly, H_{flame} would decline nonlinearly as u is kept almost constant, just as the results shown in Fig. 5.2, which can result in the

variation of the impinging flame structure. In addition, with the increase in αH_2, the active radicals would be produced much more than that without hydrogen addition. This brings about the more intensive combustion process and the brighter flame surface [173].

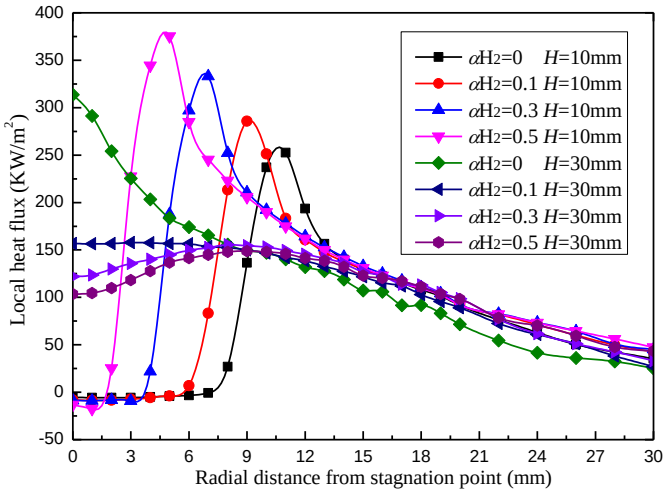

(a) Distributions of local heat fluxes

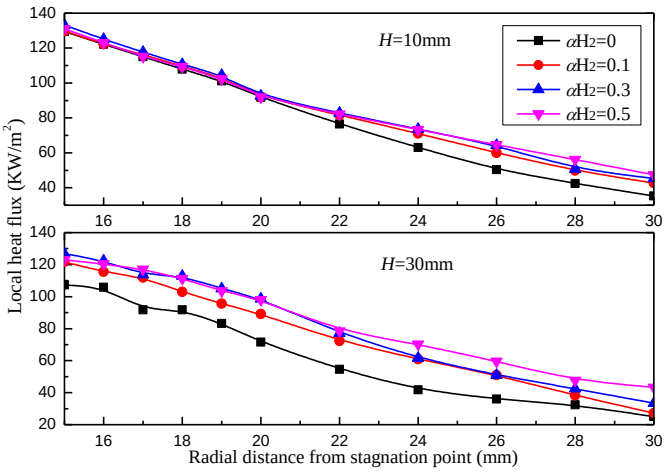

(b) Local heat fluxes in the wall jet region

Fig. 5.3 Radial heat flux profiles of the laminar premixed BG75 flames with hydrogen addition at ϕ=1.2 and *Re*=1000.

The comparison of local heat fluxes of laminar premixed BG75 flames with different αH_2 are shown in Fig. 5.3. At *H*=10mm, zero heat flux near the stagnation point means the presence of cool core, and its distribution narrows with the increase in αH_2

due to the lower flame height. Meanwhile, the maximum heat flux occurs around the cool core where the chemical reactions take place to release a large amount of heat, leading to the fast rise of the local heat flux. As the hydrogen proportion increases, the location of the peak heat flux moves towards the stagnation point with its value enhanced from around 250 to 380 kW/m^2 by more than 50%. The location movement is also the result of the reduced cool core area, while the reasons for the boosted peak heat flux can be interpreted as follows. Firstly, the enhanced flame temperature caused by the hydrogen addition can effectively improve the heat transfer process through increasing the temperature difference and the velocity of burned mixture. The increased flame tip temperature can be confirmed by the measured data shown in Fig. 5.4(a). It clearly shows the rising trend of the flame temperature at the flame tip as the αH_2 increases. Furthermore, the increased temperature can further reduce the density of burned gases, causing the accelerated velocity of burned gases according to the flow continuity law. Secondly, the large amounts of reactive species existing at the flame tip can enhance the convection by their diffusion and exothermic recombination on the impingement surface [264]. As the hydrogen fraction increases, due to its high diffusivity and flammability, the diffusion effect of species can be improved effectively while the quantity of active radicals can also be enhanced in the reaction zone [139]. This can strengthen the improvement of diffusion and exothermic recombination on the heat transfer process. Lastly, the lower flame height means the smaller cool core, which can reduce the energy and momentum loss of unburned gases induced by the impingement and the boundary layer effect. This can also make for the heat transfer process to some extent. With the increase in the radius *r*, the local heat fluxes drop fast and show little differences in the wall jet region until *r*=20mm. After that, as shown in Fig. 5.3(b), the discrepancies between different flames become

slightly evident because the improvement of the high H_2 diffusivity on the diffusion combustion becomes more manifest.

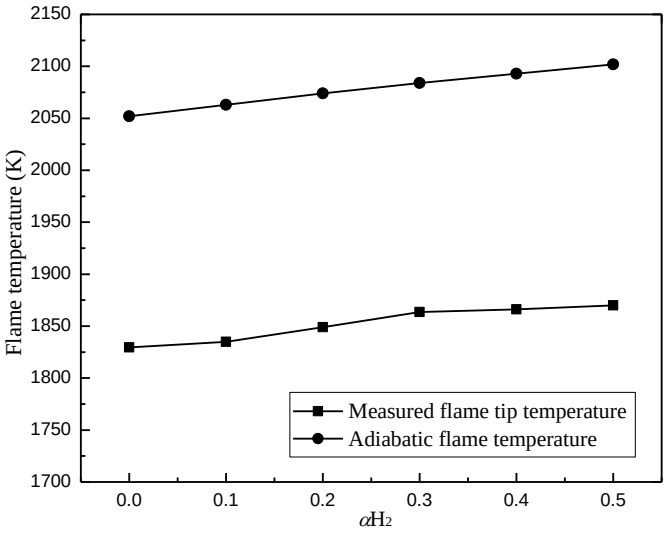

(a) Flame tip temperature and adiabatic flame temperature

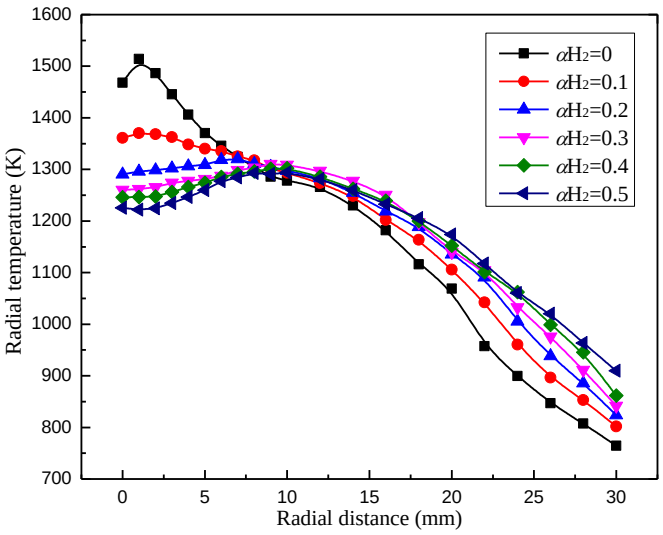

(b) Radial temperature distribution of burned gases attaching the plat surface at H=30mm

Fig. 5.4 The measured temperature distribution of the laminar premixed BG75 flames with hydrogen addition at ϕ=1.2 and Re=1000.

As shown in Fig. 5.3, more uniform distributions of heat fluxes are obtained at larger H. The higher flame height can lead to the larger stagnation heat flux due to the less cooling effect. Thus the stagnation heat flux of the raw biogas flame has a much higher value of approximate 320 kW/m^2 which is about two or three times the values

of other conditions. However, with the increase in the radius, its heat flux drops rapidly to the lowest in the wall jet region. In addition, the local heat fluxes of biogas flames with higher hydrogen fraction are lower in the stagnation region but become higher in the wall jet region as shown in Fig. 5.3. These variations can be attributed to the high diffusivity and reactivity of hydrogen. Specifically, as the hydrogen fraction in the unburned gases increases, the flame height is decreased and the flame temperature near the centerline would drop more evidently due to the cooling effect while the heat released by the diffusion combustion is hardly transferred to the stagnation point due to the outward impingement flow. These eventually result in the temperature drop at the stagnation point as shown in Fig. 5.4(b). Thus the cooling effect dominates the drop of heat flux at the stagnation point as the hydrogen addition is increased. In the wall jet region, with the increased hydrogen fraction, the high diffusivity of hydrogen can lead to the stronger mass diffusion and the impingement flow can promote the outward heat transfer effectively, which can result in a wider diffusive combustion zone and the increased flame temperature in the wall jet region as shown in in Fig. 5.1 and Fig. 5.4(b). Therefore, the flame with higher hydrogen enrichment has the larger heat fluxes in the wall jet region as shown in Fig. 5.3(b). Additionally, heat flux of the BG75 flame with high hydrogen fraction has the maximum value away from the stagnation point, and the corresponding flame temperature distribution illustrated in Fig. 5.4(b) shows a similar profile. Because of the preferential diffusion at the flame tip, the fuel with high fraction of hydrogen would suffer more intensive mass diffusion there [177], which can bring about more serious incomplete combustion while the burned gases near centerline will suffer more intensive cooling effects due to the shorter flame height. This can lead to the lower temperature distribution near the centerline and less effective heat transfer in the

stagnation zone. On the other hand, as shown in Fig. 5.4(b), the radial temperature goes up again at about r=8mm which is consistent with the position of the off-stagnation peak. This can be attributed to that the flame with higher hydrogen enrichment would have a more intensive diffusion combustion which can heat up the burned mixture around the stagnation region. Furthermore, the burned gases flow sideways due to the acceleration of the velocity component normal to the flame front after expansion, which can cause a dip in the velocity field above the flame tip [172, 232]. Eventually, the maximum heat flux of flame with more hydrogen addition occurs away from the stagnation point as shown in Fig. 5.3.

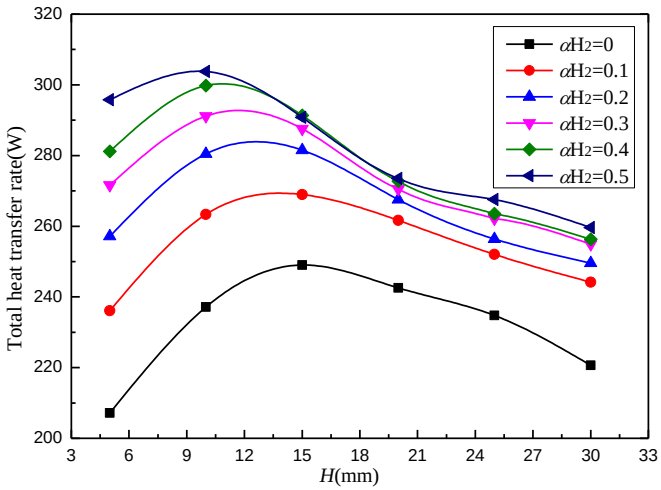

Fig. 5.5 Total heat transfer rate profiles of the laminar premixed BG75 flames with hydrogen addition at ϕ=1.2 and Re=1000.

The total heat transfer rate of laminar premixed BG75-hydrogen flames at Re=1000, ϕ=1.2 are illustrated in Fig. 5.5. With the measured local heat flux, the total heat transfer rate can be integrated up to 30mm along the radial direction in consideration of that the final results are slightly influenced with further integration. As shown in Fig. 5.5, it is apparent that the hydrogen addition can significantly enhance the total heat transfer rate at either small or large H. However, the rising rate slows down as hydrogen proportion increases, especially evident at large H. At small H, the hydrogen

addition can shorten the flame height evidently and enhance the maximum flame temperature as shown in Fig. 5.1 and Fig. 5.4(a), respectively. As a result, the mixture with higher proportion of hydrogen has the higher local heat fluxes and larger effective heating area at small *H* as shown in Fig. 5.3. Therefore, the total heat transfer rate rises evidently at *H*=5mm with the increase in hydrogen addition. When the heating distance exceeds 15mm, though the flame with higher hydrogen addition would suffer more ambient air entrainment, its higher temperature distribution in the wall jet region can compensate and overcome the cooling influences to improve the heat transfer process. Just as the previous discussion, due to the high diffusivity of hydrogen, the flame with hydrogen addition has a wider burned zone and its temperature in the wall jet region is enhanced with the increased hydrogen enrichment, as shown in Fig. 5.1 and Fig. 5.4(b). Since the annulus heating area increases significantly with the radius, the variation of the heat flux at larger radius can exert more evident effects on the total heat transfer rate. Hence the increased temperature in the wall jet region can bring about the rising trend of total heat transfer rate at larger heating distance. Additionally, as shown in Fig. 5.4 and Fig. 5.5, after the hydrogen enrichment exceeding 30%, the measured flame tip temperature shows fewer enhancements, and the total heat transfer rate varies slightly in a wide range of *H*. Hence, it can be suggested that 30% hydrogen addition can be regarded as an optimum choice to improve heating performance of laminar premixed BG75 impinging flame considering that the hydrogen enrichment exceeding 30% can only further exert limited improvement in a wide range of heating distance, especially at large *H*.

5.2.2 Effects of CO_2 composition

The direct images of laminar premixed impinging flames at ϕ=1.2, αH_2=0.1, *Re*=800 are shown in Fig. 5.6. LPG, as an important fuel for the combustion facility, is adopted as a comparison in order to help fully understand the heat transfer characteristics of biogas fuel. As shown in Fig. 5.6, LPG flame has a similar flame height with that of CH_4 flame, which is caused by their almost same laminar flame speed at this condition. With the increase in the CO_2 proportion, the flame height is enhanced obviously, denoting the decrease in the laminar flame speed. What is more, the luminescence becomes dim as the CO_2 percentage increases, suggesting the weakened combustion. When CO_2 is introduced into the mixture, it can suppress the oxidation of CO which is a critical step for hydrocarbon combustion. In addition, CO_2 can lower the flame temperature by reducing the heat release of combustible fuel, absorbing more heat due to its larger specific heat capacity, and more radiation loss caused by its molecular structure[265, 266]. As a result, the combustion can be weakened significantly.

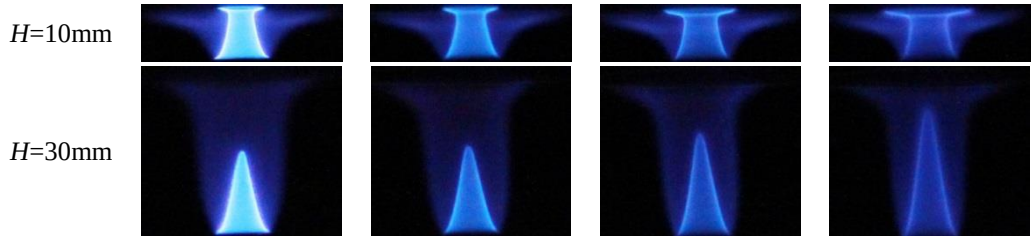

Fig. 5.6 Digital images of LPG and biogas impinging flames at ϕ=1.2, αH_2=0.1 and *Re*=800.

The local heat fluxes of four flames at ϕ=1.2, αH_2=0.1, *Re*=800 are compared in Fig. 5.7. At *H*=10mm, LPG flame shows a similar distribution of the local heat flux with that of CH_4, and the maximum local heat fluxes of these two flames are quite close with the value of about 300kW/m^2. However, LPG flame has a slightly higher heat flux than that of CH_4 flame in the wall jet region as shown in Fig. 5.7(b), which can be

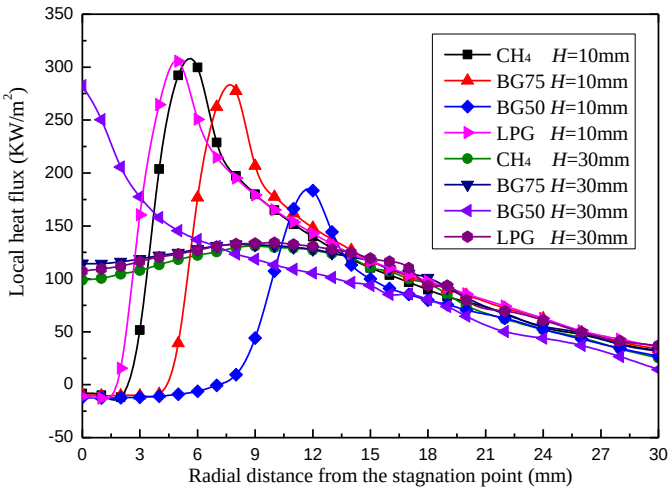

(a) Distributions of local heat fluxes

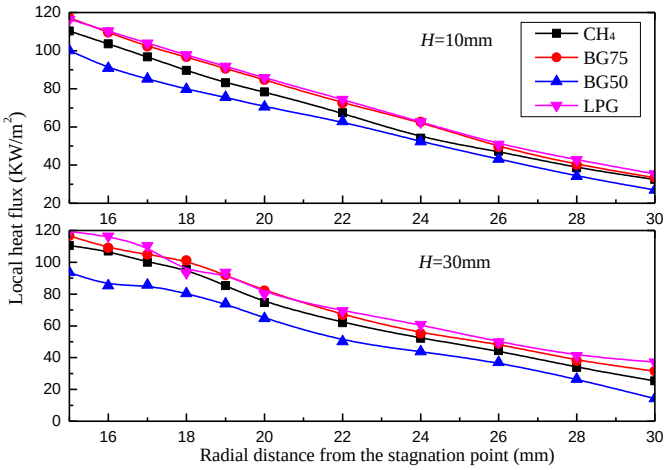

(b) Local heat fluxes in the wall jet region

Fig. 5.7 Radial heat flux profiles of the laminar premixed LPG and biogas flames at ϕ=1.2, Re=800 and αH_2=0.1.

the result of its largest energy input and more intensive diffusion combustion. Though the adiabatic flame temperature of LPG fuel is higher than that of CH_4 fuel, the measured flame temperature at the flame tip for the LPG flame is relatively lower than that of CH_4 flame as shown in Fig. 5.8(a). This can be resulted from the preferential diffusion effects which can weaken the combustion intensity of the LPG flame at its flame tip under the fuel-rich condition and strengthen its diffusion combustion [177]. As CO_2 is added, the enhanced flame height leads to the outward move of peak local heat flux position, and peak local heat flux drops by up to approximate 30%. This can

be interpreted by the lower temperature and slower velocity of burned gases. The lower temperature can be reflected by the measured data shown in Fig. 5.8(a), which indicates CO_2 can reduce the flame temperature noticeably. In particular, $CO+OH=H+CO_2$ is a quite significant element reaction for the complete combustion of hydrocarbon fuel [265]. This reaction can be remarkably suppressed by introducing a large amount of CO_2 into the unburned mixture, which can lead to the increased CO emission, meaning the incomplete combustion and less heat release. Meanwhile, the existence of CO_2 in the unburned mixture can directly reduce the energy input and consume more heat due to its larger specific heat capacity. As a result, flame temperature can be reduced apparently as shown in Fig. 5.8(a). As a result of the lower flame temperature, the velocity of burned gases will be smaller than that of higher temperature, resulting in the less effective convective heat transfer. Hence, the maximum local heat flux drops with the increase in CO_2 proportion. Additionally, it is noted that the local heat fluxes of the BG75 flame are slightly higher than that of the CH_4 flame in the wall jet region as shown in Fig. 5.7(b). This can be explained as follows. Though the existence of CO_2 can reduce the flame temperature, its larger specific heat capacity can decelerate the dropping rate of flame temperature compared to that of the CH_4 flame when they suffering the same cooling influences of ambient air. Meanwhile, the larger flame height means its burned gases can suffer relatively less cooling effects in the wall jet region. As a whole, this can lead to the higher flame temperature in the wall jet region, which can then promote the heat transfer in the wall jet region as shown in Fig. 5.7(b).

At H=30mm, it can be seen that the stagnation heat flux of BG50 flame is the maximum with a value of approximate 260 kW/m^2, while that of other flames are around 100 kW/m^2. This is resulted from the differences of flame heights as the

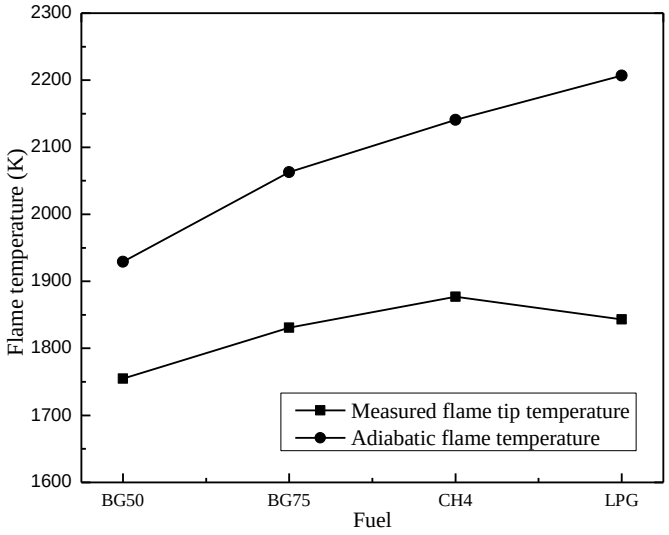

(a) Flame tip temperature and adiabatic flame temperature

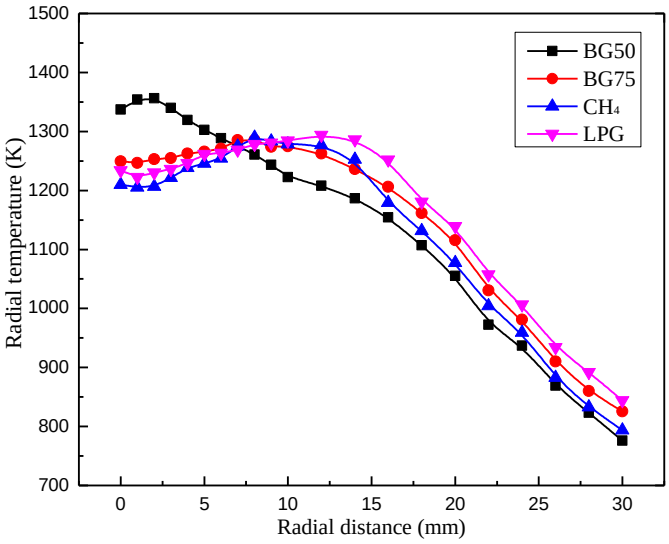

(b) Radial temperature distribution of burned gases attaching the plat surface at H=30mm.

Fig. 5.8 The measured temperature distribution of the laminar premixed LPG and biogas flames at ϕ=1.2, αH_2=0.1 and Re=800.

previous discussion. However, the heat flux of the BG50 flame has a fastest dropping trend along the radial direction. This can be attributed to that the large amount of CO_2 in the BG50 fuel weakens its diffusion combustion and reduces the heat release, which finally leads to its faster dropping trend of flame temperature along the radial direction than that of other flames as given in Fig. 5.8(b). Besides, though the flame temperature of BG75 is lower than that of CH_4 and LPG, the local heat fluxes of the

BG75 flame are slightly higher than that of other two flames in the stagnation region, while its values become lower than that of the LPG flame but are still higher than that of the CH_4 flame in the wall jet region. This can be interpreted as follows. The higher flame height of the BG75 flame makes it suffer less cooling effect near the centerline, which directly contributes to its higher heat fluxes in the stagnation region. Furthermore, due to the maximum energy input and more intensive diffusion combustion, the LPG flame can release more heat in the wall jet region, leading to its highest heat fluxes there, which can be confirmed by its radial temperature distribution as shown in Fig. 5.8(b). Meanwhile, as the previous discussion, such an amount of CO_2 addition gives rise to the larger specific heat capacity of the mixture, which leads to the higher flame temperature and the local heat flux of the BG75 flame in the wall jet region than that of the CH_4 flame as shown in Fig. 5.8(b) and Fig. 5.7(b). It is can be noted that, for the practical impingement heat transfer process, a suitable amount of CO_2 addition can slow down the decreasing trend of the temperature along the outward direction, which can overcome its negative effects to improve the heating performance.

Fig. 5.9 illustrates the total heat transfer rates of laminar premixed LPG, methane and biogas flames at ϕ=1.2, αH_2=0.1, *Re*=800. It can be seen that the data of the LPG flame have the highest values in the whole range of *H* though it has a similar flame height with that of CH_4 flame. This can be attributed to its largest energy input, more intensive diffusion combustion and the relatively high flame temperature, which contribute to the higher temperature distribution of LPG flame in the wall jet region as shown in Fig. 5.8(b), eventually leading to its higher total heat transfer rate than that of the CH_4 flame. Meanwhile, total heat transfer rates of the BG50 flame are lowest due to its least energy input and lowest flame temperature. It is noted that the BG75

flame shows a better heating performance than that of the CH_4 flame at most of heating distances even though its energy input is less than that of CH_4 flame. The total heat transfer rate of the BG75 flame is slightly smaller than that of the CH_4 flame only when *H* is less than 10mm; otherwise it is relatively stable and better than that of the CH_4 flame with its value varying between 230 and 250 kW/m^2. The better performance of the BG75 flame at large *H* can be explained by its radial temperature distribution shown in Fig. 5.8(b). It can be seen that the temperature of BG75 is firstly higher than that of CH_4 flames at the stagnation point and then becomes smaller around the stagnation region. However, it becomes higher again in the wall jet region. This trend can be elucidated as follows. The higher flame height of the BG75 flame contributes to the higher flame temperature at the stagnation point due to suffering less cooling effects. However, the more intensive diffusion combustion of the CH_4 flame gives rise to the increase of its temperature along the radial direction in the diffusion combustion zone. Thus, the flame temperature of the CH_4 flame exceeds that of the BG75 flame and approaches to the maximum at the edge of the diffusion combustion zone (around *r*=9mm). Outside the diffusion combustion zone, the cooling effects of the ambient air become increasingly evident to reduce the flame temperature. Just as the previous discussion, the CO_2 addition can reduce the decreasing rate of temperature due to its larger specific heat capacity. Thus the BG75 flame temperature drops more moderately and maintains a relatively higher value than that of the CH_4 flame in the wall jet region as shown in Fig. 5.8(b). Furthermore, it is known that the total heat transfer rate is quite sensitive to the variation of heating process in the wall jet region because of the larger element heating area there. Consequently, the BG75 flame has a higher flame temperature in larger heating area comparing to that of the CH_4 flame, which can improve the heat transfer process and then enhance the local

heat flux and the total heat transfer rate. Hence it can be concluded that the BG75 flame can show a better heating performance than that of the methane flame even though its energy input is less than that of the methane flame, which means that the BG75 is qualified to substitute methane when using the laminar premixed Bunsen flame for the impingement heat transfer.

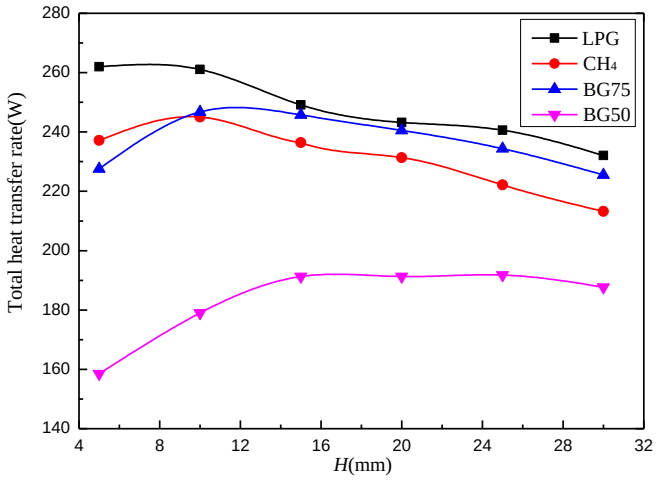

Fig. 5.9 Total heat transfer rate profiles of the laminar premixed LPG and biogas flames at ϕ=1.2, *Re*=800 and αH_2=0.1.

5.3 The correlation for the optimal heating distance

For the flame impingement heating process, the heating performance is concerned with the heat transfer process and the combustion process. This means that the optimal heating distance of the impinging flame can be affected by various parameters including fuel composition, equivalence ratio and flow rate. It is thus manifest that a correlation to describe the optimal heating distance is difficult to derive theoretically due to the complex influences of combustion process and heat transfer process. By contrast, an empirical correlation can be obtained more easily based on the experimental data and provide a reasonable accuracy for the practical utilization. Hence, an empirical correlation is expected to be obtained based on our data so as to

predict the optimal heating distance. It is known that the optimal heating distance has a close relationship with the flame height which is determined by the flow rate and laminar burning velocity. Furthermore, equivalence ratio is a critical parameter of the combustion process, which can dominate the practical flame structure and then affect heat fluxes in the wall jet region. Thus equivalence ratio can also affect the optimal heating distance. As a result, an empirical correlation is expected be derived as a function of these parameters. Before deriving the empirical correlation, effects of these parameters on the heating performance need to be discussed firstly.

5.3.1 Effects of nozzle-plate distance

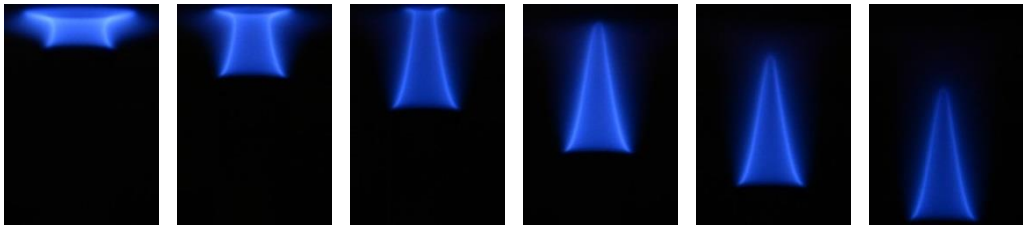

Fig. 5.10 Premixed BG75 impinging flame at ϕ=1.0, αH_2=0.1, *Re*=1000 under different nozzle-plate distances.

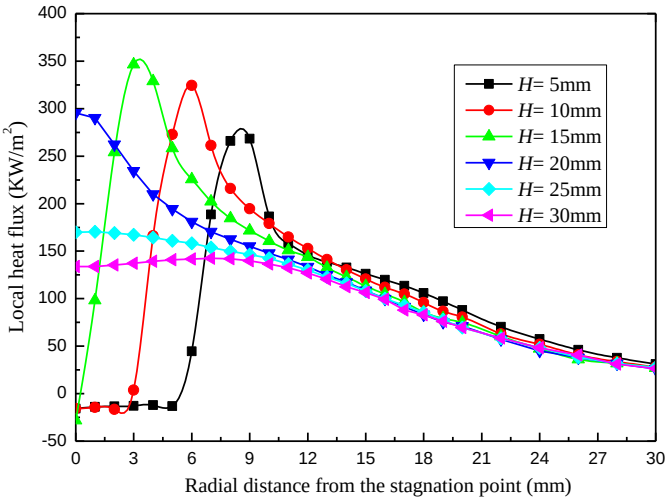

Fig. 5.11 Radial heat flux profiles of the premixed BG75 flame at ϕ=1.0, αH_2=0.1, *Re*=1000 under different nozzle-plate distances.

Fig. 5.10 shows the flame structures of BG75 premixed Bunsen flame with hydrogen enrichment at different nozzle-plate distances. Due to the strong dependence of the local heat flux on the flame structure, the effects of nozzle-plate distance on local heat flux will be discussed combined with the flame structure shown in Fig. 5.10. The measured local heat fluxes of BG75-hydrogen flames at different *H* are illustrated in Fig. 5.11. At *H*=5mm, the heat flux within around 5mm radial distance is lower than zero as a result of the presence of cool core. The temperature of unburned gases is lower than that of copper plate, which leads to the negative heat flux within this region. Around this cool core, the combustion process occurs and flame surface establishes. Therefore, the heat flux increases rapidly with the increase in radial distance until reaching to its maximum. It is noted that this peak value occurs at approximate 9mm away from the stagnation point while the flame surface establishes at about 7.6mm which is measured using the digital image of the impinging flame. The reason for this is that the maximum temperature is approached in the burned zone rather than at the flame surface (the luminous reaction zone) [267]. With the continuous increase in radial distance, there is a steady decline of the local heat flux due to the cooling effect of environmental air. Until *H* increases to 15mm, the profiles of the local heat flux still show similar trends with that of *H*=5mm. However, the peak value of heat flux rises from 289 to 348 kW/m^2 with its position moving towards the stagnation point. These variations are still dependent on the changes of flame structure shown in Fig. 5.10. Particularly, the enhanced heat flux can be attributed to the more intensive forced convection. Due to the reduced cool core, the loss in momentum and energy induced by the boundary layer effect decreases. In addition, the large amounts of reactive species existing at the flame tip enhance the convection by their diffusion and exothermic recombination on the impingement surface. Then the forced convection,

which is considered as the main mechanism of impinging heat transfer [204], is gradually strengthened in the wall jet region, leading to the rising local heat flux. Apart from this, the local heat flux slightly reduces in the wall jet region when *H* increases. This might be caused by that the position of maximum heat flux shifts outward at the smaller *H* and the decay rate of the heat flux in the wall jet region is almost the same[231].

When *H* exceeds 15mm, due to the absence of the cool core and more ambient air entrainment in the stagnation region, the maximum heat flux occurs at the stagnation point and steadily declines with the increased *H*. In addition, at larger *H*, the flame surface is well established far away from the plate, which allows forming the plug flow of burned gases. The plug flow of burned gases has the more uniform temperature and velocity distributions along the radial direction, leading to the relatively uniform radial distribution of the local heat flux at larger *H* shown in Fig. 5.11. However, it is interesting that the position of the maximum local heat flux shifts away from the stagnation point at *H*= 30mm. A possible explanation for this is that preferential diffusion is enhanced by the strong negative stretch effect at the flame tip, which leads to the stronger diffusion of unburned fuel there than that at other positions along the flame front [267]. This could bring about the weakened combustion and much lower temperature along the central axis. A little unburned fuel might diffuse to burned zone from the flame tip and would be further prohibited to react with ambient air by the surrounding burned gases. Furthermore, the burned gases flow sideways due to the acceleration of the velocity component normal to the flame front after expansion, which can cause a dip in the velocity field above the flame tip[232]. Hence, the local heat flux is a bit lower at the stagnation point. This effect is insignificant at

smaller *H* due to the more intense impingement at the plate which can effectively promote the mass and heat exchange.

5.3.2 Effects of flame jet Reynolds number

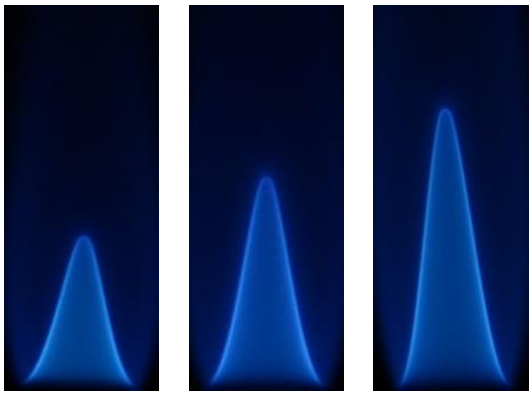

Re = 600 *Re* = 800 *Re* = 1000

Fig. 5.12 Premixed BG75 Bunsen flame at ϕ=1.2 and αH_2=0.1 under different flame jet Reynolds number.

The images of premixed BG75 Bunsen flames at ϕ=1.2 and αH_2=0.1 under three flame jet Reynolds numbers are illustrated in Fig. 5.12. Since the unburned mixture and nozzle diameter are both unchanged, according to the definition of Reynolds number, the larger flame jet Reynolds number means the higher outlet velocity. Hence the investigation on effects of flame jet Reynolds number can be reduced to study effects of the averaged outlet velocity of unburned mixture in this study. It is observed that the flame is composed of the blue inner premixed combustion zone and a nonluminous diffusive combustion zone. In addition, the flame height increases gradually with the enhancement in flame jet Reynolds numbers, which can be attributed to the constant laminar burning velocity and the increased outlet velocity of the unburned mixture at the nozzle exit. The radial distributions of local heat fluxes at different flame jet Reynolds numbers are given in Fig. 5.13. It can be seen that, at *H*=10mm, the local heat fluxes of all the flames at the stagnation point are less than zero as a result of the presence of the cool core. With the increase in flame jet

Reynolds number, the peak heat flux rises gradually and its position shifts away from the stagnation point while the local heat fluxes are still larger within the wall jet region. Due to the increased flame height, at the same *H*, the position of flame surface attaching the plate shifts away from the stagnation point, leading to the outward shift of peak heat flux position. In addition, the increased outlet velocity can effectively promote the forced convection in the stagnation region and wall jet region, which can lead to the rise in maximum heat flux and the higher heat fluxes in the wall jet region. With the increase in *H*, the heat flux in the stagnation region evidently increases because of the absence of cool core, and the stronger forced convection induced by the larger outlet velocity leads to the higher heat flux in both stagnation region and wall jet region. It is noted that the maximum heat flux at *H*=30mm reduces by approximate 50% compared to that at *H*=10mm, which is the result of cool ambient air entrainment. In addition, due to the most intensive ambient air entrainment and the relatively weak forced convection, the heat flux value of *Re*=600 is the lowest.

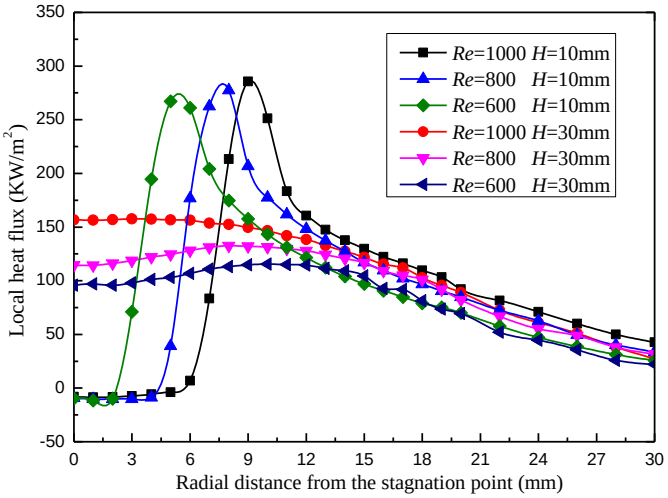

Fig. 5.13 Radial heat flux profiles of the premixed BG75 flames at αH_2=0.1 and ϕ=1.2 under different flame jet Reynolds number.

The total transfer rate, which can be affected by various parameters, such as Reynolds number, equivalence ratio and nozzle-plate distance, can be considered as one of the

most significant parameters to evaluate the heating efficiency of an impinging flame. The analysis on the total heat transfer rate can help to understand the fuel characteristics and provide useful information to improve its practical applications. The comparison of total transfer rate of BG75-hydrogen flames at different flame jet Reynolds number is shown in Fig. 5.14. Obviously, the total transfer rate increases dramatically with the rise in flame jet Reynolds number in the whole range of *H*. The maximum value of total transfer rate rises from 214 to 269 W, which is caused by the stronger forced convection and the more energy input as the outlet velocity increases. According to the Equation 3-3, if the local heat flux keeps constant, the total transfer rate of the annular heating area would increase evidently with the increase in the radius, which implies the relatively small heat flux in the wall jet region can still contribute to a considerable part of total transfer rate while the contribution of heat flux at small radius would be less significant. Thus, at small *H*, though the flame with higher outlet velocity has a bit larger area of cool core, its higher local heat flux in the wall jet region can still dominates and then leads to the increasing trends of total heat transfer rate. Meanwhile, at large *H*, in addition to the main reason of stronger forced convection and more energy input, the boosted flame height due to the larger outlet velocity can make the burned gases to suffer less cooling effect of the ambient air entrainment, which results in the higher value of total transfer rate. For the flame with a constant flame jet Reynolds number, the peak total transfer rate occurs at an appropriate *H*. The main reasons for the declines of total heat transfer rate at small and large *H* are the occurrence of cool core and the increasing ambient air entrainment, respectively. The cool core can directly reduce the heating area, and the increasing ambient air entrainment can reduce the temperature of burned gases in the stagnation region.

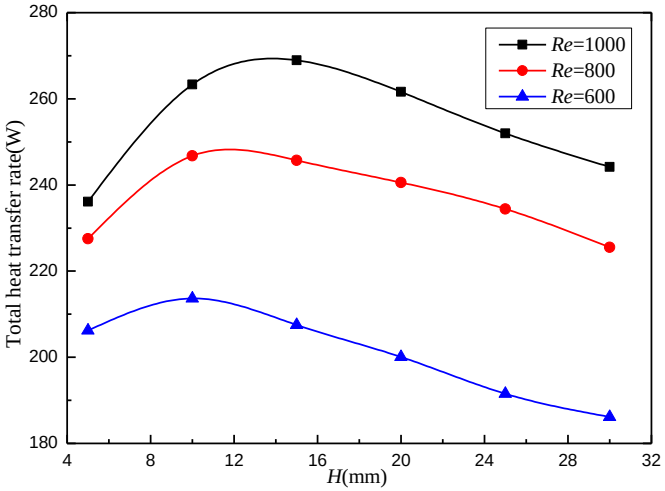

Fig. 5.14 Total heat transfer rate of the premixed BG75 flames at ϕ=1.2 and αH_2=0.1 under different flame jet Reynolds number.

5.3.3 Effects of equivalence ratio

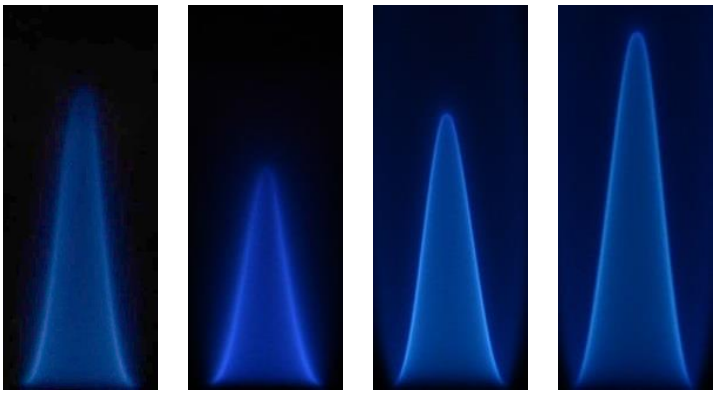

ϕ = 0.8 ϕ = 1.0 ϕ = 1.2 ϕ = 1.4

Fig. 5.15 Premixed BG75 Bunsen flame with different equivalence ratios at αH_2=0.1 and *Re*=1000.

The images of BG75-hydrogen premixed Bunsen flames at four equivalence ratio are given in Fig. 5.15. From lean to rich condition, flame becomes much brighter as a result of the more intensive combustion along the flame surface, and the flame height also changes evidently due to the different flame speed at these four conditions. With the same flame jet Reynolds number, the velocity at the nozzle exit is almost constant for all conditions, meaning that the flame speed would dominate the change of flame height. As shown in Fig. 5.16, the flame at stoichiometric condition has the minimum

flame height but the highest laminar burning velocity with the value of around 32cm/s. Since the laminar burning velocity S_L can be determined by the formation $S_L=u\cdot\sin(\alpha/2)$ when using the Bunsen flame method, therefore, according to the formation, the higher laminar burning velocity S_L would lead to the larger flame tip angle α when the average outlet velocity u keeps constant. Furthermore, with the same nozzle diameter, the larger α means the lower flame height. Hence, the flame at stoichiometric condition has the lowest flame height than that at either lean or rich condition as shown in Fig. 5.16.

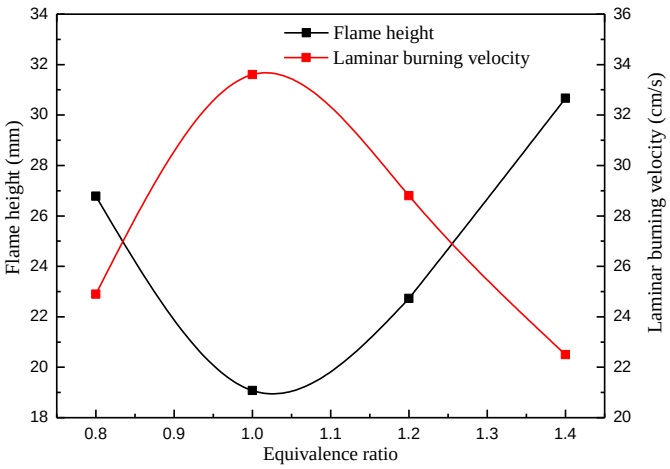

Fig. 5.16 Flame height and laminar burning velocity of the premixed BG75 Bunsen flames with different equivalence ratios at αH_2=0.1 and *Re*=1000.

The radial heat fluxes of BG75-hydrogen flames at different ϕ are given in Fig. 5.17. At *H*=10mm, the maximum heat flux at ϕ = 0.8 is the minimum with the value of 196 kW/m^2 while that at ϕ = 1.0 has the highest value of 324 kW/m^2. This discrepancy is mainly caused by the different flame temperatures at these four conditions. The flame temperature at ϕ = 1.0 is highest due to the more complete combustion, and the flame temperature at ϕ = 1.2 ranks second. Though the adiabatic flame temperatures at ϕ = 0.8 and ϕ = 1.4 is almost the same, flame at rich condition is composed of premixed zone and diffusive zone, meaning that the diffusive combustion can maintain or even

enhance the real temperature of the burned gases. Therefore, the flame at ϕ = 0.8 has the minimum value of the peak heat flux, and its local heat flux in the wall jet region is also minimum. In general, the higher flame height, the further position of peak heat flux is from the stagnation point. However, though the flame height at ϕ = 1.2 is about 4mm lower than that at ϕ = 0.8 according to Fig. 5.16, the maximum heat flux position at ϕ = 1.2 is same as that at ϕ = 0.8. This might be the result of preferential diffusion and negative stretch effect at the flame tip. The local equivalence ratio can be reduced by the combined effect of preferential diffusion and negative stretch rate at the tip of Bunsen premixed flame [267]. This reduction for lean/rich condition can lead to the weakened/intensive combustion process at the flame tip than that of other positions along the flame front, resulting in the reduction/enhancement of temperature at the flame tip. It is noted that, due to the high diffusivity of hydrogen, the biogas-hydrogen flame would suffer stronger effect of preferential diffusion at the flame tip. Thus, for the impinging flame at ϕ = 0.8, its highest heat flux might occur at smaller radius where the higher flame temperature is located, though there exists a thin layer of unburned gases between the plate and the flame surface. Meanwhile, for the flame at ϕ = 1.2, the higher temperature at the flame tip combined with the diffusive combustion might lead to the slightly outward shift of the maximum heat flux position. As a result, the peak heat flux position at ϕ = 1.2 is just equal to that at ϕ = 0.8 in this study. At *H*=30mm, due to the highest flame height at ϕ = 1.4, its heat flux at the stagnation point is maximum, while the heat flux at ϕ = 1.0 is minimum because of its shortest flame height. With the flame just touching the copper plate, peak heat flux at ϕ = 1.4 occurs at about 3mm away from the stagnation point. Though there is a small cool core at this condition, the area is so small that few unburned gases touching the plate would be heated by the high temperature around the cool core, leading to the

non-zero heat flux at the stagnation point. The diffusive combustion results in the higher heat flux in wall jet region for the rich flame. For the flame at ϕ = 1.0, its value can maintain a stable and higher level in the wall jet region compared to that at ϕ = 0.8. This can be attributed to the excess air in the unburned mixture at ϕ = 0.8, which can effectively cool down the burned gases and then lead to a rapid and evident decline of the heat flux in the wall jet region.

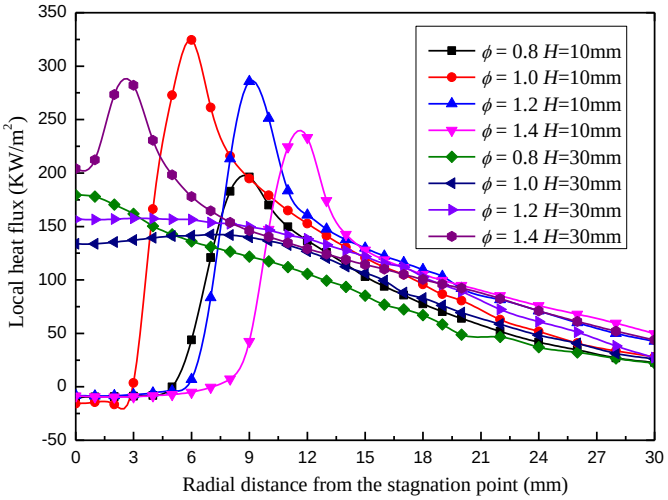

Fig. 5.17 Radial heat flux profiles of the premixed BG75 flames with different equivalence ratios at αH_2=0.1 and Re=1000.

Fig. 5.18 compares the total heat transfer rate of BG75-hydrogen flames at different equivalence ratios. As shown in Fig. 5.18, the total transfer rate at ϕ = 0.8, 1.0 or 1.2 shows a downward trend at either small or large H but that at ϕ = 1.4, which has a high flame, does so only marginally. The reasons for these declines have been explained in the previous paragraph. Additionally, it is obvious that the total transfer rate at ϕ = 0.8 is consistently lowest at all H, resulting from its lowest flame temperature and excess air. At H=5mm, the flame at ϕ = 1.0 has the maximum total transfer rate due to its highest temperature and larger effective heating area compared to that at ϕ = 1.2 and ϕ = 1.4. With the increase in H, the diffusive combustion

gradually plays a more significant role in promoting the total heat transfer rate. With the reduction of cool core area, its negative effect is weakened dramatically. Additionally, because of the diffusive combustion at rich conditions, the higher heat fluxes at large radii can significantly enhance the total transfer rate. Therefore, the flame at rich conditions can maintain a higher heating level in a quite wide range of *H*. Contrarily, the total heat transfer rate of the flame at ϕ = 1.0, which hardly has the diffusive combustion, drops rapidly with the increase in *H*. This is caused by its lower local heat fluxes in the wall jet region, which can be attributed to the cooling effect of ambient air entrainment. From above, it can be concluded that the flame under rich conditions can provide a relatively high level of total transfer rate within a wide range of nozzle-plate distance.

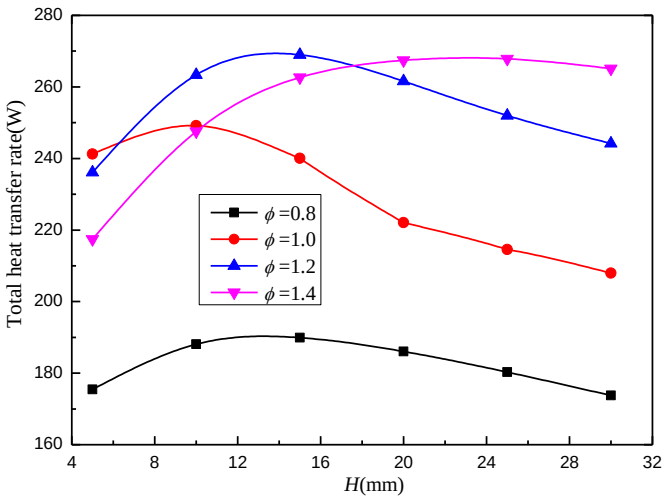

Fig. 5.18 Total heat transfer rate of the premixed BG75 flames with different equivalence ratios at αH_2=0.1 and *Re*=1000.

5.3.4 The correlation of optimal impinging heating distance

In the previous study, Hou et al. [209] qualitatively suggested that the optimal heating distance of the laminar premixed Bunsen flame is slightly less than the flame height. However, based on the above discussion, we found that the optimal heating distance is

considerably lower than the flame height and it has a nonlinear relationship with the flame height. It is thus known that the empirical correlation of the optimal heating distances can be quite useful to predict the heating distance more precisely and figure out how it is influenced by various parameters. Based on the experimental data, the nondimensional correlation of the optimal heating distance was obtained as a function of *Pr*, u/S_L and ϕ by using the multiple regression method. Apart from u/S_L and ϕ, *Pr* is also considered in the correlation because it is a dimensionless number that reflects the effects of fluid physical properties on the convection heat transfer process. The empirical correlation is expressed as follows:

$$H_m / D = 1.2152 Pr^{0.4} \left(\frac{u}{S_L}\right)^{0.6575} \left(\phi^3 \left|\frac{1}{2} - \frac{\phi}{\phi+1}\right| + \frac{1}{2}\right)^{1.52386} \quad (3.7 < u/S_L < 7.8,\ 0.8 < \phi < 1.4) \qquad \text{Equation 5-2}$$

where H_m denotes the nozzle-plate distance at which the flame has the maximum total transfer rate, and *D*, *u* and S_L represent the inner diameter of the nozzle, average outlet velocity and non-stretch laminar burning velocity, respectively. Additionally, the dependences of u/S_L and ϕ are obtained based on the experimental data, while the *Pr* dependence is adopted from Remie's work [230]. The comparison of experimental data and calculated results are shown in Fig. 5.19. It can be seen that this correlation agrees well with the experimental data in this study, the discrepancy between experimental and calculation data is less than 10% as shown in Fig. 5.19(c). This means that the correlation can be used to predict the optimal nozzle-plate distance of impinging laminar premixed Bunsen flame with a reasonable accuracy. Besides, it is manifest that the optimal distance has a positive relationship with the outlet velocity *u* and a negative relationship with the laminar burning velocity S_L, and it would be enhanced at either lean or rich condition with the different increasing rates depending on the corresponding equivalence ratios. Specifically, the rich condition can promote

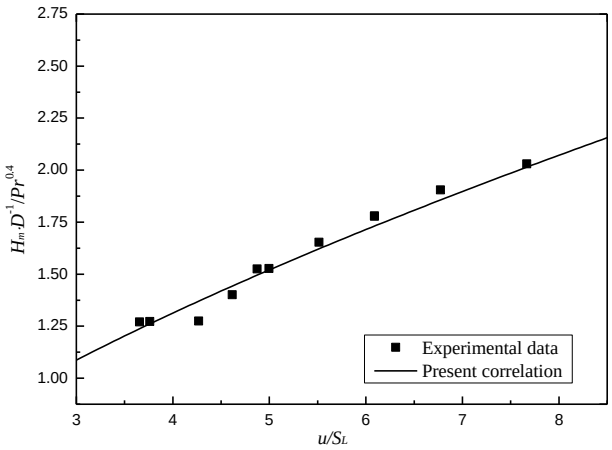

(a) Dependence of the correlation on u/S_L

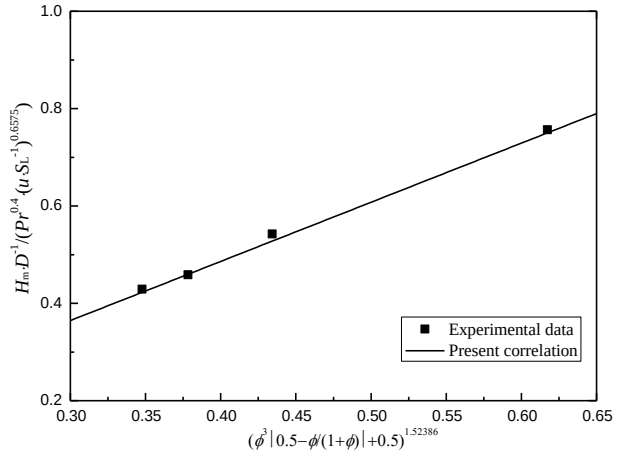

(b) Dependence of the correlation on ϕ

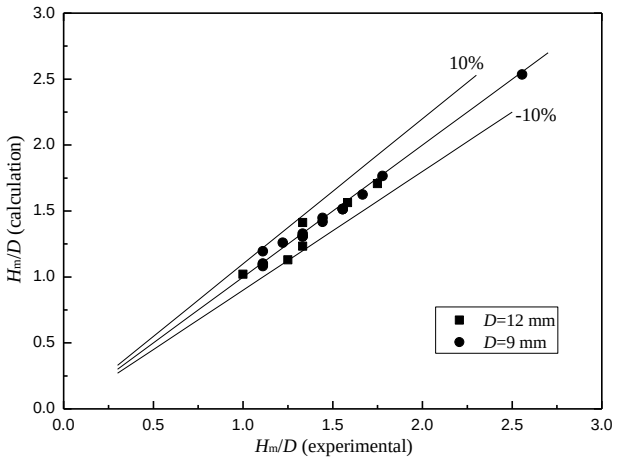

(c) Agreement of H_m/D between experimental data and the correlation for current investigated parameter range ($3.7< u/S_L<7.7$, $0.8<\phi<1.4$)

Fig. 5.19 The correlation of the optimal heating distance.

the increasing rate due to the diffusive combustion while the lean condition can impede it because of the excess air. In conclusion, it is expected that this empirical correlation can facilitate to choose the best heating distance of laminar premixed Bunsen flame more reasonably and precisely.

5.4 Summary

Experiments were conducted to investigate the heat transfer characteristics of laminar premixed biogas-hydrogen flames with different H_2 fractions and CO_2 fractions while an empirical correlation to predict its optimal heating distance was obtained. The heat fluxes and temperature distributions of biogas-hydrogen flames were measured experimentally. The total transfer rates were calculated based on the measured heat fluxes. Effects of H_2 and CO_2 compositions on the heat transfer characteristics of laminar premixed biogas-hydrogen flames were analyzed quantitatively. In order to derive the correlation of the optimal heating distance, effects of nozzle-to-plate distance, Reynolds number and equivalence ratio were also discussed. The following results were obtained:

With the increased H_2, the total heat transfer rate of biogas-hydrogen impinging flame can be enhanced by up to 50%. Besides, the optimum hydrogen addition of the BG75 flame is recommended to be αH_2=0.3 based on our work, which can exert approximately 20%-30% improvement on total heat transfer rates at all tested heating distances. The hydrogen enrichment can promote the heating performance by the higher flame temperature and the stronger fuel diffusivity. The higher temperature can improve heat transfer process directly with the larger temperature difference. Meanwhile, the strong diffusivity of hydrogen can result in a wider high temperature

zone which leads to effective and efficient improvement on the heat transfer process in the wall jet region.

The influences of CO_2 on the flame impingement heating can be exerted through the chemical effects and dilution/thermal effects. Its reactivity exerts suppressions on the CO oxidization by accelerating the backward reaction of $OH+CO=CO_2+H$ while the large amount of CO_2 in the fuel can decrease the proportion of combustible fuel and then result in the evidently reduced heat release. Furthermore, the flame temperature can be further decreased by its larger specific heat capacity. However, a suitable proportion of CO_2 in the biogas can decrease the declining rate of flame temperature in the wall jet region, which is resulted from its larger specific heat capacity, as well as the less air entrainment owing to the increased flame height. This leads to the better heating performance of BG75-hydrogen flame than that of the methane-hydrogen flame. Hence, BG75-hydrogen is eligible to replace methane-hydrogen for heating purpose when using the laminar premixed Bunsen flame.

Based on the experimental data, an empirical correlation to determine the optimal heating distance of biogas-hydrogen flames has been obtained as a function of *Pr*, u/S_L and ϕ:

$$H_m / D = 1.2152 Pr^{0.4} \left(\frac{u}{S_L}\right)^{0.6575} \left(\phi^3 \left|\frac{1}{2} - \frac{\phi}{\phi+1}\right| + \frac{1}{2}\right)^{1.52386} \quad (3.7 < u/S_L < 7.7,\ 0.8 < \phi < 1.4)$$

This correlation is able to predict the optimal heating distance of the laminar premixed biogas-hydrogen flame with the satisfactory accuracy.

6 Pollutant emissions of laminar premixed biogas-hydrogen impinging flame

6.1 Introduction

The measured pollutant emissions of laminar premixed biogas-hydrogen flames are investigated in this chapter [268]. The total emissions (NO, NOx, CO and CO_2) of biogas-hydrogen flames were measured experimentally at various conditions, and the emission indexes (EINOx, EICO and $EINO_2$) were calculated based on the measured data. The NO_2/NOx ratio was also obtained in order to investigate the NO_2 formation process at the impingement condition. In order to facilitate the analysis on the process of emission formation, a computational model was developed to calculate the biogas-hydrogen impinging flames at the same experimental conditions. More information, such as flow fields and distributions of critical intermediates, was obtained in the simulation, which can facilitate the investigation on the CO formation and oxidization process. In addition, using the numerical simulation, NO amount formed via four major mechanisms (thermal NO, prompt NO, NNH route and N_2O route) were isolated and the contributions of these routes were also obtained in the simulation. With the experimental and numerical data, the effects of impingement on the EICO, EINOx, $EINO_2$ and the NO_2/NOx ratio of biogas-hydrogen flames will be discussed quantitatively, and the contribution variations of four NO routes with the separated distance will be also investigated. Apart from this, effects of equivalence ratio, Reynolds number, hydrogen addition and CO_2 proportion on pollutant emissions of biogas-hydrogen flames will be also studied quantitatively.

6.2 Effects of separated distance and equivalence ratio on pollutant emissions

6.2.1 Effects of separated distance and equivalence ratio on EICO

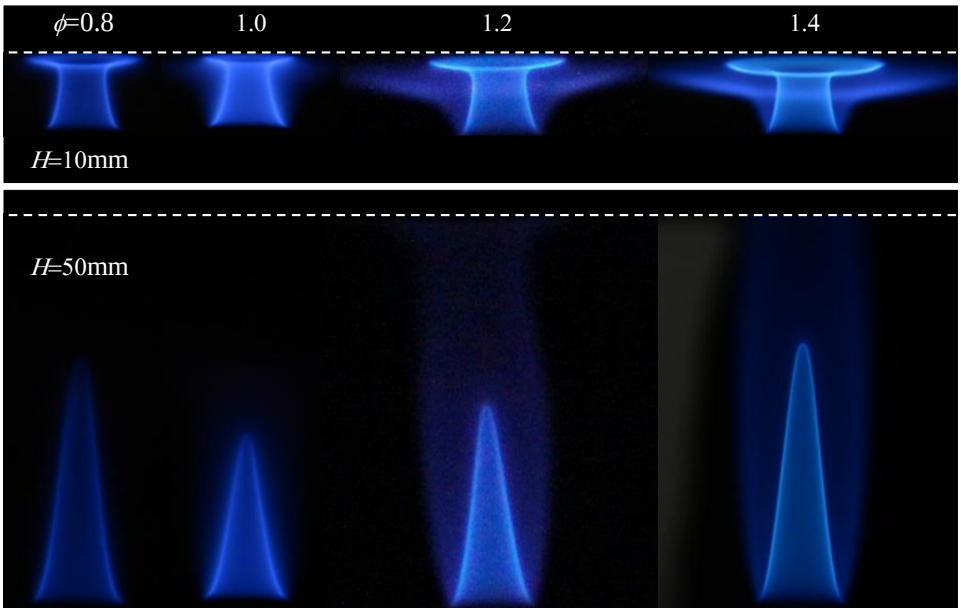

Fig. 6.1 Premixed BG75 flames with different equivalence ratio at *Re*=1000 and αH_2=0.1.

The images of the impinging premixed BG75 flame at *Re*=1000 and αH_2=0.1 under different equivalence ratios are illustrated in Fig. 6.1 while the measured EICO of these flames are illustrated in Fig. 6.2. It can be seen that the EICO variation with separated distance is similar at different equivalence ratio, which shows an increasing trend initially and then a progressive decline at large *H*. This variation can be explained as follows. At small *H*, the impingement plate can affect the premixed combustion zone directly as shown in Fig. 6.1, which can lead to the weakened combustion intensity near the plate surface and then the reduced CO production in that region. In order to confirm this, the calculated CO distribution and the intermediates related to its production and oxidization at ϕ=1.0 and *H*=10mm are illustrated in Fig. 6.3. It is observed that the HCO concentration is decreased evidently near the cooling

plate surface. Since the HCO intermediate is an excellent indicator of the premixed combustion intensity due to its close relation with the heat release rate [189], its distribution shown in Fig. 6.3 confirms the weakened premixed combustion attaching the plate surface. Furthermore, HCO is an important contributor for the CO production, thus its lower concentration near the plate surface due to the weakened premixed combustion contributes to the lower CO concentration in the post flame region near the plate surface as shown in Fig. 6.3. Hence, it is concluded that the cooling plate can weaken the premixed combustion significantly and then suppresses the fuel oxidization and CO generation at small *H*. Besides, CO oxidization depends heavily on OH radical in the flame. As shown in Fig. 6.3, due to the weakened premixed combustion and low temperature of the plate, the OH concentration also becomes quite low near the plate surface. This means that there exists a cool gas layer allowing CO to bypass the OH cloud and contributing to the increased CO emission. As *H* is increased, the reduced cool core can lead to the improved premixed combustion, which leads to the improved fuel oxidization and then enhance the CO production effectively. Furthermore, the cool gas layer along the plate surface can facilitate the CO escape to suppress its oxidization. Therefore, EICO shows the rising trends before the establishment of complete flame front. As *H* is further increased, the conical flame front is no longer influenced by the cooling plate as shown in Fig. 6.1, which means that the CO formation process become stable and OH distribution in the post flame region becomes uniform. At this condition, the CO oxidation process can be promoted efficiently due to the extended high temperature region, the more intensive air entrainment and the longer residence time at large *H*. As a result, the EICO is decreased steadily at large *H*.

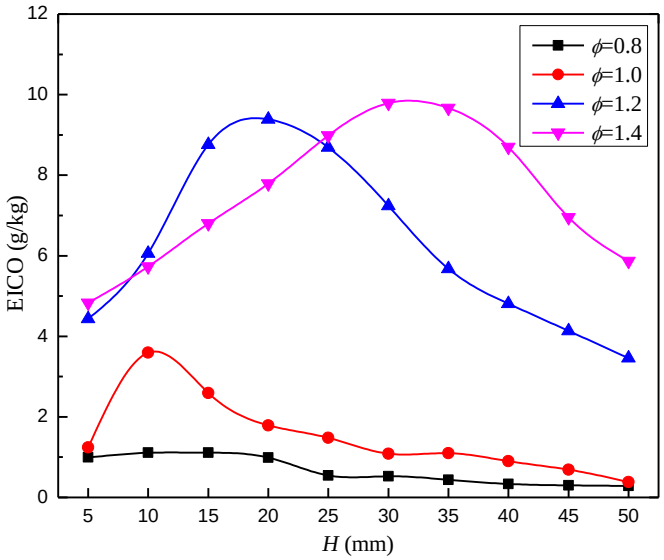

Fig. 6.2 EICO of laminar premixed BG75 impinging flames at αH_2=0.1 and *Re*=1000.

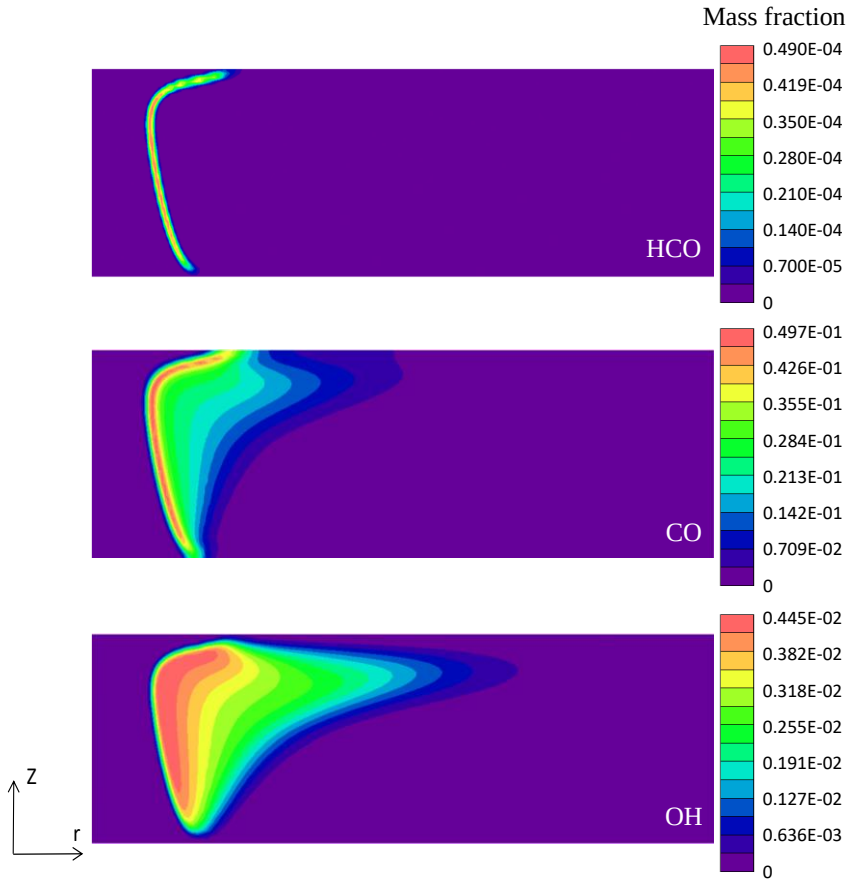

Fig. 6.3 HCO, CO and OH distributions of premixed BG75 flames at ϕ=1.0, αH_2=0.1, *Re*=1000 and *H*=10mm.

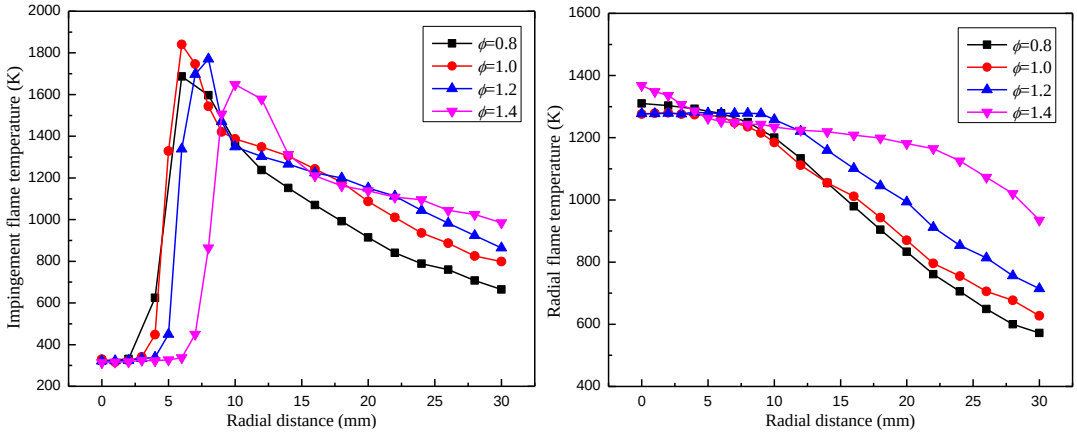

(a) H=10mm (b) H=50mm

Fig. 6.4 Measured impinging flame temperature distributions of premixed BG75 flames with different equivalence ratios at Re=1000 and αH_2=0.1.

With the increased equivalence ratio, there exists a rising trend of EICO as shown in Fig. 6.2, which can be attributed to the obviously increased fuel proportion and then the more severe incomplete fuel oxidization. It is known that the sufficient O_2 in the unburned gases results in the quite low CO emission at ϕ=0.8. However, it is noted that EICO at ϕ=0.8 becomes higher when its flame front is affected by the impingement plate. The reason is that although O_2 is sufficient in the flame, the impingement plate can cool down the burned gases effectively as shown in Fig. 6.4. Thus the CO oxidization process can be suppressed in the burned gases because it requires a high temperature to proceed. Besides, it can be seen that the rising rate of EICO at ϕ=1.2 is decreased compared with that at ϕ=1.0. With the increased H, although the fuel oxidization is improved for the flame at ϕ=1.2, the insufficient O_2 in the unburned gases, as well as its relatively lower flame temperature, can exert a suppression on the CO formation process, leading to its reduced rising rate of EICO. Furthermore, due to the further reduced O_2 amount and flame temperature, the further decreased rising rate of EICO can be observed for the flame at ϕ=1.4 in Fig. 6.2. For the maximum EICO, the evident increasing trend from ϕ=0.8 to 1.2 is dominated by

the enhanced CO production; however, when ϕ is larger than 1.2, the seriously insufficient O_2 can inhibit the CO production, which can then suppresses the CO production and eventually results in the slight increase of EICO.

6.2.2 Effects of separated distance and equivalence ratio on EINOx

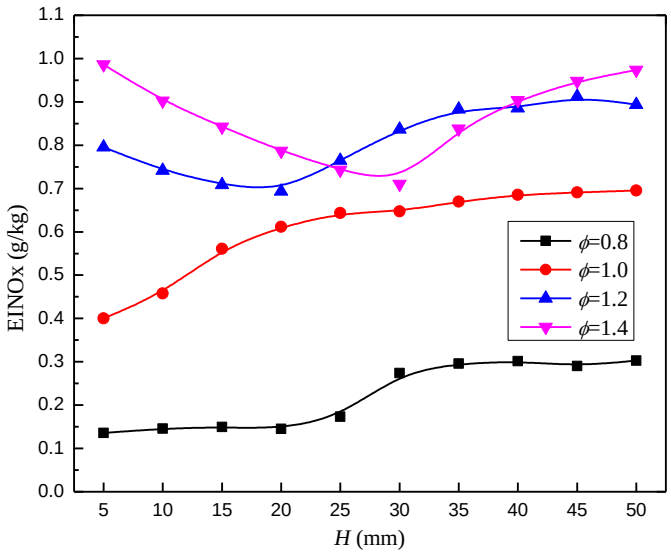

Fig. 6.5 EINOx of laminar premixed BG75 impinging flames at αH_2=0.1 and *Re*=1000.

The measured EINOx of BG75 flames at *Re*=1000 and αH_2=0.1 under different equivalence ratios are compared in Fig. 6.5 while the calculated NO amounts generated via different routes (thermal NO, prompt NO, N_2O route and NNH route) and the variations of their contributions are illustrated in Fig. 6.6 and Fig. 6.7. It can be seen that the NOx emissions of flames at ϕ=0.8 and 1.0 show the monotonous increase with the increased *H*, but the EINOx at fuel-rich condition is decreased initially and then is enhanced to its maximum. These variations can be explained by considering the NO formation via different routes. As shown in Fig. 6.6, the NO amounts of thermal and N_2O routes are both enhanced evidently with the increased *H*. By contrast, NO formed through the NNH route is increased quite slightly. Besides, it can be noted that, with the increased *H*, the prompt NO is increased slightly at the

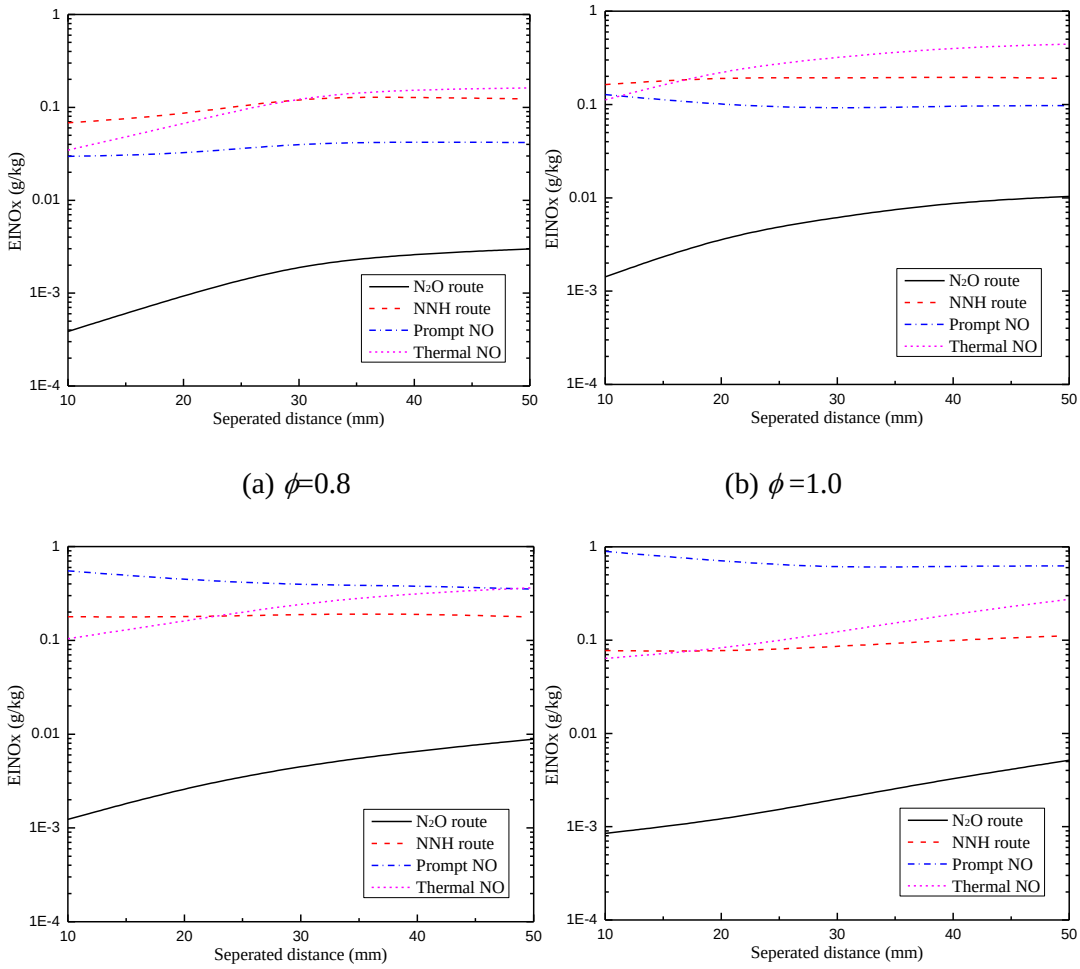

(a) ϕ=0.8 (b) ϕ=1.0

(c) ϕ=1.2 (d) ϕ=1.4

Fig. 6.6 NO formed via different routes of the laminar premixed BG75 impinging flames at αH_2=0.1 and *Re*=1000.

fuel-lean condition but decreased at other conditions. At small *H*, the cooling plate and ambient air can reduce the temperature of burned gases effectively as shown in Fig. 6.4 while the residence time is relatively insufficient. Since the thermal and N_2O routes mainly occur in the post-flame region, the lower temperature and less residence time can suppress the NO formation via these two routes at small *H*. As *H* is increased, the extended high temperature zone, more intensive air entrainment and longer residence time can improve NO production via thermal and N_2O routes, especially for the thermal route. Hence, NO amounts of thermal and N_2O routes are enhanced steadily with the increased *H*, contributing to their enhanced contributions on NO

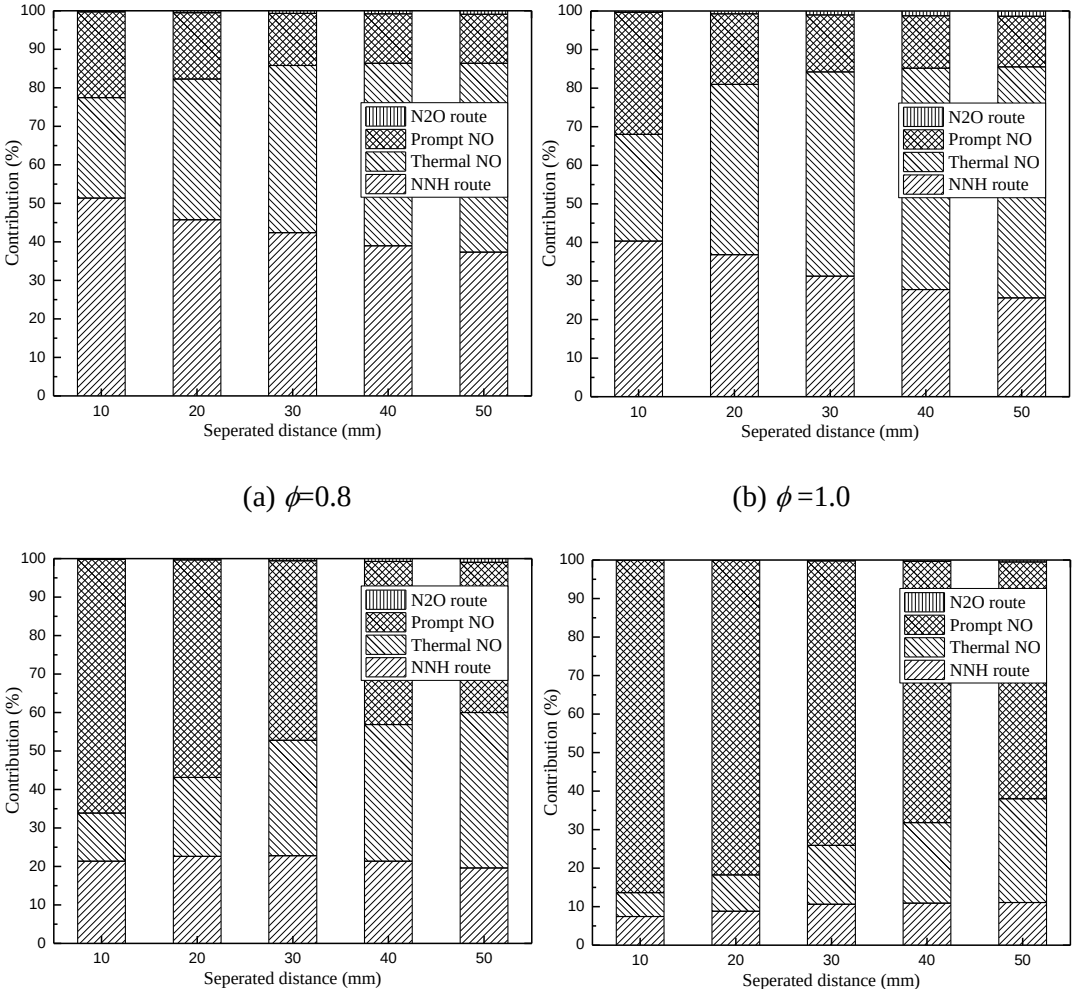

(a) ϕ=0.8 (b) ϕ =1.0

(c) ϕ=1.2 (d) ϕ =1.4

Fig. 6.7 Contributions of different routes on NO formation of the laminar premixed BG75 impinging flames at αH_2=0.1 and *Re*=1000.

formation as shown in Fig. 6.7. For the NNH route, its initiation reactions are mainly concerned with hydrocarbon-free radicals such H, OH and H_2, and the concentration of these radicals can keep a quite stable level as *H* is increased. This means that this route can maintain the stable initiation process at different separated *H*. Consequently, at large *H*, the extended high temperature region, more intensive air entrainment and longer residence time can exert limited improvements on NNH route due to the limit of its stable initiation process and finally result in the moderate increase of its NO production as shown Fig. 6.6. Furthermore, as shown in Fig. 6.7, with the increased *H*, it is known that the decreased contribution of NNH route on NO formation at ϕ=0.8

and 1.0 is caused by its relatively stable production and the steadily increased total EINOx, while its initial rising trend at fuel-rich condition can be attributed to the initial decreased total EINOx. Additionally, the prompt NO is primarily initiated by $N_2+CH=HCN+N$ and $N_2+CH_2=HCN+NH$ which primarily occur near or in the premixed combustion zone. When the flame front is affected by the impingement plate, the quenching effects on the premixed combustion process can give rise to the initiation reactions of prompt NO since fuel oxidization in the premixed combustion zone near the flame tip can be affected significantly as shown in Fig. 6.3 and then increased hydrocarbon radicals are available to react with N_2. As shown in Fig. 6.8(a), the HCN production of fuel-rich flame is improved effectively at or near the flame tip, which can be attributed to that the increased hydrocarbon radicals in that region accelerate the initiation reactions of prompt NO. Furthermore, the calculated NO distributions of SIM I and SIM II for the fuel-rich flame are given in Fig. 6.8(b). For the result of SIM I, there exists a region near the flame tip where the rising rate of NO mass fraction is apparently higher than that in other regions of the post-flame zone. Considering the HCN distribution in Fig. 6.8(a), it is known that the fast enhanced NO concentration near the flame tip is the result of the increased HCN production there. Since this phenomenon is not observed in the NO distribution of SIM II, it can be concluded that the prompt NO production is promoted effectively at small *H* because the hydrocarbon radicals are increased owing to the quenching effects of cooling plate. As *H* is increased, the effects of cooling plate on the premixed combustion is weakened, which leads to the promoted fuel oxidization and then less available hydrocarbon. As a result, the initiation process of prompt NO can be suppressed with the increased *H*, leading to the dropping trends of prompt NO at stoichiometric and fuel-rich conditions as shown in Fig. 6.6. Whereas, although the plate can affect the

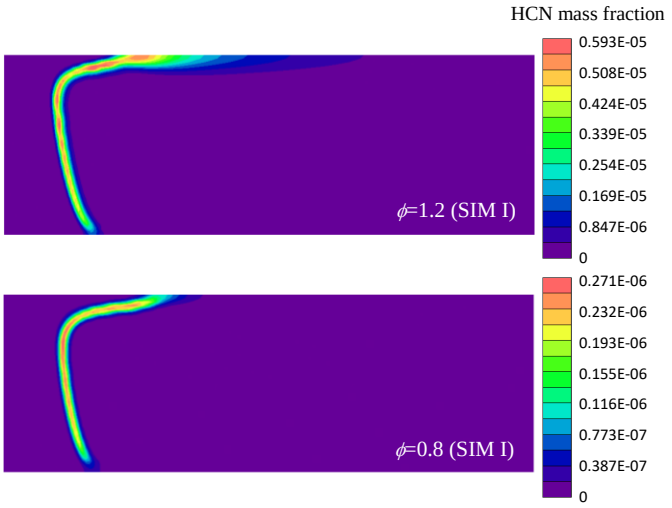

(a) HCN distribution

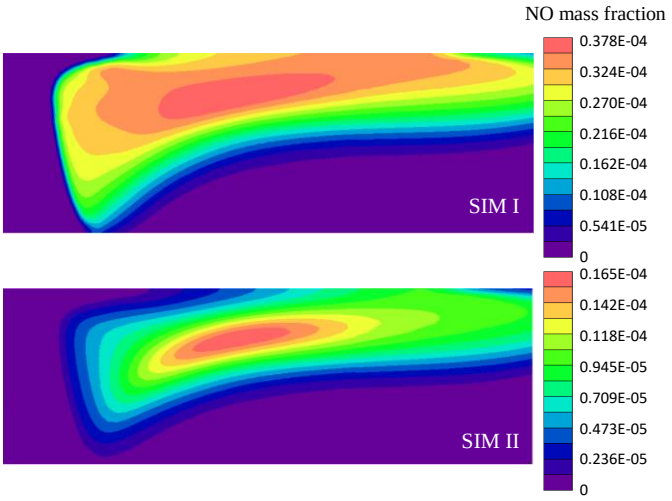

(b) NO distribution at ϕ=1.2

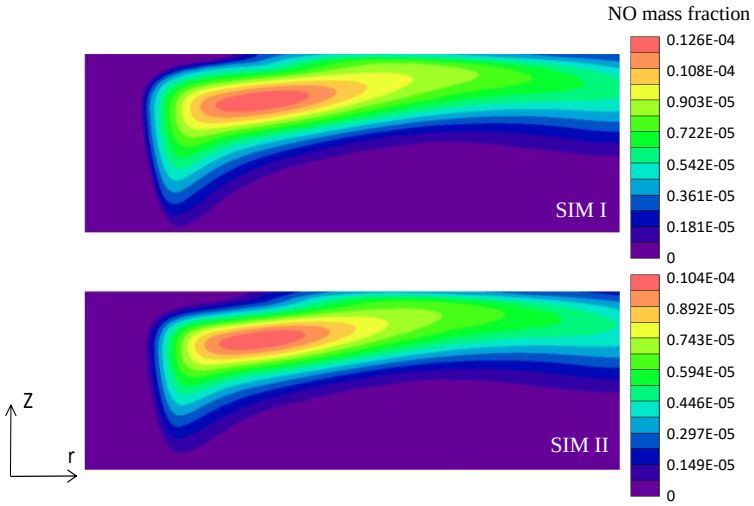

(c) NO distribution at ϕ=0.8

Fig. 6.8 Distributions of HCN and NO for BG75 flames at αH_2=0.1, H=10mm and Re=1000.

premixed combustion zone at fuel-lean condition, the sufficient O_2 in the unburned gases can still maintain a high level of fuel oxidization and reduce the possibility of reaction between hydrocarbon radicals and nitrogen. As shown in Fig. 6.8 (a) and (c), compared to that at ϕ=1.2, the HCN concentration is more uniform along the flame front at ϕ=0.8 and even declined at the flame tip while the rising rate of NO concentration in SIM I at ϕ=0.8 is not varied significantly. Thus it can be concluded that the prompt NO production of fuel-lean flame is insensitive to the effects of open flame front at small *H* owing to its sufficient oxidizer in the unburned gases. Consequently, the prompt route of fuel-lean flame is hardly influenced at small *H* and its slight improvement with *H* can be resulted from the increased temperature, intensive air mixing and longer residence time. Furthermore, it is noted that, after the establishment of the complete flame front, the concentrations of hydrocarbon radicals can keep stable in the flame. This leads to the stable initiation reactions of prompt route and then the relatively stable prompt NO production at large *H* as shown in Fig. 6.6. With the increased *H*, due to the steadily increased NO formation via other routes, the decreased prompt NO at ϕ=1.0, 1.2 and 1.4 or the moderately increased prompt NO ϕ=0.8 lead to their declined contributions as shown in Fig. 6.7.

In addition, the relative significance of different routes on NO formation is changed considerably with the equivalence ratio as shown in Fig. 6.7. Generally, with the increased equivalence ratio, the contribution of NNH route is declined with its maximum value dropping from 50.4% at ϕ=0.8 to 10.9% at ϕ=1.4 while that of prompt route is enhanced obviously to about 86.3% at ϕ=1.4. For the N_2O and thermal routes, their contributions reach their maximum at the stoichiometric condition with the peak values of around 1.4% and 59.7% respectively. In addition, it can be seen

that the thermal and NNH routes can account for approximately 70% or above of the total NO production at ϕ=0.8 and 1.0, while more than 80% of NOx emission at the fuel-rich condition are generated via the prompt and thermal routes. From fuel-lean to fuel-rich condition, the NO amount formed through NNH route is relatively stable, which shows a slight increase from ϕ=0.8 to ϕ=1.0 and then drops back to a similar level of fuel-lean flame as ϕ is increased to ϕ=1.4. Since NH and NNH radicals are mainly generated near the premixed combustion zone, the initiation process of NNH route can be influenced by the temperature variation at different ϕ. Although the concentration of H atom is much higher at fuel-rich condition, its improvement on initiation process is restrained by the lower flame temperature. Therefore, the NO amount of NNH route is highest at ϕ=1.0 due to its highest flame temperature and drops at other equivalence ratios due to the declined flame temperature as shown in Fig. 6.6. Considering the increased total EINOx, the relatively stable NO production of NNH route makes it suffer a declined contribution on NO formation. Besides, the fuel concentration is increased with ϕ, which can give rise to the prompt NO formation effectively. This leads to the apparent rising trend of prompt NO amount and its increased contribution on total NO formation as shown in Fig. 6.6 and Fig. 6.7. Since thermal route is predominated by the flame temperature, it is not surprise that the thermal NO amount and its contribution on NO formation are maximum at ϕ=1.0 as shown in Fig. 6.6 and Fig. 6.7. For the N_2O route, its decreased amount of NO at fuel-rich condition shown in Fig. 6.6 is resulted from the evident reductions in O atom concentration and the flame temperature. Additionally, compared to other conditions, the maximum flame temperature, which can improve the NO production process, gives rise to the peak NO amount of N_2O route at ϕ=1.0. Based on the above discussion, it is known that, as ϕ is increased, the variation of major contributors on

NO formation is primarily caused by the increased fuel concentration which can promote the prompt NO production efficiently, as well as the flame temperature which can affect the thermal NO formation significantly.

For the total EINOx variation, the increasing trend of EINOx with *H* for the flame at ϕ=0.8 shown in Fig. 6.5 is caused by the increase in all NO formation routes shown in Fig. 6.6. Besides, at stoichiometric condition, the prompt route contributes much less proportion of NO formation compared to that at fuel-rich condition while the thermal NO plays an increasingly important role in NO formation as shown in Fig. 6.7. Therefore, although the prompt NO amount is reduced with the *H*, this reduction can be compensated by the obviously enhanced thermal NO which finally dominates the monotonous rising trend of EINOx at ϕ=1.0 as shown in Fig. 6.5. For the fuel-rich flames, thanks to the increased fuel concentration and decreased flame temperature, the prompt NO can contribute up to about 85% of NO production at small *H* as shown in Fig. 6.7. As *H* is increased, the reduction of prompt NO cannot be compensated by the increase in other routes and then results in the initial drop of EINOx at fuel-rich condition. When the prompt NO drops to its minimum value and becomes stable at large *H*, the continuously increased thermal NO can enhance the EINOx again as shown in Fig. 6.5. Besides, as shown in Fig. 6.6, it can be seen that the increase of EINOx from ϕ=0.8 to ϕ=1.0 is caused by the improvements on these four routes, while the further increase of NOx emission at fuel-rich condition is mainly dominated by the dramatically enhanced prompt NO. Apart from this, the dropping trend of EINOx for the flame at fuel-rich condition becomes increasingly apparent with the increased ϕ. Specifically, there is an approximately 28% decline of the EINOx for flame at ϕ=1.4 with the value decreased from 0.98 g/kg to around 0.71 g/kg while the

dropping rates for flames at ϕ=1.2 is about 13%. The reason is that, at fuel-rich condition, the prompt NO is enhanced obviously with the increased ϕ while the thermal NO is reduced as shown in Fig. 6.6 and Fig. 6.7. Hence, with the increased *H*, the reduction in prompt NO is higher at ϕ=1.4 while its increase in thermal NO is lower compared to that at ϕ=1.2. This makes EINOx at ϕ=1.4 to suffer a more severe dropping trend as shown in Fig. 6.5.

6.2.3 Effects of separated distance and equivalence ratio on $EINO_2$ and NO_2/NOx ratio

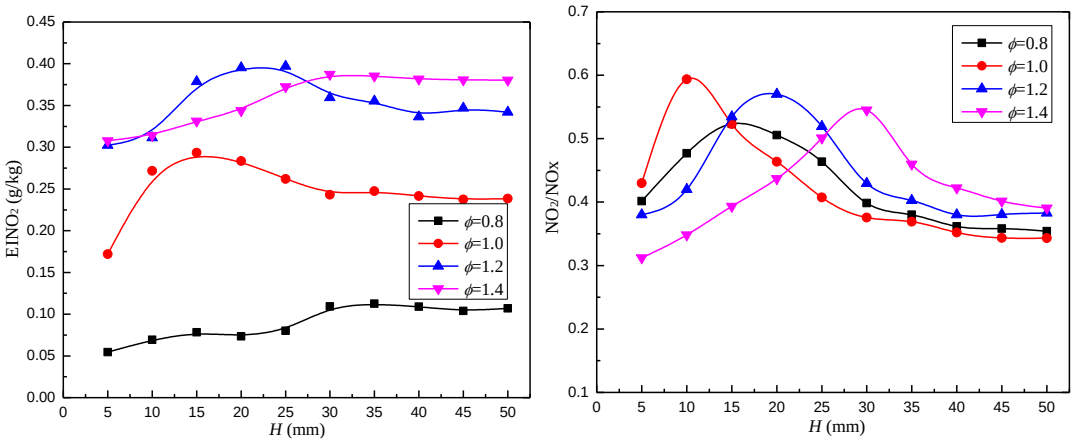

(a) $EINO_2$ (b) NO_2/NOx ratio

Fig. 6.9 $EINO_2$ and NO_2/NOx ratio of laminar premixed BG75 impinging flames at αH_2=0.1 and *Re*=1000.

The $EINO_2$ and NO_2/NOx ratios of BG75 premixed flames at *Re*=1000 and αH_2=0.1 under different equivalence ratios are compared in Fig. 6.9. With the increase in *H*, the $EINO_2$ and the NO_2/NOx ratio are both increased initially and then decreased until reaching to a relatively stable level. The NO_2 is mainly produced via the reaction of $HO_2+NO=NO_2+OH$ which generally occurs at a relatively low temperature [269], however it can be converted back to NO by reacting with H atom when temperature is higher than 1500K [270]. At small *H*, although the weakened premixed combustion

can enhance the concentration of H atom in the burned gases, the air entrainment is moderate to suppress the HO_2 formation in the air mixing region. This can restrain the NO_2 production in the burned gases. Besides, the simultaneous cooling effects of impingement plate and ambient air on the burned gases can lead to the fast drop of temperature along the downstream direction and then suppress the destruction reactions of NO_2. As *H* is enhanced, the maximum flame temperature is increased due to the improved premixed combustion, which can lead to the larger temperature gradient in the air mixing region. Furthermore, the more intensive ambient air entrainment can enhance the O_2 concentration in the air mixing region while the open flame front can provide sufficient H atom in the burned gases. Consequently, thanks to the combined effects of higher temperature and intensive air mixing, the HO_2 production can be promoted effectively in the air mixing region [271]. In addition, before the complete flame front is established, the impingement plate and ambient air can always exert the simultaneous cooling effects on the high temperature of the post flame region, which can decrease the temperature of burned gases and then exert the effective suppression on the NO_2 destruction. Hence, the NO_2 production is enhanced steadily, which contributes to the rising trend of the NO_2/NOx ratio as shown Fig. 6.9. When *H* is further increased, due to stable premixed combustion and more intensive air entrainment, the temperature gradient in the mixing region can be decreased slightly while the concentration of H atom become relatively stable. Although the more intensive air entrainment can improve the HO_2 formation, this improvement can be moderate owing to the restriction of temperature gradient and available radicals in the mixing region. Additionally, the high temperature zone in the flame can be extended due to the weakened effects of cooling plate. This extended high temperature zone in the downstream region of the flame not only promotes the NO formation in

the flame but also provides a suitable environment to accelerate the NO_2 destruction reactions of $NO_2+H=NO+OH$ and $NO_2+OH=NO+HO_2$. As a result, the NO_2 amount in the burned gases is reduced while the NO_2/NOx ratio suffers an evident drop at large *H* as shown in Fig. 6.9. Furthermore, it can be noted that the $EINO_2$ and NO_2/NOx ratio finally become relatively stable at large *H*, which can be attributed to that the NO_2 formation and destruction process reach to the equilibrium condition, as well as the NO production becomes comparatively stable at large *H* as shown in Fig. 6.5.

At small *H*, due to the moderate air mixing, the sufficient O_2 in the unburned gases at ϕ=0.8 and 1.0 can improve the HO_2 formation and then promote the NO_2 production. Furthermore, due to the higher concentration of H atom at ϕ=1.0, as well as the higher flame temperature as shown in Fig. 6.4, the NO_2 production and NO_2/NOx ratio can be further promoted at ϕ=1.0 compared to that at ϕ=0.8 as shown in Fig. 6.5. Besides, due to the absence of diffusion combustion zone, the flame temperature of the burned gases at ϕ=0.8 and 1.0 can be declined fast due to simultaneous cooling effect of plate and air entrainment as shown in Fig. 6.4(a). This can make for the NO_2 existence in the post flame region at ϕ=0.8 and 1.0. At fuel-rich condition, the higher H atom concentration can further give rise to the HO_2 formation in the air mixing region and then leads to the improved NO_2 production as shown in Fig. 6.5(a). Whereas, this improvement on NO_2 formation can be limited by the deficient O_2 in the unburned gases, as well as the moderate air entrainment at small *H*. Meanwhile, thanks to the higher contribution of prompt NO at fuel-rich condition as shown in Fig. 6.7, the NO production of fuel-rich flame at small *H* can be more rapid compared to that of flames at ϕ=0.8 and 1.0. Therefore, due to combined effects of the faster NO formation

process and limited improvement on NO_2 production, the NO amount can be accumulated at fuel-rich condition, which contributes to its lower NO_2/NOx ratio at small *H* as shown in Fig. 6.5(b). At large *H*, because of the extended high temperature region and the relatively high H concentration at ϕ=1.0, its NO_2 destruction can be improved, leading to the reduced NO_2 amount as shown in Fig. 6.5(a). Meanwhile, due to the increasingly significant role of thermal route in NO formation as shown in Fig. 6.7, the extended high temperature can promote the thermal NO production effectively at large *H*. Consequently, the NO_2/NOx ratio at ϕ=1.0 drops evidently as shown in Fig. 6.9(b). For the flame at ϕ=0.8, thanks to its lower flame temperature and less H atom, its NO_2 destruction process is quite moderate as shown in Fig. 6.5(a). Furthermore, due to its smaller high temperature region and less NO production via thermal route, the NO_2/NOx ratio ϕ=0.8 is slightly higher at large *H*. Additionally, although the much higher H concentration in the burned gases can accelerate the NO_2 destruction at fuel-rich condition, it can also improve the NO_2 production in the air mixing region. This finally contributes to its lower dropping rate of $EINO_2$ at fuel-rich condition compared to that at ϕ=1.0 as shown in Fig. 6.9(a). As a result, this leads to a comparatively higher level of NO_2/NOx ratio at the fuel-rich condition as shown in Fig. 6.5. Considering the different conditions that the maximum NO_2/NOx ratio occurs for these flames, the higher value of peak NO_2/NOx ratio at ϕ=1.0 can be resulted from its more effective HO_2 production due to the adequate H and O_2, as well as the weakened NO_2 destruction owing to intensive cooling effect on burned gases. Meanwhile, the lower values at fuel-lean and fuel-rich conditions are primarily caused by the insufficient H and O_2 respectively.

6.3 Effects of Reynolds number on the pollutant emissions

6.3.1 Effects of Reynolds number on the EICO

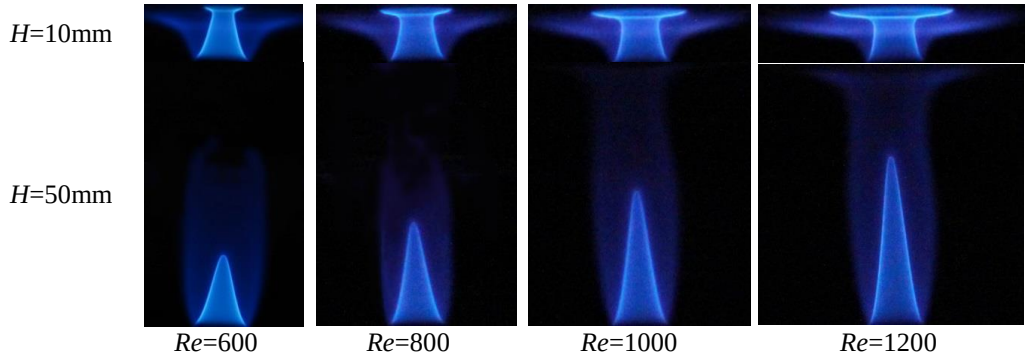

Fig. 6.10 Premixed BG75 impinging flames at ϕ=1.2 and αH_2=0.1.

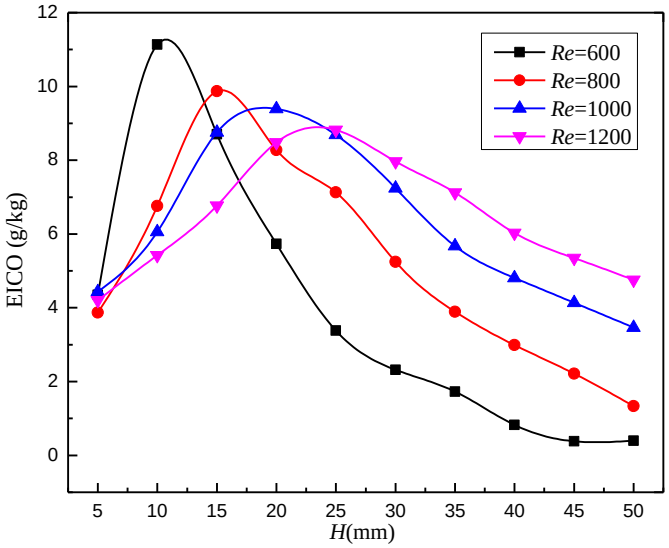

Fig. 6.11 Effects of Reynolds number on EICO of premixed BG75 flames at ϕ=1.2 and αH_2=0.1.

The flame structures of the premixed impinging BG75 flame at ϕ=1.2 and αH_2=0.1 under different Reynolds number are compared in Fig. 6.10 while the EICO of these flames are given in Fig. 6.11. It is seen that EICO is decreased with the increased *Re* when the flame front is influenced by the cooling plate, while it shows the evidently rising trend at large *H*. In addition, there exists a steady drop in the peak value of EICO as *Re* is enhanced. At small *H*, the premixed combustion zone is considerably

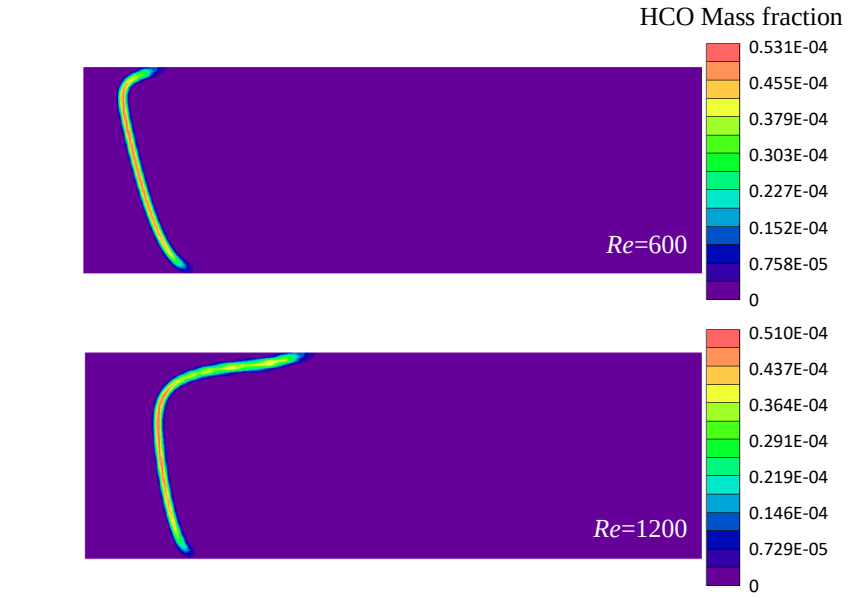

(a) HCO distribution

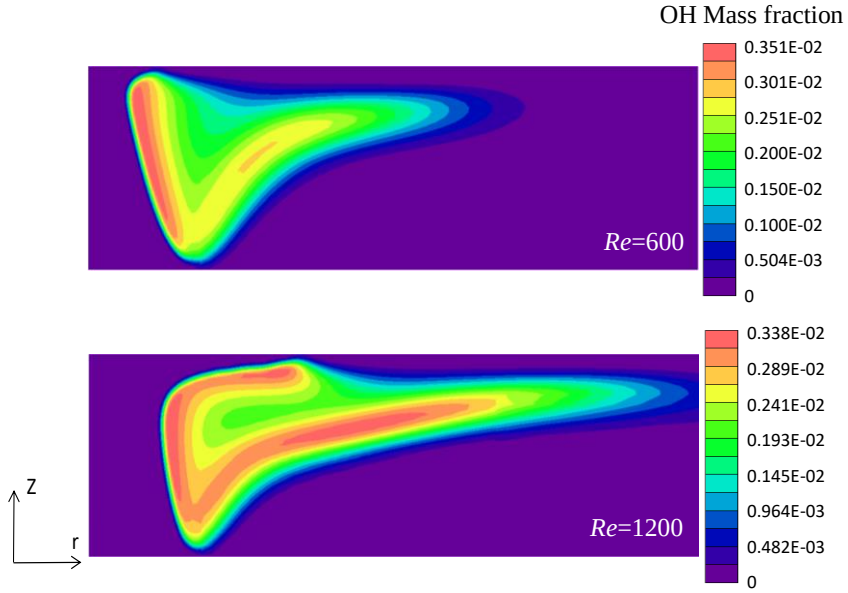

(b) OH distribution

Fig. 6.12 The calculated HCO and OH distributions of premixed BG75 flames at ϕ=1.2 and αH_2=0.1 (H=10mm).

influenced by the plate for these flames as shown in Fig. 6.10. For the flame at smaller *Re*, thanks to its lower flame height, it would suffer less cooling effect on the premixed combustion zone, leading to its stronger combustion intensity. This can be reflected by the calculated HCO distributions of impinging flames at H=10mm as

shown Fig. 6.12(a). It is seen that the HCO concentration at *Re*=600 and 1200 are both decreased near the cooling plate, indicating the weakened premixed combustion caused by the cooling effects of plate. Whereas, due to the larger cool core, the effects of cooling plate on premixed combustion is more significant at *Re*=1200, which leads to the increased part of flame front with the lower HCO concentration as shown in Fig. 6.12(a). Consequently, the flame at lower *Re* has the better fuel oxidization process and then the improved CO production. Additionally, in order to compare the effects of CO oxidization process on EICO at different *Re*, the OH distributions of flames at *H*=10mm are also given in Fig. 6.12(b). Generally, due to the cooling effects, there exists a cool gases boundary layer along the plate surface where the OH concentration is much lower as shown in the figures. This can make for the CO escape without reacting with OH radical to form CO_2. Whereas, the OH radical can maintain the high concentration in a longer zone outside the cool gases boundary layer at *Re*=1200. This means that escaped CO is likely to be oxidized by OH radical more effectively when bypassing the longer OH cloud, which can promote the CO oxidization at *Re*=1200 to some extent. Besides, the flame temperature at smaller *Re* is relatively lower and is dropped more effectively in the burned gases zone as shown in Fig. 6.13(a), which can exert more intensive suppression on the CO oxidization in comparison to other flames. Hence, the flame at smaller *Re* has an enhanced CO emission at low *H*.

At large *H*, the flame with larger *Re* has the higher flame temperature and larger diffusion combustion zone as shown in Fig. 6.13(b) and Fig. 6.10, respectively. Additionally, at the same *H*, the air entrainment can be less effective on CO oxidization for the flame with larger *Re* due to its larger fuel flow rate, which means that ambient O_2 is relatively insufficient for its CO oxidization compared to that at smaller *Re*. Therefore, although the flame with larger *Re* has the higher temperature

and larger diffusion combustion zone to improve the CO oxidization in the burned gases, the relatively moderate air entrainment can restrain its oxidization process. Apart from this, the flame with the higher flame height has the less residence time allowing CO to be oxidized to CO_2 [243]. As a result, the flame at larger *Re* has a higher CO emission at large *H* as shown in Fig. 6.11. Besides, with the increased *Re*, the decreasing trend of peak CO emission can be primarily resulted from the enhanced flame temperature and larger burned gases zone as shown in Fig. 6.10 and Fig. 6.13, which results in the more effective CO oxidization at larger *Re*.

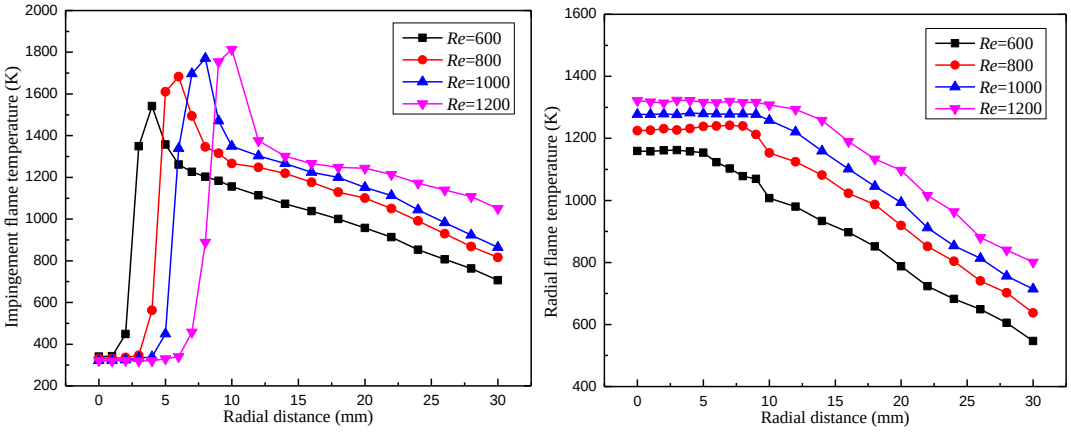

(a) *H*=10mm (b) *H*=50mm

Fig. 6.13 Radial impinging temperature of premixed BG75 flames at ϕ=1.2 and αH_2=0.1 under different Reynolds number.

6.3.2 Effects of Reynolds number on the EINOx

The EINOx of premixed BG75 flames at different Reynolds number are compared in Fig. 6.14 while the NO amounts formed via different routes at different *Re* are illustrated in Fig. 6.15. With the decreased *Re*, the total EINOx is declined steadily at either small or large *H*. Specifically, the NO formed via thermal and N_2O routes are increased while that of prompt and NNH routes are decreased. At fuel-rich condition, the prompt NO and thermal NO can account for around 80% of total NO formation as shown in Fig. 6.16. Hence, the variation of total EINOx with *Re* can be dominated by

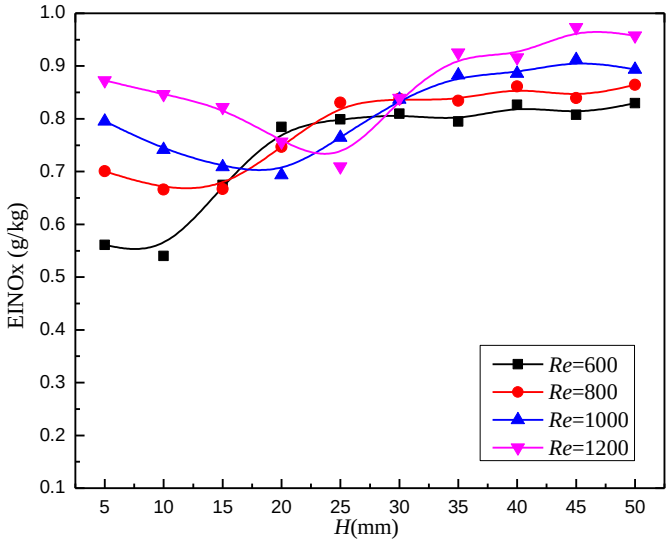

Fig. 6.14 Effects of Reynolds number on EINOx of premixed BG75 flames at ϕ=1.2 and αH_2=0.1.

the changes of NO production through prompt and thermal routes. Due to the lower flow rate, the flame at smaller *Re* suffers more effective cooling effects of ambient air and the flat plate on the burned gases, which contributes to the lower flame temperature in the diffusion combustion zone as shown in Fig. 6.13. This can suppress the NO production via these routes to some extent. Furthermore, although the lower flame height at smaller *Re* means the longer residence time for NO formation in the post flame region, it suffers the increasingly intensive cooling effects of plate and ambient air at small *H* as shown in Fig. 6.13, leading to the slight variation of NO formation via N_2O route and the decreased thermal NO as shown in Fig. 6.15. As *H* is increased, the NO formation via N_2O and thermal routes in the flame at smaller *Re* are improve effectively owing to the extended high temperature zone, the longer residence time and more intensive air entrainment. Additionally, the premixed combustion process of flame at smaller *Re* can suffer much less influence of cooling plate compared to that of flames at larger *Re*. Based on the previous discussion, the prompt NO can be promoted efficiently by the weakened premixed combustion at small *H*.

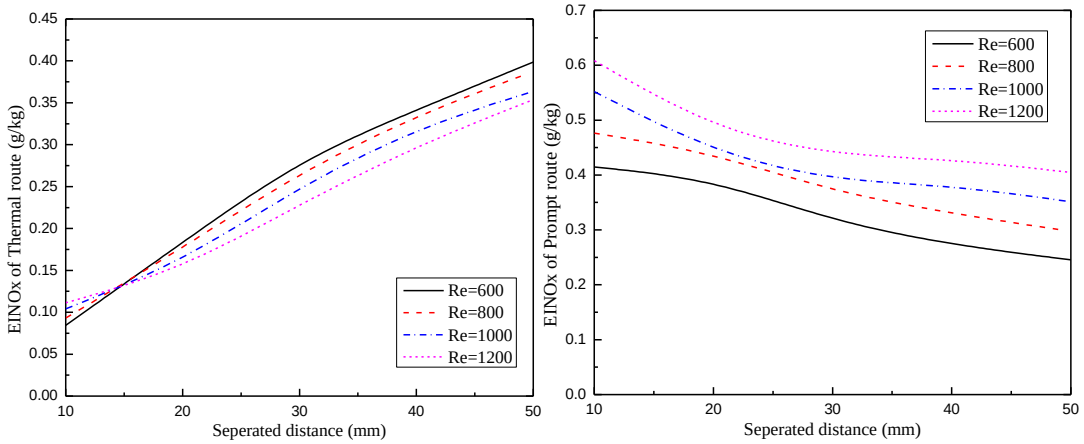

(a) Thermal route (b) Prompt route

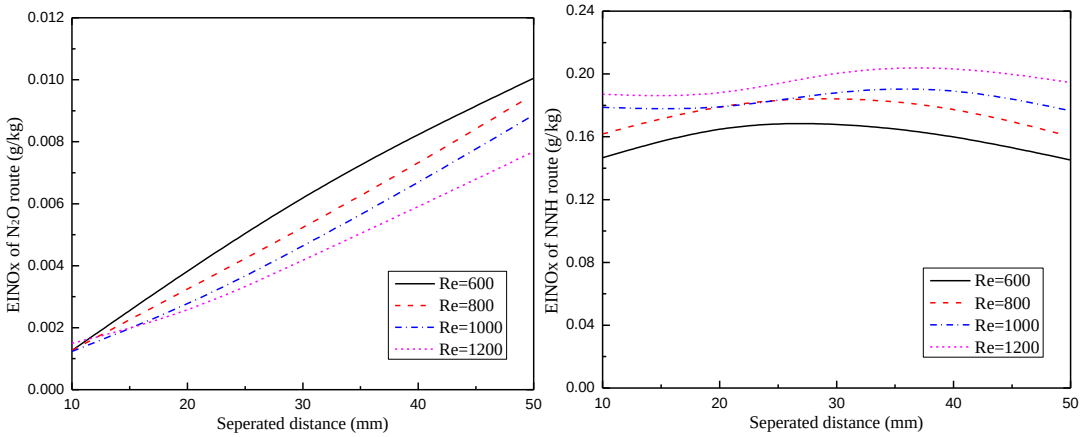

(c) N_2O route (d) NNH route

Fig. 6.15 EINOx of different routes for the laminar premixed BG75 impinging flames at αH_2=0.1 and ϕ=1.2.

Thus the less cooling effects on the premixed combustion process can restrain the initiation reactions of prompt route at *Re*=600 considerably, which can be reflected by the relatively lower HCN concentration at *Re*=600 as shown in Fig. 6.17. Consequently, due to the combined effects of lower temperature and better premixed combustion process, the initiation reactions of prompt route is inhibited effectively for the flame at lower *Re*, which leads to a significant drop of EINOx (around 30%) from *Re*=1200 to *Re*=600 as shown in Fig. 6.15. In addition, although the longer residence time and stronger air entrainment can improve the NNH route slightly in the flame with the lower *Re*, the better premixed combustion and lower fuel flow rate at lower

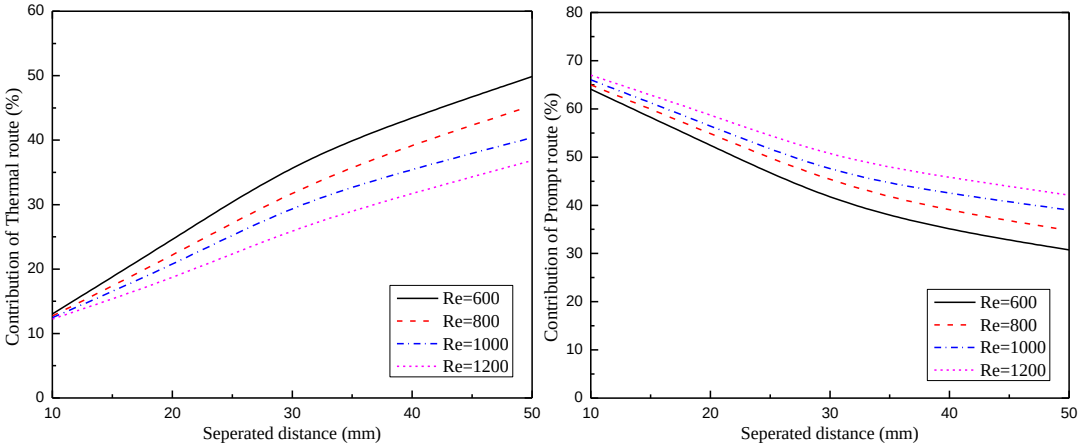

(a) Thermal route (b) Prompt route

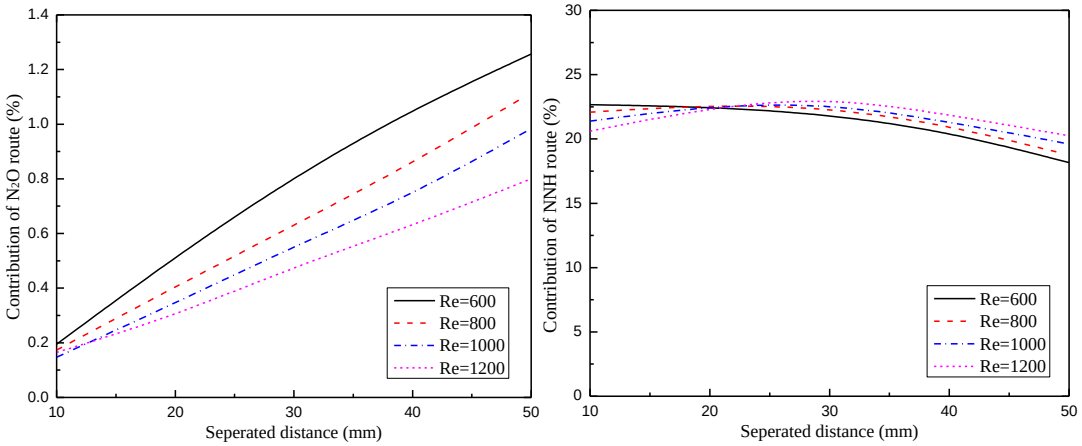

(c) N_2O route (d) NNH route

Fig. 6.16 Contributions of different routes on NO formation of the laminar premixed BG75 impinging flames at αH_2=0.1 and ϕ=1.2.

Re gives rise to less available hydrocarbon free radicals to initialize the NO production via NNH route, which gives rise to the drop in NO amount of NNH route. As a result, it is known that the steady decline of total EINOx with decreased *Re* is dominated by the evident drop of prompt NO. Besides, the contribution variations of different NO formation routes with *Re* are illustrated in Fig. 6.16. With the decreased *Re*, the drop of prompt NO contribution is caused by the considerable suppression on the initiation reactions, while the obvious rise in contributions of thermal and N_2O routes are resulted from the longer residence time and more air entrainment. Considering the relatively stable production via NNH route with the increased *H*, its

improved importance with the reduced *Re* at small *H* is primarily resulted from the significantly suppressed prompt NO, while its reduced contribution at large *H* is resulted from the stronger improvement on the thermal NO.

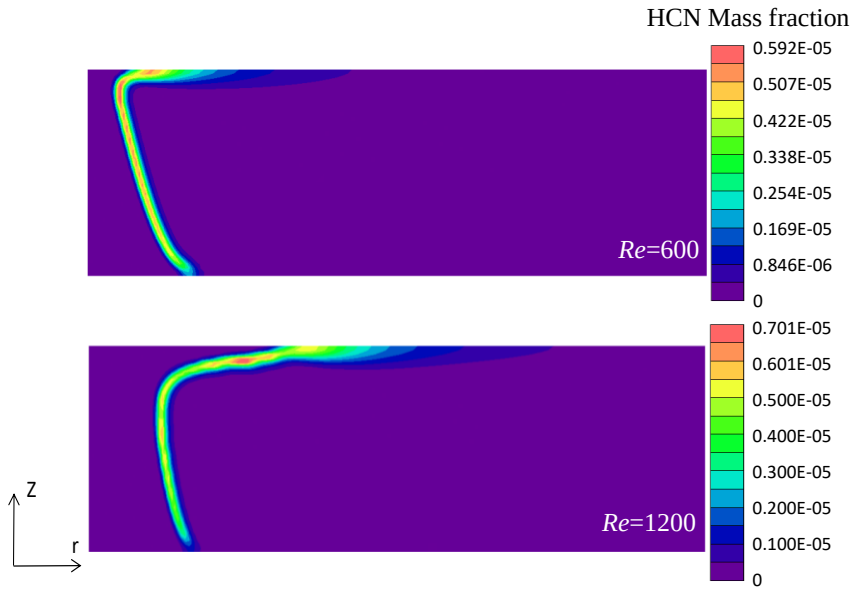

Fig. 6.17 The calculated HCN distribution of premixed BG75 flames at ϕ=1.2 and αH_2=0.1 (*H*=10mm).

6.3.3 Effects of Reynolds number on the EINO$_2$ and NO$_2$/NOx ratio

The EINO$_2$ and NO$_2$/NOx ratios of BG75 premixed flames at different Reynolds number are illustrated in Fig. 6.18. With the increased *Re*, the NO$_2$ concentration is decreased at small *H* but increased at large *H*, and the maximum percentage of NO$_2$ in the NOx shows a steady dropping trend. This can be explained as follows. Thanks to the lower flow rate, the relatively moderate air entrainment at low *H* can still exert stronger improvement on HO$_2$ production in the air mixing region of the flame at smaller *Re*, leading to the more obvious enhancement on its NO$_2$ formation in comparison to that at large *Re* as shown in Fig. 6.18. By contrast**,** although the flame temperature is higher at larger *Re*, its improvement on HO$_2$ formation would be weakened effectively due to the relatively insufficient O$_2$ compared to that at smaller

Re. Apart from this, due to the smaller flow rate and lower flame temperature at low *Re* as shown in Fig. 6.13(a), the burned gases would suffer more effective cooling influences of the impingement plate and the air entrainment at low *H*, which can lead to the lower temperature of burned gases and then make for the NO_2 existence in the burned gases. In addition, the rapid NO formation via prompt route is suppressed significantly at low *Re* due to the smaller open flame front, which can inhibit the NO accumulation at small *H*. Consequently, the $EINO_2$ and the NO_2/NOx ratio of the flame at smaller *Re* are comparatively higher at small *H*.

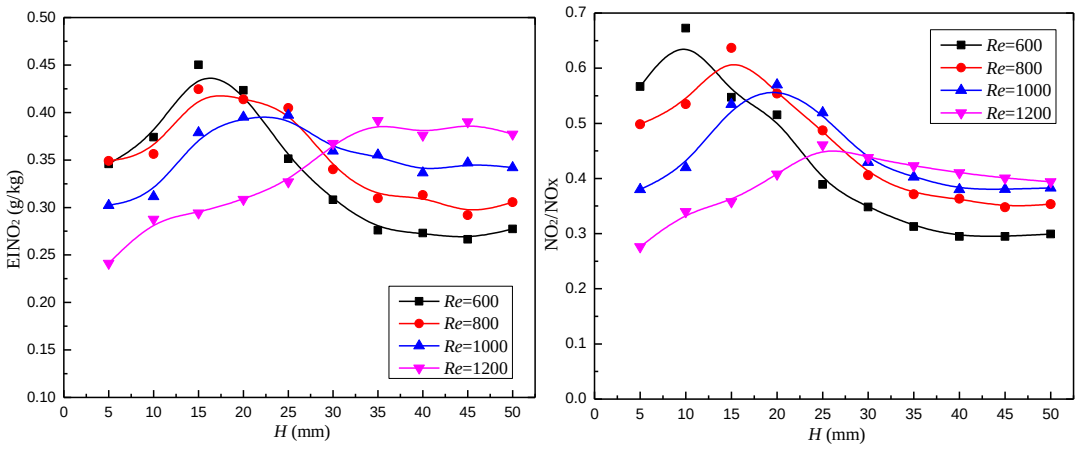

(a) $EINO_2$ (b) NO_2/NOx

Fig. 6.18 $EINO_2$ and NO_2/NOx ratio of premixed BG75 impinging flames at ϕ=1.2 and αH_2=0.1.

When *H* is increased to large *H*, the air entrainment becomes increasingly intensive, the lower temperature and less unburned fuel at smaller *Re* can reduce the HO_2 production in the air mixing region in comparison to that at larger *Re*. Furthermore, the lower flame height at smaller *Re* means the longer residence time for NO_2 destruction in the burned gases. Apart from this, the thermal NO plays an increasingly important role in NO formation of flame at smaller *Re*, which can give rise to the NO formation effectively at large *H*. Consequently, the $EINO_2$ and NO_2/NOx ratio are both declined gradually with the decreased *Re* at large *H* as shown in Fig. 6.18. In

addition, it is noted that the peak $EINO_2$ and NO_2/NOx ratio show the steady dropping trends with the increased *Re* as shown in Fig. 6.18. As *Re* is decreased, the cooling effects of the impingement plate and ambient air on the burned gases become increasingly evident due to the reduced flow rate and flame volume, which can be reflected by the impinging flame temperature as shown in Fig. 6.13(b). This creates a more suitable environment for the NO_2 existence since the NO_2 destruction process requires a relatively high temperature. Although the HO_2 formation in the air mixing zone can be improved for the flame at larger *Re* due to its larger temperature gradient, the NO_2 destruction process is also accelerated due to the increased temperature in the post-flame zone. This means that, as flame temperature is varied, there exists a competition between NO_2 formation process and NO_2 destruction process. It is thus known that the lower temperature of burned gases at smaller *Re* exerts stronger suppressions on NO_2 destruction process than that on NO_2 formation process, which makes for the NO2 accumulation in the flame and finally dominates the increased maximum $EINO_2$ and NO_2/NOx ratio with the decreased *Re*.

6.4 Effects of H_2 addition on the pollutant emissions

6.4.1 Effects of H_2 addition on the EICO

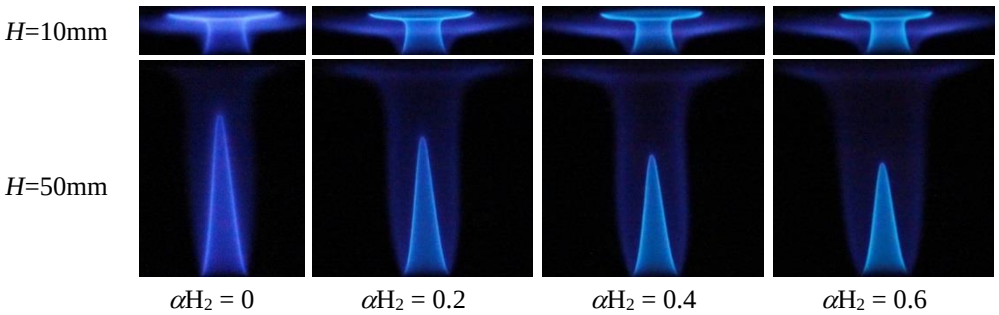

Fig. 6.19 Digital images of premixed BG75 impinging flames with different hydrogen addition at ϕ=1.2 and *Re*=1200.

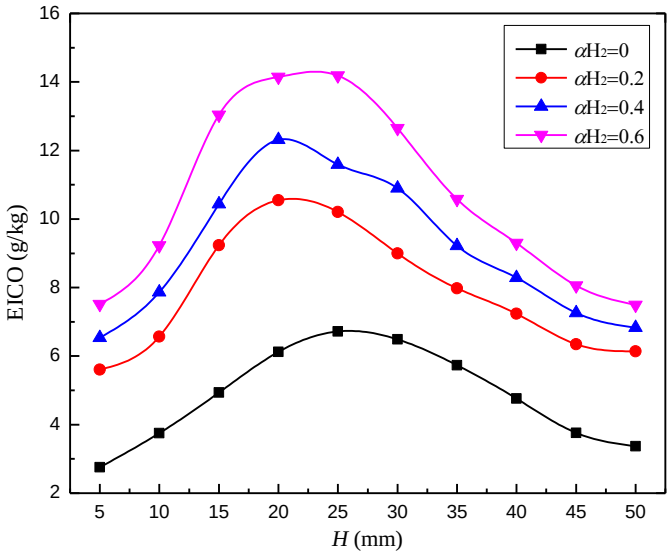

Fig. 6.20 EICO of premixed BG75 impinging flames with different hydrogen addition at ϕ =1.2 and *Re*=1200.

The images of premixed biogas-hydrogen impinging flames at ϕ =1.2 and *Re*=1200 are shown in Fig. 6.19. With the hydrogen addition, the laminar burning velocity is enhanced steadily while the flame intensity is improved due to the high reactivity and diffusivity of hydrogen, which results in the reduced flame height and the brighter flame front as shown in Fig. 6.19. The EICO variations of biogas impinging flames with the hydrogen enrichment at ϕ =1.2 and *Re*=1200 are illustrated in Fig. 6.20. It is seen that the CO emission is enhanced obviously with the hydrogen addition at either small or large *H*. At small *H*, the biogas flame with higher hydrogen addition can suffer less cooling effects on its premixed combustion due to its lower flame height, which can promote the CO production in the flame. Furthermore, it is known that the H_2 can compete with CO to react with OH radical in the flame. This can inhibit the CO oxidization effectively as a large amount of H_2 is introduced into the biogas flame, which can be reflected by the net reaction rate variation of $OH+H_2=H+H_2O$ and $OH+CO=H+CO_2$ as shown in Fig. 6.21. In order to facilitate the comparison, the net reaction rates of these two reactions are both normalized by the respective peak net

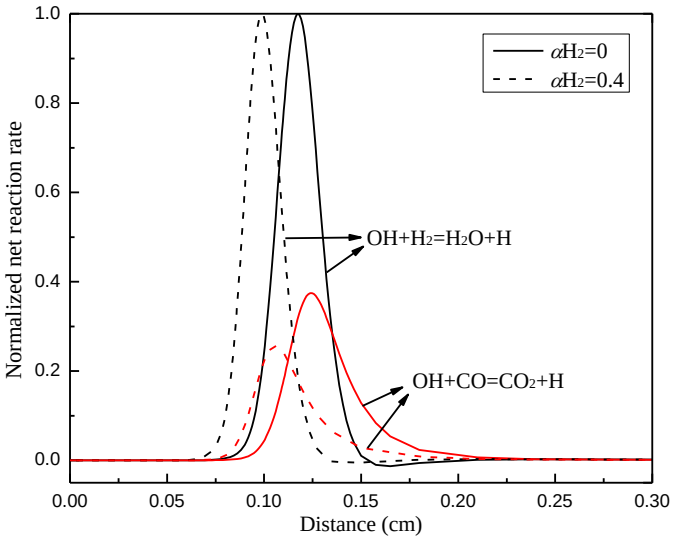

Fig. 6.21 Normalized net reaction rates of $OH+H_2=H_2O+H$ and $OH+CO=CO_2+H$ in the laminar premixed BG75 flame with hydrogen enrichment at ϕ=1.2.

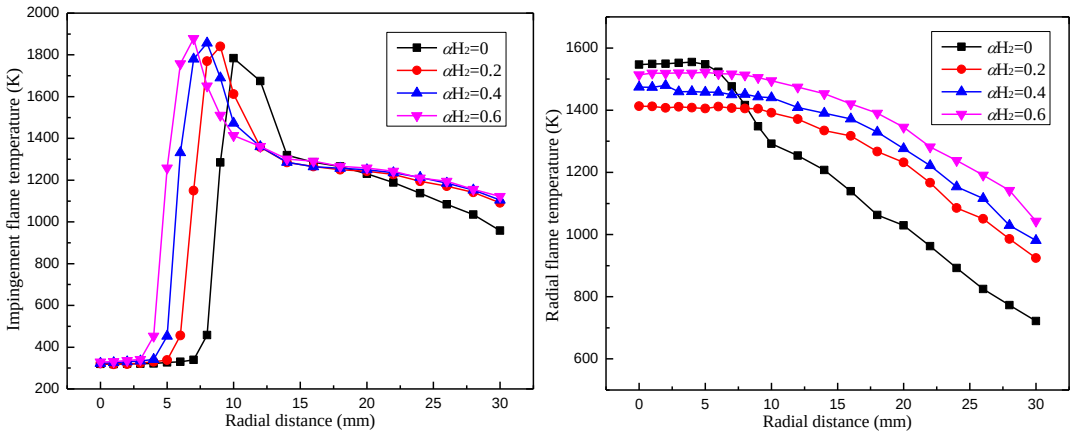

(a) H=10mm (b) H=50mm

Fig. 6.22 Radial flame temperature distribution of premixed BG75 impinging flames with different hydrogen addition at Re=1200 and ϕ=1.2.

reaction rate of $OH+H_2=H+H_2O$. It is seen that, with the increased H_2 mole fraction, the normalized net reaction rate of $OH+CO=H+CO_2$ is decreased steadily, which is resulted from the high reactivity of H_2 which can consume more OH radical faster in the flame and inhibit the CO oxidization effectively. In addition, with the hydrogen addition, although the lower flame height can make the flame to suffer more intensive cooling effects on its burned gases, the high reactivity and diffusivity of hydrogen can overcome the cooling effects and enhance the flame temperature of burned gases as

shown in Fig. 6.22. This can promote the CO oxidization process to some extent, but this improvement cannot overcome the suppressions caused by hydrogen enrichment. As a result, the CO emission is enhanced steadily at small *H* thanks to the dominated effects of the high reactivity and diffusivity of hydrogen. At large *H*, as hydrogen proportion is enhanced, the flame temperature of burned gases is increased steadily as shown in Fig. 6.22 while the residence time and high temperature zone can be promoted due to the lower flame height as shown in Fig. 6.23. These influences can improve the CO oxidization process in the post-flame region. However, the large amount of H_2 in the flame can still compete with CO for OH radical as the previous discussion, which can also inhibit the CO oxidization process at large *H* significantly. Eventually, the CO emission is still much higher at large *H*. In conclusion, the enhanced CO emission with hydrogen enrichment is primarily caused by the high reactivity and diffusivity of hydrogen which can suppress the CO oxidization efficiently through competing for OH radical in the flame.

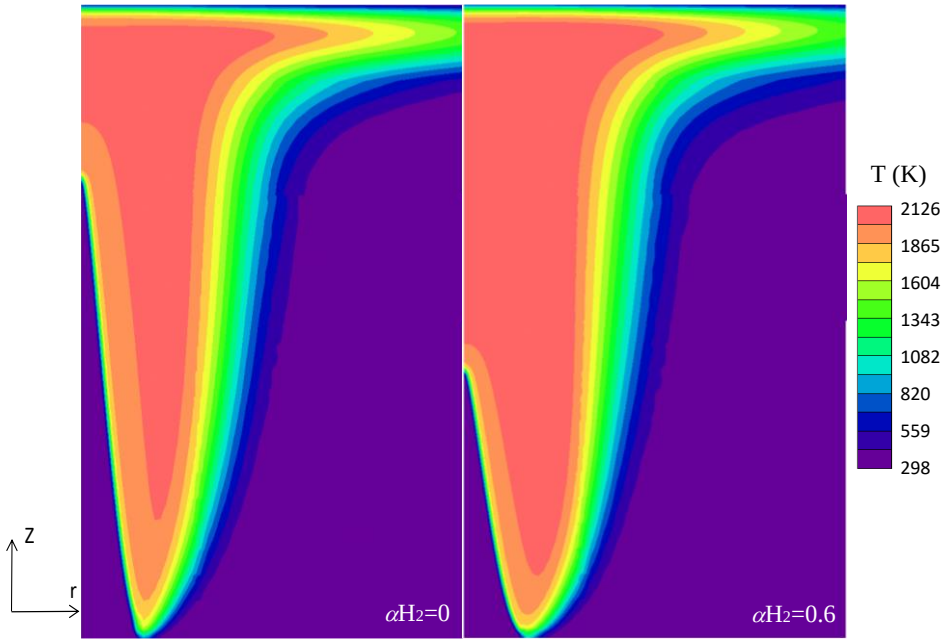

Fig. 6.23 The calculated temperature fields for premixed BG75 impinging flames with different hydrogen addition at ϕ=1.2 and *Re*=1200 (*H*=50mm).

6.4.2 Effects of H_2 addition on the EINOx

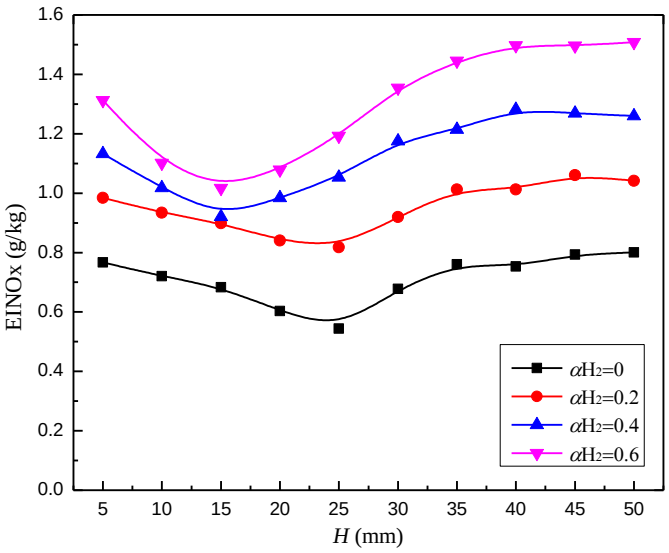

Fig. 6.24 EINOx of premixed BG75 impinging flames with different hydrogen addition at ϕ =1.2 and *Re*=1200.

The EINOx variation of biogas impinging flame with the hydrogen enrichment at ϕ =1.2 and *Re*=1200 is illustrated in Fig. 6.24, and the NO amounts generated via different routes of these flames are also compared in Fig. 6.25. It can be seen that the NO amount of four NO mechanisms are promoted effectively by the hydrogen addition, leading to the steadily enhanced NOx emission as shown in Fig. 6.24. Specifically, the hydrogen addition can not only enhance the flame temperature as shown in Fig. 6.22, but also lead to a larger high temperature zone and the longer residence time due to the lower flame height as shown in Fig. 6.23. As a result, the thermal NO formation is accelerated efficiently as shown in Fig. 6.25. For the prompt route, it can be seen that the rising trend of NO amount is decreased apparently as αH_2 is larger than 0.2. Specifically, the prompt NO is enhanced by around 0.1 g/kg as 20% hydrogen is introduced. Whereas, this value is declined to approximately 0.02g/kg when hydrogen proportion is further increased. This can be explained as follows. As hydrogen is introduced in the biogas, the flame temperature can be enhanced evidently,

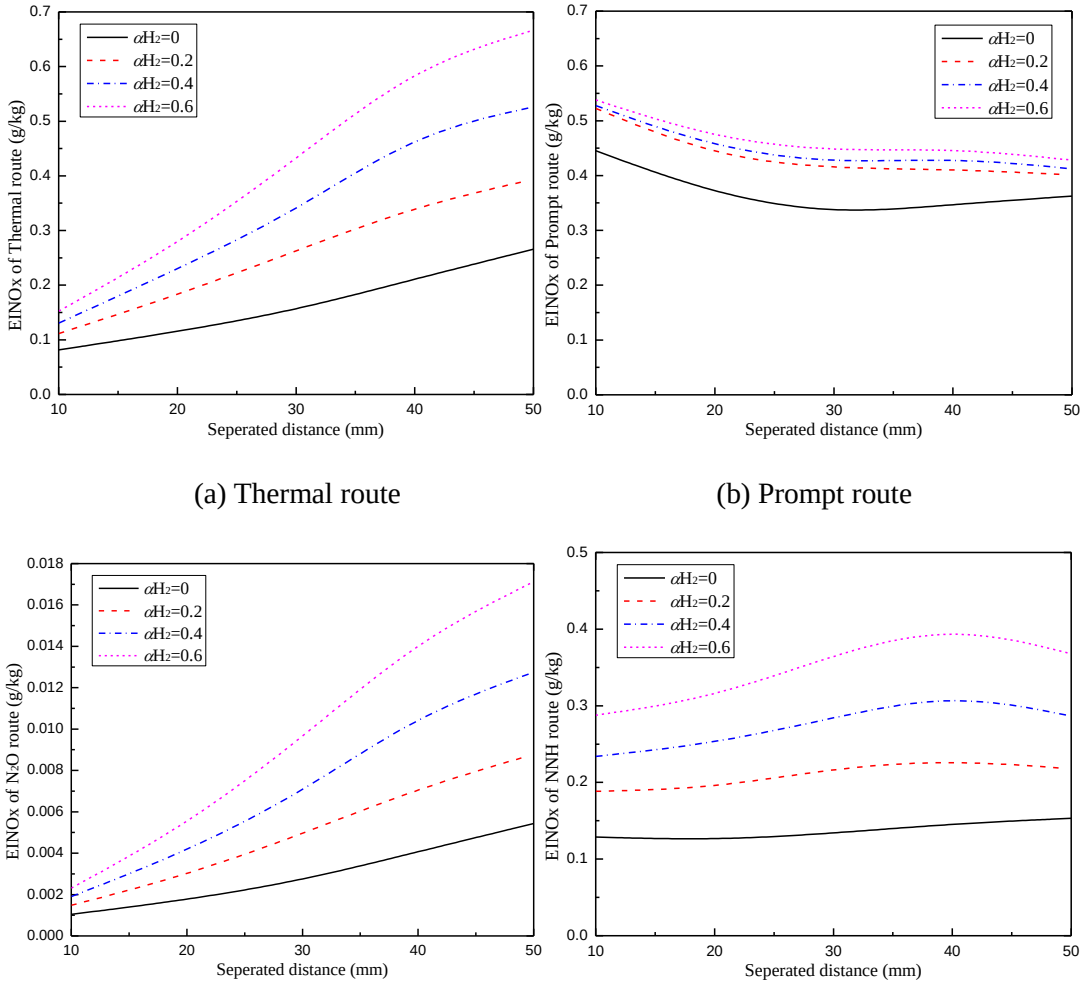

(a) Thermal route (b) Prompt route

(c) N_2O route (d) NNH route

Fig. 6.25 EINOx of different routes for premixed BG75 impinging flames with different hydrogen addition at ϕ=1.2 and *Re*=1200.

which can then promote the initiation reactions of prompt route effectively. On the other hand, the hydrogen enrichment can decrease the methane proportion in the unburned fuel considerably and give rise to the improved premixed combustion compared to that at αH_2=0 owing to the lower flame height. This can suppress the initiation reactions of prompt route at small *H* by reducing the available hydrocarbon radicals, which can be reflected by the decreased HCN concentration as shown in Fig. 6.26. At αH_2=0.2, compared to the pure biogas flame, the effective improvement of increased flame temperature on the initiation reactions of prompt NO can overcome the suppression of improved premixed combustion and reduced methane

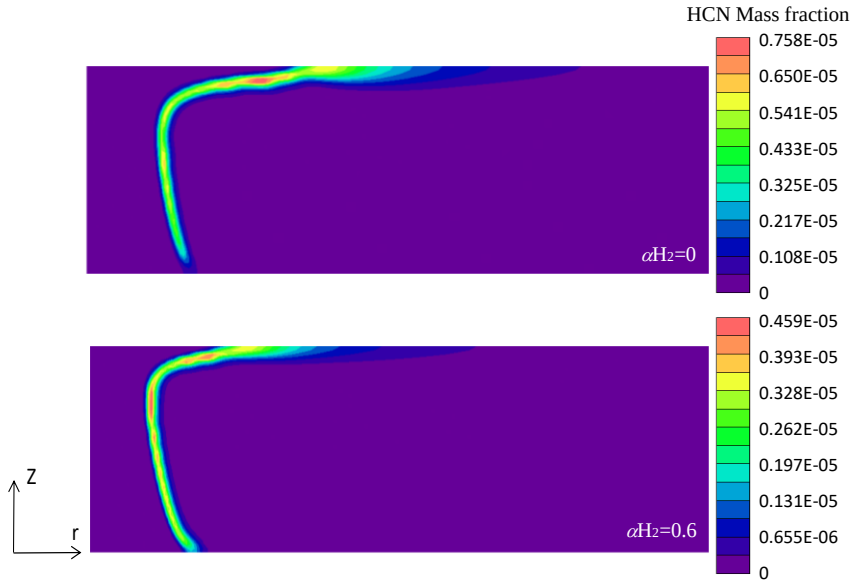

Fig. 6.26 The calculated HCN distributions for premixed BG75 impinging flames with different hydrogen addition at ϕ=1.2 and *Re*=1200 (*H*=10mm).

concentration in the fuel, which contributes to the apparent increase in prompt NO at this condition. As hydrogen addition is further increased, although the further increased flame temperature can still accelerate the prompt NO formation, the suppression on the prompt NO production can be aggravated more effectively owing to the combined effects of improved premixed combustion and decreased methane concentration in the unburned gases. Consequently, the increasing rate of prompt NO is declined due to the increasingly stronger suppressions as shown in Fig. 6.25. For the N_2O route, considering that it can be initialized in the post flame region, its steadily increased NO amount can be then attributed to the enhanced flame temperature and the larger high flame temperature zone. Furthermore, the relatively stronger air entrainment due to the lower flame height can also give rise to the NO formation via N_2O route to some extent. For the NNH route, apart from the improvement of enhanced flame temperature on the NNH route, the evidently increased H_2 concentration can give rise to the increased amount of hydrocarbon free radicals

dramatically as shown in Fig. 6.27, which can then accelerate the NNH and NH productions and lead to the stable enhancement in the NO amount of NNH route.

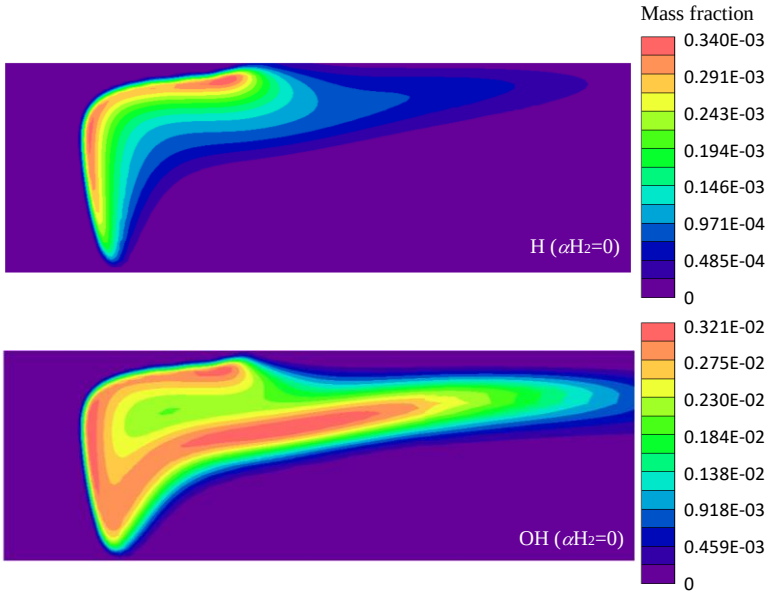

(a) αH_2=0

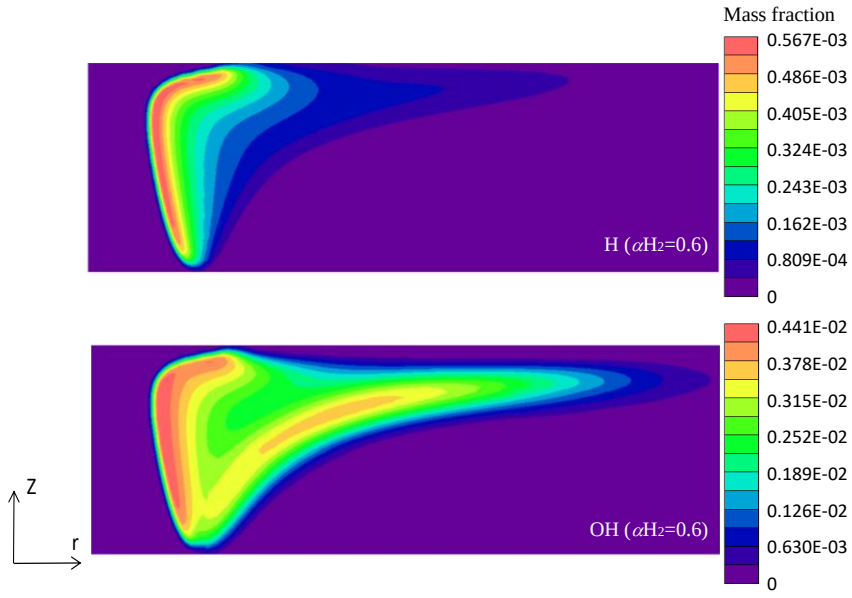

(b) αH_2=0.6

Fig. 6.27 The calculated H and OH distributions for premixed BG75 impinging flames with different hydrogen addition at ϕ=1.2 and *Re*=1200 (*H*=10mm).

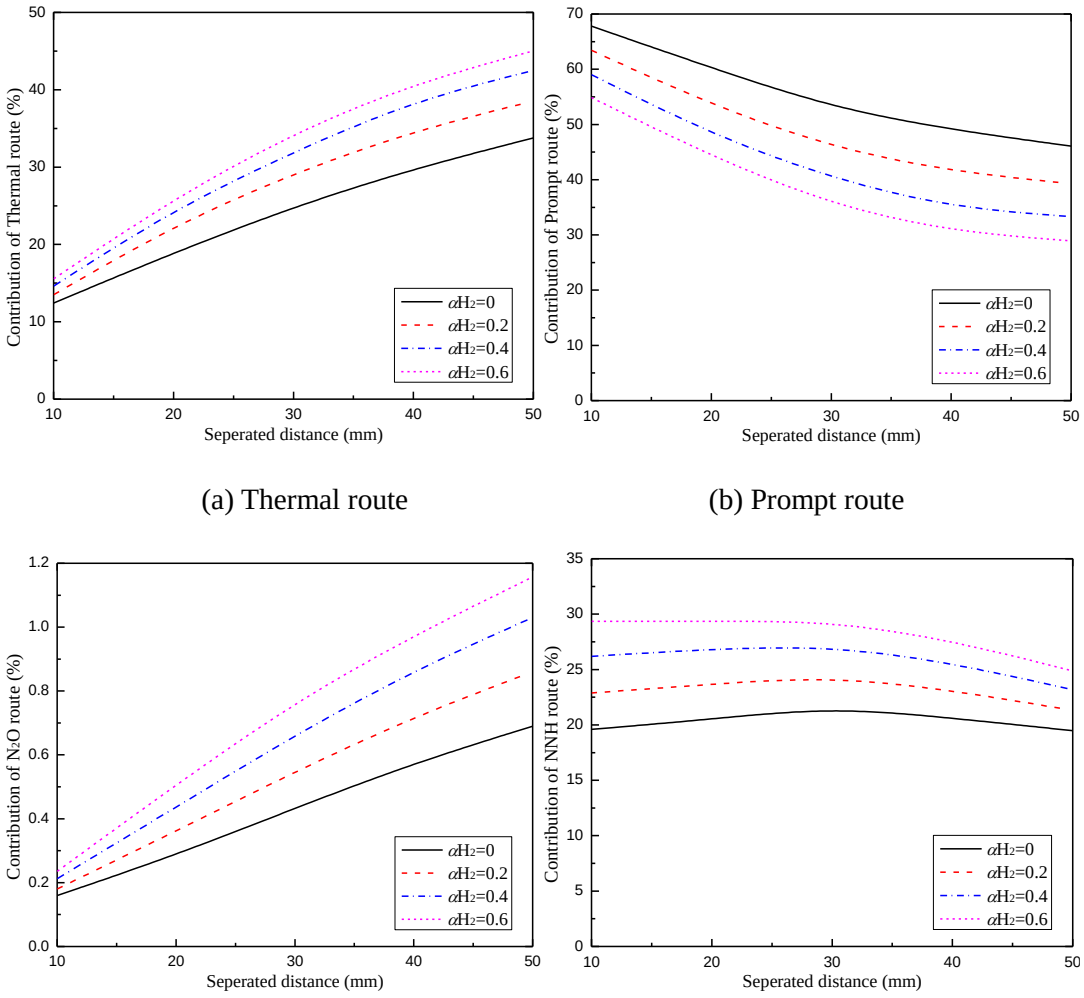

(a) Thermal route (b) Prompt route

(c) N_2O route (d) NNH route

Fig. 6.28 Contributions of different routes for premixed BG75 impinging flames with different hydrogen addition at ϕ=1.2 and *Re*=1200.

Based on the above discussion, the contribution variations of these routes on the NO formation for the biogas-hydrogen flames are compared in Fig. 6.28. It is seen that, with the hydrogen addition, the contributions of thermal, N_2O and NNH routes on the total EINOx are improved steadily owing to the enhanced flame temperature and the increased H_2 proportion, while the significance of prompt route is reduced steadily due to the evidently reduced methane amount in the flame. Furthermore, as shown in Fig. 6.28, the contribution of NNH route has the maximum rising rate at small *H* which is increased from about 20% to 30%, while the contribution of thermal route is increased most apparently at large *H*. At small *H*, the hydrogen addition can improve

the NNH route efficiently by enhancing the concentration of related radicals (H, OH and H_2) for its initiation reactions and accelerate the reaction rate by the increased flame temperature. Meanwhile, with the hydrogen addition, although the thermal NO production can be improved by the enhanced flame temperature, this improvement is weakened considerably by the insufficient residence time and moderate air mixing at small *H*. This finally leads to a quite slight increase in thermal NO contribution at small *H* as shown in Fig. 6.28. As a result, it is known that the increased EINOx with hydrogen enrichment at small *H* is primarily dominated by the promoted NNH route. Besides, as *H* is increased, the improvements of longer residence time, more intensive air mixing and extended high temperature zone can play the increasingly important roles in the NO formation, especially for the thermal NO. For the NNH route, its initiation reactions are related to the hydrocarbon free radicals which have the relatively stable concentrations at various *H*, and NNH and NH are mainly produced in or near the premixed combustion zone as shown in Fig. 6.29. Hence, due to the restraint of initiation reactions, the longer residence time, more intensive air mixing and extended high temperature zone can exert limited improvements on the NO formation via NNH route at large *H*, which leads to the comparatively moderate increase in its NO amount with the increased *H* as shown in Fig. 6.25(d). Consequently, the thermal NO can be promoted considerably by the combined improvement of hydrogen addition and the increased *H* while NNH route is primarily improved by the hydrogen enrichment. This results in the maximum increased contribution of thermal NO at large *H* eventually. It is thus concluded that the promoted thermal NO gives rise to the enhanced EINOx with hydrogen enrichment at large *H*.

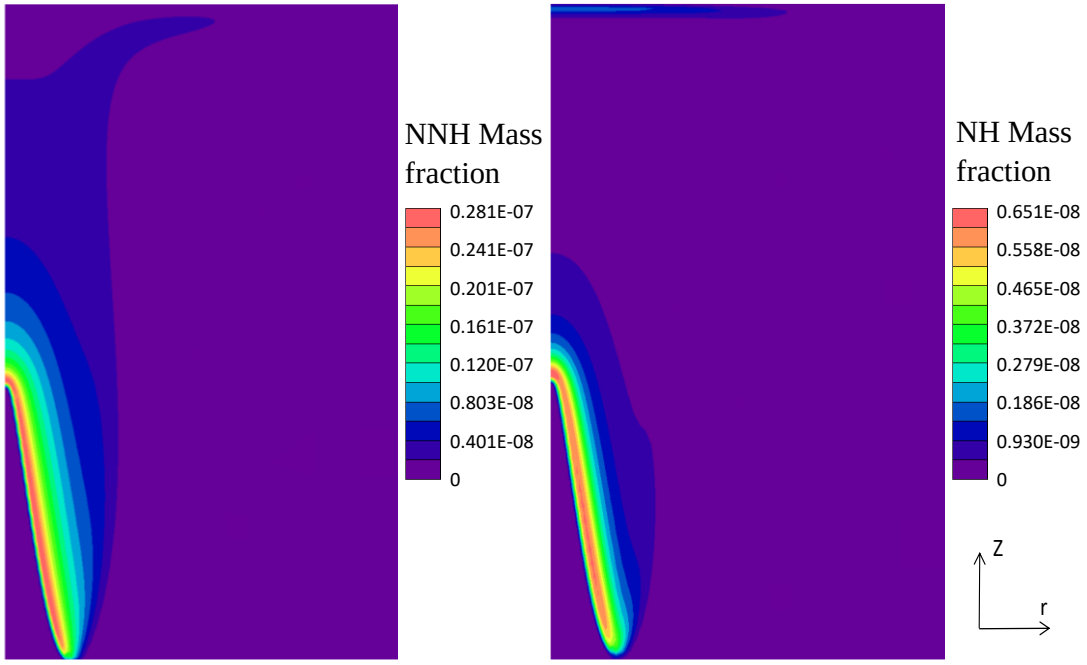

Fig. 6.29 NNH and NH distributions of premixed BG75 flame at αH_2=0.6, *Re*=1200 and ϕ =1.2 (*H*=50mm).

6.4.3 Effects of H_2 addition on the $EINO_2$ and NO_2/NOx ratio

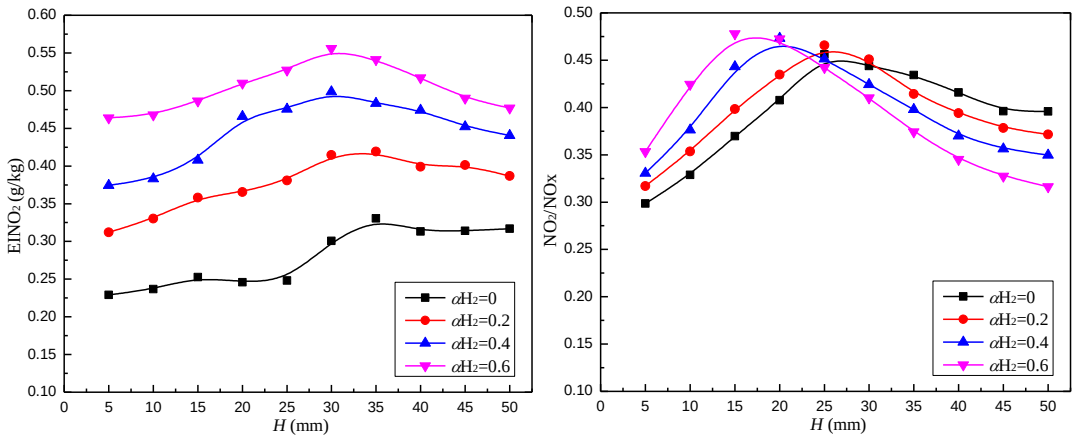

(a) $EINO_2$ (b) NO_2/NOx

Fig. 6.30 NO_2 formation of premixed BG75 impinging flames with different hydrogen addition at ϕ =1.2 and *Re*=1200.

The $EINO_2$ and NO_2/NOx of biogas impinging flame with the hydrogen enrichment are illustrated in Fig. 6.30. It is seen that the $EINO_2$ can be enhanced with the hydrogen addition, and its rising rate at small *H* is comparatively higher than that at

larger *H*. Besides, with the increased αH_2, the NO_2/NOx ratio shows a rising trend as flame front is affected by the plate, but it is decreased steadily at large *H* as shown in Fig. 6.30(b). With the increased αH_2, the hydrogen concentration can be increased obviously while the flame temperature can be enhanced. This can give rise to the HO_2 production effectively and then contribute to the increased NO_2 amount as shown in Fig. 6.30(a). Before the flame front is established completely, the simultaneous cooling effects of plate and ambient air on the burned gases can make for the existence of NO_2 in the flame based on the previous discussion. With the higher H_2 addition, in spite of the higher temperature of burned gases in the wall jet region as shown in Fig. 6.22, there is no doubt that the burned gases of flame can still suffer more intensive cooling effects due to its lower flame height. This can facilitate the NO_2 existence in the flame and contribute to the higher $EINO_2$ and NO_2/NOx ratio. Furthermore, since $OH+H_2=H_2O+H$ is a primary reaction for H production and OH consumption, the increased H_2 proportion can enhance the H atom concentration more evidently than that of OH radical as shown in Fig. 6.27. This means that the proportion of H atom in the radical pool is increased with the hydrogen addition. Combined with the stronger cooling effects on the burned gases at larger αH_2, the more evidently increased amount of H amount can exert comparatively stronger improvement on NO_2 production process and contribute to the higher NO_2/NOx ratio. Additionally, it is known that the prompt NO contribution is suppressed dramatically with the hydrogen enrichment at small *H* as shown Fig. 6.28(b). This can reduce the NO accumulation caused by the rapid NO formation, leading to the lower rising trend of NO amount with hydrogen addition at small *H* as shown in Fig. 6.24. As a result, hydrogen addition exerts the stronger improvement on NO_2 formation than that on the

NO_2 destruction, as well as the NO formation, at small *H*, which leads to evidently increased $EINO_2$ and then the rising trend of NO_2/NOx ratio at small *H*.

At large *H*, the reduced cooling effects of plate on burned gases can make for the establishment of high temperature zone, which can provide a suitable environment for the NO_2 destruction along the downstream direction. With the increased αH_2, the high temperature zone of burned gases is extended effectively due to the decreased flame height as shown in Fig. 6.23, which can promote the NO_2 destruction process in the flame. This contributes to gradually evident dropping trend of $EINO_2$ with *H* for the flame with increased hydrogen addition, as well as its declined NO_2/NOx ratio at large *H* as shown in Fig. 6.30. Additionally, thanks to the combined effects of the hydrogen addition and the moderate air entrainment at small *H*, the H atom production is likely to suffer less influence than that of OH radical at small *H*. As *H* is increased, the ambient air entrainment becomes more intensive while the premixed combustion is promoted, which exerts more effective improvement on the production of OH radical compared to that of H atom. Hence, the concentration of H atom is increased quite slightly while that of OH radical is enhanced more obviously in the flame at large *H* as shown in Fig. 6.31(a). It is thus known that the more evident increase in OH concentration can exert the stronger improvement on the NO_2 destruction process at large *H* while the HO_2 production in the air mixing regions can be improved less effectively due to the stable concentration of H atom. This means that the NO_2 destruction is further promoted at large *H* compared to that at small *H*. By contrast, the concentrations of H and OH radicals in the raw biogas flame could show the similar rising trend with the increased *H* as shown in Fig. 6.31(b). Consequently, compared to the raw biogas flame at large *H*, the biogas-hydrogen flame can suffer the stronger improvement on the NO_2 destruction process due to its more evidently

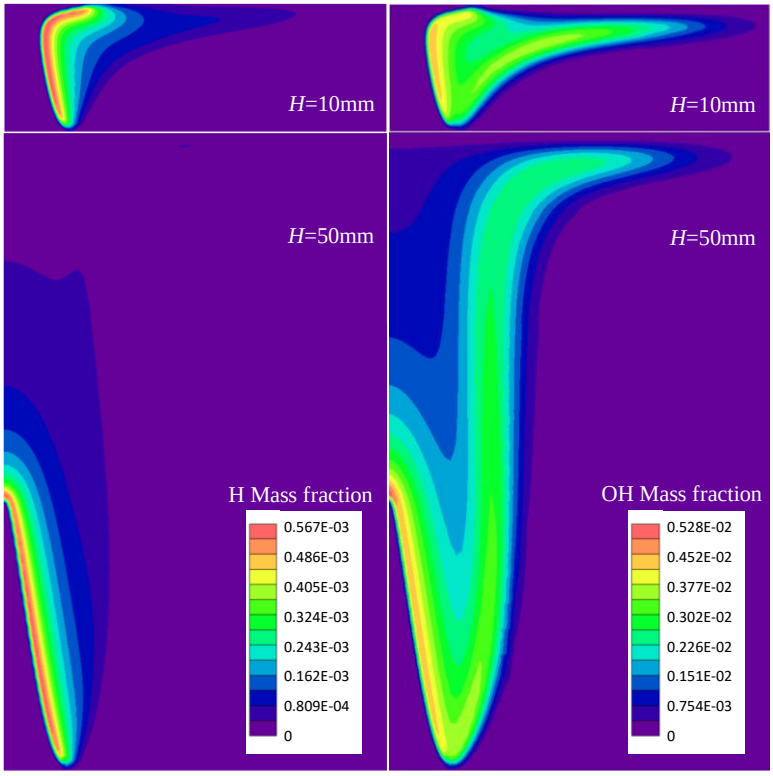

(a) H and OH distributions in the biogas-hydrogen flame at αH_2=0.6

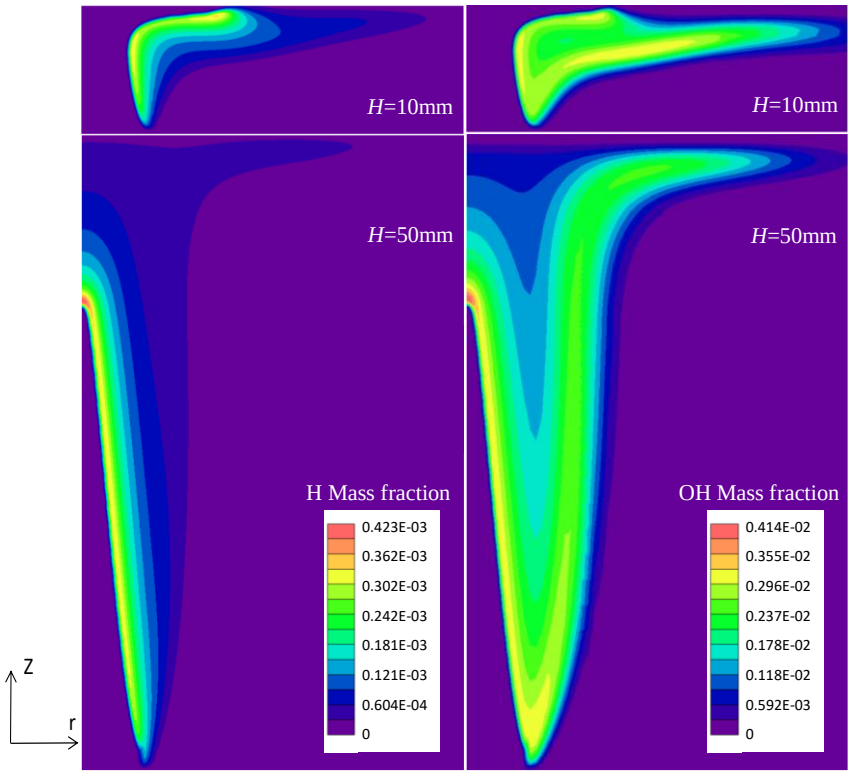

(b) H and OH distributions in the raw biogas flame

Fig. 6.31 Distributions of H and OH of premixed BG75-hydrogen flame at *Re*=1200 and ϕ =1.2.

increased OH concentration than that of H radical, as well as its extended post-flame region and enhanced flame temperature, which then gives rise to the declined NO_2/NOx ratio with increased αH_2. Besides, with the increased contribution of thermal NO at large *H*, the hydrogen addition can give rise to the thermal NO production at αH_2=0.6 more effectively compared to that of raw biogas flame, which results in the relatively higher increasing rate of EINOx at large *H* compared to that at small *H* as shown in Fig. 6.24. It is thus concluded that the increased hydrogen enrichment exerts the stronger improvements on the NO_2 destruction, as well as the NO formation, than that on the NO_2 production at large *H*, leading to the relatively smaller rising rate of $EINO_2$ at large *H* than that at small *H*, as well as the declined NO_2/NOx ratio at large *H*.

6.5 Effects of CO_2 percentage on the pollutant emissions

6.5.1 Effects of CO_2 percentage on the EICO

The images of premixed biogas and methane impinging flames at ϕ=1.2, αH_2=0.1 and *Re*=1000 are shown in Fig. 6.32. With the increased CO_2 proportion, it can be seen that the flame height is increased apparently due to the reduced laminar burning velocity while the flame becomes dimmer owing to the weakened combustion intensity. The EICO of these flames at different separated distances are compared in Fig. 6.33. As CO_2 is introduced into the unburned gases, the CO emission is decreased obviously when the flame front is affected by the impingement plate, but it is increased steadily at large *H*. Besides, the peak CO emission shows a considerable dropping trend as shown in Fig. 6.33. This can be explained as follows. Thanks to the higher proportion of methane and the reduced flame height, the premixed combustion of methane flame is more intensive and suffers less influence of cooling plate, which

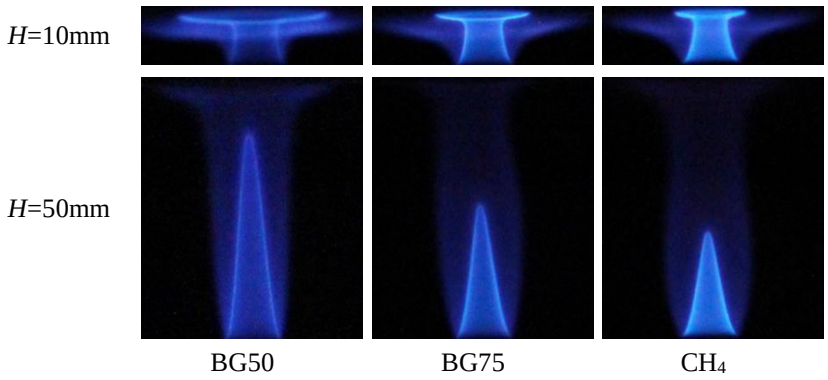

Fig. 6.32 Digital images of premixed biogas and methane impinging flames at ϕ=1.2, αH_2=0.1 and *Re*=1000.

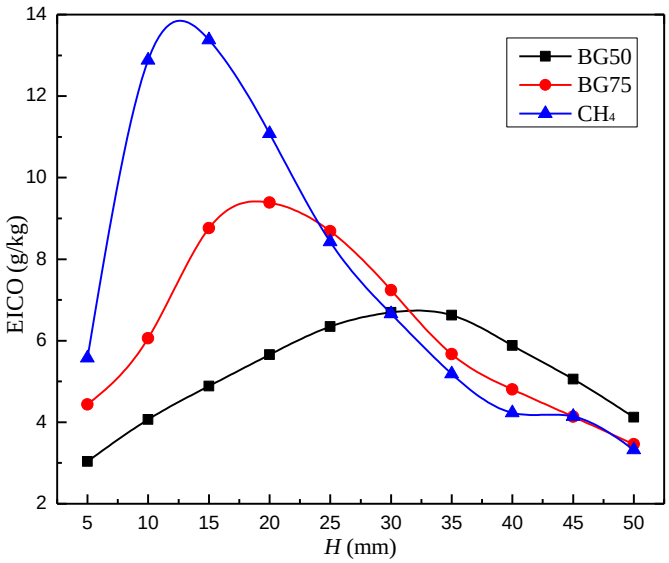

Fig. 6.33 EICO of premixed biogas impinging flames at αH_2=0.1, *Re*=1000 and ϕ=1.2.

can improve its CO production at small *H*. Furthermore, the burned gases of methane flame can suffer more cooling effects due to its lower flame height, which can suppress the CO oxidization in the post-flame region and contribute to the higher CO emission. Besides, although the increased CO_2 amount can suppress the CO oxidization and promote the CO emission in the biogas flame, the CO production can be suppressed considerably owing to the lower methane concentration and the weakened premixed combustion. The HCO distributions of BG50 and methane flames are compared in Fig. 6.34. It is seen that the HCO concentration of BG50 flame is much lower than that of methane flame due to the reduced methane proportion in the

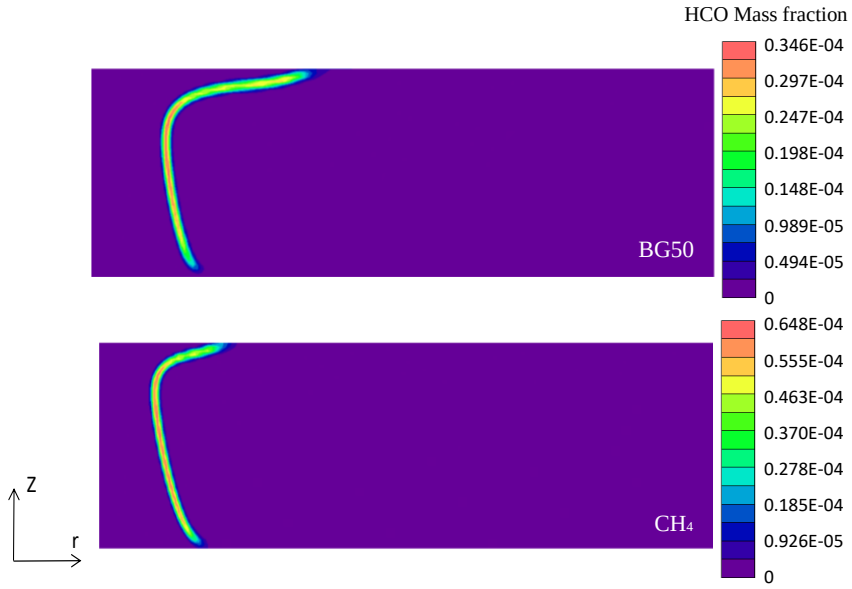

Fig. 6.34 HCO distributions of the BG50 and methane flames at αH_2=0.1, *Re*=1000 and ϕ =1.2 (*H*=10mm).

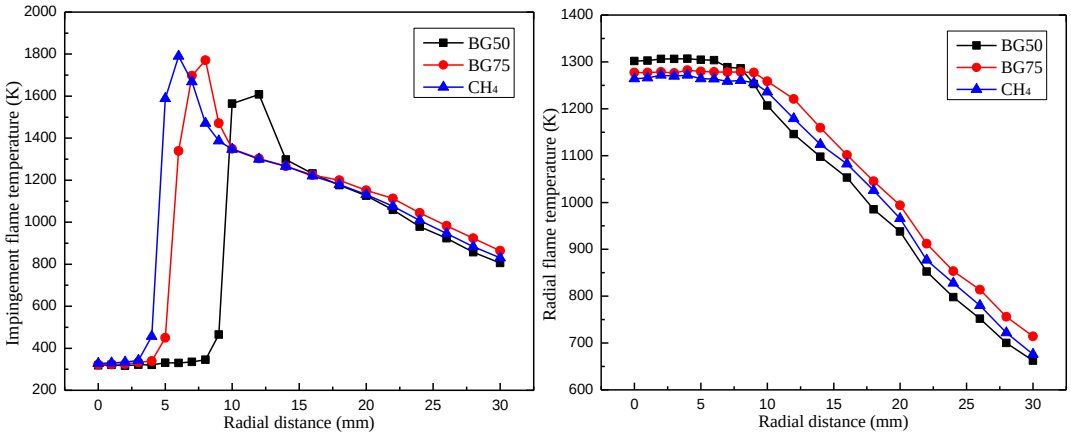

(a) *H*=10mm (b) *H*=50mm

Fig. 6.35 Radial flame temperature distribution of premixed biogas flames at αH_2=0.1, *Re*=1000 and ϕ =1.2.

fuel. Furthermore, it is noted that, compared to the methane flame, the BG50 flame has a larger part of flame front with the lower HCO concentration, which confirms that the BG50 flame suffers more intensive cooling effects on its premixed combustion due to its higher flame height. The cooling effects can thus reduce the total CO generation more effectively in the BG50 flame than that in the methane

flame. Hence, EICO is enhanced from BG50 flame to methane flame at small *H*. At large *H*, the EICO of methane flame is dropped rapidly owing to its higher flame temperature as shown Fig. 6.35, as well as the intensive air entrainment and the increased residence time. For the biogas flame, the lower flame temperature suppress the CO oxidization in the post flame region while the large amount of CO_2 in the flame can also inhibit the CO oxidization process via the reaction of $OH+CO=CO_2+H$. Furthermore, the longer flame height of biogas flame leads to the less residence time for CO_2 formation. As a consequence, the EICO is enhanced for biogas flame at large *H* as shown in Fig. 6.33.

6.5.2 Effects of CO_2 percentage on the EINOx

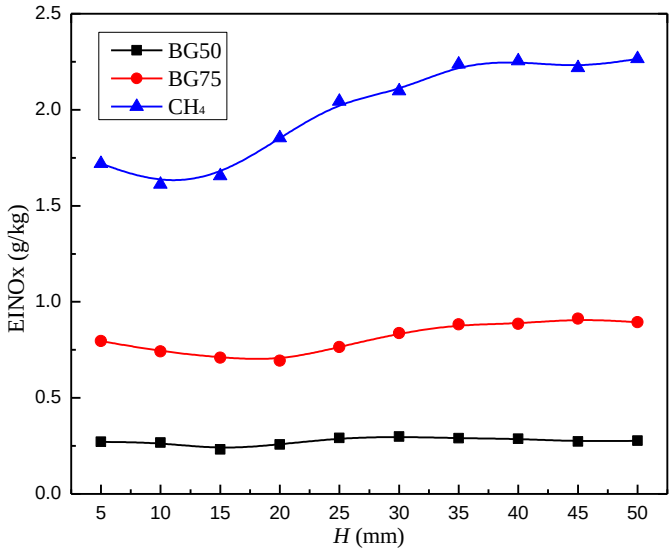

Fig. 6.36 EINOx of premixed biogas impinging flames at ϕ=1.2, αH_2=0.1 and *Re*=1000.

The EINOx of premixed biogas impinging flames at ϕ=1.2, αH_2=0.1 and *Re*=1000 are shown in Fig. 6.36. Obviously, the NOx emission is enhanced apparently as the CO_2 proportion is decreased in the fuel, which can be attributed to the increased methane concentration and the increased flame temperature. Specifically, the NO amounts formed via different routes are provided in Fig. 6.37. As CO_2 proportion is

declined, thanks to the increased methane concentration and the enhanced flame temperature, the increased amount of related intermediates can promote the initiation reactions of NO formation effectively while the increased temperature can accelerate the NO formation process in the flame. Besides, the flame height is decreased due to the increased laminar burning velocity from BG50 flame to methane flame. This allows the longer residence time and more air entrainment for NO formation in the post-flame region of methane flame.

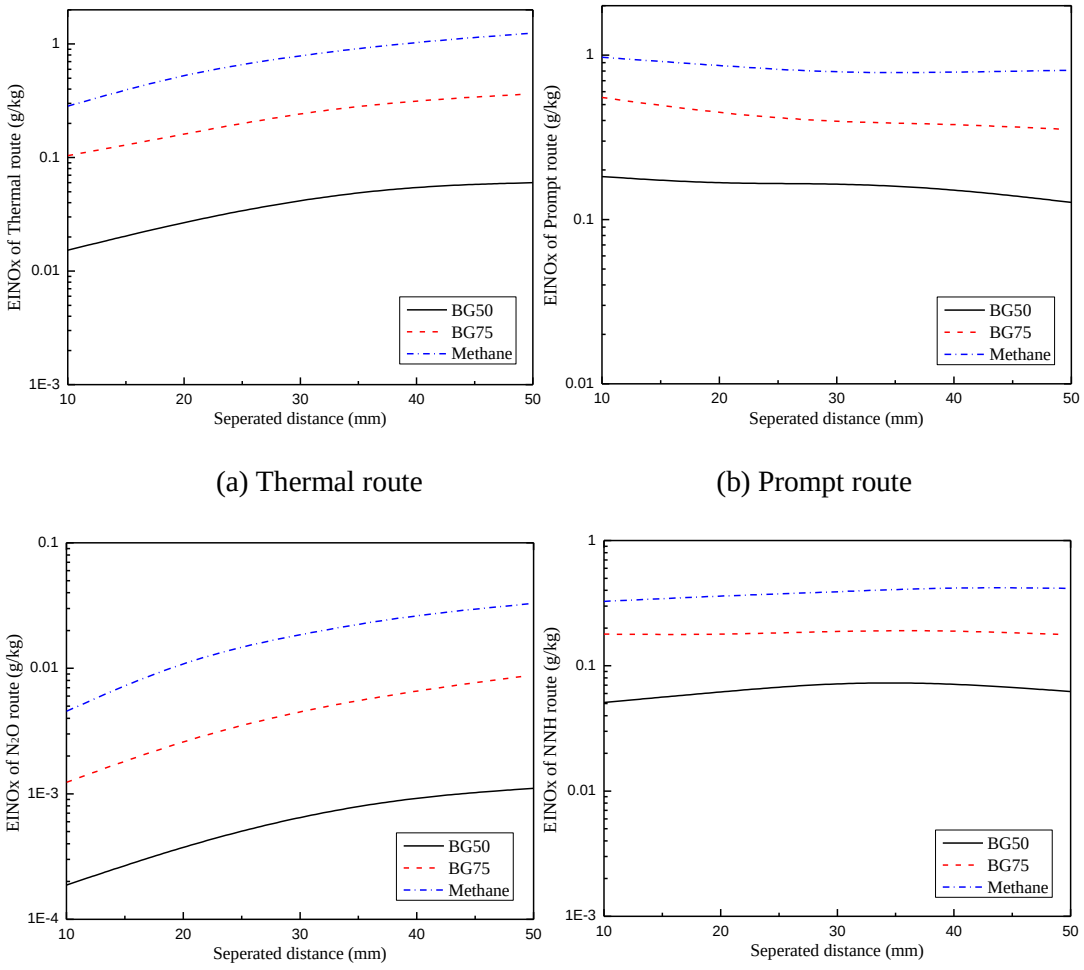

(a) Thermal route (b) Prompt route

(c) N_2O route (d) NNH route

Fig. 6.37 EINOx of different routes for the biogas and methane flames at αH_2=0.1, *Re*=1000 and ϕ=1.2.

The variations of relative importance of different routes on total NO formation for these flames are compared in Fig. 6.38. It can be seen that thermal and N_2O routes become increasingly significant with the decreased CO_2 concentration, while that of prompt and NNH routes are decreased steadily. This can be explained as follows. For the prompt route, its initiation reactions are more likely to proceed near the premixed combustion zone based on the above discussion. It is thus known that the initiation reactions of prompt route should be dominated by the premixed combustion process and suffers the moderate influence of diffusion combustion process. This means that initiation reactions in the premixed combustion process predominate the prompt NO formation in the flame, while residence time and high temperature zone of burned gases can exert limited effects on its production process. Similarly, based on the previous discussion, it is known that the NO production via NNH route suffers moderate effects of the post-flame environment due to the restriction of its initiation reactions. Whereas, considering the initiation reactions of thermal and N_2O routes, the NO production of these two mechanisms can be initialized in an extensive zone compared to that of prompt and NNH routes, which implies that the NO formation via thermal and N_2O routes can be affected by both premixed combustion process and the post-flame environment. Furthermore, since thermal NO production requires the high temperature and relatively longer residence time to proceed, the post-flame environment including residence time and high temperature zone can play a more dominated role in thermal NO production compared to other routes. Consequently, as the CO_2 concentration is declined in the flame, the prompt and NNH routes are primarily promoted by the increased amount of active radicals and the enhanced flame temperature. By contrast, for the thermal and N_2O routes, apart from improvements of the increased active radicals and enhanced flame temperature, they can be further

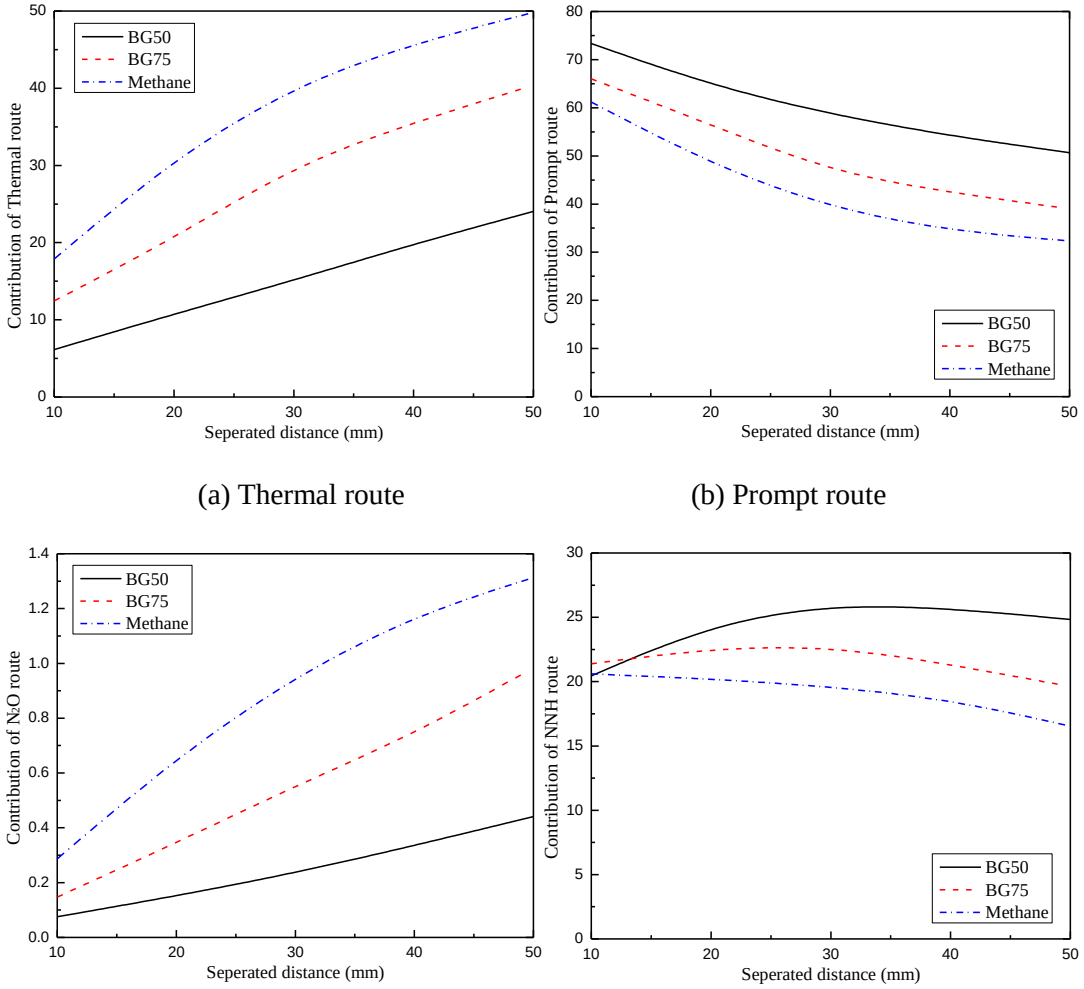

(a) Thermal route (b) Prompt route

(c) N_2O route (d) NNH route

Fig. 6.38 Contributions of different routes for the biogas and methane flames at αH_2=0.1, *Re*=1000 and ϕ=1.2.

improved effectively by the larger high temperature zone, more intensive air mixing and the longer residence time. Therefore, as CO_2 is reduced in the fuel, the contributions of thermal and N_2O routes on NO formation are increased, while that of prompt and NNH routes are decreased as show in Fig. 6.38. In addition, it is noted that the rising rate of EINOx with *H* is increased from BG50 flame to methane flame as shown in Fig. 6.36. This is attributed to the contribution variations of prompt NO and thermal NO. It is known that prompt NO and thermal NO can play significant roles at small *H* and large *H*, respectively. As the methane concentration is increased, the NO amounts of prompt and thermal routes can be both enhanced as shown in Fig. 6.37.

However, due to the decreased contribution of prompt NO and the increased contribution of thermal NO as shown in Fig. 6.38, the improvement of enhanced methane concentration on prompt NO can enhance the total NO amount less effectively at small *H*, while the improvement on thermal NO can increase the total NO amount more obviously at large *H*. Hence, the EINOx is promoted less effectively at small *H* compared to that at large *H*, which leads to the increased rising rate of EINOx with *H* as methane proportion in the fuel is enhanced.

6.5.3 Effects of CO_2 percentage on the $EINO_2$ and NO_2/NOx ratio

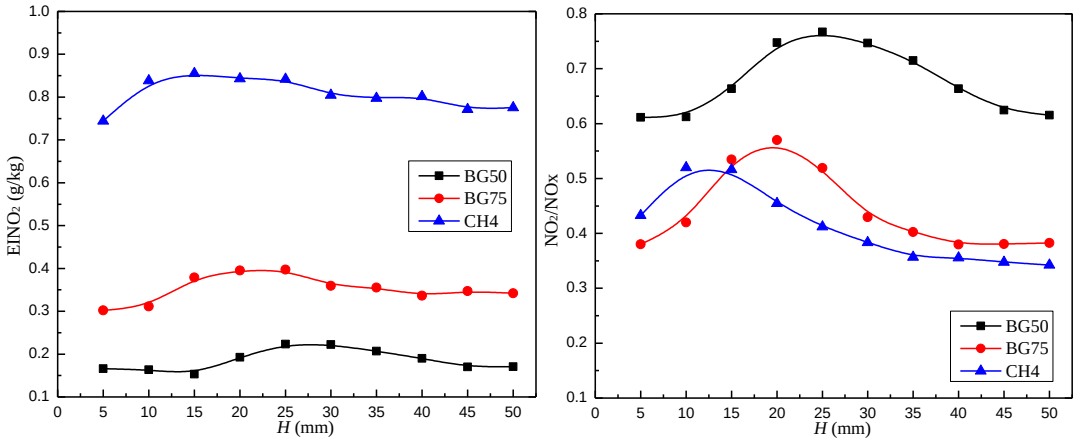

(a) $EINO_2$ (b) NO_2/NOx

Fig. 6.39 NO_2 formation of premixed biogas impinging flames at ϕ=1.2, αH_2=0.1 and *Re*=1000.

The $EINO_2$ and NO_2/NOx ratio of premixed biogas impinging flames at ϕ =1.2, αH_2=0.1 and *Re*=1000 are shown in Fig. 6.39. There is no surprise that the NO_2 amount is enhanced for the flame with lower CO_2 proportion owing to the improved NO production and the increased HO_2 concentration. However, for the NO_2/NOx ratio, it is highest for the BG50 flame in the whole range of the separated distance, while its value of BG75 flame is lower than that of methane flame at small *H* but is higher at large *H* as shown in Fig. 6.39(b). The highest NO_2/NOx ratio of BG50 flame is

primarily attributed to its lowest flame temperature and the lowest concentrations of active radicals. Specifically, the low flame temperature can make for the NO_2 existence in the burned gases by suppressing the forward reactions of $OH+NO_2=HO_2+NO$ and $H+NO_2=OH+NO$ which require the comparatively high temperature. Furthermore, due to the combined effects of low flame temperature and decreased active radicals, the NO production can be hampered considerably in the flame, while the HO_2 production in the air mixing region, as well as the NO_2 formation, can suffer less effects since it can proceeds at the lower temperature. Consequently, the BG50 flame can maintain a higher level of NO_2/NOx ratio as *H* is increased. At small *H*, the cooling effects of impingement plate on burned gases become more intensive from BG50 flame to methane flame due to the reduced cool core as shown Fig. 6.32. This means that the methane flame suffers more intensive cooling effects of plate which can reduce the temperature of burned gases more effectively as shown in Fig. 6.35(a) and then give rise to the existence of NO_2 in the post-flame region. Furthermore, considering the stronger cooling effects on the burned gases of the methane flame, the increased H atom can improve the NO_2 formation more effectively than that on the NO_2 destruction process due to the different temperatures required for reactions. Besides, due to the reduced contribution of prompt NO, the NO accumulation at small *H* caused by the rapid NO formation can be relatively weakened for the methane flame. Thus the increased methane concentration exerts the stronger improvement on NO_2 formation than that on the NO_2 destruction, as well as the NO formation, at small *H*, leading to that the methane flame has a higher level of NO_2/NOx ratio than that of BG75 flame at small *H*. At large *H*, there exist a relatively larger high temperature zone and the higher concentration of OH radical in the methane flame as shown in Fig. 6.40. Thanks to the extended post-flame

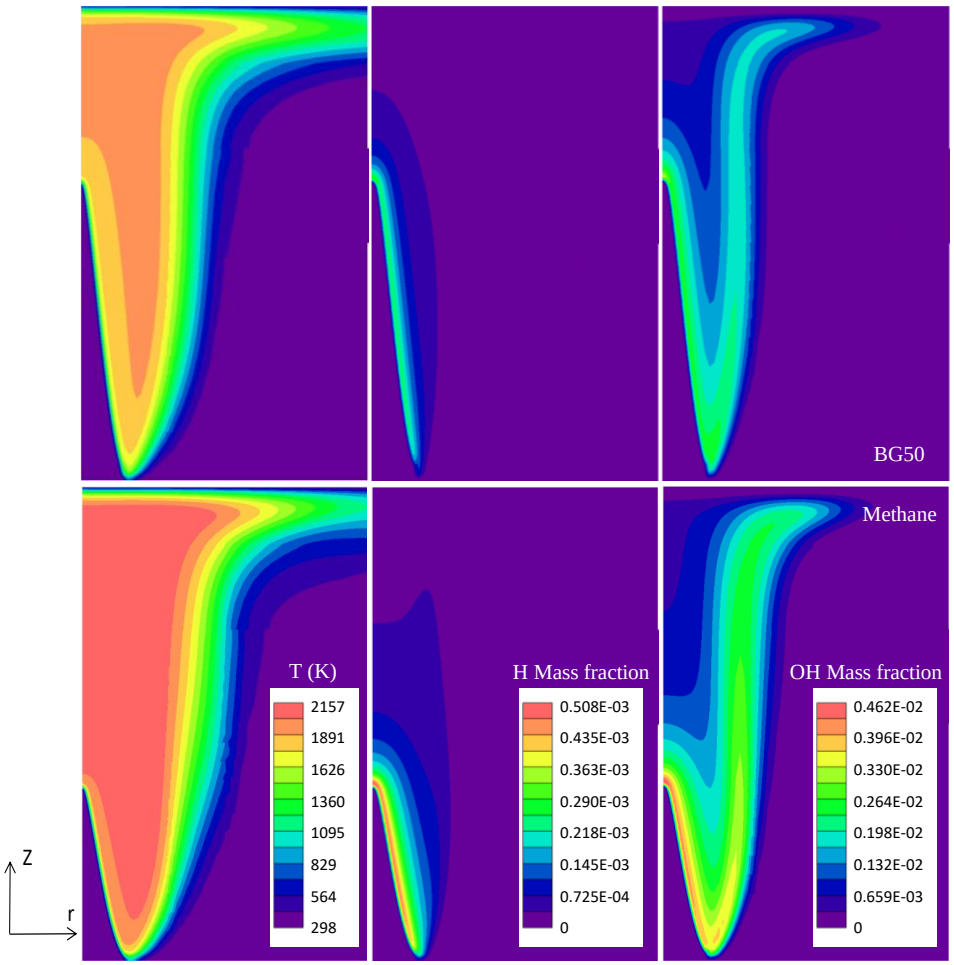

Fig. 6.40 The calculated temperature fields, H and OH distributions of BG50 (upper) and methane (lower) flames at αH_2=0.1, *Re*=1000 and ϕ=1.2 (*H*=50mm).

region, the increased amount of H and OH radicals and the enhanced flame temperature can give rise to the NO_2 destruction in the burned gases more effectively at large *H* compared to that on the NO_2 production. Additionally, due to the increased importance of thermal NO, the improvement of increased methane concentration on thermal NO can accelerate the NO accumulation in the methane flame more effectively at large *H*. This means that the improvement on NO formation, as well as NO_2 destruction, is stronger than that on NO_2 formation at large *H*. Consequently, the methane flame has the lowest NO_2/NOx ratio at large *H*. With the increased CO_2 percentage, the NO_2 destruction in the burned gases is suppressed by the decreased flame temperature, lower OH concentration and the reduced high temperature zone.

Besides, the NO accumulation can be weakened due to the reduced contribution of thermal NO at large *H*. Eventually, the NO_2/NOx ratio is enhanced from methane flame to BG50 flame at large *H* as shown in Fig. 6.39(b).

6.6 Summary

Experiments and numerical simulations were both conducted to study the pollutant emissions of laminar premixed biogas-hydrogen flames. The total emissions of biogas-hydrogen flames were measured experimentally, and then the emission indexes (EICO, EINOx and $EINO_2$) and the NO_2/NOx ratio were calculated. In the numerical simulation, the NO formation via four major routes of thermal NO, prompt NO, NNH route and N_2O route were isolated and calculated, and the contributions of these routes on the total EINOx were obtained. Effects of nozzle-to-plate distance, equivalence ratio, Reynolds number, hydrogen addition and CO_2 percentage on the emission formation of biogas-hydrogen flames were investigated quantitatively. The major results are summarized as follows:

As *H* is increased, the rising trend and dropping trend of EICO of the biogas-hydrogen flame are caused by the improved premixed combustion and the improved CO oxidization, respectively. The NO formed via thermal, NNH and N_2O routes are increased with *H* due to the extended high temperature region, more intensive air mixing and longer residence time, while the prompt NO is dropped owing to the suppression of improved premixed combustion on its initiation reactions. In addition, the contributions of N_2O and thermal routes on the NO production are enhanced with *H*, while that of prompt NO is weakened steadily. The contribution of NNH route keeps a comparatively stable level in the whole range of *H*. With the increased *H*, the enhanced $EINO_2$ and the NO_2/NOx ratio are caused by the improvement of more air

entrainment on the NO_2 formation, while their dropping trends at large *H* are caused by the extended high temperature region promoting the NO formation and the NO_2 destruction.

The EICO of biogas-hydrogen flame can be increased significantly with ϕ due to the increasingly incomplete fuel oxidization. The contributions of different routes on NO formation in the biogas-hydrogen flame are affected considerably by the equivalence ratio. The thermal NO and NNH route play the significant roles in NO formation at ϕ=0.8 and 1.0, while prompt NO and thermal NO dominate the EINOx variation at fuel-rich condition. This finally leads to the different variations of EINOx with *H* as ϕ is increased. Furthermore, the rising trend of EINOx with ϕ is dominated by the improved prompt NO production. The $EINO_2$ of biogas-hydrogen flame is enhanced with ϕ, which is primarily caused by the promoted HO_2 production in the air mixing region. Furthermore, the variation of the NO_2/NOx ratio at different ϕ is codetermined by the H and O_2 concentrations in the air mixing region, and the contribution variation of different routes on the NO formation.

With the increased *Re*, the declined EICO of the biogas-hydrogen flame at small *H* is resulted from the weakened premixed combustion suppressing the CO production, while its rising trend at large *H* is attributed to the less residence time and insufficient oxidizer. The increased EINOx with *Re* is mainly caused by the improved prompt NO production. Furthermore, as primary contributors on the NO formation at the fuel-rich condition, the importance of thermal NO is decreased with the increased *Re*, while that of prompt NO is enhanced steadily. The $EINO_2$ and the NO_2/NOx ratio of the biogas-hydrogen flame are decreased with the increased *Re* at small *H* due to the stronger suppression of cooling effects on the NO_2 destruction, as well as the

suppressed prompt NO production at small *H*. Meanwhile, the rising trends of $EINO_2$ and the NO_2/NOx ratio at large *H* are caused by the accelerated HO_2 production in the air mixing region and less residence time suppressing the NO_2 destruction, as well as the suppressed thermal NO formation.

With the hydrogen addition, the EICO of the biogas-hydrogen flame is enhanced steadily due to the higher reactivity of hydrogen which suppresses the CO oxidization by competing for the OH radical. Besides, the hydrogen addition can lead to the evidently enhanced flame temperature and the increased amount of active radicals which can accelerate the NO production via four routes, finally the total EINOx of the biogas-hydrogen flame. The contribution of prompt NO is decreased with hydrogen enrichment, while that of other routes are increased steadily. Additionally, $EINO_2$ is enhanced steadily with H_2 addition thanks to the improved HO_2 production in the air mixing region. The hydrogen addition results in the increased and decreased NO_2/NOx ratio at small and large *H*, respectively. The rising trend are caused by the weakened improvement on the prompt route and the stronger improvement of higher H/OH ratio on the NO_2 formation, while the dropping trend can be attributed to the weakened improvement on the NO_2 formation and the improved NO_2 destruction process, as well as the effectively improved thermal NO.

With the increased methane percentage in the biogas, the enhanced EICO at small *H* is primarily caused by its better premixed combustion and CO production, while the decreased EICO at large *H* can be resulted from the larger post-flame region, intensive air entrainment and longer residence time. In addition, the EINOx of biogas-hydrogen flame is improved with enhanced methane proportion due to the increased amount of active radicals and higher flame temperature. The contributions of thermal NO and

N_2O route are increased with enhanced methane proportion, while that of prompt NO and NNH route are dropped gradually. Besides, the $EINO_2$ of the biogas-hydrogen flame is increased with the increased methane concentration owing to the higher flame temperature and more available H atom to produce HO_2. In addition, the reduced NO_2/NOx ratio with increased methane concentration is primarily dominated by the increased temperature and larger post-flame region which accelerate the NO_2 destruction effectively. Furthermore, the contribution variations of prompt NO and thermal NO can also exert some influence on the NO_2/NOx ratio.

7 Conclusions and Recommendations

7.1 Conclusions

The primary objective of this study is to improve the understanding on the combustion, thermal and emission characteristics of biogas-hydrogen fuels and then promote its applications in the practical combustion facilities. The laminar premixed Bunsen flame is adopted to burn the biogas-hydrogen fuel in consideration of its simple flame structure and the important role in the combustion research. Both experiments and numerical simulations were carried out to facilitate the investigation on combustion, thermal and emission characteristics of biogas-hydrogen flames. Heat fluxes, flame temperature and pollutant emissions of biogas-hydrogen flames were measured experimentally while the computational models were developed to calculate the heat release rate, relative significances of exothermic reactions and pollutant emissions of biogas-hydrogen flames. Effects of fuel composition, nozzle-to-plate distance, equivalence ratio and Reynolds number on the heat release, heat transfer and pollutant emission characteristics of biogas-hydrogen flames were investigated quantitatively. This study contributes several valuable insights and findings to improving the understanding on the fuel features of biogas-hydrogen mixture and also provides some useful guidelines for domestic heating applications of the biogas-hydrogen mixture. The primary conclusions are summarized as follows.

7.1.1 Heat release characteristics of biogas-hydrogen combustion

The complete combustion results in the maximum global HRR of the biogas-hydrogen flame at ϕ=1.0, while the exothermic recombination of intermediates gives rise to the enhanced HRR in the post flame region at the fuel-rich condition. For the biogas-

hydrogen combustion, the paramount endothermic reaction is $H+O_2=OH+H$ while $O+CH_3=H+CH_2O$, $H+CH_3(+M)=CH_4(+M)$, $OH+H_2=H+H_2O$, $OH+CO=H+CO_2$ and $O+CH_3=>H+H_2+CO$ play significant roles in total HRR at different ϕ. Additionally, $H+O_2+H_2O=HO_2+H_2O$ and $OH+HO_2=O_2+H_2O$ cannot be neglected for flames at ϕ=0.8 and ϕ=1.0, while $H+OH+M=H_2O+M$ becomes more significant at ϕ=1.0 and ϕ=1.2 compared to that at fuel-lean condition. Besides, $2CH_3(+M)=C_2H_6(+M)$ can play an increasingly important role at the fuel-rich condition.

With the H_2 enrichment, $H+HO_2=2OH$ and $H+O_2=OH+H$ in the biogas-hydrogen flame can be accelerated effectively, which can increase the amount of active radicals at both low and high temperatures and then lead to the higher HRR. In addition, with the H_2 addition, contributions of $OH+H_2=H+H_2O$ and $OH+H+M=H_2O+M$ on HRR are enhanced most evidently, indicating their significant roles in the hydrogen enriched biogas combustion.

As the CO_2 proportion in the biogas is increased, the dropping trend of HRR is predominated by its dilution/thermal effect and further aggravated by its chemical effects. Additionally, with the increased CO_2 in the biogas, the enhanced contributions of $H+CH_3(+M)=CH_4(+M)$ and $2CH_3(+M)=C_2H_6(+M)$ on total HRR are dominated by the dilution/thermal effect, while the decreased contributions of $OH+CO=H+CO_2$ and $H+OH+M=H_2O+M$ are determined by the chemical effect and dilution/thermal effect, respectively. Furthermore, $H+CH_3(+M)=CH_4(+M)$, $2CH_3(+M)=C_2H_6(+M)$ and $OH+H_2=H+H_2O$ become increasingly significant on HRR as CO_2 is increased in the biogas-hydrogen flame.

For premixed biogas-hydrogen flames, the $O+CH_3$ reaction is found to have a stable contribution on HRR, and the $O\times CH_3$ product is demonstrated to have the best

performance on the single-valued prediction of HRR at the tested conditions, which makes it to be the most reliable indicator to reflect the HRR variation in the premixed flame with the unclear equivalence ratio. The best performance of the $O \times CH_3$ product is attributed to that concentrations of O and CH_3 can reflect the consumptions of oxidizer and fuel during the combustion process while the $O+CH_3$ reaction is a primary and stable contributor on the total HRR. HCO is still a reliable marker whose correlation with HRR is insensitive to the equivalence ratio and the fuel composition. Although the $H \times CH_2O$ and $H \times HO_2$ products have an improved linearity with the local HRR than that of the $OH \times CH_2O$ product, these three markers are not eligible for the single-valued prediction on the HRR due to their variable correlations at different equivalence ratios. The $OH \times CH_2O$ product has been adopted for the HRR visualization of premixed flames extensively, but its prediction uncertainty on HRR cannot be neglected under some conditions such as in the stratified turbulent flame which allows the simultaneous existence of different equivalence ratios.

7.1.2 Impingement heat transfer of biogas-hydrogen flames

With the increased H_2, the total heat transfer rate of biogas-hydrogen flame can be enhanced by up to 50%. Besides, the optimum hydrogen addition of the BG75 flame is recommended to be αH_2=0.3 based on our work, which can exert approximately 20%-30% improvement on total heat transfer rates at all tested heating distances. The improvements of hydrogen enrichment on the heating performance are exerted by the enhanced flame temperature and stronger fuel diffusivity. The higher temperature can improve heat transfer process directly due to the larger temperature difference. Meanwhile, the strong diffusivity of hydrogen can result in the wider high temperature zone which can lead to the enhanced heat fluxes in the wall jet region.

The influences of CO_2 on the combustion and heat transfer process of biogas-hydrogen flames can be exerted via chemical effects and dilution/thermal effects. Its reactivity can inhibit the CO oxidization through the reaction OH+CO=CO_2+H while the existence of CO_2 can reduce the fraction of combustible fuel and lead to the reduced heat release. Additionally, the flame temperature can be further decreased owing to the larger specific heat capacity of CO_2. Whereas, a suitable proportion of CO_2 in the biogas can reduce the dropping rate of flame temperature in the wall jet region, which is caused by its larger specific heat capacity, as well as the less air entrainment owing to the increased flame height. This gives rise to the better heating performance of BG75-hydrogen flame than that of the methane-hydrogen flame. Hence, BG75-hydrogen is an eligible substitute of methane-hydrogen for heating purpose when using the Bunsen type flame.

Based on the experimental data, an empirical correlation to determine the optimal heating distance of biogas-hydrogen flames is obtained as a function of Pr, u/S_L and ϕ:

$$H_m / D = 1.2152 Pr^{0.4} \left(\frac{u}{S_L}\right)^{0.6575} \left(\phi^3 \left|\frac{1}{2} - \frac{\phi}{\phi+1}\right| + \frac{1}{2}\right)^{1.52386} \quad (3.7 < u/S_L < 7.7,\ 0.8 < \phi < 1.4)$$

This correlation is able to predict the optimal heating distance of the laminar premixed biogas-hydrogen Bunsen flame with a satisfactory accuracy.

7.1.3 Pollutant emissions of biogas-hydrogen impinging flames

As H is increased, the EICO of the biogas-hydrogen flame is increased initially and then decreased steadily, which is caused by the improved premixed combustion and the improved CO oxidization, respectively. The NO production via thermal, NNH and N_2O routes are increased with H due to the extended high temperature region, more

intensive air mixing and longer residence time, while the prompt NO is dropped owing to the suppression of improved premixed combustion on the initiation reactions of prompt NO. Furthermore, the contributions of N_2O and thermal routes on NO formation are enhanced with *H*, while that of prompt NO is decreased steadily. The contribution of NNH route can keep a comparatively stable level in the whole range of *H*. Besides, with the increased *H*, the rising trends of $EINO_2$ and the NO_2/NOx ratio are attributed to the improvement of more intensive air entrainment on the NO_2 formation, while their dropping trends at large *H* are induced by the extended high temperature region which promotes the NO formation and the NO_2 destruction.

The EICO of the biogas-hydrogen flame can be increased significantly with ϕ due to the increasingly incomplete fuel oxidization. The contributions of different routes on NO formation are affected considerably by the equivalence ratio. The thermal NO and NNH route play the significant roles in NO formation at ϕ=0.8 and 1.0, while prompt NO and thermal NO can dominate the EINOx variation at fuel-rich condition. This leads to the different variations of EINOx with *H* as ϕ is increased. Furthermore, the increased prompt NO formation with ϕ finally results in the increased EINOx of biogas-hydrogen flames. The $EINO_2$ of the biogas-hydrogen flame is enhanced with the increased ϕ, which is primarily caused by the promoted HO_2 production in the air mixing region. In addition, the variation of the NO_2/NOx ratio at different ϕ is determined by combined effects of the H and O_2 concentrations in the air mixing region, and the contribution variation of different routes for NO formation.

With the increased *Re*, the declined EICO of the biogas-hydrogen flame at small *H* is caused by the weakened premixed combustion leading to the suppressed CO production, while the rising trend at large *H* is resulted from less residence time and

insufficient oxidizer. Besides, the increased EINOx of the biogas-hydrogen flame with *Re* is attributed to the improved prompt NO production. Furthermore, as the primary contributors on the NO formation at the fuel-rich condition, the contribution of thermal NO is decreased with the increased *Re*, while that of prompt NO is enhanced steadily. Additionally, the $EINO_2$ and the NO_2/NOx ratio of the biogas-hydrogen flame are decreased with *Re* at small *H*, which is resulted from the stronger suppression of cooling effects on the NO_2 destruction, as well as the suppressed prompt NO production. At large *H*, the increased $EINO_2$ with *Re*, as well as the NO_2/NOx ratio, is resulted from the improved HO_2 production in the air mixing region and less residence time suppressing the NO_2 destruction, as well as relatively suppressed thermal NO production.

With the hydrogen addition, the EICO of biogas-hydrogen flame is enhanced steadily due to the higher reactivity of hydrogen which suppresses the CO oxidization by competing for OH radical. Due to the increased H_2, the evidently enhanced flame temperature and the increased amount of active radicals give rise to the improved NO production via four routes, finally the total EINOx of the biogas-hydrogen flame. Furthermore, the contribution of prompt NO is decreased with the hydrogen enrichment, while that of other routes are increased steadily. $EINO_2$ is enhanced steadily with the hydrogen addition thanks to the improved HO_2 production in the air mixing region. The hydrogen addition leads to the increased and decreased NO_2/NOx ratio at small and large *H*, respectively. The rising trend is caused by the weakened improvement on prompt route and the stronger improvement of higher H/OH ratio on the NO_2 formation, while the dropping trend can be attributed to the weakened improvement on the NO_2 formation and the improved NO_2 destruction process, as well as the effectively improved thermal NO.

With the reduced CO_2 in the biogas, the enhanced EICO of the biogas-hydrogen flame at small *H* is primarily caused by its better premixed combustion improving the CO production, while the decreased EICO at large *H* can be resulted from the larger post-flame region, more intensive air entrainment and longer residence time. With the same H_2 addition, the EINOx is elevated from BG50-hydrogen flame to methane-hydrogen flame thanks to the increased amount of active radicals and higher flame temperature. The contributions of thermal NO and N_2O route are increased with the reduced CO_2 in the biogas, while that of prompt NO and NNH route are dropped gradually. In addition, the $EINO_2$ of the biogas-hydrogen flame is increased with the reduced CO_2 in the biogas owing to the higher flame temperature and more available H atom to produce HO_2. The reduced NO_2/NOx ratio with the decreased CO_2 in the biogas is mainly resulted from the enhanced temperature and the larger post-flame region which can accelerate the NO_2 destruction effectively. Furthermore, the contribution variations of prompt NO and thermal NO can also exert some influences on the NO_2/NOx ratio.

7.2 Recommendations

In this study, the heat release characteristics of biogas-hydrogen flames were investigated utilizing the one-dimensional laminar premixed flame. In the real combustion facilities, turbulent flames can exist more generally than the laminar flames. Since the laminar premixed Bunsen flame is an ideal prototype of turbulent premixed flame, the effects of flame stretch on the heat release characteristics should be studied utilizing the flame tip of laminar premixed Bunsen flame in the future. This can further improve the understanding on the heat release characteristics of biogas-hydrogen combustion and guide its practical applications. Furthermore, the ability of

the $O \times CH_3$ product to predict the HRR should be further evaluated in the turbulent flames and diffusion flames considering that the single-valued prediction on HRR is quite critical to these flames due to their complex combustion process. In addition, it is suggested that the experiments on HRR marker should be conducted in order to support the numerical study and further verify the applicability of the suggested markers.

The heat transfer characteristics of laminar premixed biogas-hydrogen flames were discussed utilizing the flat impingement plate. Considering the practical applications, it is necessary to conduct more studies to investigate the heat transfer characteristics of biogas-hydrogen flames under different conditions such as the inclined plate and the inclined flames, which can facilitate the applications of biogas-hydrogen flames in heating facilities. In addition, biogas contains a large amount of CO_2 while hydrogen enrichment can enhance the H_2O production. As the triatomic molecules, the radiation heat transfer of biogas-hydrogen flames is suggested to be studied in the future, which can promote the understanding on the radiation features of biogas-hydrogen flames and expand its application in heating facilities. In addition, the correlation of the optimal heating distance should be further validated and modified by utilizing more flames under various conditions.

The overall pollutant emissions of laminar premixed biogas-hydrogen flames were investigated quantitatively in this work, which provides a fundamental understanding on the emission characteristics of biogas-hydrogen flames. It is suggested that the emission formation process in the laminar premixed biogas-hydrogen flames can be studied more elaborately by considering the flame stretch effects on the local emission production. Due to high reactivity and diffusivity of hydrogen, as well as the large

amount of CO_2, the emission formation at the flame tip of the laminar premixed biogas-hydrogen flame might be affected considerably by the flow strain and flame curvature. This can facilitate the understanding on the emission formations in the turbulent biogas-hydrogen flames and then help to figure out the critical factors affecting the emission formations of the biogas-hydrogen combustion and control its pollutant emissions.

References

[1] Shafiee S, Topal E. When will fossil fuel reserves be diminished? *Energy Policy*. 2009;37:181-9.

[2] Budzianowski WM, Chasiak I. The expansion of biogas fuelled power plants in Germany during the 2001-2010 decade: Main sustainable conclusions for Poland. *Journal of Power Technologies*. 2011;91:102-13.

[3] Lantz M, Svensson M, Björnsson L, Börjesson P. The prospects for an expansion of biogas systems in Sweden—Incentives, barriers and potentials. *Energy Policy*. 2007;35:1830-43.

[4] Patterson T, Esteves S, Dinsdale R, Guwy A. An evaluation of the policy and techno-economic factors affecting the potential for biogas upgrading for transport fuel use in the UK. *Energy Policy*. 2011;39:1806-16.

[5] Makareviciene V, Sendzikiene E, Pukalskas S, Rimkus A, Vegneris R. Performance and emission characteristics of biogas used in diesel engine operation. *Energy Conversion and Management*. 2013;75:224-33.

[6] Nadaletti WC, Cremonez PA, de Souza SNM, Bariccatti RA, Belli Filho P, Secco D. Potential use of landfill biogas in urban bus fleet in the Brazilian states: A review. *Renewable and Sustainable Energy Reviews*. 2015;41:277-83.

[7] Chen L, Zhao L, Ren C, Wang F. The progress and prospects of rural biogas production in China. *Energy Policy*. 2012;51:58-63.

[8] Poeschl M, Ward S, Owende P. Prospects for expanded utilization of biogas in Germany. *Renewable and Sustainable Energy Reviews*. 2010;14:1782-97.

[9] Yang L, Ge X, Wan C, Yu F, Li Y. Progress and perspectives in converting biogas to transportation fuels. *Renewable and Sustainable Energy Reviews*. 2014;40:1133-52.

[10] Lim C, Kim D, Song C, Kim J, Han J, Cha JS. Performance and emission characteristics of a vehicle fueled with enriched biogas and natural gases. *Applied Energy*. 2015;139:17-29.

[11] Divya D, Gopinath LR, Merlin Christy P. A review on current aspects and diverse prospects for enhancing biogas production in sustainable means. *Renewable and Sustainable Energy Reviews*. 2015;42:690-9.

[12] Anggono W, Wardana I, Lawes M, Hughes K, Wahyudi S, Hamidi N. Laminar Burning Characteristics of Biogas-Air Mixtures in Spark Ignited Premix Combustion. *Journal of Applied Sciences Research*. 2012;8 4126-32.

[13] Hosseini SE, Wahid MA. Development of biogas combustion in combined heat and power generation. *Renewable and Sustainable Energy Reviews*. 2014;40:868-75.

[14] Natarajan J, Lieuwen T, Seitzman J. Laminar flame speeds of H2/CO mixtures: Effect of CO2 dilution, preheat temperature, and pressure. *Combustion and Flame*. 2007;151:104-19.

[15] Xie Y, Wang J, Xu N, Yu S, Huang Z. Comparative study on the effect of CO2 and H2O dilution on laminar burning characteristics of CO/H2/air mixtures. *International Journal of Hydrogen Energy*. 2014;39:3450-8.

[16] Pizzuti L, Martins CA, Lacava PT. Laminar burning velocity and flammability limits in biogas: A literature review. *Renewable and Sustainable Energy Reviews*. 2016;62:856-65.

[17] Shy SS, Chen YC, Yang CH, Liu CC, Huang CM. Effects of H2 or CO2 addition, equivalence ratio, and turbulent straining on turbulent burning velocities for lean premixed methane combustion. *Combustion and Flame*. 2008;153:510-24.

[18] Hosseini SE, Bagheri G, Wahid MA. Numerical investigation of biogas flameless combustion. *Energy Conversion and Management*. 2014;81:41-50.

[19] Chen Z, Reddy V, Ruan S, Doan N, Roberts WL, Swaminathan N. Simulation of MILD combustion using Perfectly Stirred Reactor model. *Proceedings of the Combustion Institute*. 2017;36:4279-86.

[20] Sorrentino G, de Joannon M, Sabia P, Ragucci R, Cavaliere A. Numerical investigation of the ignition and annihilation of CH4/N2/O2 mixtures under MILD operative conditions with detailed chemistry. *Combustion Theory and Modelling*. 2016:1-17.

[21] Cavaliere A, de Joannon M. Mild Combustion. *Progress in Energy and Combustion Science*. 2004;30:329-66.

[22] Galletti C, Parente A, Derudi M, Rota R, Tognotti L. Numerical and experimental analysis of NO emissions from a lab-scale burner fed with hydrogen-enriched fuels and operating in MILD combustion. *International Journal of Hydrogen Energy*. 2009;34:8339-51.

[23] Karellas S, Boukis I, Kontopoulos G. Development of an investment decision tool for biogas production from agricultural waste. *Renewable and Sustainable Energy Reviews*. 2010;14:1273-82.

[24] Starr K, Gabarrell X, Villalba G, Talens L, Lombardi L. Life cycle assessment of biogas upgrading technologies. *Waste Management*. 2012;32:991-9.

[25] Scholz M, Melin T, Wessling M. Transforming biogas into biomethane using membrane technology. *Renewable and Sustainable Energy Reviews*. 2013;17:199-212.

[26] Papagiannakis RG, Hountalas DT. Combustion and exhaust emission characteristics of a dual fuel compression ignition engine operated with pilot Diesel fuel and natural gas. *Energy Conversion and Management*. 2004;45:2971-87.

[27] Hansen AC, Zhang Q, Lyne PWL. Ethanol–diesel fuel blends — a review. *Bioresource Technology*. 2005;96:277-85.

[28] Burguburu J, Cabot G, Renou B, Boukhalfa AM, Cazalens M. Effects of H 2 enrichment on flame stability and pollutant emissions for a kerosene/air swirled flame with an aeronautical fuel injector. *Proceedings of the Combustion Institute*. 2011;33:2927-35.

[29] Iannuzzi SE, Valentino G. Comparative behavior of gasoline–diesel/butanol–diesel blends and injection strategy management on performance and emissions of a light duty diesel engine. *Energy*. 2014;71:321-31.

[30] Atmanli A. Comparative analyses of diesel–waste oil biodiesel and propanol, n-butanol or 1-pentanol blends in a diesel engine. *Fuel*. 2016;176:209-15.

[31] Lee CE, Hwang CH. An experimental study on the flame stability of LFG and LFG-mixed fuels. *Fuel*. 2007;86:649-55.

[32] Lee CE, Hwang CH, Lee HY. A study on the interchangeability of LFG–LPG mixed fuels with LFG quality in domestic combustion appliances. *Fuel*. 2008;87:297-303.

[33] Cardona CA, Amell AA. Laminar burning velocity and interchangeability analysis of biogas/C3H8/H2 with normal and oxygen-enriched air. *International Journal of Hydrogen Energy*. 2013;38:7994-8001.

[34] Koroll GW, Kumar RK, Bowles EM. Burning velocities of hydrogen-air mixtures. *Combustion and Flame*. 1993;94:330-40.

[35] Das LM. Hydrogen-oxygen reaction mechanism and its implication to hydrogen engine combustion. *International Journal of Hydrogen Energy*. 1996;21:703-15.

[36] Yu G, Law CK, Wu CK. Laminar flame speeds of hydrocarbon + air mixtures with hydrogen addition. *Combustion and Flame*. 1986;63:339-47.

[37] Sher E, Ozdor N. Laminar burning velocities of n-butane/air mixtures enriched with hydrogen. *Combustion and Flame*. 1992;89:214-20.

[38] Briones AM, Aggarwal SK, Katta VR. Effects of H2 enrichment on the propagation characteristics of CH4–air triple flames. *Combustion and Flame*. 2008;153:367-83.

[39] Tang C, Huang Z, Jin C, He J, Wang J, Wang X, et al. Laminar burning velocities and combustion characteristics of propane–hydrogen–air premixed flames. *International Journal of Hydrogen Energy*. 2008;33:4906-14.

[40] Niaz S, Manzoor T, Pandith AH. Hydrogen storage: Materials, methods and perspectives. *Renewable and Sustainable Energy Reviews*. 2015;50:457-69.

[41] Singh S, Jain S, Ps V, Tiwari AK, Nouni MR, Pandey JK, et al. Hydrogen: A sustainable fuel for future of the transport sector. *Renewable and Sustainable Energy Reviews*. 2015;51:623-33.

[42] Balat M. Potential importance of hydrogen as a future solution to environmental and transportation problems. *International Journal of Hydrogen Energy*. 2008;33:4013-29.

[43] Linstrom PJ, Mallard W. *NIST Chemistry Webbook*; NIST standard reference database No. 69. 2001.

[44] Cashdollar KL, Zlochower IA, Green GM, Thomas RA, Hertzberg M. Flammability of methane, propane, and hydrogen gases. *Journal of Loss Prevention in the Process Industries*. 2000;13:327-40.

[45] Babrauskas V. *Ignition Handbook: Principles and Applications to Fire Safety Engineering, Fire Investigation, Risk Management and Forensic Science*: Fire Science Publishers; 2003.

[46] Cussler EL. *Diffusion: Mass Transfer in Fluid Systems:* Cambridge university press; 2009.

[47] Vagelopoulos CM, Egolfopoulos FN. Direct experimental determination of laminar flame speeds. *Symposium (International) on Combustion*. 1998;27:513-9.

[48] Hirasawa T, Sung CJ, Joshi A, Yang Z, Wang H, Law CK. Determination of laminar flame speeds using digital particle image velocimetry: Binary Fuel blends of ethylene, n-Butane, and toluene. *Proceedings of the Combustion Institute*. 2002;29:1427-34.

[49] Borghi R. On the structure and morphology of turbulent premixed flames. *Recent Advances in the Aerospace Sciences:* Springer; 1985. p. 117-38.

[50] Peters N. *Turbulent Combustion*: Cambridge University Press, Cambridge, UK 2000.

[51] Echekki T, Chen JH. Unsteady strain rate and curvature effects in turbulent premixed methane-air flames. *Combustion and Flame*. 1996;106:184-202.

[52] Hou SS, Lin JC. The influence of preferential diffusion and stretch on the burning intensity of a curved flame front with fuel spray. *International Journal of Heat and Mass Transfer*. 2003;46:5073-85.

[53] Jin W, Wang J, Yu S, Nie Y, Xie Y, Huang Z. Cellular instabilities of non-adiabatic laminar flat methane/hydrogen oxy-fuel flames highly diluted with CO2. *Fuel*. 2015;143:38-46.

[54] Wang J, Wei Z, Yu S, Jin W, Xie Y, Zhang M, et al. Effects of stretch and preferential diffusion on tip opening of laminar premixed Bunsen flames of syngas/air mixtures. *Fuel*. 2015;148:1-8.

[55] Poinsot T, Echekki T, Mungal MG. A Study of the Laminar Flame Tip and Implications for Premixed Turbulent Combustion. *Combustion Science and Technology*. 1992;81:45-73.

[56] De Goey L, ten Thije Boonkkamp J. A flamelet description of premixed laminar flames and the relation with flame stretch. *Combustion and Flame*. 1999;119:253-71.

[57] Vu TM, Cha MS, Lee BJ, Chung SH. Tip opening of premixed bunsen flames: Extinction with negative stretch and local Karlovitz number. *Combustion and Flame*. 2015;162:1614-21.

[58] Nguyen QV, Dibble RW, Carter CD, Fiechtner GJ, Barlow RS. Raman-LIF measurements of temperature, major species, OH, and NO in a methane-air bunsen flame. *Combustion and Flame*. 1996;105:499-510.

[59] Kojima J, Ikeda Y, Nakajima T. Basic aspects of OH(A), CH(A), and C2(d) chemiluminescence in the reaction zone of laminar methane–air premixed flames. *Combustion and Flame*. 2005;140:34-45.

[60] Mulla IA, Dowlut A, Hussain T, Nikolaou ZM, Chakravarthy SR, Swaminathan N, et al. Heat release rate estimation in laminar premixed flames using laser-induced fluorescence of CH2O and H-atom. *Combustion and Flame*. 2016;165:373-83.

[61] Bouvet N, Chauveau C, Gökalp I, Lee SY, Santoro RJ. Characterization of syngas laminar flames using the Bunsen burner configuration. *International Journal of Hydrogen Energy*. 2011;36:992-1005.

[62] He Y, Wang Z, Yang L, Whiddon R, Li Z, Zhou J, et al. Investigation of laminar flame speeds of typical syngas using laser based Bunsen method and kinetic simulation. *Fuel*. 2012;95:206-13.

[63] Walsh JL, Ross C, Smith M, Harper S, Wilkins W. *Biogas Utilization Handbook*. Georgia Institute of Technology. Atlanta, USA Febrero. 1988.

[64] Stone R, Clarke A, Beckwith P. Correlations for the Laminar-Burning Velocity of Methane/Diluent/Air Mixtures Obtained in Free-Fall Experiments. *Combustion and Flame*. 1998;114:546-55.

[65] Qin W, Egolfopoulos F, Tsotsis T. Fundamental and environmental aspects of landfill gas utilization for power generation. *Chemical Engineering Journal*. 2001;82:157-72.

[66] Ratna Kishore V, Duhan N, Ravi MR, Ray A. Measurement of adiabatic burning velocity in natural gas-like mixtures. *Experimental Thermal and Fluid Science*. 2008;33:10-6.

[67] Diaz-Gonzalez C, Arrieta AA, Suarez JL. Comparison Of Combustion Properties Of Simulated Biogas And Methane. *Ct&F-Ciencia Tecnologia Y Futuro*. 2009;3:225-36.

[68] Qiao L, Gan Y, Nishiie T, Dahm WJA, Oran ES. Extinction of premixed methane/air flames in microgravity by diluents: Effects of radiation and Lewis number. *Combustion and Flame*. 2010;157:1446-55.

[69] Park O, Veloo PS, Liu N, Egolfopoulos FN. Combustion characteristics of alternative gaseous fuels. *Proceedings of the Combustion Institute*. 2011;33:887-94.

[70] Anggono W, Wardana ING, Lawes M, Hughes KJ, Wahyudi S, Hamidi N, et al. Biogas Laminar Burning Velocity and Flammability Characteristics in Spark Ignited Premix Combustion. *Journal of Physics: Conference Series*. 2013;423.

[71] Hinton N, Stone R. Laminar burning velocity measurements of methane and carbon dioxide mixtures (biogas) over wide ranging temperatures and pressures. *Fuel*. 2014;116:743-50.

[72] Zahedi P, Yousefi K. Effects of pressure and carbon dioxide, hydrogen and nitrogen concentration on laminar burning velocities and NO formation of methane-air mixtures. *Journal of Mechanical Science and Technology*. 2014;28:377-86.

[73] Anggono W, Wardana ING, Lawes M, Hughes KJ, Wahyudi S, Hamidi N, et al. The influence of CO2 in biogas flammability limit and laminar burning velocity in spark ignited premix combustion at various pressures. *AIP Conference Proceedings*. 2016;1717:030001.

[74] Nonaka HOB, Pereira FM. Experimental and numerical study of CO2 content effects on the laminar burning velocity of biogas. *Fuel*. 2016;182:382-90.

[75] Askari MH, Ashjaee M. Experimental Measurement of Laminar Burning Velocity and Flammability Limits of Landfill Gas at Atmospheric and Elevated Pressures. *Energy & Fuels*. 2017;31:3196-205.

[76] Gong J, Zhang S, Cheng Y, Huang Z, Tang C, Zhang J. A comparative study of n-propanol, propanal, acetone, and propane combustion in laminar flames. *Proceedings of the Combustion Institute*. 2015;35:795-801.

[77] Turns S. *An Introduction to Combustion: Concepts and Applications*: McGraw-Hill Education, 2000.

[78] Ju Y, Masuya G, Ronney PD. Effects of radiative emission and absorption on the propagation and extinction of premixed gas flames. *Symposium (International) on Combustion*. 1998;27:2619-26.

[79] Dupont L, Accorsi A. Explosion characteristics of synthesised biogas at various temperatures. *Journal of Hazardous Materials*. 2006;136:520-5.

[80] Wilson DA, Lyons KM. Effects of dilution and co-flow on the stability of lifted non-premixed biogas-like flames. *Fuel*. 2008;87:405-13.

[81] Dai WN, Qin CK, Chen ZG, Tong C, Liu PJ. Experimental studies of flame stability limits of biogas flame. *Energy Conversion and Management*. 2012;63:157-61.

[82] Lamige S, Min J, Galizzi C, André F, Baillot F, Escudié D, et al. On preheating and dilution effects in non-premixed jet flame stabilization. *Combustion and Flame*. 2013;160:1102-11.

[83] Saediamiri M, Birouk M, Kozinski JA. On the stability of a turbulent non-premixed biogas flame: Effect of low swirl strength. *Combustion and Flame*. 2014;161:1326-36.

[84] Guo H, Min J, Galizzi C, Escudié D, Baillot F. A numerical study on the effects of CO2/N2/Ar addition to air on liftoff of a laminar CH4/air diffusion flame. *Combustion Science and Technology*. 2010;182:1549-63.

[85] Park J, Kim SG, Lee KM, Kim TK. Chemical effect of diluents on flame structure and NO emission characteristic in methane-air counterflow diffusion flame. *International Journal of Energy Research*. 2002;26:1141-60.

[86] Charest MRJ, Gülder ÖL, Groth CPT. Numerical and experimental study of soot formation in laminar diffusion flames burning simulated biogas fuels at elevated pressures. *Combustion and Flame*. 2014;161:2678-91.

[87] Fischer M, Jiang X. An investigation of the chemical kinetics of biogas combustion. *Fuel*. 2015;150:711-20.

[88] Mameri A, Tabet F. Numerical investigation of counter-flow diffusion flame of biogas–hydrogen blends: Effects of biogas composition, hydrogen enrichment and scalar dissipation rate on flame structure and emissions. *International Journal of Hydrogen Energy*. 2016.

[89] Jahangirian S, Engeda A, Wichman IS. Thermal and Chemical Structure of Biogas Counterflow Diffusion Flames. *Energy & Fuels*. 2009;23:5312-21.

[90] Matynia A, Molet J, Roche C, Idir M, de Persis S, Pillier L. Measurement of OH concentration profiles by laser diagnostics and modeling in high-pressure counterflow premixed methane/air and biogas/air flames. *Combustion and Flame*. 2012;159:3300-11.

[91] Lee K, Kim T, Cha H, Song S, Chun KM. Generating efficiency and NOx emissions of a gas engine generator fueled with a biogas–hydrogen blend and using an exhaust gas recirculation system. *International Journal of Hydrogen Energy*. 2010;35:5723-30.

[92] Chandra R, Vijay VK, Subbarao PMV, Khura TK. Performance evaluation of a constant speed IC engine on CNG, methane enriched biogas and biogas. *Applied Energy*. 2011;88:3969-77.

[93] Avulapati MM, Anand TNC, Ravikrishna RV. Full Chemical Kinetic Simulation of Biogas Early Phase Combustion in SI Engines. *Energy & Fuels*. 2013;27:197-207.

[94] Carrera JLE, Riesco JMA, Martinez SM, Sanchez FAC, Gallegos AM. Numerical Study on the Combustion Process Of a Biogas Spark Ignition Engine. *Thermal Science*. 2013;17:241-54.

[95] Porpatham E, Ramesh A, Nagalingam B. Effect of swirl on the performance and combustion of a biogas fuelled spark ignition engine. *Energy Conversion and Management*. 2013;76:463-71.

[96] Subramanian KA, Mathad VC, Vijay VK, Subbarao PMV. Comparative evaluation of emission and fuel economy of an automotive spark ignition vehicle fuelled with methane enriched biogas and CNG using chassis dynamometer. *Applied Energy*. 2013;105:17-29.

[97] Jiang YH, Xiong SS, Shi W, He WH, Zhang T, Lin XK, et al. Research of Biogas as Fuel for Internal Combustion Engine. *Asia-Pacific Power and Energy Engineering Conference*. 2009:457-60.

[98] Visakhamoorthy S, Tzanetakis T, Haggith D, Sobiesiak A, Wen JZ. Numerical study of a homogeneous charge compression ignition (HCCI) engine fueled with biogas. *Applied Energy*. 2012;92:437-46.

[99] Bedoya ID, Saxena S, Cadavid FJ, Dibble RW. Numerical Analysis of Biogas Composition Effects on Combustion Parameters and Emissions in Biogas Fueled HCCI Engines for Power Generation. *Journal of Engineering for Gas Turbines and Power-Transactions of the ASME*. 2013;135.

[100] Bora BJ, Saha UK, Chatterjee S, Veer V. Effect of compression ratio on performance, combustion and emission characteristics of a dual fuel diesel engine run on raw biogas. *Energy Conversion and Management*. 2014;87:1000-9.

[101] Qian Y, Sun S, Ju D, Shan X, Lu X. Review of the state-of-the-art of biogas combustion mechanisms and applications in internal combustion engines. *Renewable and Sustainable Energy Reviews*. 2017;69:50-8.

[102] Kalsi SS, Subramanian KA. Effect of simulated biogas on performance, combustion and emissions characteristics of a bio-diesel fueled diesel engine. *Renewable Energy*. 2017;106:78-90.

[103] Jahangirian S, Engeda A. Biogas Combustion And Chemical Kinetics for Gas Turbine Applications. Imece 2008: *Proceedings of the ASME International Mechanical Engineering Congress and Exposition*, Vol 3. 2009:13-22.

[104] Kang JY, Kang DW, Kim TS, Hur KB. Comparative economic analysis of gas turbine-based power generation and combined heat and power systems using biogas fuel. *Energy*. 2014;67:309-18.

[105] Guessab A, Aris A, Cheikh M, Baki T. Combustion of Methane and Biogas Fuels in Gas Turbine Can-type Combustor Model. *Journal of Applied Fluid Mechanics*. 2016;9:2229-38.

[106] Sánchez AL, Williams FA. Recent advances in understanding of flammability characteristics of hydrogen. *Progress in Energy and Combustion Science*. 2014;41:1-55.

[107] Huang Z, Zhang Y, Zeng K, Liu B, Wang Q, Jiang D. Measurements of laminar burning velocities for natural gas–hydrogen–air mixtures. *Combustion and Flame*. 2006;146:302-11.

[108] Ji C, Liu X, Wang S, Gao B, Yang J. A laminar burning velocity correlation for combustion simulation of hydrogen-enriched ethanol engines. *Fuel*. 2014;133:139-42.

[109] Nilsson EJK, van Sprang A, Larfeldt J, Konnov AA. The comparative and combined effects of hydrogen addition on the laminar burning velocities of methane and its blends with ethane and propane. *Fuel*. 2017;189:369-76.

[110] Mandilas C, Ormsby MP, Sheppard CGW, Woolley R. Effects of hydrogen addition on laminar and turbulent premixed methane and iso-octane–air flames. *Proceedings of the Combustion Institute*. 2007;31:1443-50.

[111] Tang C, Zhang Y, Huang Z. Progress in combustion investigations of hydrogen enriched hydrocarbons. *Renewable and Sustainable Energy Reviews*. 2014;30:195-216.

[112] Tang CL, Huang ZH, Law CK. Determination, correlation, and mechanistic interpretation of effects of hydrogen addition on laminar flame speeds of hydrocarbon–air mixtures. *Proceedings of the Combustion Institute*. 2011;33:921-8.

[113] Wierzba I, Ale B. Rich flammability limits of fuel mixtures involving hydrogen at elevated temperatures. *International Journal of Hydrogen Energy*. 2000;25:75-80.

[114] Guo H, Smallwood GJ, Liu F, Ju Y, Gülder ÖL. The effect of hydrogen addition on flammability limit and NOx emission in ultra-lean counterflow CH4/air premixed flames. *Proceedings of the Combustion Institute*. 2005;30:303-11.

[115] Van den Schoor F, Hermanns RTE, van Oijen JA, Verplaetsen F, de Goey LPH. Comparison and evaluation of methods for the determination of flammability limits, applied to methane/hydrogen/air mixtures. *Journal of Hazardous Materials*. 2008;150:573-81.

[116] Shoshin YL, Goey LPHd. Experimental study of lean flammability limits of methane/hydrogen/air mixtures in tubes of different diameters. *Experimental Thermal and Fluid Science*. 2010;34:373-80.

[117] Miao H, Lu L, Huang Z. Flammability limits of hydrogen-enriched natural gas. *International Journal of Hydrogen Energy*. 2011;36:6937-47.

[118] Bier K, Kappler G, Wilhelmi H. Experiments on the combustion of hydrogen and methane injected transversely into a supersonic air stream. *Symposium (International) on Combustion*. 1971;13:675-82.

[119] Ju Y, Niioka T. Ignition simulation of methane/hydrogen mixtures in a supersonic mixing layer. *Combustion and Flame*. 1995;102:462-70.

[120] Fotache C, Kreutz T, Law C. Ignition of hydrogen-enriched methane by heated air. *Combustion and Flame*. 1997;110:429-40.

[121] Hui X, Zhang C, Xia M, Sung CJ. Effects of hydrogen addition on combustion characteristics of n-decane/air mixtures. *Combustion and Flame*. 2014;161:2252-62.

[122] Huang J, Bushe W, Hill P, Munshi S. Experimental and kinetic study of shock initiated ignition in homogeneous methane – hydrogen – air mixtures at engine - relevant conditions. *International Journal of Chemical Kinetics*. 2006;38:221-33.

[123] Zhang Y, Huang Z, Wei L, Zhang J, Law CK. Experimental and modeling study on ignition delays of lean mixtures of methane, hydrogen, oxygen, and argon at elevated pressures. *Combustion and Flame*. 2012;159:918-31.

[124] Donohoe N, Heufer A, Metcalfe WK, Curran HJ, Davis ML, Mathieu O, et al. Ignition delay times, laminar flame speeds, and mechanism validation for natural gas/hydrogen blends at elevated pressures. *Combustion and Flame*. 2014;161:1432-43.

[125] Mittal G, Sung CJ, Yetter RA. Autoignition of H2/CO at elevated pressures in a rapid compression machine. *International Journal of Chemical Kinetics*. 2006;38:516-29.

[126] Kalitan DM, Mertens JD, Crofton MW, Petersen EL. Ignition and oxidation of lean CO/H2 fuel blends in air. *Journal of Propulsion and Power*. 2007;23:1291-301.

[127] Kéromnès A, Metcalfe WK, Heufer KA, Donohoe N, Das AK, Sung CJ, et al. An experimental and detailed chemical kinetic modeling study of hydrogen and syngas mixture oxidation at elevated pressures. *Combustion and Flame*. 2013;160:995-1011.

[128] Lee S, Song S. Rapid compression machine studies on ignition delay changes in a methyl butanoate/n-heptane mixture by hydrogen addition. *International Journal of Hydrogen Energy*. 2016;41:19207-17.

[129] Pan L, Hu E, Meng X, Zhang Z, Huang Z. Kinetic modeling study of hydrogen addition effects on ignition characteristics of dimethyl ether at engine-relevant conditions. *International Journal of Hydrogen Energy*. 2015;40:5221-35.

[130] Man X, Tang C, Wei L, Pan L, Huang Z. Measurements and kinetic study on ignition delay times of propane/hydrogen in argon diluted oxygen. *International Journal of Hydrogen Energy*. 2013;38:2523-30.

[131] Tang C, Man X, Wei L, Pan L, Huang Z. Further study on the ignition delay times of propane–hydrogen–oxygen–argon mixtures: Effect of equivalence ratio. *Combustion and Flame*. 2013;160:2283-90.

[132] Tang C, Huang Z, Wang J, Zheng J. Effects of hydrogen addition on cellular instabilities of the spherically expanding propane flames. *International Journal of Hydrogen Energy*. 2009;34:2483-7.

[133] Law CK. *Combustion Physics*: Cambridge university press; 2010.

[134] Law C, Kwon O. Effects of hydrocarbon substitution on atmospheric hydrogen–air flame propagation. *International Journal of Hydrogen Energy*. 2004;29:867-79.

[135] Law C, Jomaas G, Bechtold J. Cellular instabilities of expanding hydrogen/propane spherical flames at elevated pressures: theory and experiment. *Proceedings of the Combustion Institute*. 2005;30:159-67.

[136] Jomaas G, Law C, Bechtold J. On transition to cellularity in expanding spherical flames. *Journal of Fluid Mechanics*. 2007;583:1-26.

[137] Askari O, Elia M, Ferrari M, Metghalchi H. Cell formation effects on the burning speeds and flame front area of synthetic gas at high pressures and temperatures. *Applied Energy*. 2017;189:568-77.

[138] Wu L, Kobayashi N, Li Z, Huang H. Experimental study on the effects of hydrogen addition on the emission and heat transfer characteristics of laminar methane diffusion flames with oxygen-enriched air. *International Journal of Hydrogen Energy*. 2016;41:2023-36.

[139] Schefer RW, Wicksall DM, Agrawal AK. Combustion of hydrogen-enriched methane in a lean premixed swirl-stabilized burner. *Proceedings of the Combustion Institute*. 2002;29:843-51.

[140] Burbano HJ, Amell AA, Garcá JM. Effects of hydrogen addition to methane on the flame structure and CO emissions in atmospheric burners. *International Journal of Hydrogen Energy*. 2008;33:3410-5.

[141] Jones HRN, Leng J. The influence of fuel composition on emissions of CO, NO, and NO2 from a gas-fired pulsed combustor. *Combustion and Flame*. 1996;104:419-30.

[142] Tseng CJ. Effects of hydrogen addition on methane combustion in a porous medium burner. *International Journal of Hydrogen Energy*. 2002;27:699-707.

[143] Verhelst S, Wallner T. Hydrogen-fueled internal combustion engines. *Progress in Energy and Combustion Science*. 2009;35:490-527.

[144] Sierens R, Rosseel E. Variable composition hydrogen/natural gas mixtures for increased engine efficiency and decreased emissions. *Transactions-American Society of Mechanical Engineers Journal of Engineering for Gas Turbines and Power*. 2000;122:135-40.

[145] Bauer C, Forest T. Effect of hydrogen addition on the performance of methane-fueled vehicles. Part II: driving cycle simulations. *International Journal of Hydrogen Energy*. 2001;26:71-90.

[146] Bauer C, Forest T. Effect of hydrogen addition on the performance of methane-fueled vehicles. Part I: effect on SI engine performance. *International Journal of Hydrogen Energy*. 2001;26:55-70.

[147] Guo H, Hosseini V, Neill WS, Chippior WL, Dumitrescu CE. An experimental study on the effect of hydrogen enrichment on diesel fueled HCCI combustion. *International Journal of Hydrogen Energy*. 2011;36:13820-30.

[148] Miyamoto T, Hasegawa H, Mikami M, Kojima N, Kabashima H, Urata Y. Effect of hydrogen addition to intake gas on combustion and exhaust emission characteristics of a diesel engine. *International Journal of Hydrogen Energy*. 2011;36:13138-49.

[149] SinghYadav V, Soni SL, Sharma D. Performance and emission studies of direct injection C.I. engine in duel fuel mode (hydrogen-diesel) with EGR. *International Journal of Hydrogen Energy*. 2012;37:3807-17.

[150] Zhou JH, Cheung CS, Leung CW. Combustion, performance, regulated and unregulated emissions of a diesel engine with hydrogen addition. *Applied Energy*. 2014;126:1-12.

[151] Du Y, Yu X, Wang J, Wu H, Dong W, Gu J. Research on combustion and emission characteristics of a lean burn gasoline engine with hydrogen direct-injection. *International Journal of Hydrogen Energy*. 2016;41:3240-8.

[152] Niu R, Yu X, Du Y, Xie H, Wu H, Sun Y. Effect of hydrogen proportion on lean burn performance of a dual fuel SI engine using hydrogen direct-injection. *Fuel*. 2016;186:792-9.

[153] Leung T, Wierzba I. The effect of hydrogen addition on biogas non-premixed jet flame stability in a co-flowing air stream. *International Journal of Hydrogen Energy*. 2008;33:3856-62.

[154] Chen S, Zheng C. Counterflow diffusion flame of hydrogen-enriched biogas under MILD oxy-fuel condition. *International Journal of Hydrogen Energy*. 2011;36:15403-13.

[155] Zhen HS, Leung CW, Cheung CS. Effects of hydrogen addition on the characteristics of a biogas diffusion flame. *International Journal of Hydrogen Energy*. 2013;38:6874-81.

[156] Zhen HS, Leung CW, Cheung CS, Huang ZH. Characterization of biogas-hydrogen premixed flames using Bunsen burner. *International Journal of Hydrogen Energy*. 2014;39:13292-9.

[157] Zhen HS, Leung CW, Cheung CS. A comparison of the heat transfer behaviors of biogas-H2 diffusion and premixed flames. *International Journal of Hydrogen Energy*. 2014;39:1137-44.

[158] Zhen HS, Leung CW, Cheung CS, Huang ZH. Combustion characteristic and heating performance of stoichiometric biogas–hydrogen–air flame. *International Journal of Heat and Mass Transfer*. 2016;92:807-14.

[159] Zhen HS, Wei ZL, Leung CW, Cheung CS, Huang ZH. Emission of impinging biogas/air premixed flame with hydrogen enrichment. *International Journal of Hydrogen Energy*. 2016;41:2087-95.

[160] Mameri A, Tabet F. Numerical investigation of counter-flow diffusion flame of biogas–hydrogen blends: Effects of biogas composition, hydrogen enrichment and scalar dissipation rate on flame structure and emissions. *International Journal of Hydrogen Energy*. 2016;41:2011-22.

[161] Xin Z, Jian X, Shizhuo Z, Xiaosen H, Jianhua L. The experimental study on cyclic variation in a spark ignited engine fueled with biogas and hydrogen blends. *International Journal of Hydrogen Energy*. 2013;38:11164-8.

[162] Porpatham E, Ramesh A, Nagalingam B. Effect of hydrogen addition on the performance of a biogas fuelled spark ignition engine. *International Journal of Hydrogen Energy*. 2007;32:2057-65.

[163] Rakopoulos CD, Michos CN, Gialcoumis EG. Studying the effects of hydrogen addition on the second-law balance of a biogas-fuelled spark ignition engine by use of a quasi-

dimensional multi-zone combustion model. *Proceedings of the Institution of Mechanical Engineers Part D-Journal of Automobile Engineering*. 2008;222:2249-68.

[164] Jeong C, Kim T, Lee K, Song S, Chun KM. Generating efficiency and emissions of a spark-ignition gas engine generator fuelled with biogas–hydrogen blends. *International Journal of Hydrogen Energy*. 2009;34:9620-7.

[165] Park C, Park S, Lee Y, Kim C, Lee S, Moriyoshi Y. Performance and emission characteristics of a SI engine fueled by low calorific biogas blended with hydrogen. *International Journal of Hydrogen Energy*. 2011;36:10080-8.

[166] Park C, Park S, Kim C, Lee S. Effects of EGR on performance of engines with spark gap projection and fueled by biogas–hydrogen blends. *International Journal of Hydrogen Energy*. 2012;37:14640-8.

[167] Pareja J, Burbano HJ, Ogami Y. Measurements of the laminar burning velocity of hydrogen–air premixed flames. *International Journal of Hydrogen Energy*. 2010;35:1812-8.

[168] Wang ZH, Weng WB, He Y, Li ZS, Cen KF. Effect of H2/CO ratio and N2/CO2 dilution rate on laminar burning velocity of syngas investigated by direct measurement and simulation. *Fuel.* 2015;141:285-92.

[169] Mazas AN, Fiorina B, Lacoste DA, Schuller T. Effects of water vapor addition on the laminar burning velocity of oxygen-enriched methane flames. *Combustion and Flame*. 2011;158:2428-40.

[170] Hu X, Yu Q, Liu J, Sun N. Investigation of laminar flame speeds of CH4/O2/CO2 mixtures at ordinary pressure and kinetic simulation. *Energy*. 2014;70:626-34.

[171] Katta VR, Roquemore WM. Numerical studies on the structure of two-dimensional H2/air premixed jet flame. *Combustion and Flame*. 1995;102:21-40.

[172] Remie MJ, Cremers MFG, Schreel KRAM, de Goey LPH. Flame jet properties of Bunsen-type flames. *Combustion and Flame*. 2006;147:163-70.

[173] Fu J, Tang C, Jin W, Thi LD, Huang Z, Zhang Y. Study on laminar flame speed and flame structure of syngas with varied compositions using OH-PLIF and spectrograph. *International Journal of Hydrogen Energy*. 2013;38:1636-43.

[174] Higuera FJ. Aerodynamics of a slender axisymmetric Bunsen flame with large gas expansion. *Combustion and Flame*. 2009;156:1063-7.

[175] Law C, Sung C. Structure, aerodynamics, and geometry of premixed flamelets. *Progress in Energy and Combustion Science*. 2000;26:459-505.

[176] Sivashinsky G. The diffusion stratification effect in Bunsen flames. *Journal of Heat Transfer*. 1974;96:530-5.

[177] Law C, Cho P, Mizomoto M, Yoshida H. Flame curvature and preferential diffusion in the burning intensity of bunsen flames. *Symposium (International) on Combustion*. 1988:1803-9.

[178] Law C, Ishizuka S, Cho P. On the opening of premixed Bunsen flame tips. *Combustion Science and Technology*. 1982;28:89-96.

[179] Mizomoto M, Asaka Y, Ikai S, Law C. Effects of preferential diffusion on the burning intensity of curved flames. *Symposium (International) on Combustion*. 1985:1933-9.

[180] Mizomoto M, Yoshida H. Effects of Lewis number on the burning intensity of Bunsen flames. *Combustion and Flame*. 1987;70:47-60.

[181] Wu CK, Law CK. On the determination of laminar flame speeds from stretched flames. *Symposium (International) on Combustion*. 1985;20:1941-9.

[182] Echekki T, Mungal M. Flame speed measurements at the tip of a slot burner: Effects of flame curvature and hydrodynamic stretch. *Symposium (International) on Combustion*. 1991:455-61.

[183] Yamamoto K, Ozeki M, Hayashi N, Yamashita H. Burning velocity and OH concentration in premixed combustion. *Proceedings of the Combustion Institute*. 2009;32:1227-35.

[184] Higuera F. Effects of fresh gas velocity and thermal expansion on the structure of a Bunsen flame tip. *Combustion and Flame*. 2010;157:1586-93.

[185] Candel SM. Combustion instabilities coupled by pressure waves and their active control. *Symposium (International) on Combustion*. 1992;24:1277-96.

[186] Ayoola BO, Balachandran R, Frank JH, Mastorakos E, Kaminski CF. Spatially resolved heat release rate measurements in turbulent premixed flames. *Combustion and Flame*. 2006;144:1-16.

[187] Swaminathan N, Xu G, Dowling A, Balachandran R. Heat release rate correlation and combustion noise in premixed flames. *Journal of Fluid Mechanics*. 2011;681:80-115.

[188] Gatowski J, Balles EN, Chun K, Nelson F, Ekchian J, Heywood JB. Heat release analysis of engine pressure data. *SAE Technical Paper*; 1984.

[189] Najm H, Knio O, Paul P, Wyckoff P. A study of flame observables in premixed methane-air flames. *Combustion Science and Technology*. 1998;140:369-403.

[190] Najm HN, Paul PH, Mueller CJ, Wyckoff PS. On the Adequacy of Certain Experimental Observables as Measurements of Flame Burning Rate. *Combustion and Flame*. 1998;113:312-32.

[191] Paul PH, Najm HN. Planar laser-induced fluorescence imaging of flame heat release rate. *Symposium (International) on Combustion*. 1998;27:43-50.

[192] Gordon RL, Masri AR, Mastorakos E. Heat release rate as represented by [OH]×[CH2O] and its role in autoignition. *Combustion Theory and Modelling*. 2009;13:645-70.

[193] Gazi A, Vourliotakis G, Skevis G, Founti MA. Assessment of Chemical Markers for Heat-Release Rate Correlations in Laminar Premixed Flames. *Combustion Science and Technology*. 2013;185:1482-508.

[194] Kariuki J, Dowlut A, Yuan R, Balachandran R, Mastorakos E. Heat release imaging in turbulent premixed methane–air flames close to blow-off. *Proceedings of the Combustion Institute*. 2015;35:1443-50.

[195] Böckle S, Kazenwadel J, kunzelmann T, Shin D-I, Schulz C, Wolfrum J. Simultaneous single-shot laser-based imaging of formaldehyde, OH, and temperature in turbulent flames. *Proceedings of the Combustion Institute*. 2000;28:279-86.

[196] Gordon RL, Masri AR, Mastorakos E. Simultaneous Rayleigh temperature, OH- and CH2O-LIF imaging of methane jets in a vitiated coflow. *Combustion and Flame*. 2008;155:181-95.

[197] Röder M, Dreier T, Schulz C. Simultaneous measurement of localized heat release with OH/CH2O-LIF imaging and spatially integrated OH* chemiluminescence in turbulent swirl flames. *Applied Physics B*. 2012;107:611-7.

[198] Zhou B, Brackmann C, Wang Z, Li Z, Richter M, Aldén M, et al. Thin reaction zone and distributed reaction zone regimes in turbulent premixed methane/air flames: Scalar distributions and correlations. *Combustion and Flame*. 2017;175:220-36.

[199] Nikolaou ZM, Swaminathan N. Heat release rate markers for premixed combustion. *Combustion and Flame*. 2014;161:3073-84.

[200] Dworkin SB, Schaffer AM, Connelly BC, Long MB, Smooke MD, Puccio MA, et al. Measurements and calculations of formaldehyde concentrations in a methane/N2/air, non-premixed flame: Implications for heat release rate. *Proceedings of the Combustion Institute*. 2009;32:1311-8.

[201] Tolocka MP, Miller JH. Measurements of formaldehyde concentrations and formation rates in a methane-air, non-premixed flame and their implications for heat-release rate. *Symposium (International) on Combustion*. 1998;27:633-40.

[202] Vagelopoulos CM, Frank JH. An experimental and numerical study on the adequacy of CH as a flame marker in premixed methane flames. *Proceedings of the Combustion Institute*. 2005;30:241-9.

[203] Hossain A, Nakamura Y. A numerical study on the ability to predict the heat release rate using CH* chemiluminescence in non-sooting counterflow diffusion flames. *Combustion and Flame*. 2014;161:162-72.

[204] Chander S, Ray A. Flame impingement heat transfer: A review. *Energy Conversion and Management*. 2005;46:2803-37.

[205] Viskanta R. Heat transfer to impinging isothermal gas and flame jets. *Experimental Thermal and Fluid Science*. 1993;6:111-34.

[206] Milson A, Chigier NA. Studies of methane and methane-air flames impinging on a cold plate. *Combustion and Flame*. 1973;21:295-305.

[207] Van der Meer TH. Stagnation point heat transfer from turbulent low Reynolds number jets and flame jets. *Experimental Thermal and Fluid Science*. 1991;4:115-26.

[208] Zhang Y, Bray KNC. Characterization of impinging jet flames. *Combustion and Flame*. 1999;116:671-4.

[209] Hou SS, Ko YC. Effects of heating height on flame appearance, temperature field and efficiency of an impinging laminar jet flame used in domestic gas stoves. *Energy Conversion and Management*. 2004;45:1583-95.

[210] Dong LL, Leung CW, Cheung CS. Heat transfer characteristics of an impinging butane/air flame jet of low Reynolds number. *Experimental Heat Transfer*. 2001;14:265-82.

[211] Wu J, Seyed–Yagoobi J, Page RH. Heat transfer and combustion characteristics of an array of radial jet reattachment flames. *Combustion and Flame*. 2001;125:955-64.

[212] Dong LL, Cheung CS, Leung CW. Heat transfer from an impinging premixed butane/air slot flame jet. *International Journal of Heat and Mass Transfer*. 2002;45:979-92.

[213] Hindasageri V, Vedula RP, Prabhu SV. Heat transfer distribution of swirling flame jet impinging on a flat plate using twisted tapes. *International Journal of Heat and Mass Transfer*. 2015;91:1128-39.

[214] Ng TK, Leung CW, Cheung CS. Experimental investigation on the heat transfer of an impinging inverse diffusion flame. *International Journal of Heat and Mass Transfer*. 2007;50:3366-75.

[215] Zhen HS, Leung CW, Cheung CS. Heat transfer from a turbulent swirling inverse diffusion flame to a flat surface. *International Journal of Heat and Mass Transfer*. 2009;52:2740-8.

[216] Dong LL, Leung CW, Cheung CS. Heat transfer of a row of three butane/air flame jets impinging on a flat plate. *International Journal of Heat and Mass Transfer*. 2003;46:113-25.

[217] Geers LG, Tummers M, Hanjalić K. Experimental investigation of impinging jet arrays. *Experiments in Fluids*. 2004;36:946-58.

[218] Hindasageri V, Vedula RP, Prabhu SV. Heat transfer distribution for three interacting methane–air premixed impinging flame jets. *International Journal of Heat and Mass Transfer*. 2015;88:914-25.

[219] Li HB, Zhen HS, Leung CW, Cheung CS. Nozzle effect on heat transfer and CO emission of impinging premixed flames. *International Journal of Heat and Mass Transfer*. 2011;54:625-35.

[220] Baukal CE, Gebhart B. Surface condition effects on flame impingement heat transfer. *Experimental Thermal and Fluid Science*. 1997;15:323-35.

[221] Zhao Z, Wong TT, Leung CW. Impinging premixed butane/air circular laminar flame jet—influence of impingement plate on heat transfer characteristics. *International Journal of Heat and Mass Transfer*. 2004;47:5021-31.

[222] Agrawal GK, Chakraborty S, Som SK. Heat transfer characteristics of premixed flame impinging upwards to plane surfaces inclined with the flame jet axis. *International Journal of Heat and Mass Transfer*. 2010;53:1899-907.

[223] Li HB, Zhen HS, Leung CW, Cheung CS. Effects of plate temperature on heat transfer and emissions of impinging flames. *International Journal of Heat and Mass Transfer*. 2010;53:4176-84.

[224] McDaniel C, Webb B. Slot jet impingement heat transfer from circular cylinders. *International Journal of Heat and Mass Transfer*. 2000;43:1975-85.

[225] Chander S, Ray A. Heat transfer characteristics of laminar methane/air flame impinging normal to a cylindrical surface. *Experimental Thermal and Fluid Science*. 2007;32:707-21.

[226] Chan T, Leung C, Jambunathan K, Ashforth-Frost S, Zhou Y, Liu M. Heat transfer characteristics of a slot jet impinging on a semi-circular convex surface. *International Journal of Heat and Mass Transfer*. 2002;45:993-1006.

[227] Fenot M, Dorignac E, Vullierme JJ. An experimental study on hot round jets impinging a concave surface. *International Journal of Heat and Fluid Flow*. 2008;29:945-56.

[228] Kataoka M. Optimal nozzle-to-plate spacine for convective heat transfer in nonisothermal, variable-density impinging jets. *Drying Technology*. 1985;3:235-54.

[229] Hou SS, Ko YC. Influence of oblique angle and heating height on flame structure, temperature field and efficiency of an impinging laminar jet flame. *Energy Conversion and Management*. 2005;46:941-58.

[230] Remie MJ, Cremers MFG, Schreel KRAM, de Goey LPH. Analysis of the heat transfer of an impinging laminar flame jet. *International Journal of Heat and Mass Transfer*. 2007;50:2816-27.

[231] Remie MJ, Särner G, Cremers MFG, Omrane A, Schreel KRAM, Aldén LEM, et al. Heat-transfer distribution for an impinging laminar flame jet to a flat plate. *International Journal of Heat and Mass Transfer*. 2008;51:3144-52.

[232] Chander S, Ray A. Experimental and numerical study on the occurrence of off-stagnation peak in heat flux for laminar methane/air flame impinging on a flat surface. *International Journal of Heat and Mass Transfer*. 2011;54:1179-86.

[233] Chander S, Ray A. An experimental and numerical study of stagnation point heat transfer for methane/air laminar flame impinging on a flat surface. *International Journal of Heat and Mass Transfer*. 2008;51:3595-607.

[234] Baukal C, Gebhart B. Heat transfer from oxygen-enhanced/natural gas flames impinging normal to a plane surface. *Experimental Thermal and Fluid Science*. 1998;16:247-59.

[235] Zhen HS, Cheung CS, Leung CW, Choy YS. Effects of hydrogen concentration on the emission and heat transfer of a premixed LPG-hydrogen flame. *International Journal of Hydrogen Energy*. 2012;37:6097-105.

[236] Hindasageri V, Vedula RP, Prabhu SV. Heat transfer distribution for impinging methane–air premixed flame jets. *Applied Thermal Engineering*. 2014;73:461-73.

[237] Singh S, Chander S. Heat transfer characteristics of dual swirling flame impinging on a flat surface. *International Journal of Thermal Sciences*. 2015;89:1-12.

[238] Kuntikana P, Prabhu SV. Air jet impingement technique for thermal characterisation of premixed methane–air impinging flame jets. *Applied Thermal Engineering*. 2016;99:905-18.

[239] Mohr J, Seyed-Yagoobi J, Page R. Heat transfer from a pair of radial jet reattachment flames. *Journal of Heat Transfer*. 1997;119:633-5.

[240] Singh G, Chander S, Ray A. Heat transfer characteristics of natural gas/air swirling flame impinging on a flat surface. *Experimental Thermal and Fluid Science*. 2012;41:165-76.

[241] Mohr JW, Seyed-Yagoobi J, Page RH. Combustion measurements from an impinging Radial Jet Reattachment flame. *Combustion and Flame*. 1996;106:69-80.

[242] Dong L, Leung C, Cheung C. Combustion optimization of a slot flame jet impingement system. *Journal of the Institute of Energy*. 2003: 80-8.

[243] Mishra DP. Emission studies of impinging premixed flames. *Fuel*. 2004;83:1743-8.

[244] Saha C, Ganguly R, Datta A. Heat Transfer and Emission Characteristics of Impinging Rich Methane and Ethylene Jet Flames. *Experimental Heat Transfer*. 2008;21:169-87.

[245] Butcher S, Rao U, Smith K, Osborn J, Azuma P, Fields H. Emission factors and efficiencies for small-scale open biomass combustion-toward standard measurement techniques. *Proceedings of Annual Meeting of the American Chemical Society: American Chemical Society, Washington, D.C.*; 1984. p. 122-8.

[246] Kline SJ, McClintock F. Describing uncertainties in single-sample experiments. *Mechanical Engineering*. 1953;75:3-8.

[247] Kee RJ, Grcar JF, Smooke MD, Miller JA. A FORTRAN program for modeling steady, laminar, one-dimensional premixed flames. *SNAD85–8240 Sandia National Laboratories*. 1993.

[248] CD-Adapco. Methodology, STAR-CD Version 4.08, 200 Shepherds Bush Rd London 2008.

[249] Guo H, Smallwood G, Liu F, Ju Y, Gulder O. The effect of hydrogen addition on flammability limit and NOx emission in ultra-lean counterflow CH4/air premixed flames. *Proceedings of the Combustion Institute*. 2005;30:303-11.

[250] Smith GP, Golden DM, Frenklach M, Moriarty NW, Eiteneer B, Goldenberg M, et al. GRI 3.0. Gas Research Institute, Chicago, IL, (http://www.me.berkeley.edu/gri_mech/).

[251] San Diego Mechanism. Chemical-Kinetic Mechanisms for Combustion, ApplicationsSan Diego Mechanism web page, Mechanical and Aerospace Engineering (Combustion Research), University of California at San Diego, (http://combustion.ucsd.edu).

[252] Peters N, Rogg B. *Reduced Kinetic Mechanisms for Applications in Combustion Systems*: Springer Science & Business Media; 1993.

[253] Wei ZL, Leung CW, Cheung CS, Huang ZH. Effects of equivalence ratio, H2 and CO2 addition on the heat release characteristics of premixed laminar biogas-hydrogen flame. *International Journal of Hydrogen Energy*. 2016;41:6567-80.

[254] Wei ZL, Leung CW, Cheung CS, Huang ZH. Single-valued prediction of markers on heat release rate for laminar premixed biogas-hydrogen and methane-hydrogen flames. *Energy*. 2017;133:35-45.

[255] Dagaut P, Nicolle A. Experimental and detailed kinetic modeling study of hydrogen-enriched natural gas blend oxidation over extended temperature and equivalence ratio ranges. *Proceedings of the Combustion Institute*. 2005;30:2631-8.

[256] Lafay Y, Renou B, Cabot G, Boukhalfa M. Experimental and numerical investigation of the effect of H2 enrichment on laminar methane–air flame thickness. *Combustion and Flame*. 2008;153:540-61.

[257] Liu F, Guo H, Smallwood GJ, Gülder ÖL. The chemical effects of carbon dioxide as an additive in an ethylene diffusion flame: implications for soot and NOx formation. *Combustion and Flame*. 2001;125:778-87.

[258] Farrow RL, Bui-Pham MN, Sick V. Degenerate four-wave mixing measurements of methyl radical distributions in hydrocarbon flames: Comparison with model predictions. *Symposium (International) on Combustion*. 1996;26:975-83.

[259] Wu Y, Bottom A, Zhang Z, Ombrello TM, Katta VR. Direct measurement of methyl radicals in a methane/air flame at atmospheric pressure by radar REMPI. *Optics Express*. 2011;19:23997-4004.

[260] Wu Y, Zhang Z, Ombrello TM, Katta VR. Quantitative Radar REMPI measurements of methyl radicals in flames at atmospheric pressure. *Applied Physics B*. 2013;111:391-7.

[261] Fuchs H, Bohn B, Hofzumahaus A, Holland F, Lu K, Nehr S, et al. Detection of HO2 by laser-induced fluorescence: calibration and interferences from RO2 radicals. *Atmospheric Measurement Techniques*. 2011;4:1209.

[262] Wei ZL, Zhen HS, Leung CW, Cheung CS, Huang ZH. Heat transfer characteristics and the optimized heating distance of laminar premixed biogas-hydrogen Bunsen flame impinging on a flat surface. *International Journal of Hydrogen Energy*. 2015;40:15723-31.

[263] Wei ZL, Leung CW, Cheung CS, Huang ZH. Effects of H2 and CO2 addition on the heat transfer characteristics of laminar premixed biogas–hydrogen Bunsen flame. *International Journal of Heat and Mass Transfer*. 2016;98:359-66.

[264] Hargrave GK, Fairweather M, Kilham JK. Forced convective heat transfer from premixed flames —Part 2: Impingement heat transfer. *International Journal of Heat and Fluid Flow*. 1987;8:132-8.

[265] Watanabe H, Arai F, Okazaki K. Role of CO2 in the CH4 oxidation and H2 formation during fuel-rich combustion in O2/CO2 environments. *Combustion and Flame*. 2013;160:2375-85.

[266] Mordaunt CJ, Pierce WC. Design and preliminary results of an atmospheric-pressure model gas turbine combustor utilizing varying CO2 doping concentration in CH4 to emulate biogas combustion. *Fuel*. 2014;124:258-68.

[267] Law CK, Sung CJ. Structure, aerodynamics, and geometry of premixed flamelets. *Progress in Energy and Combustion Science*. 2000;26:459-505.

[268] Wei ZL, Zhen HS, Leung CW, Cheung CS, Huang ZH. Experimental and numerical study on the emission characteristics of laminar premixed biogas-hydrogen impinging flame. *Fuel*. 2017;195:1-11.

[269] Sano T. NO2 Formation in the Mixing Region of Hot Burned Gas with Cool Air. *Combustion Science and Technology*. 1984;38:129-44.

[270] Chen RH. A parametric study of NO2 emission from turbulent H2 and CH4 jet diffusion flames. *Combustion and Flame*. 1998;112:188-98.

[271] Sano T. NO2 Formation in the Mixing Region of Hot Burned Gas with Cool Air—Effect of Surrounding Air. *Combustion Science and Technology*. 1985;43:259-69.